Raytrace Simulations and Experimental Studies of Luminescent Solar Concentrators

by

Rahul Bose

Submitted for the degree of
Doctor of Philosophy

from the
Department of Physics
Imperial College London

August 2013

Declaration of Originality

I, Rahul Bose, declare that this thesis, titled 'Raytrace Simulations and Experimental Studies of Luminescent Solar Concentrators' and the work presented in it are my own with the exception of contributions from other sources which are referenced accordingly.

Abstract

The luminescent solar concentrator is a planar, non-tracking device. Originally introduced more than three decades ago, it has yet to establish itself as a means of making photovoltaic solar energy more cost effective. Advances in organic luminescent centres, the emergence of inorganic nanocrystals and the development of new light trapping techniques have created promising opportunities for the LSC.

This thesis investigates novel geometries and materials for the practical exploitation of LSCs. The research is based on experimental measurements as well as computational simulations using a Raytrace Model. It is shown both experimentally and computationally that a thin-film structure produces the same efficiency as a homogeneously doped LSC.

Two building integrated applications are examined. The first one is a power generating window employing a Lumogen Violet dye that absorbs short wavelength radiation and is mostly transparent in the visible. Annual yields of over 23 kWh/m2 and a conversion efficiency of over 1 % are predicted for a 50 cm by 50 cm device. The second BIPV application is the light-bar, which is designed to act as the secondary concentrator in a Venetian blind-like system. With linear Fresnel lenses producing a primary concentration factor of ~ 20, an optimised system could generate nearly 60 W/m^2 of power at an efficiency of nearly 6 % using direct sunlight only.

Two novel luminescent materials, nanorods and phycobilisomes have been tested for their potential to reduce re-absorption losses. Despite current practical limitations, these materials are found to be promising due to enhanced Stokes shifts.

LSCs with optical concentrations of 10 to 20 could be feasible by addressing the key shortcomings in the form of unabsorbed light and escape cone losses. Their versatility with regards to shape, colour and light absorption makes LSCs particularly relevant for building integrated photovoltaics.

Acknowledgements

There are many who deserve my gratitude - friends, family and colleagues, who have supported me and enabled me to carry out my PhD. Beyond these, there are a few whom I would like to acknowledge explicitly.

During my PhD I have had the privilege to be a part of a dynamic research team, to carry out my research with a lot of freedom and responsibility, to participate in fruitful collaborations and to present my work at various international conferences. For this I express my deepest gratitude to Keith Barnham. Keith has been an inspiring supervisor with a contagious enthusiasm for what he does. I have learnt to greatly appreciate his dedication and steadfast support, especially when it came to him proofreading my drafts at 2 am the night before paper submission deadlines!

Many thanks also go to Amanda Chatten for her guidance and confidence in me, to Daniel Farrell for showing me the ropes, to Mauro Pravettoni for our joint endeavours and to Ned Ekins-Daukes for being a major influence in my academic life.

Finally, I must acknowledge Jessica Adams, Ben Browne and Markus Führer for making my PhD journey as enjoyable as it has been.

Contents

List of Figures

List of Tables

Abbreviations

AM	**A**ir **M**ass
AOD	**A**erosol **O**ptical **D**epth
BIPV	**B**uilding **I**ntegrated **P**hoto**v**oltaics
CPV	**C**oncentrator **P**hoto**v**oltaics
CSP	**C**oncentrating **S**olar **P**ower
DBR	**D**istributed **B**ragg **R**eflector
FF	**F**ill **F**actor
FIT	**F**eed-**I**n **T**ariff
FRET	**F**luorescence (R)esonance **E**nergy **T**ransfer
LSC	**L**uminescent **S**olar **C**oncentrator
MEG	**M**ultiple **E**xciton **G**eneration
NIR	**N**ear **I**nfra**r**ed
OC	**O**pen **C**ircuit
OD	**O**ptical **D**ensity
OPV	**O**rganic **P**hoto**v**oltaics
OQE	**O**ptical **Q**uantum **E**fficiency
PBS	**P**hyco**b**ili**s**ome
PL	**P**hoto**l**uminescence
PLE	**P**hoto**l**uminescence **E**xcitation
PV	**P**hoto**v**oltaic(s)
QE	**Q**uantum **E**fficiency
QY	**Q**uantum **Y**ield
SC	**S**hort **C**ircuit
SE	**S**tandard **E**rror
TF	**T**hin **F**ilm

TIR **T**otal **I**internal **R**eflection

UV **U**ltra**v**iolet

Physical Constants

Speed of Light	c	$=$	$2.998 \times 10^{8}\ \mathrm{m\,s^{-1}}$
Elementary charge	e	$=$	$1.602 \times 10^{-19}\ \mathrm{C}$
Planck's constant	h	$=$	$6.626 \times 10^{-34}\ \mathrm{J\,s}$
Reduced Planck constant	$\hbar$	$=$	$1.055 \times 10^{-34}\ \mathrm{J\,s}\ (\equiv h/2\pi)$
Boltzmann constant	k	$=$	$1.381 \times 10^{-23}\ \mathrm{J\,K^{-1}}$

Symbols

A	area	m^2
$\tilde{A}$	absorbance	dimensionless quantity
A_λ	spectral absorptance	dimensionless quantity
B	brightness	$\mathrm{s}^{-1}\mathrm{m}^{-2}\mathrm{nm}^{-1}$
C	optical concentration	dimensionless quantity
E	energy	J
G	geometric gain	dimensionless quantity
I	current	A
I_γ	(total) irradiance	Wm^{-2}
I_λ	spectral irradiance	$\mathrm{Wm}^{-2}\mathrm{nm}^{-1}$
J	current density	Am^{-2}
$\mathbf{k}$	wavevector	m^{-1}
n	refractive index	dimensionless quantity
$\tilde{n}$	number density	m^{-3}
N	particle number	dimensionless quantity
$\dot{N}$	photon rate	s^{-1}
P	power	W
r	re-absorption probability	dimensionless quantity
R_λ	spectral reflectance	dimensionless quantity
$S\lambda$	normalised light spectrum	nm^{-1}
T	temperature	K
T_λ	spectral transmittance	dimensionless quantity
V	voltage	V

α	absorption coefficient	m^{-1}
η	efficiency	dimensionless quantity
λ	wavelength	m
ν	frequency	s^{-1}
σ	absorption cross-section	m^2
Φ	photon flux	$s^{-1}m^{-2}$
Φ_λ	spectral photon flux	$s^{-1}m^{-2}nm^{-1}$
ω	angular frequency	$rads^{-1}$

Chapter 1

Introduction

1.1 Drivers for Renewable Energy

In the light of the world's ever-growing energy demands [1] and the urge to reduce greenhouse gases, the development of sustainable energy is a pressing task for science. As a renewable energy technology, photovoltaics is likely to play a key role in our future energy mix [2].

The scientific consensus is that the rapid global warming observed in the past decades is very likely due to anthropogenic factors [3]. If energy production maintains its current trend, greenhouse gases, in particular carbon dioxide emissions associated with fossil fuels, could have a detrimental impact on the global ecosystem and on human society; places already struggling with other stresses such as food security would be the most vulnerable [3]. Besides the environmental concerns, the main political motivation for a migration from fossil fuels to alternative energy sources are energy security and independence.

While renewable energy can be considered the long-term route to mitigating climate change, carbon capture and storage and nuclear energy present two significant short-term solutions related to the energy production side. In France, for instance, about 80 % of the electricity is produced by nuclear power plants [4, Electricity generation by fuel - France], which helps the country obtain carbon dioxide emissions per capita that are about 30 % lower than that of the UK [5]. Though often grouped with renewables such as wind, solar and hydroelectric energy with regard to emissions, the term "renewable" clearly

does not apply to nuclear energy. Compared to oil and gas however, the availability of nuclear fuel is large, and nuclear energy can also provide energy independence for some countries. Contrary to general perception, the immediate fatalities caused by nuclear energy are the lowest in comparison with the other major forms of energy: coal, oil, natural gas, liquefied petroleum gas (LPG) and hydroelectric. The average number of immediate deaths per terawatt-year of electricity generated lies around eight for nuclear while it is over a thousand for hydroelectric, see for instance Ref. 6. This however does not take into account any long-term effects. Moreover, nuclear energy comes with high capital costs, long construction times and the problem of radioactive waste disposal.

International agreements can exert political pressure on nations to address the energy and climate issues. The Kyoto Protocol, for instance, has set binding targets for 37 industrialised countries and the European Union for reducing green house gas emissions by 2012 [7]. Additionally, the European Commission has introduced legislation to implement its "20-20-20" targets: a reduction in greenhouse gas emissions to at least 20 % below the 1990 levels, a reduction of primary energy consumption by 20 % compared to projections and a 20 % contribution of renewable sources to the energy consumption by 2020.

The Kyoto Protocol also introduced a "carbon market" as a tool to facilitate a reduction in global greenhouse gas emissions [7]. This system allows parties to trade carbon credits, thereby rendering clean energy economically desirable. Further economic drivers are domestic governmental incentives in various countries that aim to lower the barriers for technologies such as photovoltaics. These can range from subsidies to feed-in tariffs (FITs), such as the one introduced in the UK in April 2010. Designed to increase the payback from renewable energy just enough to make it attractive for the consumer and thereby encourage the growth of the industry during its pre-competitive phase, the FIT has proven to be a powerful tool in the past, with Germany being a prime example [8]. The unexpectedly rapid growth of solar energy in Spain in the recent past, following the introduction of an evidently too generous FIT, which subsequently led to a drastic cut as government funds were diminishing [8], showed how delicate the balance of this tariff can be. In late 2011 and early 2012 several other European countries such as the UK and Germany were forced to consider cuts to their FITs. This was a result of unexpectedly high installed PV capacities along with dropping solar module prices due

to a large oversupply in 2011. In any case, a gradual reduction of subsidies is expected as photovoltaic energy becomes more cost-competitive.

The point at which electricity from renewable sources is cost-competitive with conventional electricity from the grid is called grid-parity. In the case of photovoltaics, grid-parity depends on the cost of the photovoltaic installation, the energy generated and the conventional electricity prices. The solar irradiation is dependent on geographical location and orientation of the solar panel, but does not vary notably from year to year, while technological development and economies of scale continuously drive the efficiency of photovoltaics up and the cost down. Given that two thirds of the globally generated electricity originates from fossil fuels [9, Electricity generation by fuel - World] with obviously finite supplies one can expect a rise in the cost of conventional electricity that will ultimately favour renewable sources.

Currently about a quarter of the world's population still lives without electricity [10]. Climate change and energy independence aside, renewable energy seems the only long-term, sustainable solution to the world's growing energy need and diminishing resources.

1.2 Photovoltaic Technology

Photovoltaic (PV) energy conversion via solar cells is one of several ways by which we harness the Sun's energy. One of the simplest ways is probably using the thermal energy in sunlight for water heating, quite common in sunny urban regions, where it alleviates the use of electricity or fossil fuels to do the same job. An indirect way of creating electricity from sunlight is through concentrating solar power (CSP), where focussing optics such as parabolic mirrors are used to heat a working substance that is subsequently passed through a heat engine. Since heat engines have been around for centuries, the technology is very mature and is therefore close to its theoretical efficiency limit. Subsequently, CSP is unlikely to achieve efficiencies much beyond its current level of around 40 %. Incidentally, electricity generation from fossil fuels is also based on heat engines. Photovoltaics, however, turns light directly into electricity and has huge future potential as its theoretical efficiency limit lies at 86.8 % [11]. Moreover, photovoltaics is scalable and can be decentralised, thereby affording the electrification of off-grid, rural areas.

Since the invention of the first silicon solar cell in 1954 [12], photovoltaic technology has taken on several different forms. By far the bulk of all installed solar cells is based on crystalline silicon, which can be considered a mature technology, and though research grade silicon cells can achieve efficiencies above 20 % [13], the typical efficiencies of deployed cells range from 12 to 17 %. Research into new materials has led to the emergence of thin-film technologies, such as amorphous silicon, CdTe, CIS and CIGS. These technologies have relatively low efficiencies around 10 % for average commercial cells and 20 % for champion cells, but are attractive as they use significantly less material, making them relatively inexpensive and allowing for simpler or more versatile fabrication techniques, like large-area printing onto flexible substrates.

Martin Green categorises the main photovoltaic technologies into three generations [11], the first comprising the wafer-based silicon cells, the second comprising the thin-film cells. The third generation describes high-efficiency, low-cost concepts, targeting efficiencies that outplay the first generation by several factors. Currently the best candidates for the third generation are multijunction solar cells. The Fraunhofer ISE [14], Spectrolab [15] and the National Renewable Energy Laboratory (NREL) have all surpassed the 40 % mark with triple-junction cells fabricated using different techniques [13]. These cells are still two orders of magnitude more expensive than first generation cells, which has limited their practical application mainly to space photovoltaics, where weight considerations tip the balance in favour of efficiency over cost. Silicon cells too were initially only used in space, before they became ubiquitous on Earth. In 1958 the satellite Vanguard I was the first to feature solar cells, made of silicon. Today, virtually all satellites sent into orbit are equipped with multijunction solar cells, and they are gradually finding terrestrial application in concentrator photovoltaics (CPV). CPV systems typically focus several hundred times the intensity of sunlight onto small arrays of solar cells with the aid of lenses or mirrors, thereby minimising the amount of expensive cell material. Besides making the cells more cost-effective, concentration also enables higher efficiencies.

The solar cell technologies mentioned so far are all based on inorganic materials. A fairly new branch of PV is organic PV (OPV), which emerged only within the last decade. Most of the materials required for OPV are cheap and abundant, and the fabrication is very inexpensive, so that organic solar cells can undercut crystalline silicon and thin-film solar cells in terms of cost. Further advantages are that they can be thin and

flexible. Challenges for OPV are currently low efficiencies around 5 % and short lifetimes compared to inorganic technologies, for which the industrial standard lifetime is around 25 years. However, a short lifetime would not be a problem for disposable use. As a low capital cost technology OPV lends itself well to off-grid application in developing countries. Figure 1.1 gives an overview of the different PV technologies and their record efficiencies. It shows how photovoltaics is a dynamic and continually progressing research field.

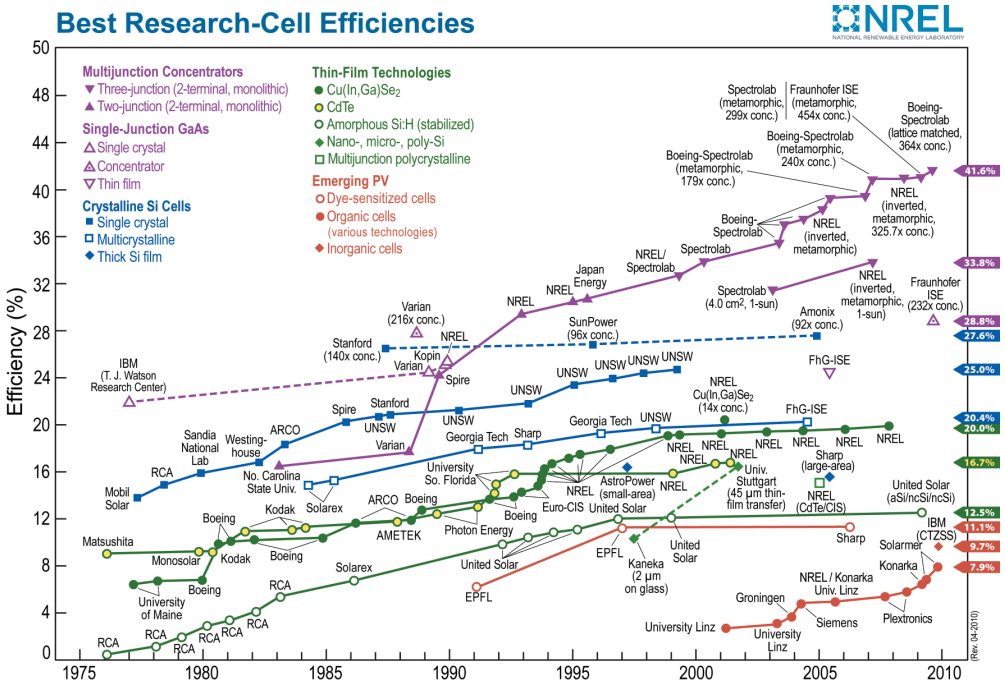

FIGURE 1.1: Best research-cell efficiences, updated 2010 (data compiled by Lawrence Kazmerski, NREL) [16].

1.3 The Luminescent Solar Concentrator

The idea of the luminescent solar concentrator (LSC) is to make photovoltaics more cost-effective, by boosting the power conversion of solar cells with the use of a relatively inexpensive, versatile concentrator (see Figure 1.2). It is a planar low-concentration device employing luminescent centres such as dyes or nanocrystals and is particularly well suited to building integrated photovoltaics (BIPV).

The LSC was originally proposed in the 1976 [17], and a comprehensive review was published by A. Goetzberger in 1977 [18]. It attracted much interest in the years to

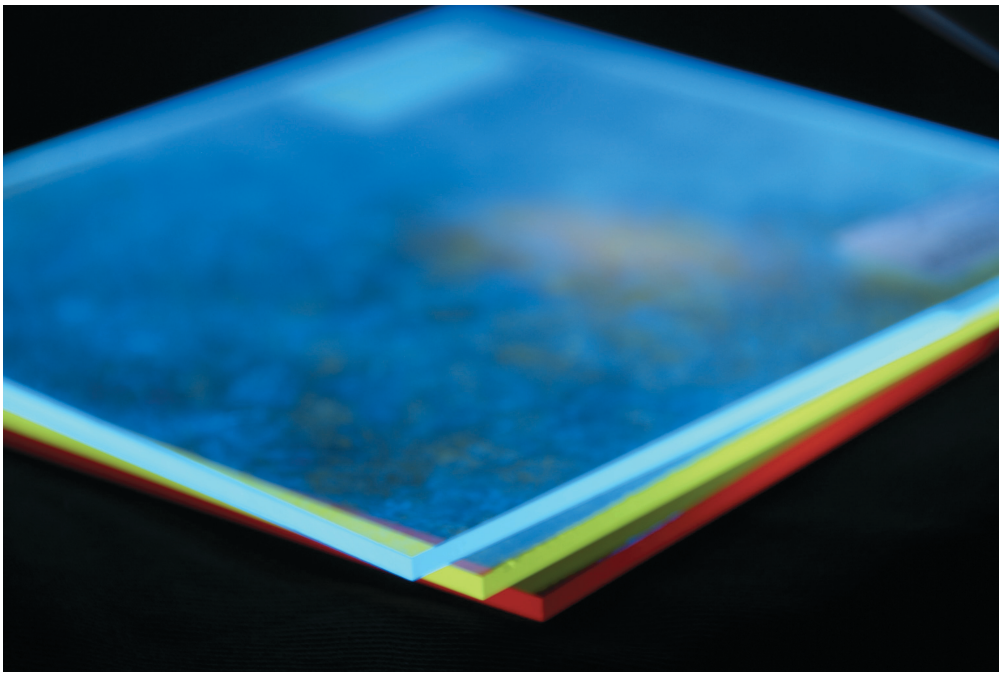

FIGURE 1.2: A picture of three luminescent solar concentrators. Each concentrator absorbs a different part of the incident spectrum over the top surface and emits light in a concentrated, narrow spectrum out of the edges.

follow [19–23]. The first LSCs used organic dyes as luminescent species which turned out to degrade in sunlight [24], posing a major obstacle to the production of commercially viable concentrators. In the past decade there has been a renewed interest in the LSC resulting from a number of factors, including the availability of photo-stable organic dyes with high luminescence quantum yields (QYs). In addition, higher efficiency cells have become available, and novel luminescent centres such as quantum dots have been proposed [25] and studied.

The LSC can collect direct as well as indirect light and, unlike geometrical concentrators, does not require tracking. Costing more than the solar cells, tracking is the highest single expenditure in CPV systems [26]. The non-tracking approach of LSCs alleviates space, cost and maintenance requirements, allowing for a different range of applications. The LSC outputs a narrow, red-shifted spectrum, which can be matched to the PV cell absorption. This way the light coupled into the cell is converted more efficiently. Because the thermalisation of the radiation happens in the LSC, unwanted heating of the cell can be avoided. Furthermore, a stacked arrangement of LSCs [18] can be used to utilise the broad solar spectrum more efficiently by spectrally separating the light and guiding it to the appropriate PV cells. The LSC is versatile in that it can be designed

to be semi-transparent or coloured, as well as flexible. By reducing the amount of solar cells required, the LSC could help make photovoltaic energy generation more viable.

This thesis explores the feasibility of the LSC, quantifying its advantages, shedding light on limiting factors and highlighting possible solutions. The focus of this PhD has been on characterisation and modelling, and as such, most of the samples studied were fabricated by the Fraunhofer IAP and the luminescent materials were sourced from commercial suppliers or academic collaborators. The computational modelling was conducted using a raytrace model that was developed within the scope of the author's PhD.

Chapter 2 provides the background and theory to the LSC, while the materials and experimental as well as computational methods are described in Chapter 3. Chapter 4 presents several short experiments based on the computational raytrace model. In the first main results chapter, Chapter 5, the concept of the thin-film LSC is introduced and compared with the conventional, homogeneously doped LSC. The focus is on the question whether the thin-film configuration is advantageous and, in particular, whether it can reduce optical losses. The topic of Chapter 6 is the light-bar, a linear variant of the LSC for use as a secondary concentrator in a building integrated photovoltaic application. A series of investigations is carried out with the aim to determine the design choices that yield the best optical efficiencies. Finally, nanorods and phycobilisomes, two kinds of novel luminescent materials that could reduce self-absorption, one of the main loss mechanisms of the LSC, are explored in Chapter 7 before concluding the thesis.

Chapter 2

Background and Theory

2.1 Chapter Introduction

The luminescent solar concentrator(LSC) works in conjunction with solar cells, and therefore it seems appropriate to start this chapter with a section on the principles of photovoltaics. This section is followed by an explanation of the functioning of the standard LSC as well as the theory describing performance calculations and efficiency limits. There have been over 30 years worth of research on the LSC, and a review of key approaches and notable advances are described in this chapter.

2.2 Principles of Photovoltaics

Photovoltaics describes the direct conversion of light to electricity (see for example Ref. 27). The basic principle is the absorption of light to create mobile charge carriers, which then pass through an electric circuit, where some of their energy is extracted as work. Ideally, both the absorption of photons and the voltage at which the charge carriers are extracted are maximised.

2.2.1 Energy from the Sun

Light from the Sun comes in a broad spectrum. The temperature at the Sun's surface (5,760 K) gives rise to a blackbody spectrum as described by Planck's radiation law [28]:

$$I_\lambda(\lambda) = \frac{2\pi hc^2}{\lambda^5} \frac{1}{e^{\frac{hc}{\lambda kT}} - 1} \tag{2.1}$$

where h is Planck's constant, k is the Boltzmann constant, T is the temperature (in Kelvin), c is the speed of light, λ is the wavelength and I_λ is the spectral irradiance. The spectral irradiance is the incident radiant power per unit area per unit wavelength and is sometimes called intensity. It is converted to the spectral photon flux Φ_λ by dividing it by the photon energy $^{hc}/_{\lambda}$. The overall irradiance I_γ is the integral of I_λ over all wavelengths and has standard units of Wm^{-2}.

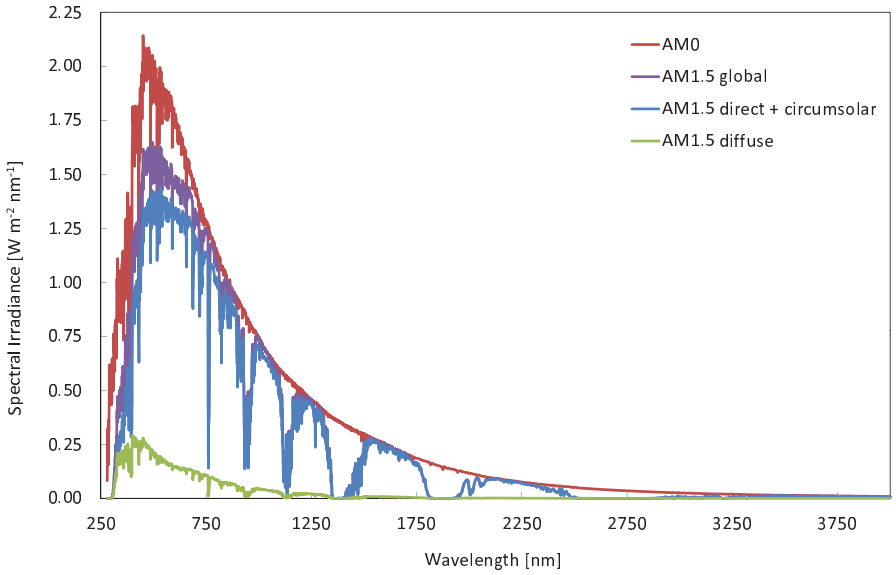

FIGURE 2.1: The AM0 and AM1.5 solar spectra. AM0 is the sun's extraterrestrial blackbody spectrum, while AM1.5 shows absorption features from the Earth's atmosphere. This data has been retrieved from the ASTM G-173 reference spectrum (NREL) [29].

The spectrum reaching Earth's surface shows atmospheric absorption features, mainly due to water vapour. The extent of the attenuation depends on the latitude, since it determines the effective thickness of the atmosphere that the light has to pass through, and it is quantified by an air mass (AM) number: AM 0 is the unattenuated extraterrestrial spectrum, AM 1 the terrestrial spectrum at normal incidence and AM 1.5 at 48.2 ° angle with respect to the normal. AM 1.5 (see Figure 2.1) is the standard spectrum for

Solar spectrum	Integrated power [kWm^{-2}]
AM0	1.35
AM1.5 global	1.00
AM1.5 direct and circumsolar	0.90
AM1.5 diffuse	0.10

TABLE 2.1: Power of different solar spectra, integrated over all wavelengths.

characterising solar cells. The AM1.5 global spectrum has a power of 1 kWm^{-2} (see Table 2.1). For luminescent solar concentrators it will be important to distinguish between the direct (including the circumsolar) and the diffuse spectrum. The latter is assumed to be incident over a hemisphere and is more blue-rich as it is predominantly the shorter wavelength light that scatters in the atmosphere, creating the blue sky. There are various other factors such as the aerosol optical depth (AOD) that subtly affect the spectrum.

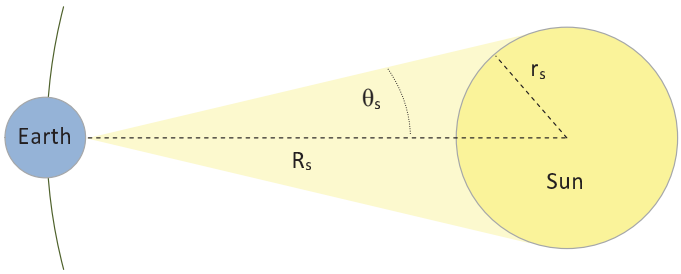

FIGURE 2.2: The concentration limit of sunlight depends on diameter of the Sun and its distance to Earth.

The concentration of sunlight is measured in units of suns, where 1 sun denotes the terrestrial irradiance without concentration. Given that concentrating sunlight onto a target is equivalent to moving the target closer to the Sun, it can be concluded that the intensity under maximum concentration is equivalent to the intensity at the Sun's surface. One can approximate the concentration limit by simply comparing the surface areas of the spheres with radii R_s and r_s as shown in Figure 2.2:

$$C_{\max} \approx \frac{4\pi R_s^2}{4\pi r_s^2} = \left(\frac{R_s}{r_s}\right)^2 \cong 46,300 \tag{2.2}$$

where R_s is the Earth-Sun distance (1.496×10^8 km) and r_s is the radius of the Sun (6.955×10^5 km). Landsberg and Baruch [30] have calculated the maximum concentration

achievable in air with geometric concentrators using a thermodynamic approach:

$$C_{\max} = \frac{1}{\sin {\theta_s}^2} \cong 46,200 \tag{2.3}$$

where θ_s is the half-angle subtended by the Sun when viewed from Earth (4.654×10^{-3} rads). By immersing the solar cell in a material of refractive index above 1, higher concentrations can be achieved [31].

2.2.2 The p-n Junction Solar Cell

Most solar cells are inorganic and based on semiconductor p-n junctions. A semiconductor can only absorb photons with above-bandgap energies, which promote electrons from the valence to the conduction band. A promoted electron leaves an empty state in the valence band, which can be filled by a nearby electron by vacating its own position. This way the vacancy can move within the valence band, in the opposite direction to the electrons. Therefore the vacancy, called a hole, is considered a positively charged quasi-particle. Below-bandgap photons are not absorbed, and any excess photon energy beyond the bandgap is lost. The latter is due to thermalisation: interactions with phonons, which manifest themselves in the heating of the cell. Thermalisation down to the band-edge happens on a much shorter timescale than the band-to-band recombination, which generally occurs via spontaneous emission of a photon since phonons cannot bridge the electronic bandgap. Though a solar cell under illumination is not in thermal equilibrium, the electrons in the conduction band and holes in the valence band reach a quasi-equilibrium within their respective bands, and one assigns respective quasi-Fermi levels to the electron and hole populations.

The generation of charge carriers is counteracted by their recombination. There are three main recombination processes: band-to-band (essentially radiative) recombination, Shockley-Read-Hall (SRH) recombination and Auger recombination. Radiative recombination is the only loss mechanism that fundamentally cannot be completely avoided. It is the dominant mechanism in pure, direct bandgap semiconductors. SRH recombination is a thermal process via defect or impurity states energetically within the bandgap. In an Auger process, a conduction band electron recombines with a hole by losing its energy to another conduction band electron, which in turn loses this additional energy through thermalisation to the bottom of the conduction band. The reverse process of two holes

colliding can also occur. Auger recombination occurs mainly in indirect semiconductors, where the momentum imparted during the electron-electron interaction can provide the wavevector required for the indirect gap transition. Since it is a two-electron process, the rate of Auger recombination increases with the electron population in the conduction band and can therefore become dominant under high bias or light concentration. It can also become dominant at high doping, even in direct semiconductors.

The probability of an incident photon of a given wavelength contributing to the photocurrent is expressed in the spectral quantum efficiency $QE(E)$. Besides going to zero at low energies that cannot bridge the bandgap, the QE also vanishes at high energies because of surface recombination: the absorption coefficient for highly energetic photons is very large, and they are therefore absorbed close to the top surface. However, the surface embodies a termination of the periodic lattice and contains dangling bonds, which present recombination sites.

Besides the absorption of photons, the transport of the charge carriers and their extraction at the terminals is important for electrical current generation. In a simple semiconductor, the charge carriers would move in a random path and have no net direction, so that the rate of extraction would be very small compared to the rate of recombination. In a p-n junction, however, there is a built-in electric field, which spatially separates electrons and holes and drives them towards their respective terminals. This built-in field arises from carrier concentration gradients at the junction and the resulting diffusion of electrons in the conduction band of the n-type material to the p-type and diffusion of holes in the valence band from p to n. The positive ions remaining on the n-side and the negative ions on the p-side create an electric field and a drift current that eventually balances the diffusion. For practical purposes, one conventionally uses a simplified description of the p-n junction consisting of three zones: a quasi-neutral p-type zone, a quasi-neutral n-type zone and a space-charge (or depletion) zone in-between. The electric field spans the space-charge zone, which contains the ionised atoms and is void of stationary free charge carriers. In a solar cell under illumination, the photo-generated conduction band electrons are extracted from the n-side and pass through an electrical circuit to recombine with holes in the valence band on the p-side.

The power P generated by a solar cell is the product of the current I and the voltage V. The quasi-Fermi level separation at the terminals determines the voltage the solar

cell delivers, and it increases with the bandgap. Meanwhile, a lower bandgap allows for a greater part of the spectrum to be absorbed and results in a higher photocurrent. This means that there is an optimum bandgap that maximises the power for a given spectrum.

At short circuit the photocurrent of an idealised solar cell is proportional to the incident above bandgap photon flux. The current density at short circuit can be expressed as [27, pp. 7,8]:

$$J_{SC} = e \int_E QE(E)\, \Phi(E)\, dE \tag{2.4}$$

where e is the elementary charge, E the energy, and $\Phi(E)$ the spectral photon flux. When a load is connected to a solar cell under illumination, the resistance of the load limits the flow of photo-generated charge carriers. Consequently, larger electron populations build up on the n-side and hole populations on the p-side, biasing the cell to create a current opposing the photocurrent. To quantify this so-called dark current, one can consider the solar cell under external bias without illumination. In the dark most solar cells behave like diodes, and their current-voltage characteristics can be described by the diode equation [27, pp. 9-15]:

$$J_{\text{dark}}(V) = J_0 \left(e^{\,eV/(nkT)} - 1 \right) \tag{2.5}$$

where J_0 is the dark saturation current density, V the voltage applied across the terminals of the diode, k the Boltzmann constant, T the temperature (in Kelvin) and n the ideality factor, which is a number between 1 and 2 that reflects the non-ideality of real diodes. An ideal diode would have an ideality factor of 1. J_0 is a measure of the leakage current and constant for a given solar cell. In a more complete description there would be two independent components contributing to the dark current, a radiative and a non-radiative one. In analogy to Ref. 27 (pp. 9,10) the superposition approximation is applied in this thesis, which states that the overall current (also called light current) can be approximated by the superposition of short-circuit current and dark current:

$$J(V) = J_{SC} - J_{\text{dark}}(V)\,. \tag{2.6}$$

From Equation 2.6 the voltage at which there is no net current, i.e. the voltage at open circuit can be deduced:

$$V_{OC} = \frac{kT}{e} \ln\left(\frac{J_{SC}}{J_0} + 1\right). \tag{2.7}$$

The maximum power generated by the solar cell is

$$P_m = I_m V_m \tag{2.8}$$

where the subscript m denotes the maximum power point. P_m is related to the short-circuit current and the open-circuit voltage via the fill factor $FF = I_m V_m/(I_{SC} V_{OC})$ and can be expressed as:

$$P_m = FF\, I_{SC}\, V_{OC}\,. \tag{2.9}$$

2.2.3 Solar Cell Efficiency

The efficiency η_{PV} of a solar cell is the ratio of power output to incident power:

$$\eta_{PV} \equiv \frac{P_{\text{out}}}{P_{\text{in}}} = \frac{FF\, I_{SC}\, V_{OC}}{P_{\text{in}}} \tag{2.10}$$

where the incident power under AM1.5 global illumination is $1\,\text{kW/m}^2$ by convention.

In 1961 Shockley and Queisser [32] introduced a detailed balance method for calculating the limiting efficiency of the p-n junction solar cell under 1 sun, i.e. no concentration. In this approach, the electrical current drawn from the cell is equated to the difference between the rates of photon absorption and emission. Since then, the detailed balance method has been extended to more general cases, including calculating the ultimate efficiency limit for solar cells of 86.8 % achievable in theory with an infinite number of junctions under maximal solar concentration [33].

The single p-n junction solar cell has drawbacks mainly due to loss of sub-bandgap photons and thermalisation of above bandgap photons. Up-conversion of sub-bandgap photons is a possible solution to the former problem, and down-conversion via photon multiplication or multiple exciton generation (MEG) [34–37] a solution to the latter. Instead of matching the spectrum to the cell, the multijunction approach [14, 15, 38, 39] addresses both problems by collecting different parts of the spectrum with matching sub-cells connected in series. Spectral splitting [40] also utilises the broad spectrum in a

similar way, but with the added freedom of connecting the sub-cells individually. Another proposed solution is the introduction of an intermediate band to facilitate the absorption of sub-bandgap photons [41]. The highest efficiency is theoretically achieved with an infinite number of p-n junctions spanning the entire spectrum in infinitesimally narrow increments. Moreover, the detailed balance limits are obtained by using thermodynamic approaches [42, 43], in which the solar cell is considered a heat engine between an absorber heated by the Sun and the Earth as cold reservoir. This emphasises that these limits are fundamental and cannot be overcome with novel solar cell concepts such as the hot carrier cell [44, 45].

As long as the superposition approximation is valid, which generally is the case for direct bandgap solar cells, light concentration enhances the power conversion efficiency: the incident intensity scales linearly with concentration, and so does the short-circuit current, as shown in Equation 2.4. The additional logarithmic increase in the open-circuit voltage following Equation 2.7 leads to the efficiency enhancement. The underlying reason is that concentration creates larger electron and hole populations in the conduction and valence band, respectively, and thereby increases the quasi-Fermi level splitting. This manifests itself in a voltage increase in addition to the photocurrent increase. This relationship does not hold for silicon solar cells, where Auger recombination becomes dominant under high light bias, reducing the voltage and hence the efficiency. The theoretical limiting efficiency for PV is obtained assuming maximum solar concentration. From an entropic point of view this is illustrated by considering the solid angles of photon acceptance and emission: emission into the solid angle of acceptance is unavoidable, but all other emission constitutes a loss called étendue loss. A solar cell typically emits over 4π radians. With a back reflector the emission occurs over a hemisphere, in which case the solid angles of emission only matches the acceptance at maximum concentration. This consideration also hints at the fact that by restricting the emission, for example by placing the cell in the centre of a mirrored dome with a small aperture for incident light, the aforementioned limiting efficiency can also be achieved under 1 sun [46].

2.3 Principles of the LSC

There are two main principles that govern the luminescent solar concentrator: light capture and waveguiding. A typical LSC as depicted in Figure 2.3 consists of a transparent plate doped with luminescent centres. Incident light is absorbed by these centres and re-radiated. Due to the difference in refractive index between the plate and the surrounding air a large fraction of the luminescent radiation is trapped within the plate by total internal reflection (TIR). The trapped luminescence is wave-guided to the plate edges where it is converted by PV cells. Ideally, the output is in a narrow spectrum that is matched to the cells. The geometric ratio between the top surface and the edges leads to the concentration.

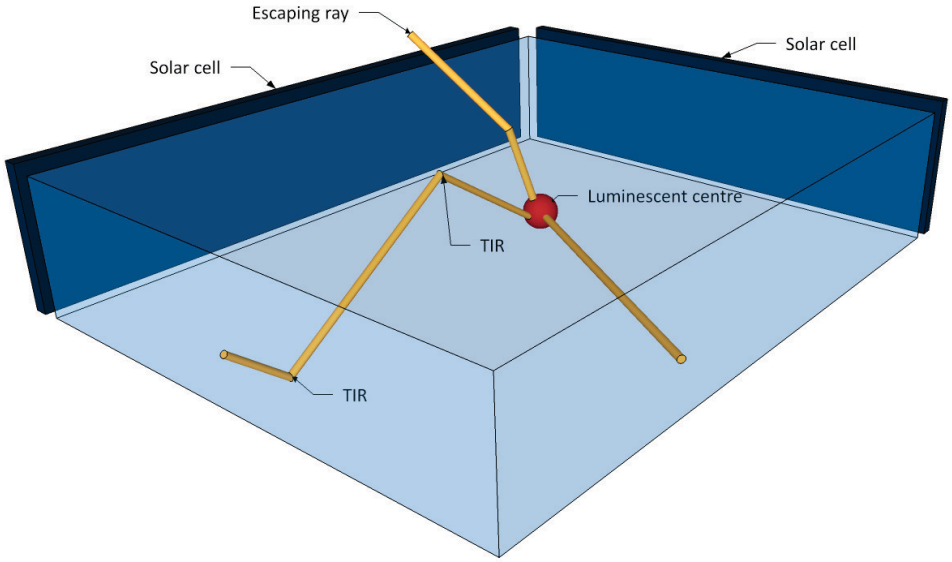

FIGURE 2.3: A schematic representation of the luminescent solar concentrator (LSC). Incident light from the top is absorbed by a luminescent centre and re-emitted. An escaping ray, a ray emitted toward an edge and a ray trapped by total internal reflection (TIR) are depicted. Solar cells on the edges collect the emission.

2.3.1 Light Capture

Light impinging on the surface of an LSC is either reflected or transmitted into the LSC. The LSC is a dielectric waveguide and as such has a refractive index n that is higher than that of its surrounding, i.e. higher than 1 in the case of air. Following an approach by Joannopoulos *et al.* [47, pp. 27-30], transmitted light gets refracted (see Figure 2.4) according to conservation of energy and momentum, which for a photon

are $\hbar\omega$ and $\hbar\mathbf{k}$, respectively. Translational symmetry parallel to the interface dictates that the parallel component of the wavevector $\mathbf{k}$ is conserved at transmission, since a homogeneous surface cannot change the momentum parallel to it:

$$|\mathbf{k_1}| \sin\theta_1 = |\mathbf{k_2}| \sin\theta_2. \tag{2.11}$$

Since $|\mathbf{k}| = {}^{n\omega}/_{c}$, and since the angular frequency ω is constant due to energy conservation, as is the speed of light c, this yields the well known Snell's law:

$$\frac{\sin\theta_1}{\sin\theta_2} = \frac{n_2}{n_1}. \tag{2.12}$$

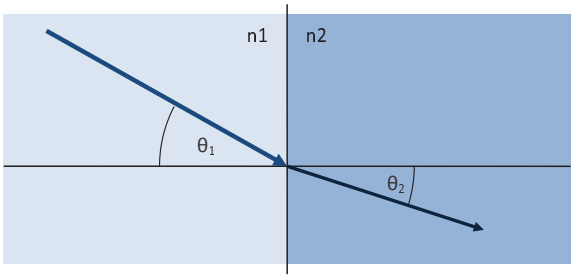

FIGURE 2.4: Snell's law describing the refraction of light at the interface between two media of different refractive indices.

The refractive index change at the interface to the LSC also gives rise to Fresnel reflection described by the Fresnel equations. Light incident on a surface can have two polarisations: if the electric field vector of the light wave is within the plane of incidence, i.e. the plane containing the incident ray and the surface normal, it is p-polarised; if it perpendicular to this plane it is s-polarised. The two polarisations have different Fresnel equations associated with them:

$$R_s = \left(\frac{n_1\cos\theta_1 - n_2\cos\theta_2}{n_1\cos\theta_1 + n_2\cos\theta_2}\right)^2 \tag{2.13}$$

$$R_p = \left(\frac{n_1\cos\theta_2 - n_2\cos\theta_1}{n_1\cos\theta_2 + n_2\cos\theta_1}\right)^2 \tag{2.14}$$

Variations of the refractive index with wavelength can generally be disregarded in the case of the LSC. A typical LSC made of glass or poly(methyl methacrylate) (PMMA) has a refractive index of $\sim$1.5, which yields a coefficient of reflection of $\sim$4 % for light at normal incidence. As an aside, p-polarised light incident at Brewster's angle undergoes

perfect transmission, as can be seen in Figure 2.5. At this angle the electric field vector of the light, which creates the electric dipole oscillations in the dielectric medium that cause the reflection, is parallel to the angle of reflectance. Since an electric dipole cannot emit a photon along the axis of its oscillation, there cannot be any reflectance in this case. For practical application of the LSC it is safe to assume that the incident light is unpolarised, in which case the average of the two reflection coefficients is taken (see Figure 2.6). Moreover, when light reflects off a medium of higher refractive index, the phase changes by π. This does not affect a simple LSC, but is of significance for the distributed Bragg reflectors discussed in Section 2.5.2.

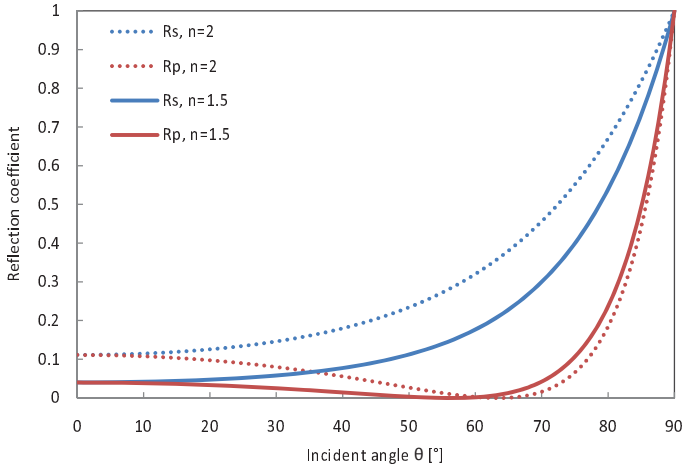

FIGURE 2.5: The Fresnel reflection coefficients of s- and p-polarised light incident from air onto media with refractive indices of 1.5 and 2.0.

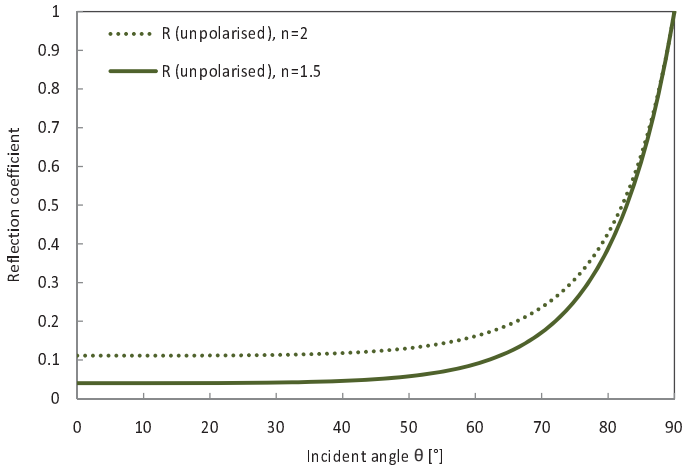

FIGURE 2.6: The Fresnel reflection coefficients for unpolarised light incident from air onto media with refractive indices of 1.5 and 2.0.

In this thesis, the light capture efficiency η_{capture} is defined as the ratio of photons absorbed (by luminescent centres) to incident photons. Figure 2.6 shows that reflection is only dominant at large angles above $\sim 60\,^{\circ}$, which indicates that reflection has a small effect on the light capture efficiency. A more detailed study in Section 4.2 verifies this point. Therefore the level of the absorption by the luminescent material is the crucial factor. Essentially, the capture efficiency can be expressed in terms of the incident spectral photon flux Φ_λ and the spectral absorptance A_λ, defined as the fraction of light absorbed at a specific wavelength:

$$\eta_{\text{capture}} = \frac{\int_\lambda \Phi_\lambda(\lambda)\, A_\lambda(\lambda)\, d\lambda}{\int_\lambda \Phi_\lambda(\lambda)\, d\lambda}\,. \tag{2.15}$$

Under the assumption of no scattered light, A_λ is related to the spectral reflectance R_λ and transmittance T_λ as follows:

$$A_\lambda + R_\lambda + T_\lambda = 1\,. \tag{2.16}$$

Internally, i.e. in the absence of reflection, the transmittance is defined by the Beer-Lambert law as

$$T_{\lambda,internal}(\lambda,\theta) = \frac{I_\lambda(z)}{I_\lambda(0)} = e^{-\alpha(\lambda)z(\theta)} \tag{2.17}$$

where $I_\lambda(0)$ is the initial light intensity and $I_\lambda(z)$ the attenuated intensity after passing through a thickness z, which depends on the angle of incidence θ. The absorption coefficient $\alpha(\lambda)$ is the product of the absorption cross-section $\sigma(\lambda)$ and the number density of the luminescent centres, henceforth denoted by $\tilde{n}$:

$$\alpha = \sigma\,\tilde{n}\,. \tag{2.18}$$

In accordance with Equation 2.17 the internal spectral absorptance is

$$A_{\lambda,internal}(\lambda,\theta) = 1 - e^{-\alpha(\lambda)z(\theta}\,. \tag{2.19}$$

Neglecting scattering losses due to surface roughness, absorption in the host material and multiple Fresnel reflections from the back and front interfaces, the capture efficiency can be rewritten in terms of the internal spectral absorptance and the spectral reflectance

for reflection from the front surface and the spectral absorptance:

$$\eta_{\text{capture}} = \frac{\int_\theta \int_\lambda \Phi_\lambda(\lambda,\theta)\, A_{\lambda,internal}(\lambda,\theta)\,(1 - R_\lambda(\theta))\; d\lambda\, d\theta}{\int_\lambda \Phi_\lambda(\lambda)\, d\lambda}\,. \tag{2.20}$$

The capture efficiency is sensitive to the spectrum of in the incident irradiation, which, in terms of the LSC, is an external quantity.

2.3.2 Waveguiding

In contrast to the light capture, the waveguiding is a purely internal property of the LSC. The waveguiding efficiency $\eta_{\text{waveguide}}$ is defined as the ratio of photons guided to the LSC edges to photons absorbed. In order to trap light in a waveguide, a change in its direction is required since light that enters a planar waveguide will also leave it due to the symmetry of light paths. The LSC achieves this change in direction through absorption and subsequent emission of light by luminescent centres from within the waveguide. Inside the LSC Fresnel reflection leads to a critical angle beyond which light undergoes total internal reflection (TIR), as shown in Figure 2.7. The critical angle θ_c is the one at which the refracted ray travels parallel to the interface. For a ray travelling from a medium of refractive index n_2 to n_1 ($n_2 > n_1$) it is defined as

$$\theta_c = \arcsin\left(\frac{n_1}{n_2}\right). \tag{2.21}$$

Even though in real systems TIR is never perfect, reflectances of 99.99 % are not uncommon, and thus for all practical purposes TIR in the LSC can be treated as being perfect. For comparison, a reflectance of 95 % in the visible is considered very good for a metal. Light emitted within an escape cone will leave the waveguide, unless it is subjected to re-absorption along its path or to standard Fresnel reflection at the interface. Spherical polar coordinates, in which an infinitesimal element of solid angle is $d\Omega = d\phi \sin\theta d\theta$ ($0 \leq \phi \leq 2\pi$ and $0 \leq \theta \leq \pi$), are used to obtain the solid angle of the escape cone by integrating the azimuthal angle ϕ over the entire circle and the polar angle θ up to the critical angle θ_c (under the assumption of isotropic luminescence):

$$\Omega_{\text{escape}} = \int_0^{2\pi} d\phi \int_0^{\theta_c} \sin\theta\, d\theta \;\; = 2\pi\left[1 - \cos\theta_c\right]. \tag{2.22}$$

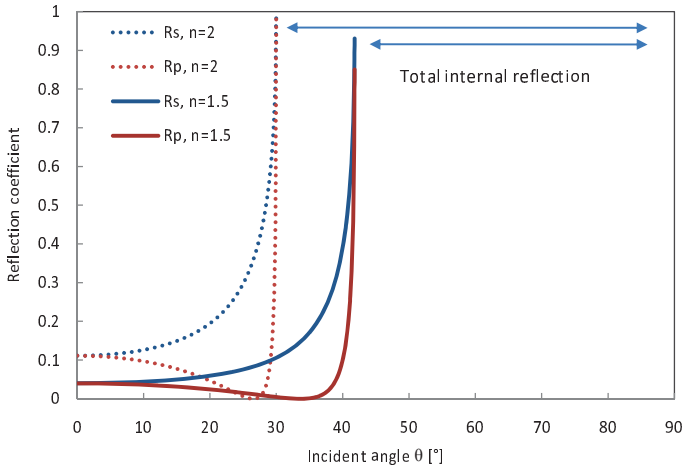

FIGURE 2.7: Fresnel reflection leads to total internal reflection at an interface to a medium of lower refractive index, as shown here for interfaces between air and media with refractive indices of 1.5 and 2.0.

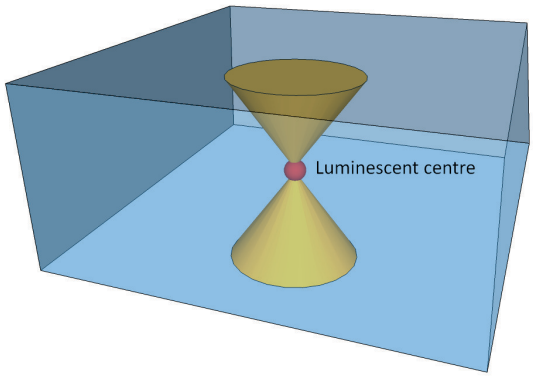

FIGURE 2.8: Escape cones. Luminescence that is not trapped by total internal reflection can escape out of the top or the bottom of the concentrator.

Assuming that light travelling towards the concentrator edges is collected by solar cells, there are only two escape cones out of which light can be lost: one out of the top and one out of the bottom surface. This is also valid when a mirror is placed on the bottom surface, since light within the bottom escape cone will exit out of the top upon reflection. So, in the case of isotropic luminescence, the fraction of light lost in a single emission step through escape cones, η_{escape}, is twice the ratio of Ω_{escape} to the solid angle of the sphere (4π):

$$\eta_{\text{escape}} = \frac{2\Omega_{\text{escape}}}{\Omega_{\text{total}}} = 1 - \cos\theta_c. \tag{2.23}$$

Consequently, the single emission trapping efficiency is

$$\eta_{\text{trap}} = 1 - \eta_{\text{escape}} = \cos\theta_c\,. \tag{2.24}$$

Substituting the expression from Equation 2.21 yields

$$\eta_{\text{trap}} = \sqrt{1 - \sin^2 \theta_c} = \sqrt{1 - \frac{{n_1}^2}{{n_2}^2}}. \tag{2.25}$$

The assumption of isotropic luminescence is a simplification. The electronic transition dipole of a luminescent centre dictates the angular dependence of both absorption and emission, and in dyes this dipole is generally directional, so that the emission profile from an individual dye is anisotropic (see for examples Refs. 48, 49). In the case of an ensemble of isotropically oriented dyes, the dyes with a dipole oriented perpendicular to the incoming light absorb more strongly. Due to the symmetry between the absorption and emission angular dependence, they also emit more strongly out of the escape cone, as explained in Refs. 50, 51. The overall emission profile, obtained by averaging the profiles of all luminescent molecules, has an escaping fraction that is actually higher than it would be in the case of isotropic emission. According to calculations by Ref. 50 the percentage of photons emitted into top and bottom escape cones in a matrix with a refractive index of 1.586 can vary by 15 % between normal incidence and an 75 ° incidence. In an accurate description of the trapping efficiency, the distribution of incoming angles needs to be taken into account. The simplified description (assuming isotropic emission) is considered to be sufficient in this thesis.

Based on the typical refractive indices of $n_1 = 1$ (air) and $n_2 = 1.5$ (LSC), 75% of the initial luminescence is trapped within the LSC according to Equation 2.25. However, light can be re-absorbed and re-emitted along its path. Assuming no other losses due to the luminescence quantum yield or absorption in the host material, the overall trapped fraction can be computed with respect to the number of (re-)emissions. Figure 2.9 shows the dramatic loss of trapped light with multiple re-emissions. While it is evident from Equation 2.25 that a higher refractive index results in smaller escape cones and better trapping, Figure 2.6 shows that a higher index also leads to more surface reflection and worse light capture. In theory, this trade-off would have to be optimised individually for every LSC. In practice, the range of refractive indices of materials with high transparency in the visible is fairly limited: 1.5 - 1.9 for optical glass and 1.3 - 1.8 for polymers. Although transparent ceramics offer high refractive indices above 2 [52], they are of interest for optical equipment like camera lenses and do not appear to be feasible for an inexpensive, large-scale device such as the LSC. Within the given limits, a higher

refractive index is always advantageous for the LSC since the light trapping efficiency has a much greater impact on LSC performance than the capture efficiency. Besides trapping light, a good waveguide also needs to transmit it well. The host materials used for LSCs typically have absorption coefficients below $1\,\mathrm{m}^{-1}$ in the visible spectrum, and for high quality glass or PMMA they can be as low as $0.3\,\mathrm{m}^{-1}$.

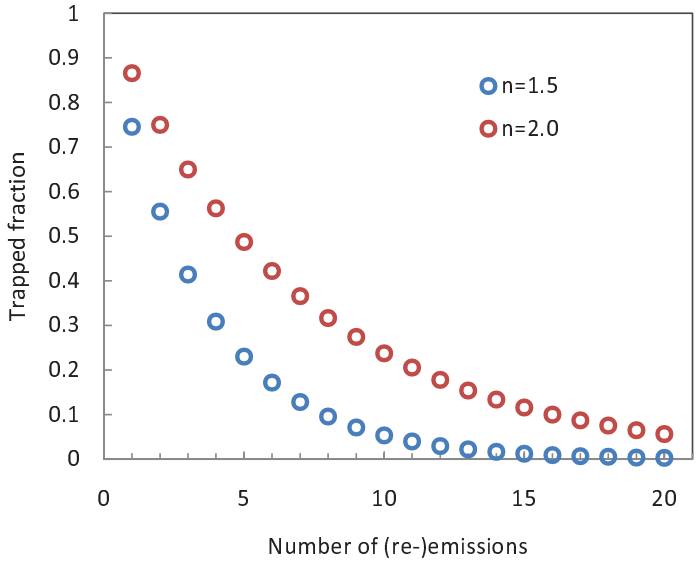

FIGURE 2.9: The fraction of light trapped by total internal reflection (TIR) decreases exponentially with the number of re-emissions, as shown for waveguides with refractive indices of 1.5 and of 2.0.

The waveguiding efficiency is not straightforward to analyse. It clearly depends on the trapping efficiency to some degree. Other factors that play a role are the luminescence quantum yield (QY) and the self-absorption of the luminescent centres, both measured at very low concentration, i.e., as close to a single molecule as possible. High self-absorption amplifies QY losses and escape cone losses as photons are re-absorbed several times before they are emitted out of the LSC edge. QYs above 90 % are routinely obtained with organic dyes. The trapping efficiency, i.e. the probability of light trapping upon a single emission, of a waveguide with a typical refractive index of 1.5 is only 75 %. Even with a refractive index of 2.0, which is unrealistically high for an LSC waveguide, the trapping efficiency is 87 %, still lower than the typical QY. This means that the bottleneck in the waveguiding efficiency are the escape cone losses.

2.3.3 Luminescent Centres

Photons absorbed by a luminescent centre promote electrons from a ground state to an excited state. They lose their added energy thermally via interactions with phonons or radiatively via the emission of photons. The luminescence quantum yield (QY) is the ratio of emitted photons to absorbed photons for an ensemble of luminescent centres, or the probability of emission following an absorption for an individual luminescent centre. Not taking into account photon multiplication, an ideal luminescent centre for the LSC would have a QY of 1 and a strong absorption across a large part of the solar spectrum. It would also have a relatively narrow emission spectrum that is matched to the solar cells attached to the LSC and be photo-stable for the lifetime of the LSC. Moreover, it is important to minimise self-absorption, which can be achieved with a small overlap between the absorption and emission spectra. Organic dyes have been the conventional choice of luminescent material in LSCs. Today, there are alternatives such as inorganic nanocrystals.

In a dye an absorbed photon excites an electron from the highest occupied molecular orbital (HOMO) to the lowest unoccupied molecular orbital (LUMO). Each orbital contains vibrational states, and the electron loses any excess energy through phonon interactions, which occur on a timescale orders of magnitude faster than spontaneous emission, until it reaches the lowest energy states in the LUMO. Consequently, when the electron relaxes to the HOMO, it emits a photon of lower energy than the absorbed one. This difference in energy between the absorption and emission peaks is the Stokes shift.

In a semiconductor nanocrystal, the valence and conduction bands are the equivalents of the HOMO and LUMO in an organic molecule, and in a similar fashion to dyes, quick relaxation of excited electrons to the conduction band edge and holes to the valence band edge leads to a Stokes shift.

A large Stokes shift clearly leads to a loss of photon energy, which translates to a lower voltage generated in the solar cell. However, the Stokes shift is important for the reduction of self-absorption by the luminescent material, which heavily compromises the trapping efficiency as shown in Figure 2.9. Self-absorption (or re-absorption) is followed by two kinds of losses in the LSC: non-radiative loss of photons due to sub-unity QYs and radiative loss of photons out of the escape cones, the latter typically being

predominant. Since each re-absorbed photon is emitted with a Stokes shift, multiple re-absorptions increase the overall redshift of the emission from the LSC. The absorptance, the probability of a photon of given wavelength being absorbed, depends on its path length in the medium and the absorption coefficient of the luminescent material. While a greater absorptivity means that more of the incident light is captured, it also increases self-absorption.

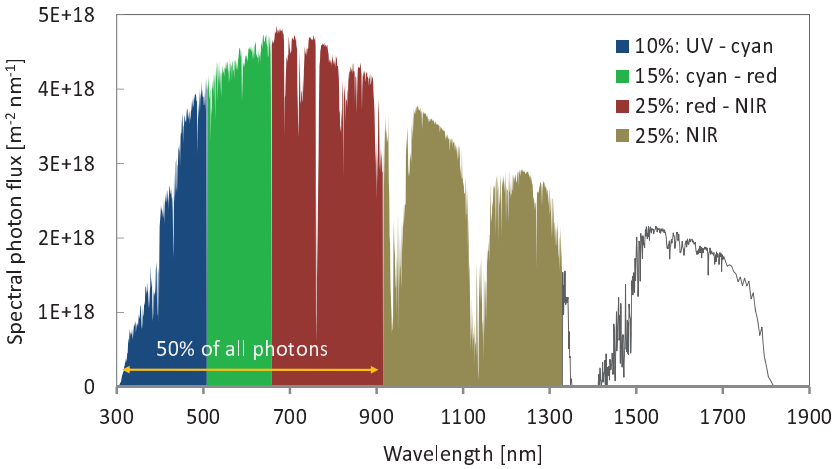

FIGURE 2.10: The AM1.5 direct solar photon flux per wavelength. The shaded areas indicate different fractions of the entire flux. Half of all photons in the AM1.5 direct spectrum are within the first three shaded areas; 75 % within the entire shaded area. Only part of the solar spectrum, which extends to about 4000 nm, is shown here.

The LSC can incur a significant loss in efficiency due to incident light that is not absorbed. A highly efficient luminescent concentrator would absorb the entire spectral range up to nearly the band edge of the PV cell that it outputs to. What matters is not the energy of the photons absorbed, as long as it is above the cell bandgap, but the number of photons, as it translates to the number of charge carriers generated in the solar cell. Figure 2.10 illustrates the AM1.5 direct solar spectral photon flux. It shows that the spectrum up to approximately 900 nm contains half of all photons. Moreover, the highest density of photons is in the range from 500 nm to 900 nm.

2.3.4 Concentration and Efficiency

The optical efficiency of the luminescent solar concentrator is the ratio of photons guided to the edges (or coupled into solar cells) to photons incident over the top surface. It is

the product of the capture efficiency and the waveguiding efficiency:

$$\eta_{\text{optical}} = \eta_{\text{capture}}\,\eta_{\text{waveguide}}\,. \tag{2.26}$$

The optical efficiency is fundamentally smaller than one, due to several loss mechanisms. The losses can be split into external ones, pertaining to incident light that is not absorbed, and internal ones, pertaining to absorbed light that is lost to non-radiative processes in the luminescent centres or the host or to radiative emission out of escape cones. External losses are reflected in η_{capture} and internal ones in $\eta_{\text{waveguide}}$. Internal losses are amplified by re-absorptions, rendering escape cone losses in particular a predominant loss mechanism.

The optical concentration (or photon concentration) C, defined as the ratio of the photon flux out of the edges to photon flux incident on the top surface, is the product of the geometric gain G and the optical efficiency:

$$C \equiv \frac{\Phi_{\text{out}}}{\Phi_{\text{in}}} = G\,\eta_{\text{optical}} \tag{2.27}$$

where G is the ratio of LSC collection surface area to solar cell area. For a concentrator with a square top surface (the top surface being the surface where the input light is incident) of length and width l and depth d with solar cells attached to all four edges the geometric gain is given by

$$G \equiv \frac{A_{LSC}}{A_{PV}} = \frac{l^2}{4ld} = \frac{l}{4d}\,. \tag{2.28}$$

The LSC concentrates all light it captures in the same way, regardless of whether it is direct or diffuse. A geometric solar concentrator only focusses direct sunlight, which is collimated to a high degree. Applying the entropic argument, concentration of direct light can be afforded because the reduction in areal spread of the beam is compensated by the increase of its angular spread, so that the overall disorder or entropy of the system is not reduced. Since diffuse light already has the highest degree of angular disorder, concentration in accordance with the Second Law of Thermodynamics is only possible under certain conditions. In fact, without spectral modification, diffuse light can only be focussed by coupling it into a material of refractive index n higher than

air, so that the angular spread is reduced from a hemisphere to a cone bound by the critical angle. In this case the maximum theoretical concentration is limited to n^2 [53]. For further concentration, an energy penalty has to be paid, and this is what the LSC accomplishes by spectrally down-shifting solar radiation. Based on an approach by Ross [54], Yablonovitch [55] derived the LSC concentration limit from thermodynamics by considering the entropy change associated with the absorption and emission by the LSC. The maximum concentration under terrestrial conditions is approximated as

$$C \leq \left(\frac{\nu_2}{\nu_1}\right)^2 e^{\frac{\nu_1-\nu_2}{kT}} \tag{2.29}$$

where h is Planck's constant, k the Boltzmann constant, T the temperature (in Kelvin), ν_1 the frequency of the incident light and ν_2 the frequency of the emitted light. Hence, $\nu_1 - \nu_2$ is the Stokes shift of the luminescence. Figure 2.11 shows the maximum concentration as a function of Stokes shift. The dependency of the concentration limit on the incident wavelength is exemplified by three different wavelengths. Realistic concentrations are substantially smaller than the thermodynamic limit. Nevertheless, Equation 2.29 emphasises how light concentration via the LSC is fundamentally linked to the luminescent down-shift.

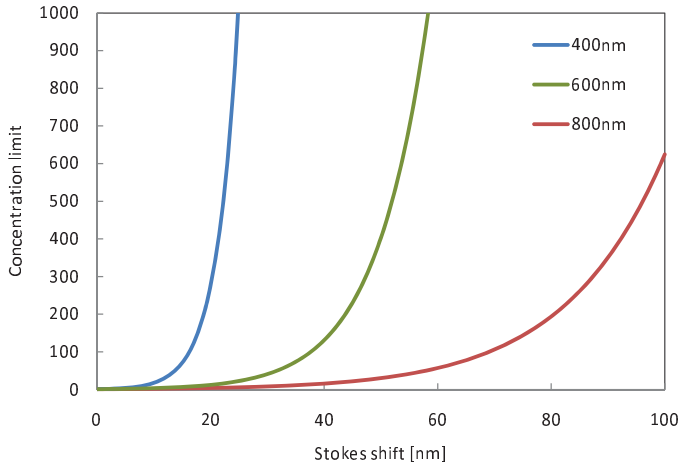

FIGURE 2.11: The thermodynamic limit for photon concentration via the LSC. According to Equation 2.29 the upper limit for concentration depends on the Stokes shift. It is represented here in units of wavelength for three different incident wavelengths.

An LSC with solar cells attached to it is called an LSC module. The system efficiency of such a module is defined as electrical power out over incident radiative power and depends on the PV cell efficiency as well as the optical efficiency of the LSC. The

bandgap of the cell limits the absorption range of the LSC. While a large Stokes shift increases the concentration limit (see Equation 2.29) is also represents a loss of energy, and this trade-off needs to be taken into account for the efficiency considerations. By matching the luminescence to the cell QE, the cell can convert the concentrated light more efficiently than the broad solar spectrum. In addition, the concentration increases the efficiency of the power output, as explained in Section 2.2.3.

The theoretical system efficiency limit of the LSC has been calculated using a Monte Carlo approach [56] as well as an analytical approach [57]. In both cases, a photonic structure in the form of a spectrally selective reflector on the top surface was included in the calculation to reflect escaping luminescence back into the waveguide while letting incident light within the absorption spectrum pass (see Section 2.5.2). It was found that the efficiency limit of the LSC module matched the detailed balance limit of a single bandgap solar cell under 1 sun of 31% as proposed by Shockley and Queisser (see Section 2.2.3).

The optical efficiency of the LSC decreases with the size of the top surface area, while the geometric gain increases linearly with the top surface. As long as the rate of decrease of η_{optical} is smaller than the rate of increase of G, the concentration increases. Since the power incident on the LSC is proportional to the top surface area, the reduction in optical efficiency leads to a decrease of the system efficiency with top surface area and hence with geometric gain. The optimal LSC configuration balances concentration and system efficiency to maximise the power-to-cost ratio of the module, assuming no constraint of space.

2.3.5 Cost per Watt

In order to make the LSC competitive with other PV technologies, the efficiency, i.e. the power generated over a given area, will need to meet certain minimum requirements. However, the priority is to minimise the cost-to-power ratio (or cost per Watt). The cost per Watt depends on the cost of the components and the energy conversion efficiency. The power out of a solar cell of area A with a conversion efficiency η_{PV} under an irradiance I_γ is

$$P = I_\gamma \, A \, \eta_{PV} \, . \tag{2.30}$$

It should be noted, that solar cells are rated under standard conditions assuming an irradiance of 1,000 $\mathrm{W/m^2}$, and in a real environment the efficiency can vary with irradiance, spectrum and temperature. The cost per unit power, symbolised here by $\$/P$, in the case of a PV cell is given by

$$\left(\frac{\$}{P}\right)_{PV} = \left(\frac{\$}{A}\right)_{PV} \left(\frac{P_{PV}}{A}\right)^{-1} = \left(\frac{\$}{A}\right)_{PV} \frac{1}{I_\gamma \, \eta_{PV}} \,. \tag{2.31}$$

It is clear that this ratio becomes more favourable under higher irradiance. However, within the scope of solar cell design, the only factors that can be optimised are efficiency and areal cost $\$/A$. A module consisting of LSC and PV cell collects light over a larger area. It has a combined efficiency η_{LSC+PV} and can have reduced areal costs. The cost per unit power in this case is

$$\left(\frac{\$}{P}\right)_{LSC+PV} = \left(\frac{\$}{A}\right)_{LSC+PV} \frac{1}{I_\gamma \, \eta_{LSC+PV}} \,. \tag{2.32}$$

The combined areal cost can be expressed in terms of the geometric gain G as

$$\left(\frac{\$}{A}\right)_{LSC+PV} = \left[\left(\frac{\$}{A}\right)_{LSC} + G^{-1} \left(\frac{\$}{A}\right)_{PV}\right] \,. \tag{2.33}$$

The areal cost ratio of LSC to PV can be defined by γ:

$$\gamma = \left(\frac{\$}{A}\right)_{LSC} \left(\frac{\$}{A}\right)_{PV}^{-1} \,. \tag{2.34}$$

Clearly, γ needs to be considerably smaller than 1. Using the expression for γ, the combined areal cost is simplified to

$$\left(\frac{\$}{A}\right)_{LSC+PV} = \left(\gamma + G^{-1}\right) \left(\frac{\$}{A}\right)_{PV} \,. \tag{2.35}$$

The combined efficiency is defined as the output power divided by the incident power over the LSC collection area (as opposed to the PV cell area alone). Although it depends on various factors, such as the spectral match between the LSC and the cell or the output intensity, the system efficiency is approximated for the sake of this calculation using the optical efficiency η_{optical}:

$$\eta_{LSC+PV} \approx \eta_{\mathrm{optical}} \, \eta_{PV} \,. \tag{2.36}$$

An accurate way to determine the system efficiency would involve measuring the short-circuit current and calculating the power by following the steps outlined in Section 3.4.2. Assuming spectral matching between the cell and the LSC output, the actual system efficiency would be higher than the above approximation since the effective cell efficiency would be higher, because it would be illuminated by quasi-monochromatic light.

Substituting the expressions from Equations 2.35 and 2.36 into 2.32 yields

$$\left(\frac{\$}{P}\right)_{LSC+PV} = \left(\frac{\$}{A}\right)_{PV} \frac{\gamma + G^{-1}}{I_\gamma \, \eta_{\text{optical}} \, \eta_{PV}} = \left(\frac{\$}{P}\right)_{PV} \frac{\gamma + G^{-1}}{\eta_{\text{optical}}} \,. \tag{2.37}$$

This equation allows us to calculate the cost advantage of the LSC module over the PV cells alone for given γ, G and η_{optical}. Assuming that the LSC design does not influence γ substantially, it is concluded that reducing the cost-to-power ratio means optimising both G and η_{optical}, bearing in mind that these two factors are linked. It can be seen from Equation 2.37 that an accurate optimisation would depend on γ as well, but the studies presented here focus on G and η_{optical} alone.

2.3.6 Geometries

The LSC geometry mainly affects the geometric gain G, but it can also affect the light capture efficiency through reduced reflection of incident light and the transport of light to the cells, which depends on the waveguiding efficiency and the average pathlength to the cells. The conventional LSC is flat, since a thin shape produces a high geometric gain. Recently, a theoretical study by McIntosh *et al.* [58] has shown that under certain conditions, when the emission occurs close to the concentrator surface, a cylindrical geometry can produce an optical concentration that is almost twice that of a square planar LSC of the same collection area and volume. This is mainly due to the greater geometric gain of the cylinder with solar cells on the two ends. In addition, a design comprising multiple cylinders aligned next to each other can achieve a further increase of the concentration by several percent as a result of improved light capture from multiple reflections between neighbouring cylinders. Studies of the cylindrical design are presented in Section 6.4.

Increasing the LSC performance cannot be achieved simply by increasing the geometric gain, for example by increasing the collection area while keeping the thickness constant.

As the dimensions of the waveguide increase, the optical efficiency inevitably decreases since photons have longer paths on average before being collected. A longer path leads to increased self-absorption and host absorption losses, so the rate of the decrease in optical efficiency depends on the transparency of the waveguide and the extent of the self-absorption. The relationship between G and η_{optical} means that the increase of the optical concentration C (see Equation 2.27) with growing G eventually flattens off. For a given set of parameters, including the cost ratio γ, there are optimal dimensions that minimise the cost-to-power ratio. G is scale invariant, but η_{optical} is not, due to the constant absorption coefficient of the host material. This means that compared to a large LSC with identical shape and absorbance a small LSC would have a smaller fraction of host absorption losses. In practice, this effect is not expected to affect the scaling of the LSC noticeably since host absorption losses are small and outweighed by more substantial loss mechanisms.

Within the scope of planar concentrators, it is straightforward to calculate gains. Let us assume a thickness d and solar cells around the entire perimeter p of the shape. The gain for any shape of surface area A is

$$G = \frac{A}{p\,d}\,. \tag{2.38}$$

In the case of a square geometry with side l this yields

$$G_{\text{square}} = \frac{l^2}{4l\,d} = \frac{l}{4d}\,. \tag{2.39}$$

For a circle of radius r, for example, one obtains

$$G_{\text{circle}} = \frac{r}{2d}\,. \tag{2.40}$$

In order to compare the gains, one can normalise to the area of the square

$$\pi r^2 = l^2 \tag{2.41}$$

$$r = \frac{l}{\sqrt{\pi}} \tag{2.42}$$

which in turn yields

$$G_{\text{circle}} = \frac{l}{2\sqrt{\pi}\,d} = \frac{2}{\sqrt{\pi}}\,G_{\text{square}}\,. \tag{2.43}$$

However, in most practical applications the LSC will probably be required to tessellate. The only polygons that fulfil this criterion are the triangle, the square and the hexagon. Table 2.2 shows the gains for the different shapes with a thickness d. The circular geometry produces the highest gain for a given area. Consequently, the best tessellating shape is the hexagon, since it comes closest to the circle, and the worst is the triangle. However, the additional geometric gain the hexagon provides compared to the square is only 7 %. Raytrace simulations carried out by Kennedy *et al.* [59], comparing the optical concentrations for the same four geometries as shown in Table 2.2, produced results that support the findings presented in this section. Moreover, the results are also in agreement with experimental measurements by Roncali *et al.* [60]. Kennedy *et al.* draw the conclusion that despite the slightly higher concentration achieved with the hexagonal design, cost considerations would favour the square geometry. A further theoretical study by Loh *et al.* [61] reinforces that variations in the planar geometry have little effect on the performance of the LSC.

Shape	Perimeter	Area	G	G/G_{square}
Square	$4l$	l^2	$\frac{l}{4d}$	1
Equilateral Triangle	$3s$	$\frac{\sqrt{3}}{4}s^2$	$\frac{s}{4\sqrt{3}d}$	$\frac{2}{27^{1/4}} \approx 0.88$
Hexagon	$6s$	$\frac{3\sqrt{3}}{2}s^2$	$\frac{\sqrt{3}s}{4d}$	$\sqrt{\frac{2}{\sqrt{3}}} \approx 1.07$
Circle	$2\pi r$	πr^2	$\frac{r}{2d}$	$\frac{2}{\sqrt{\pi}} \approx 1.13$

TABLE 2.2: Geometric gains calculated from first principles for different concentrator geometries.

It should be noted, that Goetzberger *et al.* [62, 63] suggest a triangular concentrator with mirrors on some of its edges as the optimal configuration. This geometry is not prioritised due to the findings regarding the use of mirrors, as discussed in Section 4.3.

2.4 Review of Luminescent Materials

While organic dyes were the conventional choice of luminescent centres, various other materials are being used in LSCs today. This section presents the main types of luminescent materials along with their strengths and weaknesses.

2.4.1 Dyes

During the early years of LSC research, the laser dyes employed, typically rhodamine or coumarin compounds, had lifetimes of the order of days or shorter [21, 64]. Since then, the photo-stability of dyes has improved significantly, and recent developments in the encapsulation of organic molecules in the OLED industry make lifetimes of up to 30 years appear viable [65].

In a degradation study by Slooff *et al.* [66] a BASF Lumogen F Red 305 dye incorporated in a homogeneous LSC made of the commercial polymer matrix Plexit 55 (a mixture of PMMA and MMA) was examined. The LSC was illuminated continuously with a 1/3 sun white light source without UV component for a period of 250 days. The dye was found to degrade initially over a period of approximately 50 days, leading to a loss in the LSC short-circuit current of 20 %, but it then remained stable for the subsequent 200 days. An outdoor study of BASF dyes in PMMA by Mansour [67] showed that the BASF 241 dye degraded by only 6.2 % in terms of its absorbance after a year of exposure to daylight. Further degradation studies by Wilson *et al.* [68] on five Lumogen F series dyes in PMMA showed a degradation of only 5 to 15 % in the absorption coefficient of four of the dyes after a 5 week exposure to light, humidity and temperature in a QUV exposure machine. The Violet 570 dye degraded by 60 % as it was the most susceptible to the UV light. Red 305 was found to be most suitable in terms of stability and absorption properties, whilst also having a high QY.

Dyes are particularly attractive due to their high QYs, typically $> 90\,\%$, and availability in large quantities at low costs. However, most dyes have relatively narrow absorption spectra with respect to the solar spectrum available for photovoltaic energy conversion.

2.4.2 Nanocrystals

Inorganic nanocrystals such as quantum dots (QDs) have been proposed as an alternative to dyes [25], since competitive QYs are attainable [69]. Commercial QDs are reported to have QYs ranging from 20% to 90% [70] depending on their band gap. Some advantages of nanocrystals are their broad absorption spectrum, extending into the blue and UV, and a the tunability of their absorption edge via control of their size [25, 71]. One of the current drawbacks of nanocrystals is that they are a relatively expensive luminescent material.

Mostly, the nanocrystals are prepared through colloidal synthesis. In this scalable technique, the nanocrystals are grown under thermal control via nucleation processes in a solution containing precursor compounds. The nanocrystals generally consist of group II-VI compounds such as PbS, PbSe, CdS, CdSe, ZnSe and ZnS. PbSe and PbS absorb in the NIR, the others in the visible.

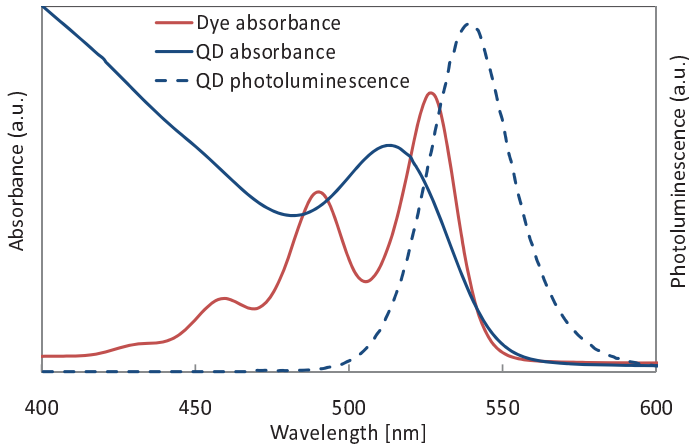

FIGURE 2.12: The spectra of quantum dots from Nanoco (SD396) are shown in comparison to the absorbance of a Lumogen F Orange dye from BASF. The broader absorption spectrum of the QDs is apparent. An exciton feature is observed around 510 nm in the absorbance of the QDs.

Figure 2.12 shows the broad absorption spectrum of a QD compared to a dye with similar absorption edge. Although the absorbance of the semiconductor nanocrystals grows consistently towards shorter wavelengths, a comparison of the absorptance with the photoluminescence excitation (PLE) spectrum indicates a loss in the luminescence quantum yield at short wavelengths (see Section 7.2.1). A challenge that remains is the development of NIR absorbing nanocrystals with high QYs. Shcherbatyuk *et al.* [72]

have reported a liquid LSC with dimensions of 45 mm×12 mm×3 mm that employed commercial PbS QDs from Evident Technologies with QYs of 50 % and below. These QDs absorbed in the visible as well as the NIR spectrum. This particular LSC was designed with a spectral match to silicon solar cells in mind and achieved an optical efficiency of 12.6 %.

The QDs used in recent LSC development have typical dimensions of several nanometres, containing hundreds to thousands of atoms (see Figure 2.13). These structures cannot be considered 0-dimensional; in fact, they have an approximately 3D density of states. The QD absorption spectrum is related to the bandgap of the bulk material, but quantum confinement alters the energy states, providing a degree of freedom in tuning the absorption spectrum: a smaller QD size leads to a higher bandgap energy and vice versa. For example, the bandgap of CdS can be varied from 2.5 eV to 4 eV via quantum confinement [73]. Moreover, the spread in the QD sizes determines the Stokes shift in accordance with the generalised Planck equation [25].

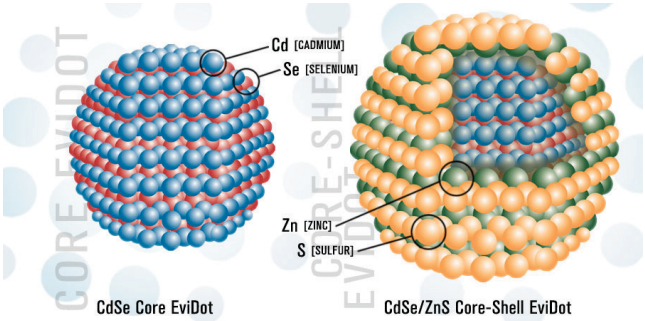

FIGURE 2.13: Schematic of the composition of quantum dots from Evident Technologies [70].

As in a bulk semiconductor, the absorption cross-section of a QD increases with increasing photon energy (or decreasing wavelength), which leads to a broad absorption band (see Figure 2.12). Photo-generated electron-hole pairs tend to form excitons, bound states, which can move within the QD. If they reach the surface of the QD before spontaneous photon emission takes place, non-radiative recombination is very likely since the surface contains defect and recombination sites. Due to the large ratio of surface area to volume, QDs suffer significant losses from surface recombination. This loss mechanism is reduced by passivating the surface, for example with organic ligands, but the resulting luminescence quantum yields are generally still below 10 % [71]. A significant improvement is achieved by adding a QD shell (see Figure 2.13) made of a higher bandgap

semiconductor. This creates either a type I QD, in which the electron and hole are in the same material in their lowest excited state, or a type II QD, in which they are in separate regions [74]. Surface recombination can be suppressed by confining the excitons to the core. It is possible to achieve this by confining the hole alone to the core while the electron is delocalised in the entire QD [75]. The core-shell approach leads to QYs above 50 % [69, 76] and even close to 100 % in some cases [75]. An example of the band structure of such a core-shell QD is shown in Figure 2.14. Multiple shells can improve the passivation further and also alter the spectral properties of the QD [77]. In fact, the indirect exciton induced in a type II QD leads to a strong red-shift because the energy of the emission depends on the band offsets of the core and the shell materials, which can be smaller than the bandgap of either material [74].

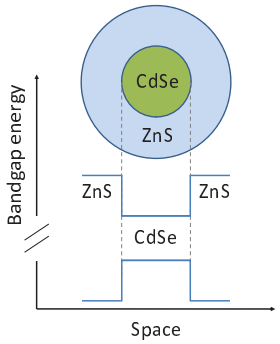

FIGURE 2.14: Schematic of the bandgap energies of a core-shell quantum dot.

It has been found that besides the size, the shape of a nanocrystal also affects its optical properties [78]. Nanocrystals can be grown with a high level of control in an elongated core-shell structure comprising a spherical (0-D) core (e.g. CdSe) and a rod-like (1-D) shell (e.g. CdS) [79]. Such a structure, referred to as a nanorod, can offer a large absorption cross-section like a quantum dot and QYs of $\sim 80\,\%$ [80]. Efficient energy transfer from the shell to the core leads to a large, length dependent Stokes shift. Nanorods are discussed in Chapter 7.

Since they consist of semiconductor material, nanocrystals are expected to be potentially more stable than organic luminescent materials. However, simple nanocrystals tend to degrade in the presence of oxygen. To prevent this, core-shell structures are usually used since the shell not only enhances the luminescence quantum yield, but also improves the stability [75]. A degradation study carried out on five nanocrystal LSCs indicated a reasonably good photo-stability [81]. Homogeneous polymer LSCs with surface areas

of 10-25 cm^2 and a thickness of 4 mm were prepared using a CdSe/CdS/CdZnS/ZnS core-multishell QD labelled Syn14, fabricated by R. Koole from Utrecht University. The QD had a diameter of 6.7±0.8 nm and a QY of 60 % in solution. The absorption and emission spectra of the QD in solution are shown in Figure 2.15. Table 2.3 provides an overview of the QD LSC samples and their properties.

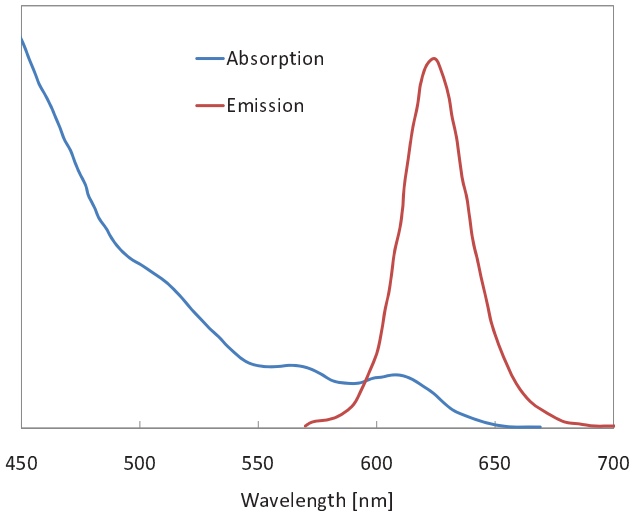

FIGURE 2.15: Absorption and emission spectra of a CdSe/CdS/CdZnS/ZnS core-multishell quantum dot with a QY of 60 % in dispersion.

Sample	QD concentration [µmol/l]	QY
1 (ECN792)	0.11	9.0 %
2 (ECN793)	0.11	18.1 %
3 (ECN805)	0.67	45.4 %
4 (ECN807)	0.52	44.2 %
5 (ECN806)	0.32	33.3 %

TABLE 2.3: Homogeneous quantum dot LSC samples for a degradation study. A core-multishell QD labelled Syn14 was used with a QY of 60 % in solution. The QY in the polymer matrix varies with the QD concentration and matrix composition. Sample 1 was prepared with twice as much UV-initiator as Sample 2.

The stability tests were carried out by recording the short-circuit current from an a-Si PV cell attached to one LSC edge at regular intervals while the samples were under continuous irradiation. The light source was a 1000 W sulphur lamp with a good spectral match to the solar irradiation, in particular in the UV region, which is assumed to have the greatest contribution to degradation. Figure 2.16 shows the change in the short-circuit currents relative to the respective original values before illumination. The test

was carried out for 280 hours, which is comparable to three months of outdoor exposure. After this duration, four of the samples degraded by less than 5 %. However, longer stability tests would be required to assess the feasibility of quantum dot LSCs with lifetimes of the order of 10 to 20 years.

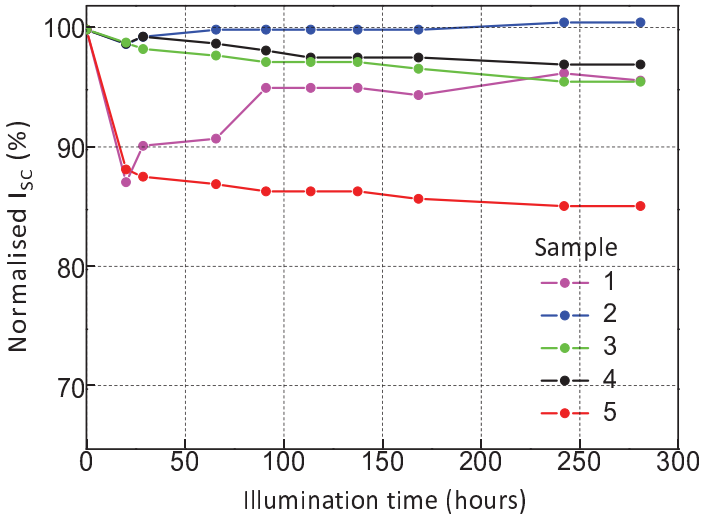

FIGURE 2.16: Degradation study of five quantum dot doped LSCs [81]. The short-circuit current measured at one edge is shown relative to the original value while the samples were illuminated continuously with a 1000 W sulphur lamp. The maximum duration of 280 hours is equivalent to approximately 3 months of outdoor exposure. Most of the samples showed less than 5 % degradation.

Peng *et al.* [75] carried out a degradation study on CdSe/CdS core-shell QDs over 4 months in air under room lighting. The change in the absorption spectrum was minimal, while the QY decreased from 90±10 % to 75±10 % over this period. Zhou *et al.* [82] showed that encapsulation of quantum dots in silica can also dramatically enhance the stability as well as the quantum yield. They demonstrated how a CdSe QD that due to photo-oxidation degraded in its absorbance to approximately 1/3 of the original value within 6 days in an air could be stabilised through silica coating such that it produced no noticeable (< 2 %) degradation over the same period. In a less realistic setting in the absence of oxygen, a comparison of CdSe/ZnS quantum dots with a Lumogen F Red 300 dye was reported in which the QD photo-degraded five times slower than the dye and fully recovered after a prolonged dark cycle [83].

2.4.3 Materials with Minimal Self-Absorption

Minimal self-absorption, i.e. a small overlap between the absorption and emission spectra can reduce escape cone losses and ideally limit them to the initial loss of $\sim 25\,\%$. Besides the typical dyes, a range of alternative luminescent materials and approaches has been considered in the search for minimal self-absorption, which generally relies on the same principle: the relaxation of the absorbed photon energy to a energetically lower state at a rate much faster than the rate of spontaneous emission. The absorbing component needs to have a significantly higher absorptance than the emitting component.

Non-radiative energy transfer has been proposed in the early years of LSC research as a method to minimise self-absorption [22]. Fluorescence (or Förster) resonance energy transfer (FRET) is such a mechanism, in which light is absorbed by a large concentration of donor molecules and transferred to a small concentration of acceptor molecules, which emit photons that are significantly red-shifted. The efficiency of FRET depends crucially on the separation r between the donor and acceptor molecules [84]:

$$\eta_{\mathrm{FRET}} = \frac{1}{1 + (r/R_0)^6} \tag{2.44}$$

where R_0 is the Förster distance, at which the transfer efficiency is $50\,\%$. R_0 is determined by the overlap integral of the donor emission and the acceptor absorption spectra and the relative transition dipole orientation. The small separations (of the order of nanometres) required for efficient FRET can be attained using the thin-film configuration described in Chapter 5. For example, Bailey *et al.* [85] reported nearly $100\,\%$ efficient FRET in a 3-dye LSC. Moreover, FRET has been achieved from organic luminescent centres to quantum dots [86] as well as the other way around [87] with FRET efficiencies of the order of $65\,\%$. The latter seems attractive for the LSC as the broad absorption of inorganic nanocrystals could be combined with the near unity QY of organic dyes. More interesting research in the field of resonance energy transfer between organic and inorganic luminescent materials is being carried out by G. Calzaferri's group (see for example Refs. 88, 89).

Another approach, utilised for example by Currie et at. [90], is intersystem crossing in organic molecules. Incident photons are absorbed by the electron pairs that form the chemical bonds between the atoms of the molecule. Each electron has a spin of $\pm\hbar/2$.

A singlet state describes an electron pair with an overall spin of 0. In this case the two electrons are correlated, and the Pauli exclusion principle dictates opposing spins. In a triplet state one of the electrons is excited, and the spins of the two electrons are aligned, so that the overall spin magnitude is $\hbar$. This gives rise to 3 quantum numbers (-1, 0 and 1), which explains the name of the triplet state. Excitation from a singlet ground state to a singlet excited state is more probable than to a triplet state since the latter involves a forbidden spin transition. Intersystem crossing occurs when the excited singlet state transitions non-radiatively to a triplet state, which can subsequently relax radiatively to the ground state in a process called the phosphorescence. A red-shifted emission is attained due to the lower energy of the triplet state compared to the excited singlet.

In rare-earth lanthanide complexes such as neodymium (Nd^{3+}) or ytterbium (Yb^{3+}) studied by Refs. 91, 92, 93, 94, 95, 96, forbidden or weakly allowed transitions lead to a very large separation between the absorption and emission spectra and a narrow emission peak. A further consequence is a very weak absorption cross-section, but sensitising the complexes with organic ligands is proposed as a solution. This involves intersystem crossing from the singlet to the triplet state in the ligand and non-radiative energy transfer to the lanthanide complex, which acts as the emitter. The efficiency of this energy transfer depends also on the energy gap between the sensitiser and the emitter. If the energy gap is too large, then the efficiency of the energy transfer is compromised. However, if the gap is too small, then thermally activated back-energy transfer can occur from the emitter to the sensitiser, which of course degrades the luminescence quantum yield. With lanthanide complexes, the elimination of self-absorption at quantum yields of $\sim$86 % is possible [94], but a narrow absorption spectrum remains an issue.

Saraidarov *et al.* [97] have investigated a compound, called diheptyl-bipyridyl-diol, that has virtually no self-absorption due to a phenomenon called anomalous Stokes shift. Low quantum yields (< 30 %) appear to pose a challenge for this compound.

Chapter 7 investigates two further luminescent centres that could deliver low self-absorption: nanorods, where the asymmetrical shape leads to a shift between absorption and emission spectra [78], and phycobilisomes, where efficient FRET leads to a large Stokes shift [98].

2.4.4 Multiple Luminescent Species

Many luminescent materials such as dyes have the drawback that their absorption spectrum is relatively narrow. In this section the use of multiple luminescent species is considered with the aim to broaden the absorption spectrum of the LSC.

The first group to propose multiple luminescent dyes in the LSC were Swartz *et al.* [19]. In this concept, the incident radiant energy is absorbed by one out of several dyes that collectively span a wide spectrum. The energy is cascaded down to the lowest energy dye for final emission. The emission spectrum of each dye needs to be matched to the absorption spectrum of the next lower energy one. The absorption spectrum of the collective would be the combined spectrum of each individual dye, while the emission spectrum would be that of the lowest energy dye alone, assuming ideal energy transfer. There are two competing energy transfer processes: radiative and non-radiative in form of fluorescence resonance energy transfer (FRET). The advantage of FRET over radiative energy transfer is that escape cone losses can be bypassed. The efficiency of FRET is very sensitive to the intermolecular separation. Swartz *et al.* fabricated LSCs with two dyes, Coumarin 6 (C6) and Rhodamine (Rh6G). Because their LSCs were homogeneously doped, the concentrations of the dyes were too small by an order of magnitude to facilitate efficient FRET.

The high dopant concentrations required for FRET can be achieved with the thin-film configuration, which has been chosen in several recent approaches using multiple dyes [85, 99–101]. Bailey *et al.* [85] reported a 3 dye LSC with highly efficient FRET close to 100%. The dyes used in their research were derivatives of a molecule designed by a collaborative partner. The multiple dye LSC showed an increase in output of 45-170 % compared to single dye LSCs comprising the individual dyes. Richards *et al.* [99] modelled LSCs containing up to seven dyes from the BASF Lumogen series, including near-infrared (NIR) absorbing dyes. They found that the highest system efficiency of 4.4 % was obtained with five dyes, while adding further dyes with lower quantum yields lowered the system efficiency.

An alternative approach to the ones described above, suggested by Ref. 102, comprises multiple luminescent species without spectral overlap, so that the emission spectrum has separate peaks. By coupling the output to a multijunction solar cell one could achieve

similar results as with an LSC stack (see Section 2.7), but without the need for several layers.

2.4.5 Directional Emission

Escape cone losses can be avoided in an LSC with preferential emission in the plane of the waveguide. This approach requires the alignment of anisotropic, directionally emitting luminescent centres. Batchelder *et al.* [20] predicted that this could potentially reduce the probability of emission into escape cones from 26 % to 9 % for an LSC with refractive index of 1.49. M. Debije's group [103, 104] was the first to carry out research on dye alignment in liquid crystal layers, recently followed by M. A. Baldo's group [105, 106] and T. W. Schmidt's group [51]. These approaches are based on the thin-film LSC.

The main alignments of interest are the planar one (with the molecules aligned in the plane of the waveguide) and the homeotropic one (perpendicular to the plane of the waveguide). Both the absorption and emission of a luminescent centre is governed by its transition dipole moment. Homeotropic alignment maximises the coupling of incident light into waveguide modes and thereby enhances the waveguiding efficiency, but the dipole orientation also weakens the absorption strength and hence the capture efficiency. The opposite applies to planar alignment. Debije *et al.* [103] demonstrated the concept by showing an improved waveguiding efficiency, but an enhancement of the optical efficiency was not achieved due to the losses in the light capture. A tilted alignment was suggested as a compromise between the homeotropic and the planar. Further studies [104] revealed another potential drawback of directional emission: in the homeotropic alignment, the absorption and emission dipoles are arranged in a way that amplifies self-absorption. Even if escape cone losses are reduced, the LSC remains susceptible to QY losses, which increase in the presence of self-absorption.

Mulder *et al.* [106] modelled luminescent molecules as Hertzian dipoles and predicted that the trapping efficiency of a waveguide with a refractive index of 1.5 would increase from 71 % to 91 % under homeotropic alignment and decrease to 66 % under planar alignment. Using a homeotropically aligned Coumarin 6 dye and a refractive index of 1.7 they reported an experimentally measured increase of η_{trap} from 66 % to 81 %. With a diffuser on top of the LSC to compensate for the weakened absorption a 16 % relative increase in the optical efficiency was achieved compared to the isotropic case.

As an aside, Mulder *et al.* [105] also proposed the exploitation of the dichroism in the absorption (the polarisation dependent absorption) of anisotropic dyes to replace linear polarisers in the flat panel display technology. These polarisers typically eliminate half of the light emitted by the display and turn it into heat. With a linearly polarised LSC, up to 38 % of the incident photons polarised parallel to the dyes can be coupled out of the LSC edges. The proposed concept presents a way to recycle otherwise wasted energy in flat panel displays, with potentially large advantages in portable devices.

Another way to make use of directional emission is to emit preferentially towards two of the four LSC edges, thereby reducing the solar cell area required [107]. It was found that a planar dye layer produced a 60 % higher emission out of the edges parallel to the alignment direction than out of the edges perpendicular, as well as a 30 % higher maximum emission than a isotropic layer.

The research described in this subsection has so far been focussed on dyes, but anisotropic nanocrystals in the form of nanorods could also lend themselves to directional emission. Alignment of nanorods has already been demonstrated on a micrometre scale [108] and could possibly be extended to the LSC scale in the future.

2.5 Additional Structures

The main losses in the LSC are due to insufficient absorption of incident light and emission out of escape cones. Mirrors mainly aid the absorption of incident light, as do plasmonic layers. Selective reflectors address the escape cone losses.

2.5.1 Mirrors

Mirrors or reflectors can improve LSC efficiencies, however at the cost of any partial transparency that may be desirable for certain applications. A metallic surface produces a specular reflection, meaning that the reflected angle is equal to the incident angle. A specular reflector on the back of the LSC effectively doubles the thickness of the LSC and hence the path of incident light, without increasing the solar cell area. A bottom mirror cannot remove the escape cone losses out of the bottom since reflected light within the bottom escape cone would simply escape out of the top. The advantage of

the bottom mirror is that the longer pathlength aids the absorption of incident light and gives light within the bottom escape cone a greater chance of being re-absorbed and redirected before escaping. The absorption probability could also be increased by raising the concentration of luminescent centres, but this would simultaneously amplify unwanted self-absorption. To a small degree, a mirror can also reflect light at high angles of incidence close to the LSC edges directly towards the PV cells. This effect is only significant along the perimeter of the LSC. The thickness of the LSC determines the required vicinity of the incident light to the edge. At a fixed thickness, the contribution of reflected light to the overall optical efficiency would decrease with increasing top surface area and hence with increasing geometric gain. At practical LSC dimensions, the effect of reflected light is considered to be insignificant. Since the reflectance of a metal reflector cannot compete with TIR it is advantageous to leave an air gap between the reflector and the LSC so that TIR is preserved.

A specular back reflector could be accommodated in the capture efficiency (Equation 2.20) by using a correction factor for the pathlength $z(\theta)$ (see Equation 2.19). In the case of a perfect reflector, the corrected pathlength would be

$$z_{\text{mirror}}(\theta) = 2z(\theta)\,. \tag{2.45}$$

A sheet of white paper or any other matt white solid produces diffuse reflection. Diffuse reflection is the result of multiple scattering of light under the surface of a material or from a rough surface (see for example Ref. 109). Light impinging on a diffuse reflector such as white paint enters the top layers and is randomly scattered internally until is exits out of the surface. The light scattered from the surface has a direction that is independent of the angle of incidence. The intensity profile of reflection from a flat, diffuse reflector is described by Lambert's cosine law:

$$I_{\text{reflected}} \propto I_{\text{incident}}\, \cos\theta \tag{2.46}$$

where $I_{\text{reflected}}$ and I_{incident} are the reflected and incident intensities, respectively, and θ is the inclination of the reflected ray to the surface normal. The intensity of the reflection is highest at the surface normal and drops off with the inclination. Lambertian reflection has the property that the apparent brightness of the reflecting surface is the same at all

viewing angles. The brightness is a measure of photon flux observed per unit area of the apparent emitter. According to Equation 2.46 the photon flux decreases with the cosine of the inclination, but so does the apparent width of the reflecting surface, resulting in a constant brightness.

By attaching a diffuse reflector to the back surface without an air gap, incident light could be partially directed towards the edges at angles that undergo TIR at the top surface. However, without TIR at the bottom surface, light travelling within the waveguide could be reflected out again by the diffuse reflector. The net effect is that no concentration (above the n^2 factor discussed previously) can be achieved with a non-luminescent concentrator that relies only on a diffuse back reflector [53]. This has also been verified with raytrace simulations (see Section 4.4). A non-luminescent concentrator has been proposed by Ref. 110, based on their raytrace simulations, but these simulations assumed isotropic reflection from the back surface, which, in the author's opinion, is unphysical: according to Ref. 111 no flat, reflecting surface can create an isotropic reflection that is independent of the angle of incidence.

Simulations of back reflectors are presented in Section 4.4. Replacing some of the cells on the LSC edges by mirrors has been proposed as a way of further reducing the cell area, but the study presented in Section 4.3 suggests that this configuration does not yield any advantages.

2.5.2 Selective Reflectors

A wavelength (or energy) selective reflector placed on the top surface of the LSC can confine the escape cone emission, as shown in Figure 2.17. Combined with a back reflector, this approach affords trapping beyond the limitations of TIR. The desired properties of a selective reflector are a high spectral transmittance over the LSC absorption range and a high reflectance over the emission range. Using this method, the light capture efficiency can be maintained for the most part whilst the waveguiding efficiency is boosted. The approach relies on the Stokes shift between the absorption and emission spectra, but since most luminescent materials have a finite overlap between the absorption and emission despite a Stokes shift, even an ideal selective reflector cannot eliminate escape cone losses entirely without paying a penalty in terms of the capture efficiency.

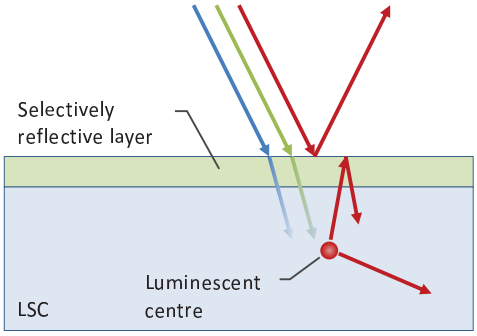

FIGURE 2.17: Schematic of a selectively refractive layer that transmits higher energy light within the absorption spectrum of the luminescent centres and reflects lower energy light within the emission spectrum.

Richards *et al.* [101] first proposed the use of a selective reflector for the LSC in the form of a distributed Bragg reflector (DBR), also referred to as a hot-mirror or dichroic filter. A DBR consists of a sequence of dielectric layers with alternating refractive indices. Fresnel reflection at the interfaces between the layers leads to interference, which governs the reflective properties of the DBR. The optical thickness (the product of refractive index and geometric thickness) of the layers is generally a quarter or a half of the peak wavelength the DBR is designed to reflect. The same principle of interference also applies to anti-reflective coatings, where either the optical thickness or the arrangement of the layers is changed to produce the opposite effect of DBRs. For a sharp onset of the reflectance, a large number of layers is required. A variant of the DBR is the Rugate filter, in which the alternating refractive indices are sinusoidally modulated to produce a better spectral reflectance profile. Goldschmidt *et al.* [112–115] have fabricated LSCs with Rugate filters and achieved relative enhancements in the system efficiency of 20 %.

As an aside, TIR is not affected by index mismatched dielectrics attached to the LSC without an air gap. A ray emitted from a doped waveguide with refractive index n_w gets refracted at the interface to air as follows:

$$\sin\theta_{\text{out}} = \sin\theta_{\text{in}}\,\frac{n_w}{n_a} \tag{2.47}$$

where n_a is the refractive index of air and θ_{out} and θ_{in} are the outgoing and incoming angles, respectively. When an arbitrary number p of varying refractive index materials

is placed between the emitting material and air, the overall refraction remains the same:

$$\sin\theta_{\text{out}} = \sin\theta_{\text{in}} \frac{n_w}{n_1} \prod_{i=1}^{p-1} \frac{n_i}{n_{i+1}} \frac{n_p}{n_a} \tag{2.48}$$

$$= \sin\theta_{\text{in}} \frac{n_w}{n_a} . \tag{2.49}$$

This means that TIR is maintained.

A drawback of the DBR is its angular dependence: since the optical path governing the interference depends on the angle of incidence, the spectral reflectance profile is shifted when light is not normally incident, making it difficult to optimise the DBR response for the LSC. Though is has been suggested to utilise the angular dependence in the design of an LSC with an angularly selective filter [116], it is the author's opinion that such a device would forfeit one of the main selling points of the LSC as it would be limited to only small acceptance angles for incident light. The drawback of DBRs can be addressed with 3-dimensional photonic structures. Photonic structures are designed on the light wavelength scale and exploit the analogy between electron waves in a periodic atomic lattice and electromagnetic waves in a photonic crystal [117]. In a similar fashion to the electronic bandgap in a semiconductor, a photonic bandgap in a photonic structure prohibits the propagation of light that is energetically within the bandgap. A DBR is essentially a 1-dimensional photonic structure. 3-dimensional photonic structures eliminate the angular sensitivity and are therefore attractive as a selective reflector. A naturally occurring 3-dimensional photonic structure is the opal. However, photonic crystals with reflectance profiles tailored to the LSC need to be made artificially.

Selective reflection can also be achieved with cholesteric coatings made from liquid crystals. Liquid crystals are organic molecules that can be in a liquid phase whilst still maintaining a crystal structure. In the cholesteric phase, also referred to as the chiral nematic phase, the liquid crystals are aligned within individual layers, with a twisting of the directionality between adjacent layers resulting in a helical structure. This structure requires chiral dopants, i.e. molecules with no inversion symmetry, which also leads to a chirality (or handedness) of the cholesteric phase. A cholesteric coating reflects only circularly polarised light of matching handedness within a narrow wavelength band ($\sim 75\,\text{nm}$). The position of the reflection band can be tuned via the amount of chiral

dopant. Since the emission from the LSC is unpolarised, a combination of two cholesterics with opposite handedness would be required to create a practical selective reflector. The use of cholesteric coatings on LSCs has been pioneered by Debije *et al.* [118] and shown to recover more than 30 % of the waveguiding losses in 50 mm×50 mm×3 mm samples [119, 120]. Much like the DBRs, cholesteric coatings suffer from a strong angular dependence of the reflectivity profile [121]. An advantage of the cholesteric coating over inorganic reflectors is that it can be deposited from solution, enabling large area roll-to-roll processing.

2.5.3 Plasmonic Layers

A further development of the LSC is the use of plasmonic layers to enhance the fluorescence from dyes [122–124]. A plasmon is a quantum of plasma oscillations (collective oscillations of the free electron gas), which can couple with electromagnetic radiation to create a quasi-particle called a plasmon polariton [125]. A plasmonic layer on top of the LSC can also scatter light and couple it into waveguide modes. Although this also enables the reverse path (the coupling out of light within waveguide modes) the longer pathlengths of scattered light can aid absorption. A plasmonic layer usually consists of microscopic metal islands. The geometry and size of the structures determines the optical properties of the plasmons. Since the interactions with light are based on the wave optics, low areal densities of the metal islands around 5 % can be sufficient to have strong plasmonic effects. Another property of surface plasmons that could be interesting for LSC research is their effect on the emission from luminescent centres. Zhang *et al.* [126] reported an enhancement of the fluorescence of perylene dyes in close proximity to silver island films. In recent PV research, plasmons have been successfully used to enhance solar cells performances [127, 128].

2.6 Record LSC Efficiencies

In recent years, LSC module efficiencies around 7 % have been reported based on different approaches: Marc Baldo's group received much media attention for a publication by Currie *et al.* presenting a series of LSCs and LSC stacks that achieved efficiencies up to 6.8 % [65, 90] using organic luminescent materials exhibiting FRET or phosphorescence.

Goldschmidt *et al.* [114] measured a maximum efficiency of 6.7 % using a stack of dye doped LSCs including a photonic structure as selective reflector. An efficiency of 7.1 % from a single LSC module was reported by Slooff *et al.* [129, 130]. It should be noted, however, that the efficiency alone is not a sufficient measure of LSC performance. The aforementioned LSC modules had geometric gains of 3, 2.1 and 2.5, respectively. In fact, one may argue that in some of these cases there is actually no concentration and the cells alone would generate more power under direct illumination than in combination with the LSC. However, at larger LSC sizes with large geometric gains, this can change, provided that the optical efficiency does not decrease too fast with G. In conclusion, scalability is very important. It turns out that the high efficiency published by Slooff *et al.* is partly due to contributions of incident light coupling directly into the solar cells due to a spread of incident angles. This effect does not scale with G and would diminish at larger LSC sizes. Meanwhile, the design by Currie *et al.* [65, 90] exhibits very little self-absorption and can therefore maintain relatively high efficiencies of up to 6.1 % even at a geometric gain of 45. This constitutes a relative loss of only ~ 10 % at a 15-fold increase in geometric ratio. The highest concentration factor reported by Currie *et al.* is 11, but according to their projections, concentrations up to 50 should be feasible. Such a concentration could be achieved with a geometric gain of 250 (e.g. dimensions of 1 m by 1 m by 1 mm with cells on all edges) and an optical efficiency of 20 %.

2.7 Variants of the LSC

One variant of the LSC is the thin-film (TF) LSC. It consists of an optically dense active layer on top of a transparent, index matched substrate. In order to achieve an absorbance comparable to a homogeneously doped LSC, the concentration of luminescent centres in the active layer needs to compensate for its small thickness, typically between 10 µm and 100 µm. As shown in Figure 2.18, the entire film-substrate composite acts as the waveguide.

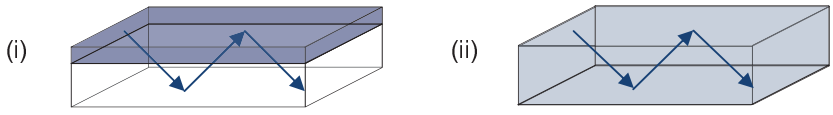

FIGURE 2.18: The schematic of a thin-film LSC (i) in comparison with a homogeneously doped LSC (ii). The thin-film LSC absorbs light in a thin active layer, while the luminescence travels within the entire film-substrate composite.

The thin-film approach allows for a greater freedom in the choice of waveguide materials. For example, glass can be used as a substrate. Since glass absorbs UV light, which can degrade luminescent species, the substrate could be used to protect the active layer. This would require a configuration in which the active layer is on the bottom or sandwiched between two substrates. The fabrication of TF LSCs appears to be simpler than that of the homogeneous one, and this could give the TF LSC a commercial advantage. In fact, the LSC fabrication could utilise the standard industrial procedures of placing optical coatings on glass. Moreover, the small molecular separation between the luminescent centres in the film can be beneficial for fluorescence resonance energy transfer. However, it should be noted that the TF LSC is sensitive to the index matching between the film and the substrate. A mismatch can substantially affect the performance as light gets trapped in the optically dense film and lost via re-absorptions. The comparison of the thin-film LSC with the conventional, homogeneously doped LSC is the subject of Chapter 5.

High LSC system efficiencies can be achieved with the stack (see for example Refs. 18, 63, 131): it consists of several LSCs absorbing different parts of the spectrum and with matching cells attached to them, placed on top of each other. In this way, the broad solar spectrum is converted more efficiently. The LSC with the highest energy absorption band is placed on top; lower energy light passes through and is absorbed in lower layers, much like in a multijunction solar cell. However, since the solar cells on the edges can be connected individually, unlike the multijunction cell, the LSC stack is not subject to current matching constraints. Air gaps between the layers are required to maintain the waveguiding within each layer. Practical difficulties in fabricating stacks include the availability of luminescent materials required to cover the solar spectrum and the availability or cost of suitable solar cells. Stacks also offer advantages in terms of colour considerations for indoor lighting solutions [132]. Most conclusions drawn from this thesis based on individual LSCs can equally be applied to stacks.

Another consideration is the position of the solar cells. In the conventional design the cells are placed on the waveguide edges. N. Boling [133] patented a design with a cell attached to the bottom of the LSC. Rau *et al.* [56, 134] also place the cells on the bottom surface of the LSC, covering only a small fraction of the area and thereby maintaining a high geometric gain. With the cells being index matched to the surface (for instance via a viscous index matching fluid) light can couple into them, while the area without cells

continues to act as a waveguide. The same theoretical limitations on concentration and efficiency apply to this design as to the conventional one, but one practical advantage is that the cells can absorb any directly incident light that the LSC cannot collect. It is not obvious whether covering the back surface with solar cells is simpler in terms of fabrication than covering the edges. Having cells and electrical connections on the back, however, can affect the aesthetic properties of the LSC and would place limits on the extension to a stack. In the studies presented in this thesis, the solar cells were placed on the edges only.

LSC related concepts have been proposed for a range of alternative applications. A major one is luminescent up- or down-conversion, which boosts solar cell efficiency by better matching the incident spectrum to the cell [135, 136]. In this concept, a down-converting layer is placed on top of the solar cell to absorb high-energy photons and convert them to lower energy photons via photon multiplication; an up-converting layer is placed below of the cell to collect multiple sub-bandgap photons and convert them to above-bandgap photons. An up-conversion efficiency of 16 % was recently reported by T. W. Schmidt's group using rubrene molecules [137]. Up-conversion can provide more substantial efficiency improvements than down-conversion, but since it is a non-linear process, requiring at least two-photons and the population of intermediate energy states, it is more challenging to achieve under sunlight. However, in the recent past, up-conversion using low-intensity non-coherent light has been demonstrated with a quantum yield above 1 % [138]. Both up- and down-conversion have been proposed as ways to increase the power output of the LSC [139]. Another process, similar to down-conversion, is luminescent down-shifting, where a the energy of a photon is downgraded without creating multiple photons. This process occurs in the LSC, and unlike down-conversion, down-shifting cannot exceed a QY of 1. Efficiency enhancements via such down-shifting have been observed in real solar cells [140].

A novel and interesting modification of the LSC that exploits liquid crystal display technology could lead to a type of smart window [141]: anisotropic luminescent molecules (as discussed in Section 2.4.5) are placed in a liquid crystal layer such that their alignment and hence their absorptance is controlled by an externally applied voltage. Using this method the LSC can be switched instantly from a transparent state, in which it acts as a window, to an absorbing state in which it generates power. Initial results [141] showed

a 31 % difference in the overall absorption between the two states and demonstrated the concept of this promising technology.

There has been some recent, theoretical work based on a wave-optics approach to substantially enhance the optical efficiency of the LSC [142, 143]. In the proposed designs, the luminescent material is integrated in a nanometre-sized host layer of low refractive index, sandwiched between transparent sheets (e.g. glass) of higher refractive index. By having the active layer act as a cavity, resonance effects can be exploited that are expected to achieve a more than twofold increase in the optical concentration ratio of the LSC [142].

Other applications based on LSC technology include indoor daylighting systems [144–147] and a recently proposed inexpensive large-area photosensor for use as an interactive screen [148].

As an aside, the luminescent centres can be integrated in a solid matrix or dissolved in a liquid contained within a transparent, index matched enclosure [149]. While the liquid LSC allows for easy replacement of the luminescent material, the solid matrix has been found to improve the photo-stability of dyes [63].

2.8 Chapter Conclusion

This chapter described the principles of photovoltaic cells and the luminescent solar concentrator (LSC). The LSC offers the unique advantage that it concentrates diffuse as well as direct sunlight. The energetic down-shift of collected light is the key to concentration via the LSC. An LSC module with solar cells attached to the edges is not expected to outperform the cells alone in terms of power per area, but theoretical considerations show that high system efficiencies could be attainable, while maintaining a lower overall cost.

The cost-to-power ratio was defined for LSC modules, and its dependency on the geometric gain G, the optical efficiency η_{optical} and the cost ratio of LSC to PV cell γ was established. Assuming that γ is relatively insensitive to the LSC configuration, the focus should be on improving G and η_{optical}, bearing in mind that these two quantities are linked: η_{optical} inevitably decreases with increasing G. It has been established that the

circular geometry produces the highest geometric gain amongst the planar LSC geometries. The best tessellating structure is the hexagon, followed by the square and then the triangle. However, in the author's opinion, the differences are marginal and do not create a compelling reason to favour a specific geometry based on the gain.

Besides dyes there is a range of luminescent materials being employed in LSCs today, such as semiconductor nanocrystals, material systems utilising resonance energy transfer or rare-earth lanthanide complexes. The main aims are to broaden the absorption, to maintain a high luminescence quantum yield and to enhance the Stokes shift. While shortcomings in the stability of the luminescent centres had posed a problem during the early days of LSC research, recent degradation studies on dyes as well as quantum dots indicate that the desired lifetimes of approximately 20 years could be feasible.

The main losses of the LSC are due to unabsorbed incident light and luminescence lost out of escape cones. Different approaches to improving the LSC have been reviewed in this chapter. These include the use of luminescent materials with little self-absorption, directional emission, back-reflectors and photonic structures on top of the LSC.

The LSC is essentially a low-concentration device: based on current developments concentration factors up to 20 can be considered a feasible target. High-concentration cells based on III-V materials are designed to work under several hundred suns concentration and can thereby justify costs per area that are orders of magnitude larger than that of crystalline silicon cells. Although high-efficiency cells have been considered for the LSC in the past [150], it is the author's opinion that the choice of solar cells for the LSC is currently limited to relatively inexpensive silicon or thin-film cells, unless the LSC is used as a secondary concentrator (see Chapter 6) so that high concentrations can be achieved.

Given the anticipated low cost of the LSC, even a small concentration can lead to cost advantages. For example, to generate the same power as a given solar cell under direct illumination, an LSC module with a concentration of 5 (a conservative example given that Currie *et al.* have already reported a concentration factor of 11 [65]) would require only 1/5 of the solar cell material. In fact, with the right choice of luminescent species the LSC output spectrum can be matched to the cell QE so that the cell works more efficiently than under AM1.5, and even less cell material would be required. A cost benefit would remain as long as the cost of the LSC makes up less than 4/5 of the cell.

It should be noted, however, that in a practical application the efficiency plays a role as well, since space also comes at a price. In the author's opinion, a commercially viable opaque LSC would require an efficiency of at least 5 %, given that thin-film solar cells with approximately 10 % efficiencies could be considered a competitor to such an LSC. However, LSCs can target different markets, as they can be designed in different colours and even semi-transparent and can be integrated into building facades. Incidentally, the current application of luminescent waveguides is predominantly limited to visual or decorative purposes, but recent developments indicate that the LSC has the potential to make photovoltaic energy more cost-effective.

Chapter 3

Materials and Methods

3.1 Chapter Introduction

The materials and the processes used in the fabrication of LSC and the samples themselves are described in this chapter. Moreover, several standard methods of characterising the LSC are explained. Some experiment-specific methods are incorporated in later chapters. Many of the studies presented in this thesis are based on a computational method, the Raytrace Model described in Section 3.5.

3.2 Sample Preparation

The LSCs studied were fabricated by A. Büchtemann and J. Quilitz from the Fraunhofer Institute for Applied Polymer Research (IAP), who were collaborators on the EU FP6 Integrated Project FULLSPECTRUM. Homogeneously doped concentrators were made using polymer matrices. In the fabrication process, the luminescent centres are blended into a monomer solution. Polymerisation initiators are added to the mixture, which is then poured into a sample mould for polymerisation and activated either thermally or with UV light. In this process, the monomers form polymer chains via chemical reactions. The final product is a solid plate.

In the case of thin-film LSCs, the polymerisation step is bypassed: the polymer is dissolved, the luminescent centres are added to the solution, and the blend is drop or spin cast onto a transparent, index matched substrate, typically glass or PMMA. The

solvent then evaporates, leaving a thin active layer on the substrate. The flatness of these layers was not measured for the samples presented in this thesis. The materials and fabrication methods are described in detail in the following subsections.

3.2.1 Materials

Two types of luminescent centres (excluding the phycobilisomes discussed in Section 7.3) were employed in the samples characterised for this thesis, organic dyes and inorganic core-shell nanorods. An overview of the luminescent centres is given in Table 3.1. The dyes were commercially available ones, while the nanorods were provided by collaborators: JHN46 by P. Alivisatos' group at the University of Berkeley, CA, and AR DRT26 by L. Manna's group at the NNL-National Nanotechnology Laboratory in Italy [108]. The quantum yields stated in Table 3.1 are approximate values, as they can be affected by several factors, such as the host matrix.

Label	Description	Emission peak [nm]	QY [%]
Lumogen F Red 300	Perylene dye from BASF	613	98
Fluorescent Red	Coumarin dye from Bayer	608	95
Fluorescent Yellow	Coumarin dye from Bayer	485	95
AR DRT26	CdSe/CdS nanorods	600	$\sim$67
JHN46	CdSe/CdS nanorods	630	$\sim$50

Table 3.1: Luminescent materials used for LSC fabrication.

The spectral properties of the dyes and the nanorods are illustrated in Figure 3.1 and Figure 3.2, respectively.

Homogeneous LSCs are typically fabricated using a polymer host matrix because they allow the incorporation of luminescent centres and offer high transparencies in the visible spectrum at relatively low costs. The samples characterised in this thesis were mostly based on poly(methyl methacrylate) (PMMA) and poly(lauryl methacrylate) (PLMA). The refractive index in the visible of these polymers is approximately 1.49. Based on measurements on several host matrices at a wavelength $\sim 630\,\mathrm{nm}$ the absorption coefficient of PMMA was generally found to be around or below $1\,\mathrm{m}^{-1}$ [102, p. 92] and as low as $0.3\,\mathrm{m}^{-1}$ in the case of commercially acquired PMMA. For PLMA the absorption coefficient was found to be similarly low (see Figure 3.3). In the case of thin-film LSCs,

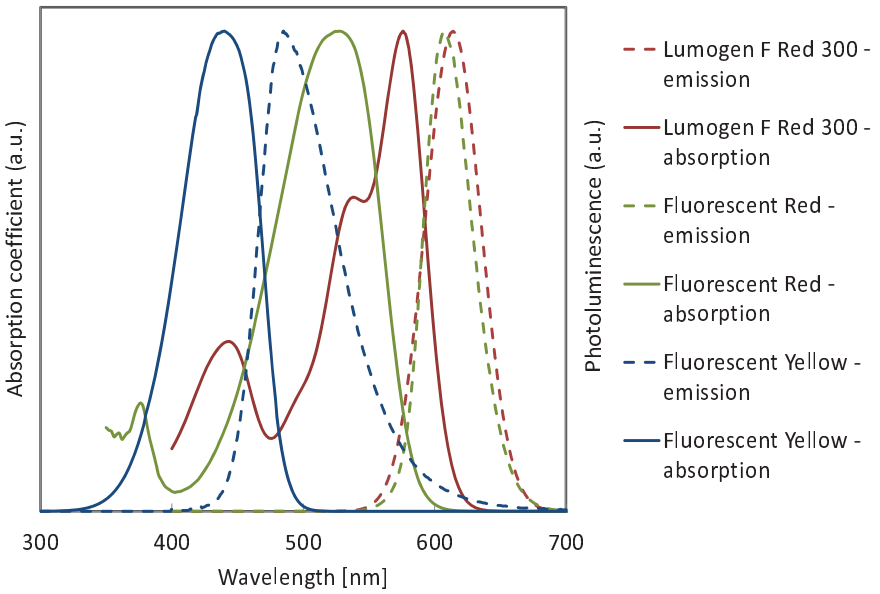

FIGURE 3.1: Absorption and emission spectra of three dyes used to fabricate LSCs.

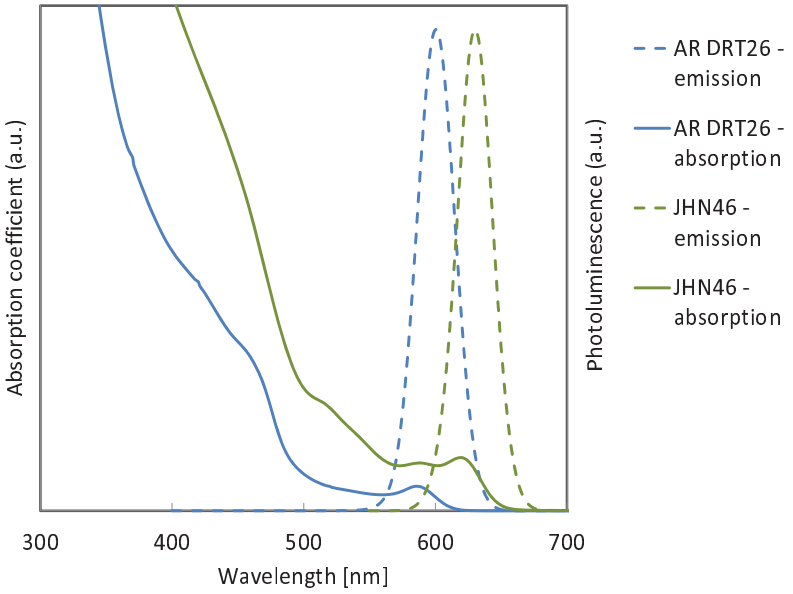

FIGURE 3.2: Absorption and emission spectra of two nanorods used to fabricate LSCs.

glass can also be used as the host material, with refractive indices and absorbances in the visible that are comparable to those of PMMA.

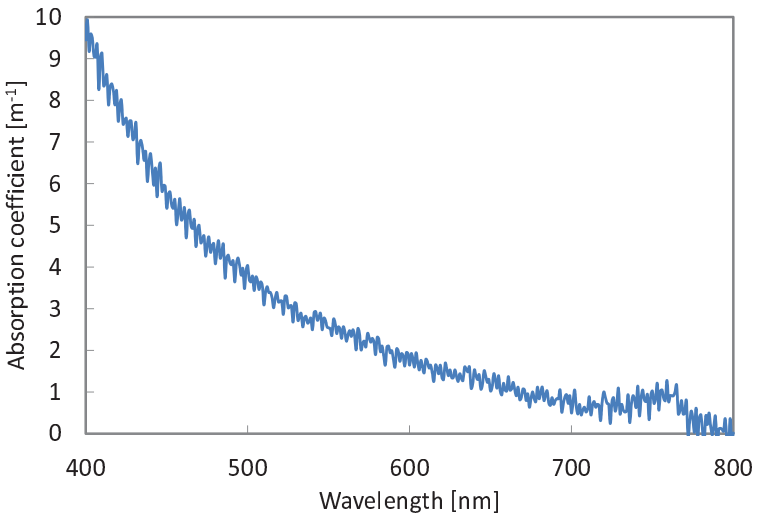

FIGURE 3.3: Absorption coefficient of a 1 mm thick PLMA matrix including 25 % ethylene glycol dimethacrylate (EGDM), measured as described in Section 3.4.1 and correcting for reflection using Equation 3.4. The EGDM concentration is a result of a trial and error approach to achieve cross-linking of monomers (explained in the following section). It should be noted, that at long wavelengths (approximately above 750 nm) the deduced absorption coefficient may be a little too low, generating an artificial peak. This is because a constant refractive index was assumed for simplification. In reality, the refractive index of polymer matrices decreases as the wavelength increases, so that the impact of reflection at long wavelengths should actually be slightly smaller than assumed.

Thin-film LSCs can also be made using a glass substrate. Though glass can often have a high background absorption compared to polymers, high optical quality glass, such as N-BK7 from Schott [151], can match the low absorption coefficients of the high quality polymers in the visible of $\sim 0.3\,\mathrm{m}^{-1}$ (see Figure 3.4).

3.2.2 Fabrication of Homogeneous LSCs

The homogeneous samples were fabricated by A. Büchtemann and J. Bomm from the Fraunhofer IAP. The samples were fabricated by filling a liquid reaction mixture into a custom-made, flat cuvette, which acted as the sample mould for the polymerisation. The polymerisation was carried out thermally or via UV light. The thickness of the fabricated LSC-samples was between 3 mm and 1 cm. The largest plates fabricated had top surface areas of 18 cm×26 cm. The cuvettes were made of thoroughly cleaned glass plates of 3-5 mm thickness, conjoined via elastic spacers to produce a cavity matching

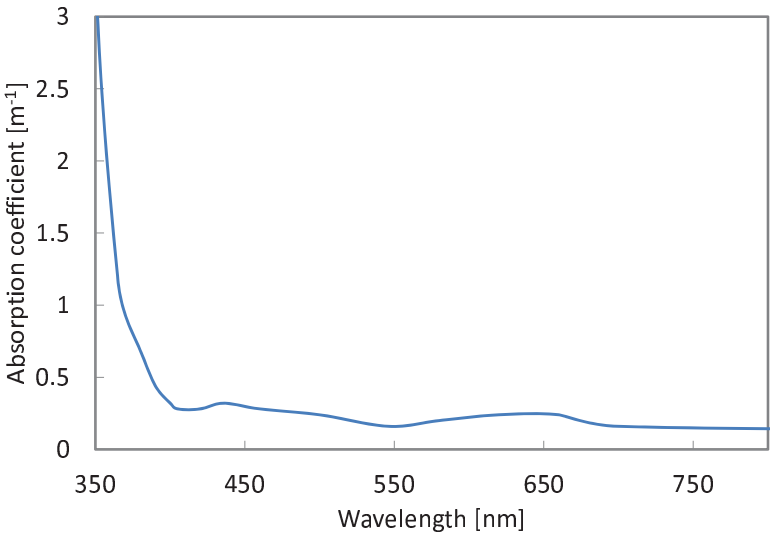

FIGURE 3.4: Absorption coefficient of N-BK7 optical glass from Schott [151]. This type of glass was chosen for its high transmittance in the visible.

the desired LSC thickness. The construction was held together by clamps initially and by a steel frame later on. Standard float glass was used for the cuvette walls. The glass surface was prepared (through coating with ClearShield or NanoTop) in a way that allowed easy removal of the polymerised, solid sample. Initially, the spacers were made from silicone, which was previously cleaned in acetone. The silicone was later replaced by fluorinated ethylene-propylene (FEP), which is chemically more inert. The spacers need to be elastic because the polymer shrinks during the polymerisation process. Rigid spacers would either lead to breakage of the glass, when there is strong adhesion between the polymer and the glass during the shrinking, or to an uneven polymer surface, when there is weak adhesion between the polymer and the glass. Elastic spacers allow the cuvette to shrink simultaneously with the polymer and help create polymer surfaces as flat as the cuvette walls.

The preparation of the reaction mixture depends on the type of luminescent material and monomer used. Initial samples were thermally polymerised and mostly made from Plexit, a commercial mixture of methyl methacrylate (MMA) and PMMA, while later ones mostly used MMA that was distilled in-house and stored at -18 °C. Through the distillation the stabiliser is removed, yielding purer MMA that polymerises faster. When the viscosity of the monomer is low (e.g. in the case of MMA), the initiator and the luminescent material can be blended directly with the monomer. Typically, the materials are dissolved in a small amount of monomer using an ultrasonic bath, before

more monomer is added. When the viscosity of the monomer is high (e.g. in the case of Plexit), the luminescent material and the initiator are first dissolved in a solvent or a diluting agent. The solution is then mixed with the monomer. In cases where the luminescent material is not soluble in the monomer, a suitable solvent needs to be found via trial and error. The dye doped samples that were UV-polymerised were made from MMA/(hydroxyethyl)methacrylate (HEMA) (1:1) mixtures. A variety of reaction mixtures was tested to dissolve inorganic nanocrystals, including MMA, lauryl methacrylate (LMA), lauryl acrylate (LA) and HEMA with varying initiator concentrations and compositions. The best results were achieved using monomer blend consisting of 75-80 % LMA by weight (without stabiliser) and 25-20 % ethylene glycol dimethacrylate (EGDM), which is a cross-linking agent. The stabiliser in the LMA was removed through solvent extraction in NaOH.

To achieve a high degree of homogeneity, the reaction mixture was stirred intensively with a Teflon coated stirrer. Subsequently the mixtures were evacuated at approximately 200 mbar and poured into the cuvette. Care needed to be taken to pour the mixture at the right pace; pouring too quickly can lead to the formation of air bubbles, while pouring too slowly can lead to the formation of films that compromise that optical homogeneity. It was found that bubbles formed during the pouring often rise to the surface if the cuvette is left standing before polymerisation. In the case of thin samples the mixture was sometimes inserted into the cuvette with a syringe.

The thermal polymerisation of the Plexit based samples was carried out in a programmable drying oven, in which the samples underwent a cycle of several temperature steps for heating and cooling: 30 minutes at 30 °C, 30 minutes heating to 45 °C, 3 hours at 45 °C, 30 minutes heating to 55 °C, 3 hours at 55 °C, 30 minutes heating to 70 °C, 10 hours at 70 °C, 30 minutes cooling down to 55 °C, 30 minutes cooling down to 45 °C, 30 minutes cooling down to 40 °C, 1 hour cooling down to 30 °C. After inspection the samples were left for 2 hours at 80 °C, followed by a few more hours at 100 °C to enhance the curing. The cuvettes were sealed before the thermal process to avoid oxygen contamination and evaporation losses. The initiator was azobisisobutyronitrile (AIBN), added in concentrations of 0.05 % to 0.1 % in a trial and error approach.

The samples based on distilled MMA were thermally polymerised in a water bath for 25 hours at 50 °C, allowing a better dissipation of reaction heat. Subsequently, the samples

were cured in the drying oven for a few hours at 70 °C, 80 °C and 110 °C. For the water bath treatment, the cuvettes were sealed with silicone rubber. AIBN at a concentration of 0.05 % was used as the initiator for this thermal process.

The UV-polymerisation was carried out in custom-built boxes comprising a sample space, electrical connections, and 36 W UV-A emitting light bulbs on two opposing inner walls and a transparent cover that blocked off UV light. The cuvette was placed in the middle of the sample space, parallel to the UV bulbs on either side at a distance of 10 cm. The intensity of the UV irradiation could be controlled continuously. A low intensity was used for dye doped samples to avoid overheating. The duration of this polymerisation process was approximately 20 hours. The process took longer when nanocrystals are present in the reaction mixture as they absorbed a substantial amount of the UV radiation. After initial solidification the samples were removed from the sample cuvette and left for 1 to 4 hours for further polymerisation under UV light. Besides being quicker than the thermal process, the UV-polymerisation has the advantage, that a pipe can be connected to the cuvette to continually flush the remaining volume above the reaction mixture with nitrogen. This removes the atmospheric oxygen, which inhibits the polymerisation. The addition of initiators was based on a trial and error approach. For the dye doped samples, the liquid UV-initiator Irgacure 1700 was used at a concentration of 0.4 %, and often 0.04 % of AIBN was added. All nanocrystals samples were UV-polymerised, using Darocur 4265 as the initiator at concentrations between 0.05 % and 0.5 %. The nanocrystal concentrations were varied from 0.008 % to 0.5 %.

3.2.3 Fabrication of Thin-Film LSCs

The thin-film LSCs were fabricated by A. Büchtemann and J. Bomm from the Fraunhofer IAP. The two typical fabrication methods for thin-film LCSs are drop casting and spin-coating. All samples presented in this thesis were fabricated using the casting method. Generally, 5 cm×5 cm×1 mm plates made of glass or PMMA were used as substrates. Both the luminescent material and the polymer needed to be dissolved in the process. Several solvents were used for different polymers: 15 % PMMA dissolved in ethyl acetoacetate (EAA); Paraloid B72 (an acrylate) dissolved in ethyl acetate (EA) or EA/EAA;

10 % PMMA in chloroform; 2.5 % cellulose triacetate (CTA) in dichloromethane/chloroform (1:1). The first two combinations were used for various dye doped samples, whereas the latter two were used for nanocrystals.

The dyes themselves were dissolved mostly in EAA, dimethylformamide (DMF) or dichloromethane with the aid of an ultrasonic bath. The dye solution was blended into the polymer solution by stirring for approximately 5 minutes.

The nanocrystals were often provided already dispersed in chloroform, so that the solution only needed to be diluted and added to the polymer solution. If the nanocrystals were dissolved in toluene, this solvent was largely evaporated, and the desired solvent was subsequently added. After an ultrasonic treatment the new solution was blended into the polymer solution.

The thin films were fabricated in a cleanroom. After the substrates were thoroughly cleaned, 1-2 ml of the solution containing the luminescent material and the polymer, depending on the desired film thickness, were dropped onto them with a pipette and spread across the entire surface, while avoiding any spill over the edges. The substrates were stored on a levelling table and covered with another glass plate until the solvent had evaporated. Subsequently the samples were left to dry at room temperature for a day, after which they were stored for 1 to 2 hours at 80 °C to remove any remains of the solvent. When a PMMA substrate is used (as opposed to a glass substrate), the luminescent centres can partly diffuse into the substrate as the solution cast onto the substrate dissolves its surface.

3.3 List of Samples

The following is a list of samples that were characterised in this thesis. Details of the sample properties and the fabrication methods are given along with descriptions of the experiments they were used for. The concentrations stated in this thesis are mass concentrations. The phycobilisome samples discussed in Section 7.3 are not described here, but in said section.

3.3.1 Samples in Chapter 3

Sample: **Red-l**

Description: Red dye doped homogeneous sample used for the computational model validation (Section 3.5.3)

Dimensions: 4.8 cm×1.8 cm×2.6 mm

Luminescent material: Bayer Fluorescent Red coumarin dye (QY 95 %)

Host material: Plexit (refractive index of 1.49, background absorption coefficient in the visible of $\sim 2\,\mathrm{m}^{-1}$)

Made by: Fraunhofer IAP

3.3.2 Samples in Chapter 4

Sample: **Red-a**

Description: Red dye doped homogeneous sample used for angular response measurements (Section 4.2)

Dimensions: 10.6 cm×10.6 cm×5 mm

Luminescent material: Bayer Fluorescent Red coumarin dye (QY 95 %)

Host material: PMMA

Made by: Fraunhofer IAP

3.3.3 Samples in Chapter 5

Sample: **ECN555**

Description: Homogeneous sample A used for the comparison of thin-film and homogeneous LSCs (Section 5.2) and the angular emission profile measurements (Section 5.4)

Dimensions: 5.0 cm×5.0 cm×3 mm

Luminescent material: BASF Lumogen F Red 300 (QY 95 %) at a concentration of 0.062 %

Host material: Plexit

Made by: Fraunhofer IAP

Sample: **ECN690**

Description: Homogeneous sample B used for the comparison of thin-film and homogeneous LSCs (Section 5.2)

Dimensions: 5.0 cm×5.0 cm×3 mm

Luminescent material: BASF Lumogen F Red 300 (QY 95 %) at a concentration of 0.0175 %

Host material: Plexit

Made by: Fraunhofer IAP

Sample: **ECN1096**

Description: Thin-film sample A used for the comparison of thin-film and homogeneous LSCs (Section 5.2) and the angular emission profile measurements (Section 5.4)

Dimensions: 5.0 cm×5.0 cm×3 mm plus 74 µm film

Luminescent material: BASF Lumogen F Red 300 (QY 95 %) at a concentration of 0.25 % relative to the PMMA in the film

Host material: PMMA substrate (Plexiglas GS 233); 10 % PMMA/chloroform solution used for film (1.5 ml solution cast on substrate)

Made by: Fraunhofer IAP

Sample: **ECN1089**

Description: Thin-film sample B used for the comparison of thin-film and homogeneous LSCs (Section 5.2)

Dimensions: 5.0 cm×5.0 cm×3 mm plus 53 µm film

Luminescent material: BASF Lumogen F Red 300 (QY 95 %) at a concentration of 1.0 % relative to the PMMA in the films

Host material: PMMA substrate (Plexiglas GS 233); 10 % PMMA/chloroform solution used for film (1.5 ml solution cast on substrate)

Made by: Fraunhofer IAP

3.3.4 Samples in Chapter 6

Sample: **Cylinder-g**

Description: Commercially acquired, homogeneously doped, cylindrical LSC used for experimental light-bar measurements (Section 6.3)

Dimensions: 40 cm length, 2 mm radius

Luminescent material: Bayer Fluorescent Yellow coumarin dye (QY 95 %)

Host material: PMMA

Made by: - (commercially acquired)

3.3.5 Samples in Chapter 7

Sample: **ECN785**

Description: Homogeneous nanorod sample (Section 7.2.2)

Dimensions: 4.0 cm×1.3 cm×4 mm

Luminescent material: 0.05 % AR DRT26 nanorods

Host material: P(80 % LMA+20 % EGDM)

Made by: Fraunhofer IAP

Sample: **ECN1162**

Description: Thin-film nanorod sample (Section 7.2.2)

Dimensions: 5.0 cm×5.0 cm×3 mm plus 9 µm film

Luminescent material: 1.0 % AR DRT26 nanorods

Host material: CTA on glass substrate

Made by: Fraunhofer IAP

Sample: **ECN1165a**

Description: Thin-film nanorod sample (Section 7.2.2)

Dimensions: 5.0 cm×5.0 cm×3 mm plus 15 µm film

Luminescent material: 2.0 % AR DRT26 nanorods

Host material: CTA on glass substrate

Made by: Fraunhofer IAP

Sample: **ECN823**

Description: Homogeneous nanorod samples used in size dependence measurements (Section 7.2.4)

Dimensions: Several samples of different top surface areas, thickness 0.795-0.830 mm

Luminescent material: 0.05 % AR DRT26 nanorods

Host material: P(75 % LMA+25 % EGDM)

Made by: Fraunhofer IAP

Sample: **ECN821**

Description: Homogeneous nanorod sample C1 used in doping dependence measurements (Section 7.2.3)

Dimensions: 5.0 cm×5.0 cm×0.82-0.86 mm

Luminescent material: 0.03 % JHN46 nanorods

Host material: P(75 % LMA+25 % EGDM)

Made by: Fraunhofer IAP

Sample: **ECN816**

Description: Homogeneous nanorod sample C2 used in doping dependence measurements (Section 7.2.3)

Dimensions: 5.0 cm×5.0 cm×0.77-0.80 mm

Luminescent material: 0.05 % JHN46 nanorods

Host material: P(75 % LMA+25 % EGDM)

Made by: Fraunhofer IAP

Sample: **ECN820**

Description: Homogeneous nanorod sample C3 used in doping dependence measurements (Section 7.2.3)

Dimensions: 5.0 cm×5.0 cm×0.83-0.87 mm

Luminescent material: 0.06 % JHN46 nanorods

Host material: P(75 % LMA+25 % EGDM)

Made by: Fraunhofer IAP

Sample: **ECN822**

Description: Homogeneous nanorod sample C4 used in doping dependence measurements (Section 7.2.3)

Dimensions: 5.0 cm×5.0 cm×0.85-0.89 mm

Luminescent material: 0.10 % JHN46 nanorods

Host material: P(75 % LMA+25 % EGDM)

Made by: Fraunhofer IAP

Sample: **ECN819**

Description: Homogeneous nanorod sample C5 used in doping dependence measurements (Section 7.2.3)

Dimensions: 5.0 cm×5.0 cm×0.83-0.89 mm

Luminescent material: 0.16 % JHN46 nanorods

Host material: P(75 % LMA+25 % EGDM)

Made by: Fraunhofer IAP

Sample: **ECN831**

Description: Sample A (homogeneous nanorod LSC) used in position dependence measurements (Section 7.2.5)

Dimensions: 5.0 cm×5.0 cm×0.8-0.9 mm

Luminescent material: 0.32 % JHN46 nanorods

Host material: P(75 % LMA+25 % EGDM)

Made by: Fraunhofer IAP

Sample: **ECN833**

Description: Sample B (homogeneous nanorod LSC) used in position dependence measurements (Section 7.2.5)

Dimensions: 5.0 cm×5.0 cm×0.8 mm

Luminescent material: 0.05 % AR DRT26 nanorods

Host material: P(75 % LMA+25 % EGDM)

Made by: Fraunhofer IAP

3.4 Experimental Methods

The characterisation of LSCs requires a range of experimental methods. With respect to the active component, the luminescent material, spectral measurements in the form of absorbance and photoluminescence (PL) measurements play a central role. Photoluminescence excitation (PLE) measurements can complement the absorbance measurements (see for example Section 7.2.1). Determining the luminescence quantum yield (QY) of the luminescent material ideally requires an integrating sphere (see for example Ref. 152) and is less straightforward than PL measurements. While in some cases the QY was measured with a Hamamatsu Absolute PL Quantum Yield Measurement System by a collaborator, the main approach used in this thesis was to fit PL measurements using the Raytrace Model with the QY as the free parameter. This proved to be a useful method, since an adequate QY measurement system including an integrating sphere was not available.

3.4.1 Spectral Measurements

The absorbance of LSCs was measured in a Shimadzu UV-2550 UV/Vis spectrophotometer. In this setup, monochromatic light is produced using a deuterium lamp (190 to 350nm) and a halogen lamp (330 to 1100nm) together with a grating (1200 lines/mm). The light is split into two beams travelling towards two separate silicon photodiode detectors, as depicted in Figure 3.5, with the sample under examination placed in one of the beam paths. The spectrometer carries out transmission measurements over a chosen range of wavelengths and deduces the optical density *OD* based on the Beer-Lambert law (Equation 2.17). The *OD* is linked to the absorbance, henceforth denoted by $\tilde{A}$, by a factor of $\ln 10$ and is converted into the absorption coefficient α as follows:

$$\alpha = \frac{\tilde{A}}{d} = \frac{OD \ln 10}{d} \tag{3.1}$$

where d is the thickness of the sample.

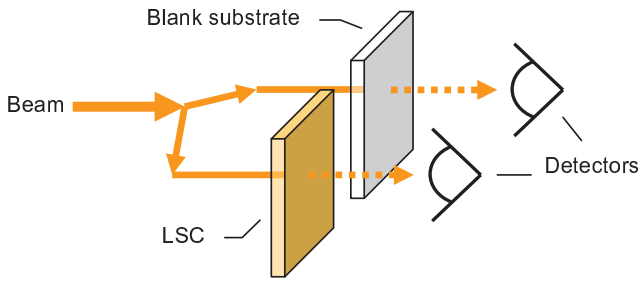

FIGURE 3.5: Absorbance measurement in a UV/Vis spectrometer. A monochromatic beam is split so that it travels along two paths to two separate detectors. The sample under investigation is placed in one path and generally a clear reference sample in the other.

In order to account for absorptions and reflections from the host material, a clear (undoped) reference sample is placed in the other beam path. Alternatively, the true absorption can be calculated retrospectively by correcting the measured *OD* for the spectral reflectance and the host absorption. The overall transmittance for normally incident light in a non-absorbing waveguide with a reflection coefficient r at each interface is

$$T_\lambda = \frac{1-r}{1+r}\,. \tag{3.2}$$

In an absorbing waveguide of thickness d and absorption coefficient α it is

$$T_\lambda = \frac{(1-r)^2\ e^{-\alpha d}}{1-r^2\, e^{-2\alpha d}}\,. \tag{3.3}$$

For a given transmittance T_λ and a reflection coefficient r, which can be deduced from the refractive index using the Fresnel equations (Equation 2.13 and Equation 2.14), the above equation can be solved for the absorptance:

$$e^{-\alpha d} = \frac{-(1-r)^2 + \sqrt{(1-r)^+ 4r^2T^2}}{2r^2T}\,. \tag{3.4}$$

Generally, it is assumed that the refractive index of the host materials is relatively constant across the relevant spectral range (typically the visible spectrum), so that the reflection coefficient can be approximated to be wavelength independent.

In theory, the spectrophotometer could also absorb luminescent light from a sample. Though the wavelength of the luminescence would likely differ from the reference beam, it would be detected by the photodiode just the same. This would increase the apparent transmitted photon count and wrongly lead to the conclusion of a smaller absorbance. In practice, this effect was assumed to be negligible: firstly, only a small fraction of the isotropically emitted fluorescence would be emitted into the direction of the detector (whereas the entire reference beam is directed towards the detector), and secondly, the fact that transmissions of close to zero percent can be measured, confirms that luminescence even from a highly absorbing sample is not significant enough to increase the apparent transmission.

Instead of being absorbed by the luminescent centres, light could also be scattered by particles inside the LSC or by a rough LSC surface. Rayleigh scattering, in particular, can occur when the size of the particles is much smaller than the wavelength of the scattered light, which is the case in the LSC, where the luminescent centres are a few nanometres large at the most (in the case of nanocrystals; much smaller in the case of dyes) and therefore two orders of magnitude smaller than the wavelength of visible light. Shorter wavelengths are more susceptible to Rayleigh scattering than longer ones. In principle, it is possible that scattering could affect the absorbance measurements, but this was not further investigated or accounted for in this thesis. For the relatively small samples characterised in this thesis ($\sim 5\,\mathrm{cm}\times 5\,\mathrm{cm}$) the good quantitative agreement

between experimental measurements and raytrace simulations indicate that scattering effects are not significant.

In the case of the materials used as LSC waveguides, the host absorption coefficient is relatively constant across the visible spectrum and was therefore often approximated by the experimental baseline at wavelengths where the luminescent material does not absorb (though preferably, undoped samples were measured to obtain the host absorption coefficient).

Photoluminescence (PL) measurements were mainly carried out in a SPEX FluoroMax-3 spectrofluorometer with a 150 W continuous output xenon arc lamp. Inside the spectrofluorometer, the LSC plate is positioned in the path of a monochromatic excitation beam. As shown in Figure 3.6, the detector is positioned at a right angle to the incident beam. The excitation beam generates luminescence, and the detector records the photon count as it scans the emission spectrum. The LSC should be oriented so that only luminescent radiation enters the detector. Since only a part of the emission is detected, the PL measurement does not provide an absolute luminescence intensity.

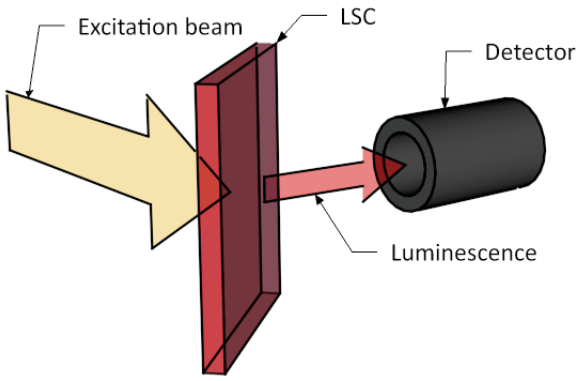

FIGURE 3.6: Schematic of the photoluminescence (PL) measurement using the FluoroMax spectrofluorometer. A monochromatic beam incident on the sample excites the luminescent centres, while a detector resolves the PL spectrum.

The position of illumination by the excitation beam affects the measured PL spectrum, since the pathlength of the luminescence within the LSC governs the probability of self-absorption, which in turn governs the red-shift of the spectrum. Therefore, the PL measured is generally not the fundamental PL one would obtain from a single luminescent centre. Measurements on very dilute samples (with absorbances at the first exciton peak of 0.1 or less) can provide an approximation to the fundamental PL. Another, more practical method that was applied in this thesis, is to minimise re-absorptions by

minimising the pathlength that detected photons have inside the LSC. This is achieved by positioning the LSC at an angle (in this case 45 °), so that most of the luminescence reaching the detector has a pathlength inside the LSC that is close to the thickness of the LSC. The LSC should be oriented facing away from the detector, such that the excitation beam is not reflected towards the detector. An example of this method is presented in Section 7.2.3, where a set of LSCs with varying dopant concentrations is examined: a consistent PL peak for all concentrations when measured at a 45 ° orientation confirms the validity of this method to obtain the fundamental PL.

Photoluminescence excitation (PLE) measurements were also carried out using the spectrofluorometer. In this measurement, the excitation wavelength is swept across the absorption spectrum of the luminescent material while a monochromatic detection is carried out, ideally at the emission peak. The shape of a PLE measurement follows the spectral absorptance, provided that the QY is independent of energy. An example, where the PLE does not match the absorptance is presented in Section 7.2.1.

Further PL measurements were carried out using a portable Ocean Optics spectrometer coupled to an optical fibre with integrated lens that could be placed in contact with LSC surfaces to measure the spectrum. With a lens aperture of $\sim$1 mm^2 and very small acceptance angles, this method allowed for a spatial and directional resolution of the spectrum. Concentrators that were too large for the FluoroMax could be characterised with this spectrometer.

A Hamamatsu C9920 Absolute PL Quantum Yield Measurement System was used for QY measurements. This system deduces the QY based on the absolute PL emitted from a sample upon excitation. A 150 W continuous output xenon light source is used with a monochromator to produce the excitation beam incident on the sample, tuned to the absorption peak. An integrating sphere with separate entrance and exit ports ensures that practically all of the emission from the sample is collected and detected by a CCD spectrometer that resolves the emission spectrum. Contributions from the excitation light that was not absorbed by the sample are subtracted from the detected spectrum in order to isolate the absolute PL flux. For this to work, the bandwidth of the excitation beam needs to be small compared to the PL Stokes shift. Based on the rate of excitation photons absorbed by the sample and the detected emission rate, the fluorescence quantum yield (i.e. the ratio of emitted photons to absorbed photons) is

computed. A critical source of error in this measurement can be self-absorption, which can occur either before a photon is emitted from the sample or if an emitted photon enters the sample again upon reflection within the integrating sphere. Especially in low QY samples, self-absorption leads to a smaller detected photon flux, thereby resulting in a lower apparent QY (if no correction is made). To minimise the effect of self-absorption, the QY measurements were generally carried out on dilute and small test samples.

3.4.2 Electrical Measurements

The short-circuit current of a photovoltaic system is a key factor of its power conversion efficiency (see Equation 2.10). The main method of I_{SC} measurement applied in this thesis used a small PV cell of known spectral response to scan the emission out of the edges of a concentrator under illumination [153] (see Figures 3.7 and 3.8): a 3-axis translation stage was used to position the cell so that it touched the LSC edge. The photocurrent generated in the cell at short circuit was measured with a multimeter or with a lock-in amplifier if the signal was weak. The solar cell used for this measurement was a silicon photodiode with an area of 2.65 mm×2.65 mm and a quantum efficiency (QE) as shown in Figure 3.9.

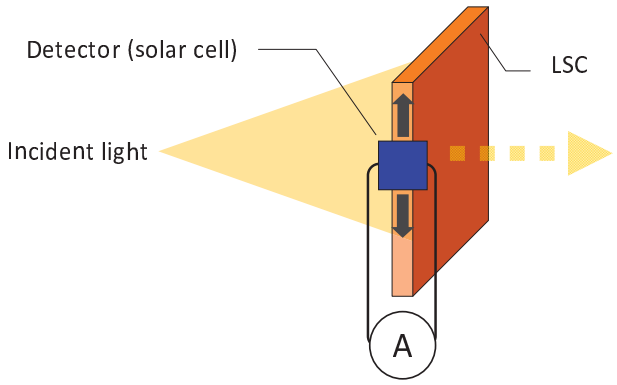

FIGURE 3.7: Schematic of the short-circuit current measurement. A calibrated PV cell is used to spatially scan the edge emission of the LSC under approximately uniform radiation from a lamp or solar simulator of known spectrum and intensity. The current generated in the cell is recorded.

The QE measurement of the reference solar cell was carried out under illumination from a tungsten-halogen light source. A Bentham monochromator, based on a diffraction grating, was used to split the tungsten-halogen spectrum and emit monochromatic light, the bandwidth of which was controlled via the exit aperture. A matched pair of lenses

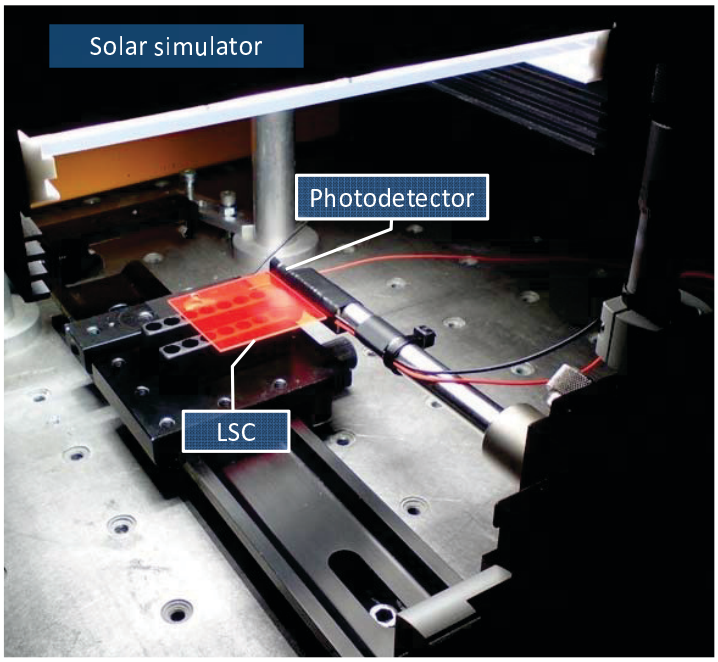

FIGURE 3.8: Photograph of the short-circuit current measurement setup under the solar simulator.

focussed the image of the output collimator of the monochromator, projected through a pinhole of diameter 600 microns, onto either the solar cell or a calibrated photodetector. The short-circuit current was measured using a lock-in amplifier, which was synchronised with a chopper placed between the light source and the monochromator, in order to filter out noise. The calibrated photodetector provided the reference against which the solar cell I_{SC} was compared to obtain the QE.

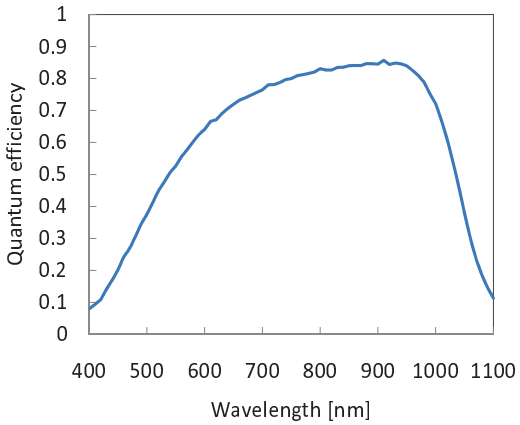

FIGURE 3.9: Quantum efficiency of the reference solar cell used for the short-circuit current measurement of the LSC.

The reference solar cell (silicon photodetector) had an anti-reflective coating that led to

low reflectivities in the visible spectrum, as shown in Figure 3.10. The angular response was relatively flat up to large angles, as depicted in Figure 3.11. The reflectivity and the angular response were measured using the same light source and basic setup as in the QE measurements described above.

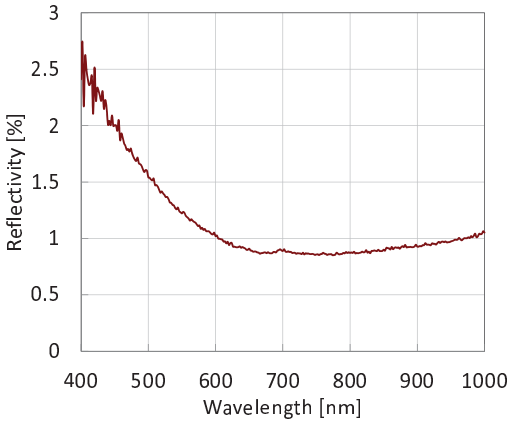

FIGURE 3.10: Reflectivity of the reference solar cell, measured at normal incidence. An anti-reflective coating facilitates the low reflectivity in the visible spectrum.

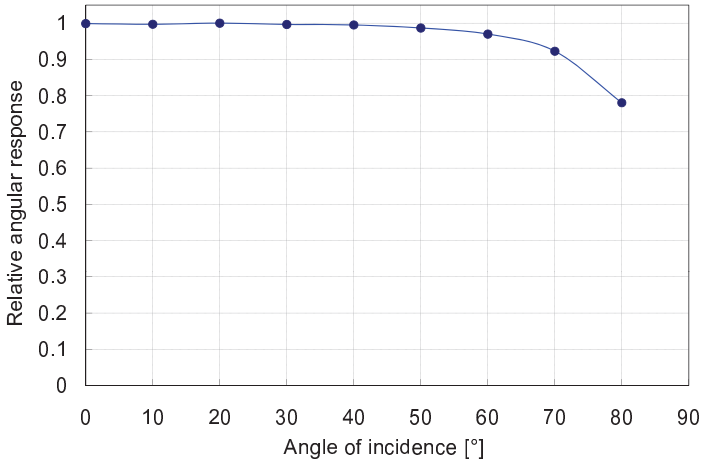

FIGURE 3.11: Angular response of the reference solar cell, measured in the visible. The angle is defined as the inclination of the incident light against the surface normal.

In order to predict the power generated by an LSC module, the dark current characteristics of the cell are required. As explained in Section 2.2.2 the dark current is a representation of the diode characteristics of the cell and is measured by externally biasing the cell without illumination and recording the current as a function of voltage. For the cells and the light concentrations used in the LSC characterisation, the superposition approximation (Equation 2.6) was assumed to be valid: additivity between the

short-circuit current and the dark current was used to determine the power as outlined in Section 2.2.2.

The I_{SC} measurements were initially carried out using a 100 W tungsten-halogen bulb with an approximate 3000 K blackbody spectrum as the light source (see Figure 3.12). A blue band-pass filter was used to limit the spectral range over which characterisations needed to be made. The light source was coupled to an optic fibre with an integrated diffuser at the exit. The sample was placed at a distance of approximately 0.5 m to improve the uniformity of the illumination (at the expense of signal strength). All measurements were carried out in the dark to avoid stray light affecting the results. As Figure 3.13 illustrates, this light source still exhibited large spatial variations of up to 25 % due to the diverging beam. The beam divergence also meant that special care was taken to avoid incident light to reach the reference solar cell directly. For this reason, a metal plate was used to shield the cell from direct light. The samples characterised using the tungsten-halogen lamp setup were Red-l (Section 3.5.3), the samples in Chapter 5 and the samples in Section 7.2.2.

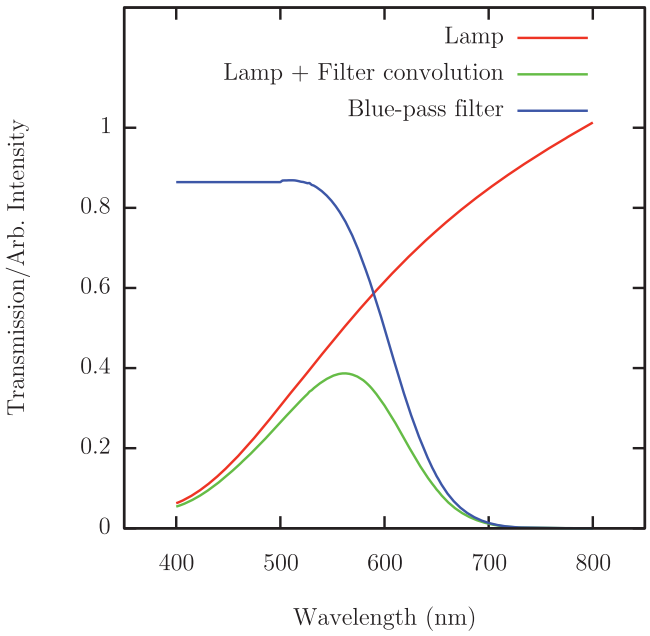

FIGURE 3.12: The tungsten-halogen lamp spectrum, alone and with a blue band-pass filter [102, p. 64].

All other broadband short-circuit current measurements presented in this thesis were carried out using a Steuernagel Lichttechnik solar simulator. The solar simulator was acquired at a later point in time and replaced the tungsten-halogen lamp. This simulator

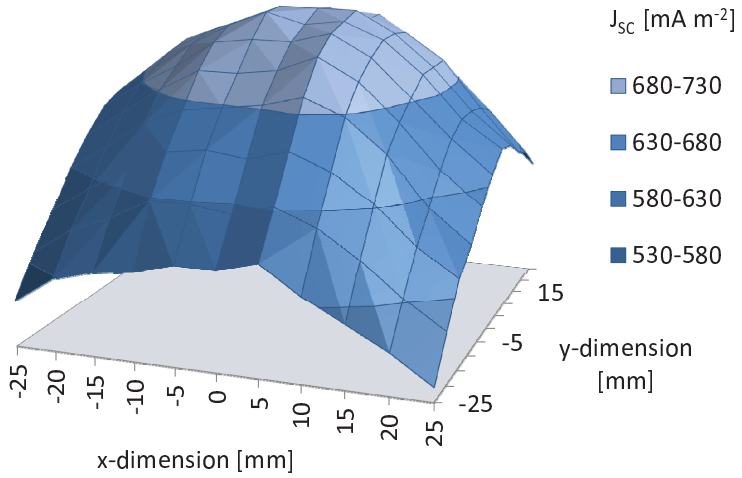

FIGURE 3.13: Tungsten-halogen lamp emission uniformity used for calibration. This intensity map was obtained by scanning the target area with a small silicon photodiode and measuring the short-circuit current density.

had an Osram HMI 575 W/SE discharge tube and was graded class B. It produced a broadband spectrum (see Figure 3.14) with a relatively good uniformity along one axis and a mediocre uniformity along the other, at a distance of approximately 20 cm (see Figure 3.15). Ambient laboratory light entering the LSC or the cell was not found to be a problem, because the solar simulator intensity was sufficiently high. Care was taken to prevent solar simulator light from reflecting off parts of the setup and entering the cell: mostly black components were used, and metallic surfaces were covered with black tape as can be seen in Figure 3.8.

For illumination position dependent measurements such as the ones described in Section 7.2.5, a 5 mW blue laser at a wavelength of 404 nm was used to produce a monochromatic spot illumination.

In the following, the I_{SC} measurement using the solar simulator is described in more detail, using the set of samples from Section 7.2.3 as an example. Firstly, for calibration, the output from the solar simulator reaching the target area, where the LSC would be placed, was measured using the same reference cell used for the I_{SC} measurements of the LSC. This yielded the intensity map shown in Figure 3.15. By integrating or averaging over the entire area (which produces similar results in this case), the total photon flux incident on the LSC was obtained by following the same procedure as detailed later and leading to Equation 3.6. This calibration step would not need to be repeated for every measurement if the spectrum and the uniformity of the solar simulator remained

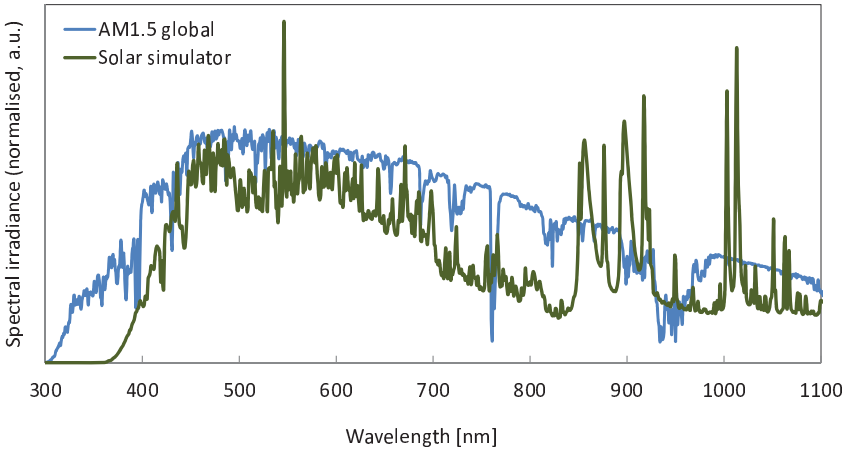

FIGURE 3.14: The solar simulator spectrum in comparison with AM1.5 global.

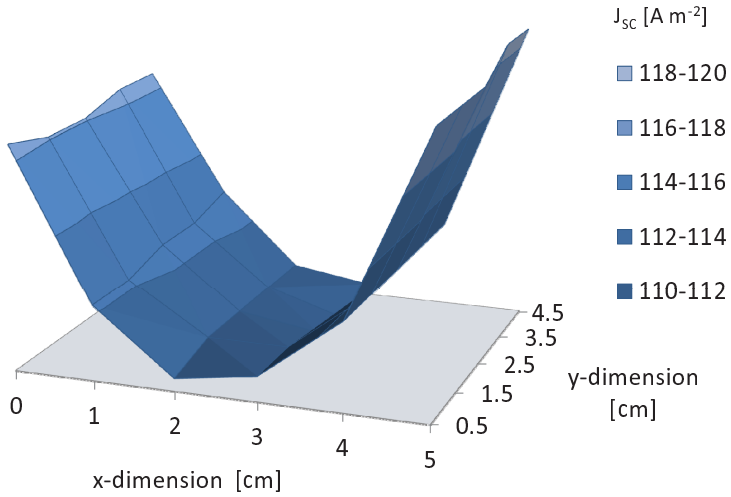

FIGURE 3.15: Solar simulator emission uniformity used for calibration. There is noticeable variation along the x-dimension, but little along the y-dimension.

constant over time. However, the intensity was found to vary by approximately 5 % between different experimental runs. Therefore, a second solar cell was positioned at a constant distance to the solar simulator to record the short-circuit current as a measure of the relative intensity between different runs. The resulting intensities were compared to the intensity corresponding to the calibration measurement, and the incident photon flux was rescaled accordingly.

The reference solar cell was moved as close as possible to the LSC edge and moved along the y-dimension in Figure 3.15 to record the short-circuit current at several positions. The current density was obtained by dividing by the active area of the reference cell. The short-circuit current density measured at each position along the LSC edge was

then averaged and multiplied by the overall edge area to get the total I_{SC} one would obtain with a full coverage of the LSC edges with solar cells. This approximation is valid because the LSC output is adequately uniform. Raytrace simulations support this, as can be seen in Figure 3.16. In the case of uniform illumination, the majority of luminescence exiting the edge originates close to the edge. Line illumination was simulated to explore whether the uniformity of the emission behaves differently when the luminescence originates further away from the edge. In both cases the edge output was found to be relatively uniform.

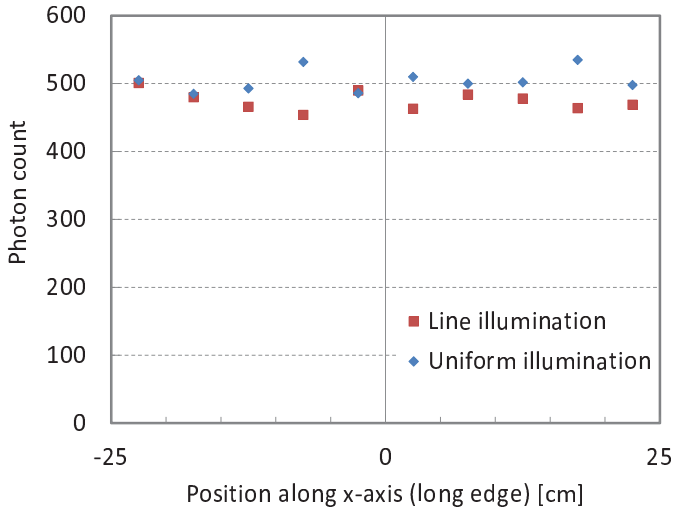

FIGURE 3.16: The uniformity of LSC edge emissions, simulated with the Raytrace Model (based on sample ECN555). Uniform illumination means that the entire LSC front surface was illuminated uniformly, whereas line illumination means that the illumination was focussed along a line along the centre and across the length of the LSC, parallel to the detection edge. In both cases, the edge output is found to be relatively uniform.

More importantly, the measured I_{SC} values in Table 3.2 confirm that the standard deviation is only around 5 %, with the exception of sample C1, where the low dopant concentration is thought to be the reason for a weak signal and a large error.

With a known cell response $QE(\lambda)$ and normalised emission spectrum $PL(\lambda)$, the emitted photon rate out of the LSC edges $\dot{N}$ is deduced from the I_{SC}:

$$I_{SC} = e\,\dot{N} \int_{\lambda} QE(\lambda)\,PL(\lambda)\,d\lambda \tag{3.5}$$

$$\dot{N} = I_{SC} \Big/ \left(e \int_{\lambda} QE(\lambda)\,PL(\lambda)\,d\lambda \right) \tag{3.6}$$

	Short-circuit current [µA]				
Position [cm]	C1	C2	C3	C4	C5
0.5	58	65	68	70	83
1.5	52	65	63	73	86
2.5	47	64	63	73	91
3.5	37	65	57	72	92
4.5	39	73	62	78	93
Average [µA]	47	66	63	73	89
Standard deviation	19 %	6 %	6 %	4 %	5 %

TABLE 3.2: Example of short-circuit current measurements on samples C1-C5 from Section 7.2.3. The values shown are before rescaling according to the intensity calibration of the solar simulator. The axis along which the measurements were taken corresponds to the y-dimension in Figure 3.15.

where e is the elementary charge. This calculation assumes no variation of the solar cell response with angle of incidence. Though Fresnel reflection leads to a weaker response at larger angles, the approximation is justified by a relatively constant angular response of the solar cell up to large angles (see Figure 3.11) and the LSC emission profile, which peaks at angles close to the normal (see Section 5.4). The optical efficiency is obtained by comparing the rate of emission from the edge to the incident rate:

$$\eta_{\text{optical}} = \frac{\dot{N}_{edge}}{\dot{N}_{incident}} \tag{3.7}$$

$$= \frac{I_{edge} / \left(e \int_{\lambda} QE(\lambda)\, PL_{LSC}(\lambda)\, d\lambda\right)}{I_{incident} / \left(e \int_{\lambda} QE(\lambda)\, PL_{Source}(\lambda)\, d\lambda\right)} \tag{3.8}$$

where PL_{LSC} and PL_{Source} are the emission spectra from the LSC edge and from the light source (solar simulator), respectively.

There are several sources of error in the short-circuit current measurement and the subsequent calculation of the emitted photon rate. The latter is affected by accuracy of the cell QE and the emission spectrum (see Equation 3.6), as well as the validity of assuming a constant angular response of the cell. Generally, the errors arising from these quantities were assumed to be negligible compared to the error in the I_{SC} measurement.

The significant error was assumed to be due to the alignment of the reference cell on the LSC edge. Even a small gap between the LSC edge surface and the cell could lead to a substantial decrease in the I_{SC} measured at the edge. To quantify this error, the

standard deviation from the set of measurements at the different sampling positions was taken (see Table 3.2). In some cases the measurement was carried out twice to reduce the error. Typical errors were around 5 %.

When calculating the optical efficiency, the I_{SC} measurement of the incident light was required (see Equation 3.8). The error in this measurement was related to the uniformity of the incident light (see Tables 3.3 and 3.4). It was obtained by calculating the standard deviation of all measurement points across the target area. The error was ∼3 % under illumination from the solar simulator and ∼7 % in the initial setup using the tungsten-halogen lamp. Though the overall intensity of the solar simulator could vary by about 5 % between different runs, it was sufficiently constant during a single measurement run. The reading errors from the calibration cell used to measure the relative intensity were considered negligible.

	Short-circuit current [µA]					
Position on axis [cm]	0	1	2	3	4	5
0.5	116	112	110	111	113	118
1.5	116	112	111	111	113	118
2.5	116	113	111	110	113	118
3.5	116	113	111	110	113	119
4.5	116	113	111	110	113	119
Standard deviation: 3 %						

TABLE 3.3: Error calculation for the solar simulator output. The standard deviation of the light uniformity at the target area (where the LSC sample is placed) is calculated from a set of short-circuit current measurements across several points. The columns correspond to positions along the x-axis and the rows along the y-axis as shown in Figure 3.15.

The standard error (SE) in the optical efficiency (Equation 3.8) is given by the combined error of the incident and edge measurements:

$$\frac{SE_{\eta_{\text{optical}}}}{\eta_{\text{optical}}} = \sqrt{\left(\frac{SE_{I_{edge}}}{I_{edge}}\right)^2 + \left(\frac{SE_{I_{incident}}}{I_{incident}}\right)^2}. \tag{3.9}$$

Using the solar simulator setup, the typical error in the optical efficiency would be ∼6 %.

	Short-circuit current [µA]										
Position [cm]	-2.5	-2.0	-1.5	-1.0	-0.5	0	0.5	1.0	1.5	2.0	2.5
-2.5	561	579	586	589	596	596	604	586	571	557	539
-2.0	586	604	614	629	629	625	632	621	604	582	564
-1.5	607	625	639	654	657	654	661	650	632	607	589
-1.0	629	646	664	675	679	682	689	679	657	625	604
-0.5	646	664	682	696	696	700	711	696	671	643	621
0	661	679	693	711	714	714	721	707	682	657	636
0.5	668	686	704	718	729	721	725	714	693	664	646
1.0	671	693	707	718	729	729	729	714	693	664	643
1.5	671	696	707	714	721	725	718	711	693	661	632
2.0	661	686	700	707	714	707	718	700	679	654	625
2.5	646	668	682	689	693	689	689	675	661	636	611
Standard deviation: 7 %											

TABLE 3.4: Error calculation for the tungsten-halogen lamp output. The standard deviation of the light uniformity at the target area (where the LSC sample is placed) is calculated from a set of short-circuit current measurements across several points. The columns correspond to positions along the x-axis and the rows along the y-axis as shown in Figure 3.13.

3.4.3 List of Solar Cells

Figure 3.17 shows the quantum efficiencies of the solar cells used in this thesis. The reference Si cell is the standard cell used for characterisation. Some of the measurements in Chapter 7 were conducted with the ECN GaAs cell. The measurements conducted

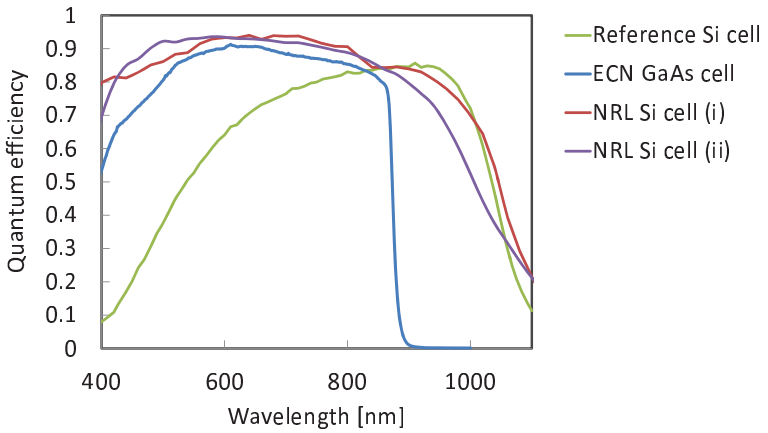

FIGURE 3.17: Quantum efficiencies of the solar cells used in this thesis.

at the US Naval Research Laboratory (Chapter 7) were carried out with the two Si cells shown.

3.4.4 List of Light Sources

Figure 3.18 shows the emission spectra of the light sources used in this thesis. Most characterisations were carried out with the Steuernagel Lichttechnik solar simulator. The measurements conducted at the US Naval Research Laboratory (Chapter 7) were carried out with the Spectrolab X-25 solar simulator. In addition to light sources shown in the figure, monochromatic laser light was used for some of the characterisations.

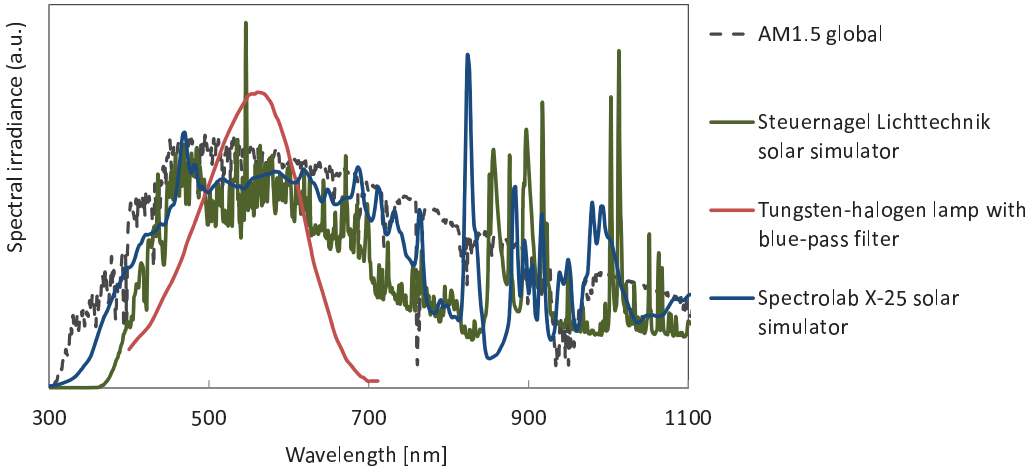

FIGURE 3.18: Emission spectra of the light sources used in this thesis in comparison with the AM1.5 global spectrum.

3.5 The Raytrace Model

The Raytrace Model of the luminescent solar concentrator is a Monte Carlo model: it generates random numbers to determine the outcome of physical processes based on statistical distributions. It treats light as rays, as opposed to waves, since the processes governing the LSC can generally be described by geometric optics alone.

Early Monte Carlo models of the LSC were already published in the 1980s [22, 61, 154–160], and many research groups today employ similar models [56, 59, 94, 99, 106, 161, 162]. Reisfeld *et al.* [160, 163] used a raytrace model to compute optical efficiencies of LSCs, which could also model thin-film structures. However, no comparison of thin-film

and homogeneous LSCs (as carried out in Chapter 5) has been published by any of these authors.

The model presented here has been developed by the author in C++ code and can be applied to a variety of concentrator configurations, including LSC stacks, thin-film LSC and LSCs with reflectors on surfaces or with multiple luminescent species. The concentrator dimensions can be modified arbitrarily, but the geometry is essentially limited to planar shapes and cylinders. These limitations are not considered major drawbacks since the square planar geometry appears to be the most practical one. Being based on geometric optics, the model cannot describe anti-reflective coatings or distributed Bragg reflectors (DBRs) from fundamental principles, since these rely on interference effects governed by wave optics. However, phenomenological spectral and angular reflectance or transmittance data can be input to emulate these optical structures. Solar cells on the edges can also be simulated to produce short-circuit currents, based on their QE. Due to its statistical nature, the model requires a large number of rays to obtain reliable results. A million rays, enough to produce reasonably accurate results for a typical concentrator, can be traced in a matter of minutes on a standard desktop PC.

The Raytrace Model can shed light on the internal processes of the LSC via comparison with experimental observations. It can also be used as a quick and efficient tool for the optimisation of parameters, such as absorber concentration or concentrator dimensions, by step-by-step variation of one parameter at a time. Furthermore, it can be used to make performance projections on the basis of realistic input data.

3.5.1 Program Architecture

Photons are described in the model as rays with position and direction vectors in 3-dimensional space and a wavelength. The concentrator is described by its bounding surfaces and material properties, such as refractive index and background absorption. The concentrator can consist of several host materials, which, in turn, can be doped with one or several types of luminescent centres.

Most experiment-specific parameters are defined in a setup file. The setup information also specifies the type of light source and luminescent species to be modelled. The incident spectrum as well as the absorption and emission spectra and the luminescence

quantum yields (QYs) of the luminescent centres are read from their respective data files. This data can be acquired from experimental measurements or computer generated. The concentration and quantum efficiency of luminescent centres can be easily manipulated for the purposes of optimisation or performance projection. There are no restrictions on the spectra used.

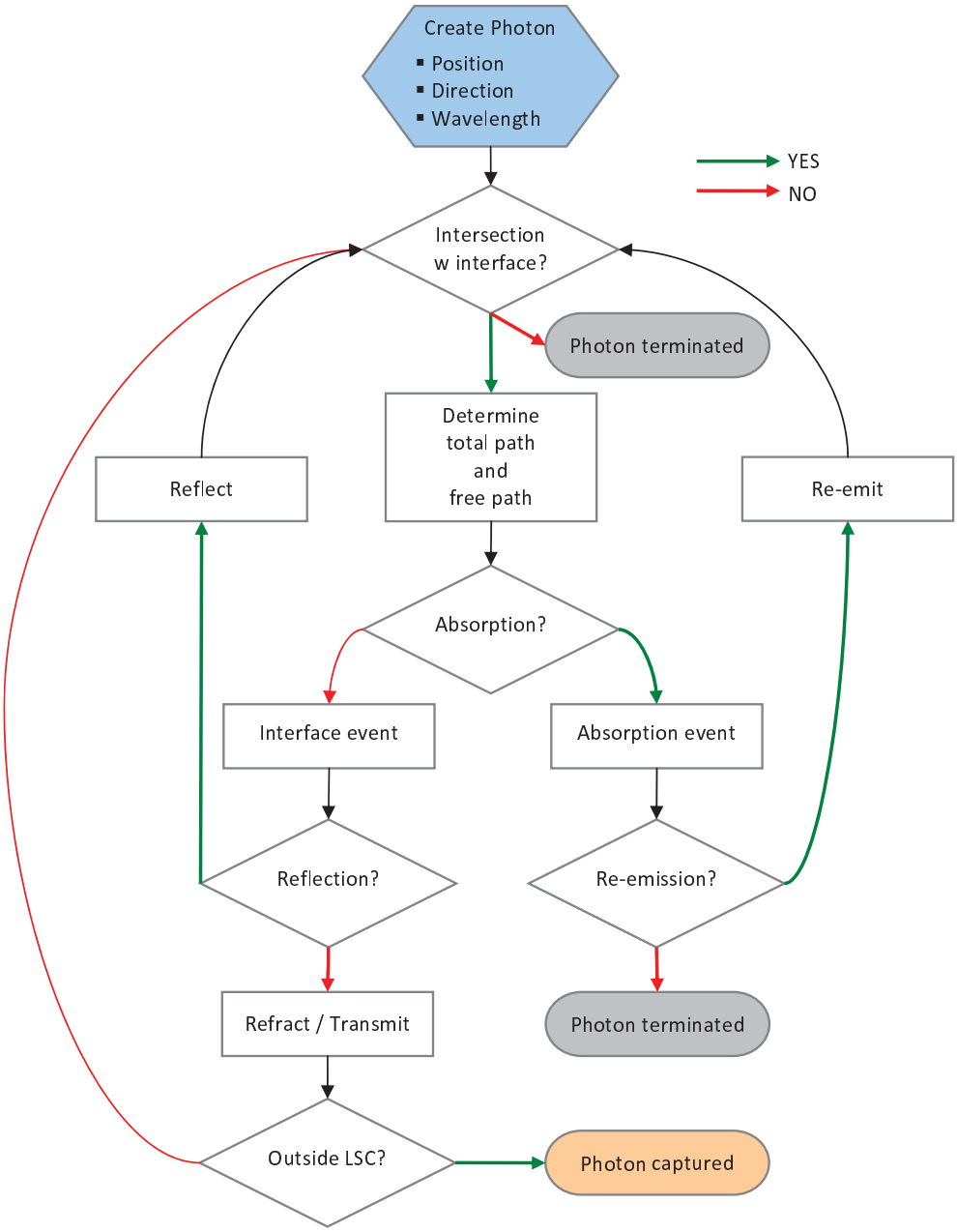

FIGURE 3.19: Flowchart of the Raytrace Model. Processing steps are represented by rectangles, decisions by diamonds and termination points by rounded rectangles.

The flowchart in Figure 3.19 illustrates the structure of the computer program. Rays are

simulated one at a time, and each ray is traced in a step-by-step process. The number of rays at each wavelength is in proportion to the spectrum of the given light source. At each step, the potential surface of intersection in the absence of absorption is computed, depending on the position and direction of the ray relative to the concentrator surfaces. Subsequently, an algorithm based on random numbers weighted by an exponential decay determines the pathlength of the light travelling in the medium. If this pathlength is larger than the distance to the surface of intersection, the ray travels to the surface, where a reflection or refraction takes place in accordance with the Snell's law (2.12). The probability of reflection or refraction of the ray is given by the Fresnel equations (Equations 2.13 and 2.14). If the pathlength is shorter, an absorption event takes place, which can lead to a subsequent emission or to the termination of the ray.

A typical trace can entail many of the aforementioned events before the ray exits the LSC or is terminated. On completion of a run, various outputs can be recorded, including optical efficiencies, concentration ratios, short-circuit currents, the spectra exiting the surfaces, the number of re-emissions and the final photon positions.

3.5.2 Absorption and Emission

At an absorption event, the first step consists of determining the absorber from several possible luminescent centres as well as the host material, with the probability weighted by the relative absorption coefficients of the possible absorbers at the wavelength of the ray. In the case of absorption by a luminescent centre, another random number determines whether the ray is re-emitted, in accordance with the quantum yield. The wavelength of an emitted ray is randomly generated weighted by the emission spectrum of the luminescent centre. The direction of emission is generally assumed to be isotropic, but anisotropic emission can also be modelled. Scattering centres could be modelled as luminescent centres with a QY of 1 and no wavelength change upon emission, but scattering is assumed to be negligible in the cases modelled.

The weighting of the emission from luminescent centres is ideally based on their fundamental photoluminescence (PL) spectrum, which does not have a redshift due to re-absorption. In practice, the fundamental PL is approximated using the method described in Section 3.4.1 or by measuring a sample containing a low density of luminescent

centres, such that the redshift in the PL due to re-absorptions is negligible. Alternatively, the fundamental PL can also be extracted using the model via comparison with experimental measurements of a red-shifted PL, as shown in Figure 3.20.

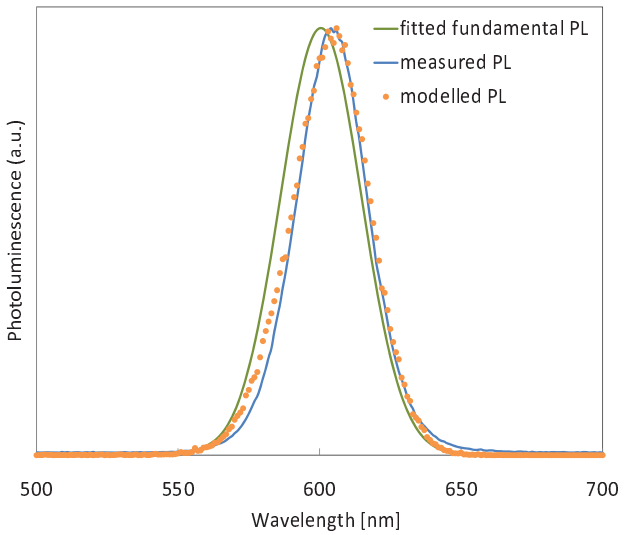

FIGURE 3.20: An example of fitting the fundamental PL with the Raytrace Model via comparison with experimentally measured data. The fundamental spectrum is adjusted until the modelled emission matches the experimental spectrum. This example is based on the thin-film sample ECN1165a which has an absorbance of ~ 0.053 at the first exciton peak (585 nm).

For the emission wavelength generating algorithm, the PL spectrum (as a function of wavelength) is integrated and mapped against a probability distribution ranging from 0 to 1, so that each random number in this range corresponds to a wavelength. Under the assumption that a re-emitted photon cannot have a higher energy than the absorbed one, the emission spectrum is terminated at the absorption wavelength. An alternative method involving time-consuming experimental measurements is chosen by other raytrace developers [161], using experimental photoluminescence excitation (PLE) data with excitation wavelengths over the entire range modelled. Comparisons with experimental PL measurements presented in the following chapters show that the PL is reproduced by the Raytrace Model correctly despite the simplified approach.

The pathlength generator is a key algorithm in the model and is governed by the absorption coefficient. Inside an absorbing medium and in the absence of reflection, the Beer-Lambert law (Equation 2.17) is used to express the spectral absorptance as follows:

$$A_\lambda = 1 - T_\lambda = 1 - e^{-\alpha z}\,. \tag{3.10}$$

The probability of absorption at thickness z is described by dA_λ/dz. This can be mapped onto the uniform probability distribution p of the random number γ:

$$\frac{dA_\lambda}{dz}\,dz = p\,d\gamma \tag{3.11}$$

where p is constant since γ is random. With γ ranging from 0 to 1, normalisation requires that p is 1:

$$\int_0^1 p\,d\gamma = 1 \tag{3.12}$$

$$p\int_0^1 d\gamma = 1 \tag{3.13}$$

$$p = 1\,. \tag{3.14}$$

Integration yields

$$A_\lambda = \gamma \tag{3.15}$$

$$1 - e^{-\alpha z} = \gamma \tag{3.16}$$

$$z = -\frac{ln(1-\gamma)}{\alpha}\,. \tag{3.17}$$

Since γ is randomly distributed between 0 and 1, an equivalent, more compact form of the pathlength generator is

$$z = -\frac{ln(\gamma)}{\alpha}\,. \tag{3.18}$$

3.5.3 Validation of the Model

The Raytrace Model has been tested against experimental measurements, a Thermodynamic Model developed by A. Chatten [153, 164–168] and a raytrace model from the Energy research Centre of the Netherlands (ECN) [169]. A small rectangular LSC doped with a red dye (sample Red-l as described in Section 3.3) was used for reference. The sample was characterised using the spectral measurements described in Section 3.4.1 and the short-circuit current measurement using the tungsten-halogen lamp described in Section 3.4.2. The host absorption coefficient was deduced from transmission measurements on a 20 cm long blank sample consisting of the same host matrix.

The uncertainty of raytrace simulations was deduced by carrying out several simulation runs and calculating the standard deviation. For similar simulations, one can simply model the collective number of rays in a single run to obtain the same uncertainty. However, it one needs to bear in mind that it is not just the overall number of rays simulated that governs the uncertainty, but the number of rays contributing to the calculated quantity. For instance, with a given number of incident rays, the emission out of a single edge surface will have a higher uncertainty than the emission out of all edge surfaces. Further sources of error are the parameters that serve as inputs to the model, such as incident spectra or solar cell quantum efficiencies.

The experimentally measured short-circuit current density of the reference LSC was compared against the output from the Raytrace Model and the Thermodynamic Model. The values, shown in Table 3.5, were found to be consistent.

	J_{SC} [mA/m^{-2}]
Experiment	53 ± 2
Raytrace Model ICL	52 ± 1
Thermodynamic Model ICL	~ 52

TABLE 3.5: Validation of the Raytrace Model via the experimental measurement and the thermodynamic computation of the short-circuit current density of a reference LSC.

Moreover, the fraction of the incident light output from the different LSC surfaces was compared using the three computational models. The results depicted in Figure 3.21 and show a good agreement between all three models, validating the Raytrace Model discussed in this thesis.

The good match between the results from the Raytrace Model and the Thermodynamic Model is remarkable, considering the fundamentally different approaches taken by the two models: while the Raytrace Model is rooted in a microscopic description of the concentrator, the Thermodynamic Model is based on the principle of detailed balance. The Thermodynamic Model assumes thermodynamic equilibrium between the radiation field and the luminescent absorbers and employs radiative transfer methods to compute the detailed balance equation. The detailed balance method equates the change in the spectral photon flux of the photon field within the LSC, $\Phi(\nu)$, to the absorption and the spontaneous emission of light. By applying Kirchhoff's radiation law, which states the spectral emissivity of a grey body equals its spectral absorptivity, the detailed balance

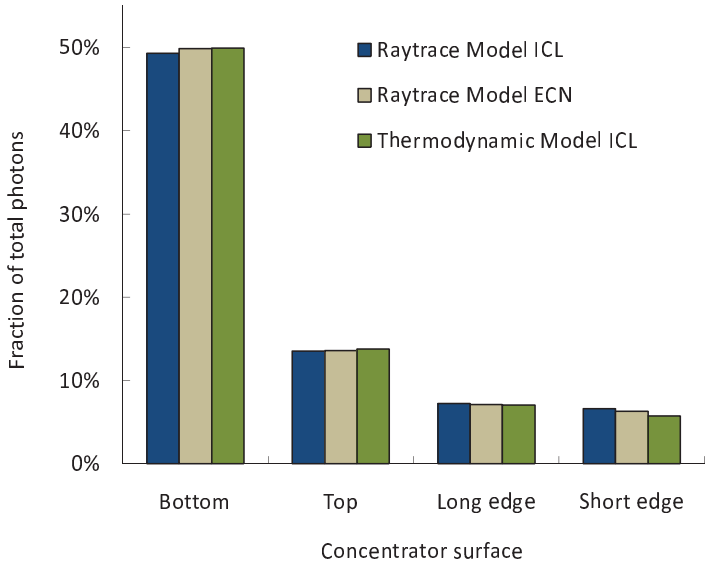

FIGURE 3.21: A comparison of computational models. The photon fractions exiting the surfaces of a rectangular LSC were computed using the Raytrace Model described here, the Thermodynamic Model from Imperial College London (ICL) and the model from the Energy research Centre of the Netherlands (ECN).

can be expressed by the following equation:

$$\nabla\Phi(\nu) = -\alpha(\nu)\,\Phi(\nu) + \alpha(\nu)B(\nu)\,\frac{\Omega_{\text{trap}}}{4\pi} \tag{3.19}$$

where α is the absorption coefficient, Ω_{trap} is the solid angle of trapped emission and B is the brightness of the radiation field, which governs the spontaneous emission, defined as

$$B(\nu) = \frac{8\pi\, n^2\nu^2}{c^2}\,\frac{1}{e^{(h\nu-\mu)/(kT)}-1} \tag{3.20}$$

where μ is the photon chemical potential and all other symbols have their usual meanings. By applying appropriate boundary conditions, the Thermodynamic Model can predict the photon fluxes and spectra exiting individual LSC surfaces.

Comparisons between experimental measurements and modelling results presented in this thesis, for example in Chapter 5, further support the accuracy of the Raytrace Model.

3.5.4 Post-Processing

When making predictions of the power output for LSC systems with different solar cells it is convenient to output an optical quantum efficiency (OQE) of the LSC. The OQE indicates the fraction of incident light at a given wavelength that is coupled out of the edges. This has the advantage that the OQE values can be combined with an arbitrary input spectrum to give an overall optical efficiency η_{optical}, and this can be done quickly using spreadsheets, avoiding unnecessary repeats of time-consuming simulations. The OQE is LSC specific and needs to be recalculated if any of the LSC parameters, such as size or luminescent material are varied. Assuming that the output spectrum remains approximately constant under different input conditions, the short-circuit current, open-circuit voltage and maximum power can be computed for a variety of solar cells using just the OQE and photoluminescence data. However, some inaccuracy needs to be accepted with this method as different solar cells could have different reflectances. Moreover, the OQE would have to be computed for the case of cells coupled via index matching and the case of cells attached with an air gap separately.

The optical efficiency based on a normalised incident spectrum S_λ is given by

$$\eta_{\text{optical}} = \int_\lambda OQE(\lambda)\, S_\lambda(\lambda)\, d\lambda\,. \tag{3.21}$$

The rate at which photons are emitted out of the LSC edges is then calculated as follows:

$$\dot{N} = \eta_{\text{optical}} \Phi_{\text{incident}} A_{\text{surface}} \tag{3.22}$$

where Φ_{incident} is the incident photon flux and A_{surface} the area of the LSC collection surface. The I_{SC} is obtained by substituting the expression for $\dot{N}$ into Equation 3.6:

$$I_{SC} = e\, \Phi_{\text{incident}} A_{\text{surface}} \int_\lambda OQE(\lambda)\, S_\lambda(\lambda)\, d\lambda \int_\lambda QE(\lambda)\, PL(\lambda)\, d\lambda\,. \tag{3.23}$$

By subtracting the dark current of the solar cell from the short-circuit current one can obtain the I-V characteristics of the cell and hence determine the power, as explained in Section 2.2.2.

3.6 Chapter Conclusion

The research strength of our group lies in characterisation and modelling of LSCs. In this chapter the materials and sample preparation were presented along with the main experimental and computational methods, highlighting intricacies and limitations and describing the Raytrace Model developed by the author. The model was shown to reproduce experimental measurements and to be in good agreement with other models such as the Thermodynamic Model. The characterisation of the LSC involves spectral measurements of the luminescent material as well as the characterisation of the QE as a function of wavelength and angle of solar cells used in combination with the LSC. The model is a useful tool for making performance projections, optimising parameters and advancing the understanding of the internal mechanisms of the concentrator.

Chapter 4

Applications of the Raytrace Model

4.1 Chapter Introduction

This chapter describes a number of experiments based on raytrace simulations. The first experiment examines the angular response of the LSC and is complemented by experimental measurements. As an extension of this experiment, the LSC outputs under direct and diffuse sunlight are compared. The research question of the second study is whether mirrors on the edges produce any practical advantage. The subsequent section investigates the effect of specular and diffuse back surface reflectors. This is followed by simulations of a tapered geometry with the aim of improving the internal light guiding properties of the LSC. The final study investigates a potential BIPV application of the LSC in the form of a power generating window.

4.2 Angular Response of the LSC

Averaged over the year, 60 % of the sunlight received in central Europe is diffuse [62]. The main claim differentiating the luminescent concentrator from geometric ones is its effectiveness in a non-tracking setup and under diffuse irradiation. Using the LSC as a static concentrator means that the angle of the direct component of solar irradiation that it receives changes during the day. Regarding the diffuse light, a generally accepted

approximation is that it is incident and isotropic over an entire hemisphere. Thus, quantifying the angular response of the LSC is important for practical applications. This study was carried out experimentally and with the aid of the Raytrace Model.

4.2.1 Experimental Details

The experimental setup is illustrated in Figure 4.1. The sample was a 10.6 cm×10.6 cm square, 5 mm thick LSC labelled Red-a (see Section 3.3), doped homogeneously with a Fluorescent Red dye from Bayer with a QY of 95 %. The host material was PMMA with a refractive index of 1.49 and an absorption coefficient in the visible of $\sim 2\,m^{-1}$. A 5 mW blue laser with a wavelength of 404 nm was used as the light source since a narrow, collimated beam was required. The laser beam had a cross-section of $\sim 2\,\mathrm{mm}^2$ and was incident on the centre of the LSC top surface. At normal incidence the absorptance of the LSC was $\sim 10\,\%$ at the laser wavelength. Short-circuit current measurements (see Chapter 3) were carried out while the LSC was rotated through a range of incident angles. The relatively large dimensions of the LSC ensured that spatial variations in the illumination spot with changing angle did not significantly affect the distance between the illuminated area and the detection edge. Due to a relatively weak signal arriving at the edge a lock-in amplifier was used for the measurement. Changing the angle of incidence from the normal reduces the incident photon flux by the cosine of the angle. However, since the LSC was illuminated over a small spot and not uniformly over its entire surface, the change in the photon flux with the angle of incidence did not affect the overall rate of photons incident on the LSC. It is important to note that in a practical application one would assume uniform illumination, which would lead to a reduction of incident photon rate with shallower angle of incidence.

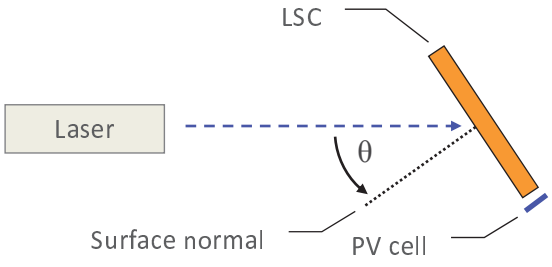

FIGURE 4.1: Setup for the measurement of incident angle dependence.

A sufficiently large separation between the illumination spot and the PV cell ensured that incident light could not reach the cell directly. Moreover, due to the reversibility of light paths, it is clear that incident light cannot couple into a waveguide mode via refraction through the top surface or reflection from the back surface. Due to the planar symmetry of the waveguide, light entering through the top surface inevitably exits out of the back, unless it is absorbed, scattered or subjected to Fresnel reflection off the back surface. It is therefore safe to assume that the signal detected by the PV cell originated almost exclusively from luminescent light. Given that the spatial variations of the illumination spot were negligible and that the luminescence was isotropic, it is safe to assume that the incident angle dependence measurement is symmetric about the normal angle.

4.2.2 Results and Discussion I

The experimental results for the incident angle dependence are presented in Figure 4.2. For comparison, the experiment was also simulated with the Raytrace Model. The short-circuit current density measured by a reference PV cell at the LSC edge was used as the performance indicator. The values are plotted on an arbitrary scale since only the relative variation of the output with angle of incidence was under examination. The cosine factor in the photon flux arising from the angle of incidence has been excluded in this visualisation, so that purely the response of the LSC as a function of angle of incidence can be examined.

Surprisingly, the edge output was found to increase with increasing angle of incidence up to $\sim 70\,^{\circ}$, after which it dropped off sharply (see Figure 4.2). This observation was confirmed by the Raytrace Model. The explanation for this behaviour is that the absorption coefficient of the LSC was relatively low at the laser wavelength. Only $\sim 10\,\%$ of the light at normal incidence was absorbed. In such a case, a large fraction of normally incident light simply passes through the LSC. Though a larger angle of incidence increases the reflection off the top surface, it also increases the pathlength of the light in the material and hence the absorbance. In a lightly doped LSC, the gain from the additional absorbance can outweigh the loss from the reflectance up to large angles.

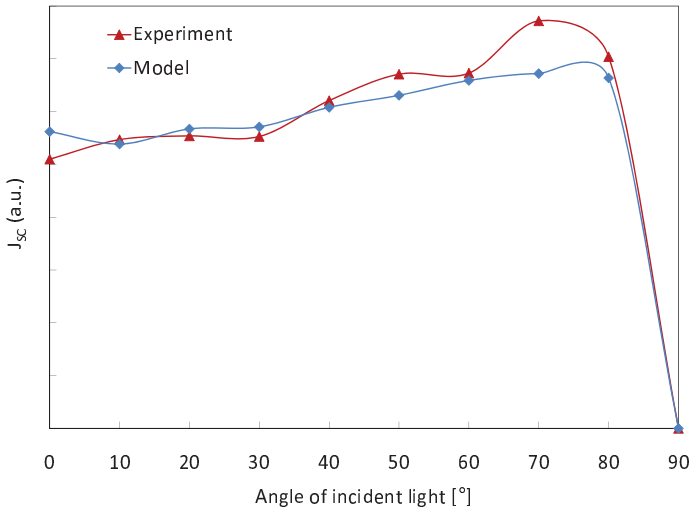

FIGURE 4.2: Angular response of the LSC from experimental measurements and from raytrace simulations. The relative short-circuit current density generated by a solar cell attached to an edge of the LSC is plotted against the angle of incident light. Since the illumination spot was small compared to the LSC surface, the reduction of the incident photon flux by the cosine of the angle of incidence did not affect the results. Therefore, the graph purely shows the LSC response as a function of incident angle.

4.2.3 Results and Discussion II

While the initial results show a very optimistic incident angle dependence of the LSC, they are not considered to be representative since the reference sample was not optimally doped. Therefore, a further raytrace study was carried out by modelling an LSC that absorbed $\sim 90\,\%$ of the light at normal incidence. The results of this study are shown in Figure 4.3 and show a slight increase in the output up to $\sim 60\,°$. The transmittance taking in multiple reflections of incident light through the top surface, calculated by subtracting the Fresnel reflectance (see Equations 2.13 and 2.14) from unity, is plotted for comparison. As expected, there is a strong correlation between the transmittance and the edge output, but the positive effect of increased pathlengths with increasing angle is noticeable. This effect exists not only in lightly doped LSCs, but also in optimally doped ones, since a longer pathlength of incident light improves the absorption without the drawbacks of a higher concentration of luminescent centres, which would escalate re-absorption losses.

For comparison the angular response of the LSC from Figure 4.3 is plotted next to the response of typical encapsulated silicon PV cells in Figure 4.4. Two curves are shown for the Si cell, one from experimental measurement of the cell described in Section 3.4.2

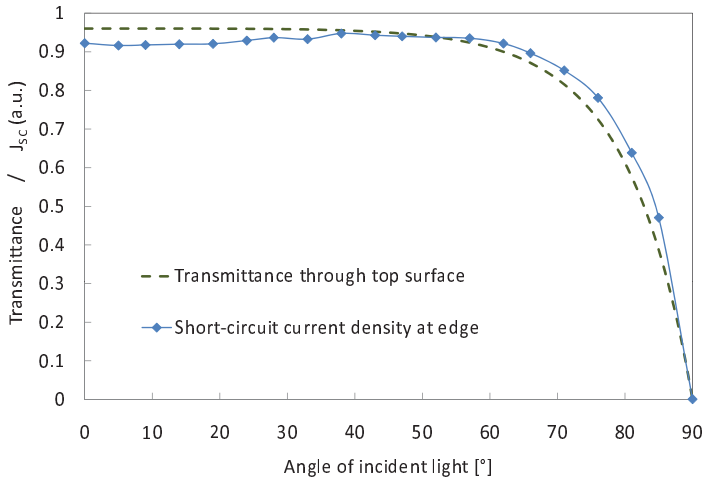

FIGURE 4.3: Angular response of the LSC simulated with the Raytrace Model for an optically dense LSC. The transmittance of incident light through the top surface is shown for comparison.

and one from the literature [170]. The latter was a multi-crystalline silicon substrate cell processed with edge-defined film-fed growth (EFG) technology and encapsulated in a cerium doped low-iron front glass followed by an ethylene vinyl acetate (EVA) layer and float glass. Interestingly, this comparison indicates that the reflectance of the encapsulated silicon cell, which contains several layers spanning a range of refractive indices (from that of glass to that of silicon), can be comparable with the reflectance of the LSC, i.e. the reflectance glass or PMMA with a refractive index of 1.49.

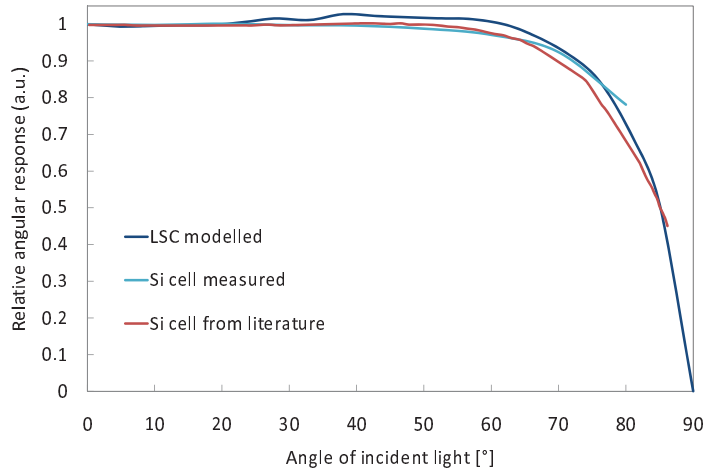

FIGURE 4.4: Comparison of the angular response of an optically dense LSC (modelled) with a typical encapsulated silicon PV cell (from experimental measurement and from literature [170]). One can see that the responses are very similar.

In conclusion, it has been established that the LSC is reasonably insensitive to a change

in angle of incidence up to approximately 70 ° from the normal. Yet the angular response of the LSC is not notably better than that of standard encapsulated silicon cells. One could argue, that adding an anti-reflective coating to the LSC would produce a superior angular response (without compromising TIR, as shown in Equation 2.49), but adding coatings may compromise the economics of the LSC. In any case, compared to geometric concentrators, the LSC has a clear advantage in terms of angular response.

4.2.4 Capture of Direct vs. Diffuse Light

The solar irradiance has a diffuse component that can be higher than the direct component in regions like the UK. Figure 4.5 shows the direct and the diffuse components of the AM1.5 spectrum, where the diffuse is defined as the difference between the global spectrum (AM1.5g) and the direct (AM1.5d) (see Ref. 29). Under AM1.5, 90 % of the total power of 1000 $\mathrm{Wm}^{-}2$ is in the direct component and 10 % in the diffuse. In Figure 4.5, the spectra are shown with arbitrary units as the relative intensities may vary based on geographical location. The diffuse spectrum is blue-rich, since blue light is more effectively scattered in the atmosphere. The performance of the LSC under diffuse irradiation is clearly linked to the incident angle dependence. A large (1 m×1 m×5 mm) LSC was modelled with the same properties (apart from the dimensions) as the one in the previous section, i.e. a PMMA host doped with the Fluorescent Red dye as active material. Simulations were carried out under a direct AM1.5 spectrum incident at a normal angle and compared with a diffuse AM1.5 spectrum incident over a hemisphere. Of course, a normal angle of incidence over the course of a day is not obtainable without solar tracking, but this simplification is justified by the low angular sensitivity of the LSC established in the previous section. An equal ratio between the direct and diffuse components was assumed.

The final distribution of photons shown in Figure 4.6 provides an insight into the differences in LSC performance under direct and diffuse irradiation. It should be noted that only the spectrum up to the silicon band gap of approximately 1100 nm was modelled, and thus the percentages shown in Figure 4.6 are relative to only a part of the AM1.5 spectrum. Diffuse light incident close to an LSC edge can reach the PV cell directly. However, the contribution of incident light coupling into cells was found to be negligible compared to the contribution from luminescent light. This is an expected result due to

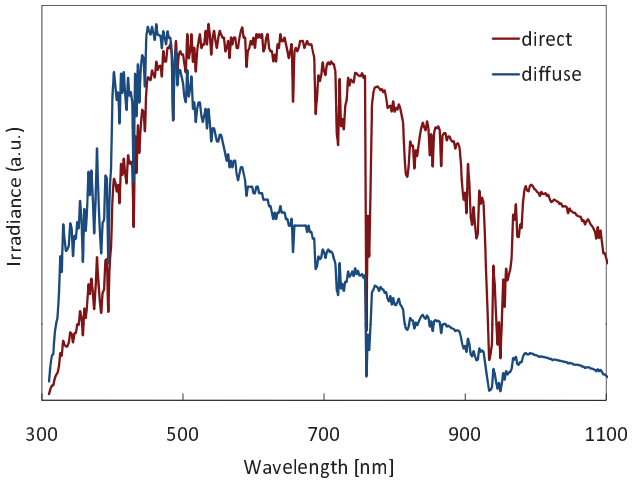

FIGURE 4.5: The AM1.5 direct and diffuse spectra. The intensity ratio chosen here is arbitrary as it varies with geographical location. According to Ref. 62 central Europe receives more diffuse than direct irradiation.

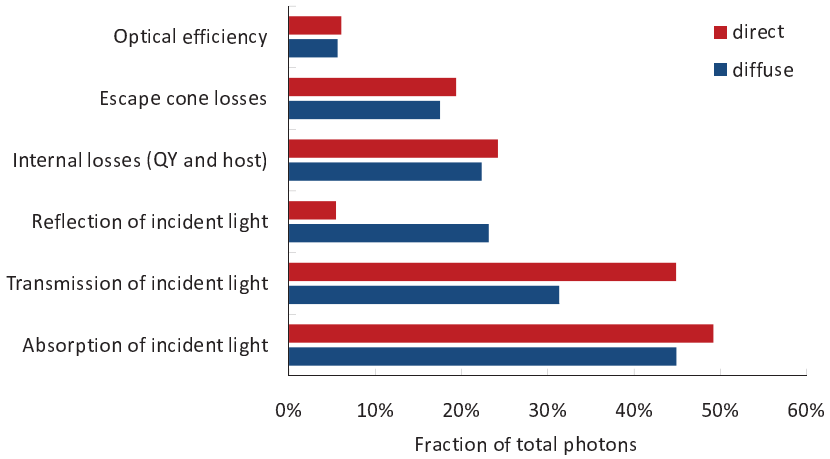

FIGURE 4.6: Raytrace simulation comparing the LSC performance under direct and diffuse AM1.5 irradiation. The top five bars (for each direct and diffuse) add up to 100 %. The absorption of incident light needs to be ignored in the final balance as it leads to the emission out of one of the surfaces or to an internal loss, both of which are already accounted for.

the large geometric gain of LSC that was modelled. In such a case, the collection area close to the LSC edge where incident light can be coupled out to the PV cell directly is small compared to the overall collection area of the LSC.

The optical efficiency, the escape cone losses and the internal losses are similar under both types of irradiation, but slightly higher under direct light. The difference is proportional to the greater absorption of direct light. As expected, in the diffuse case there is more reflection from the top surface and consequently less absorption of light and

less transmission through the bottom compared to the direct case. However, despite significantly less diffuse light being transmitted into the LSC the absorbed fraction of diffuse light is only slightly smaller than that of direct light. This is a result of the longer pathlengths of diffuse light in the LSC. This simulation shows that the contribution from diffuse irradiation to the LSC output is comparable to the contribution from a simplified calculation of direct irradiation. Based on the presented simulation, the optical efficiency of an LSC under AM1.5 direct is higher than under AM1.5 diffuse by less than 10 % relative (6.1 % to 5.6 %, respectively).

4.3 Mirrors on Edges

Mirrors are often used to replace solar cells on some of the LSC edges (see for example Ref. 129). The advantage of such a configuration for characterisation purposes is obvious: mirrors are usually easier to attach to the LSC than solar cells because they do not require electrical connections. Whether edge mirrors bring an advantage to the practical application of LSCs is investigated in this section, using a graphical, an analytical and a computational approach.

Goetzberger [62] proposed mirrors on edges as they increase the effective area of the solar cells, as illustrated in Figure 4.7. The motivation to use edge mirrors is that the cost of mirrors is significantly lower than that of solar cells. If the power output can be preserved, mirrors could reduce the cost-to-power ratio by essentially providing a higher effective geometric gain.

Having demonstrated in Section 2.3.6 that a square geometry is convenient, this investigation can be limited to mirrored geometries that are equivalent to square shapes without mirrors. This is the case for modules (b) and (c) depicted in Figure 4.7.

Recalling that the geometric gain G (see Equation 2.28), based on real areas, is defined as

$$G = \frac{A_{LSC}}{A_{PV}} \tag{4.1}$$

where A_{LSC} is the real LSC collection surface area and A_{PV} is the real area covered by PV cells, one can show that the modules (a), (b) and (c) have the same geometric gain.

With an LSC thickness d, the respective geometric gains (based on real areas) are:

$$G_a = \frac{A_{LSC,a}}{A_{PV,a}} = \frac{L^2}{4Ld} = \frac{L}{4d} \tag{4.2}$$

$$G_b = \frac{A_{LSC,b}}{A_{PV,b}} = \frac{(L/2)^2}{Ld} = \frac{L}{4d} \tag{4.3}$$

$$G_b = \frac{A_{LSC,c}}{A_{PV,c}} = \frac{1/2 A_{LSC,b}}{1/2 A_{PV,b}} = \frac{L}{4d}\,. \tag{4.4}$$

It has previously been shown with a raytracing approach that a square configuration with perfect mirrors on three edges does not have any advantage over a configuration with cells on all four edges [59]. In this section a square LSC with mirrors on two adjacent edges will be compared to one without mirrors. Due to the equivalent transformations shown in figure 4.7, the conclusions drawn from this comparison are also valid for the right angled isosceles triangle described in Ref. 62 and shown in Figure 4.7.

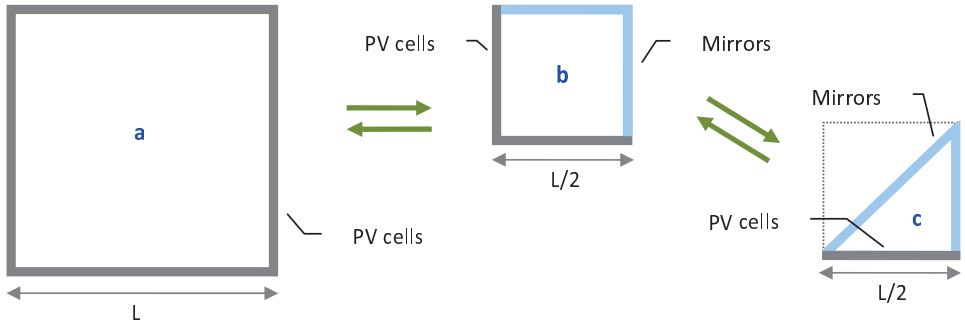

FIGURE 4.7: Mirrors on some of the LSC edges can increase the effective area covered by solar cells. Internally, the large square without mirrors (a) is equivalent to the small square (b) with two adjacent mirrors, which in turn is equivalent to the triangle (c) with two mirrors (assuming 100 % reflectivities). Of course, the absolute collection area for incident light does not transform by using mirrors. The collection area of module (a) is 4 times that of module (b) and 8 times that of module (c). The geometric gain, however, is the same in all cases.

The optical efficiency decreases with increasing concentrator size because of the longer average path length resulting in more self-absorption and background absorption. A more detailed investigation of this effect is presented in Section 7.2.4. Since a mirror effectively increases the area, it also reduces the optical efficiency. Edge mirrors would only be favourable if the cost savings from the smaller solar cell area outweighed this loss in optical efficiency. The following sections explore whether this is the case, focussing only on optimal LSC dimensions.

4.3.1 Graphical Reasoning

The mirrors in module (b) (see Figure 4.7) effectively double the length along each dimension and quadruple the concentrator surface area, making it internally equivalent to module (a).

Given the restricted secondary absorption lengths in current LSC technology the dimensions of an efficient mirrored module are likely to be smaller than the overall area to be covered for a practical application. This means, that several mirrored modules (b) would need to be arranged next to each other. By choosing the arrangement shown in configuration (d) in Figure 4.8 one can see that modules (a) and (d) are effectively indistinguishable: the pathlength of a photon from the point of emission to the PV cell is identical in both cases (a) and (d), independent of the initial position or direction of the photon. Consequently, under the assumption of perfect mirrors, both modules (a) and (d) have the same optical efficiency and generate the same power. The only difference in the cost-to-power ratio is that module (d) includes additional mirror costs. This suggests that it is favourable to omit the mirrors.

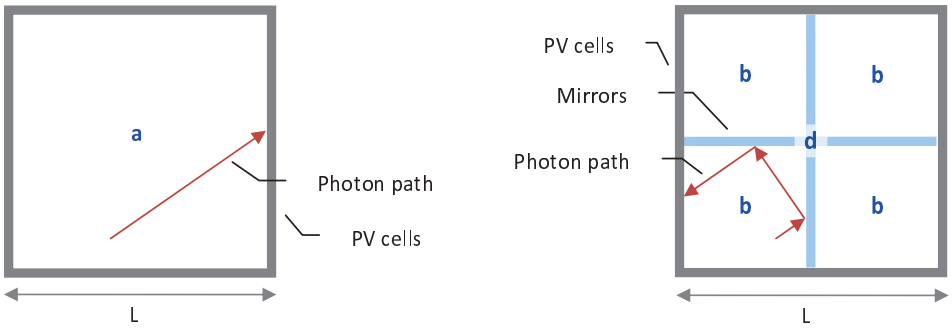

FIGURE 4.8: Comparison of a module without mirrors (a) and a module with mirrors (d), consisting of 4 units of module (b) as depicted in Figure 4.7. One can see that the photon pathlength before reaching a solar cell is the same in both cases.

4.3.2 Analytical Investigation

The power output of the LSC module is approximated by

$$P = I_\gamma \, A \, \eta_{\text{optical}} \eta_{PV} \, . \tag{4.5}$$

Since P scales with LSC surface area A, the power generated by module (a) is 4 times as large as the power generated by module (b) (from Figure 4.7), given that their optical efficiencies are equal:

$$P_a = 4P_b\,. \tag{4.6}$$

Moreover, module (a) has 4 times as many solar cells as (b). The cost-to-power ratio is calculated as follows:

$$\left(\frac{\$}{P}\right)_b = \frac{\$_{PV(b)} + \$_{LSC(b)} + \$_{\text{mirrors}}}{P_b} \tag{4.7}$$

$$= \frac{\frac{1}{4}\$_{PV(a)} + \frac{1}{4}\$_{LSC(a)} + \$_{\text{mirrors}}}{\frac{1}{4}P_a} \tag{4.8}$$

$$= \left(\frac{\$}{P}\right)_a + \frac{\$_{\text{mirrors}}}{P_b}\,. \tag{4.9}$$

The cost-to-power ratio of module (b) is higher due to the additional mirror costs. This means that for any given module of type (b) one could select a corresponding module (a) which offers a lower cost per unit power. The mirrored configuration would only be preferable if the availability of area restricted the choice to a small LSC.

4.3.3 Raytrace Simulation

The Raytrace Model was applied to compare the two types of configurations at different sizes. Typical LSC characteristics were input (a thickness of $\sim 3\,mm$, a refractive index of 1.49, a background absorption coefficient of $2\,m^{-1}$, which is regarded by the author a good, realistic value, and a Lumogen Violet dye with a QY of 95 % and a peak absorption coefficient of $\sim 2150\,m^{-1}$), and perfect mirrors were modelled. The resulting optical efficiencies are shown in Figure 4.9. A decrease in optical efficiency with increasing collection area is observed, which can be attributed mainly to increased self-absorption as well as host background absorption. It is also evident that the optical efficiency of the 50 cm×50 cm module without mirrors is identical, within errors, to that of the 25 cm×25 cm module with mirrors. The same applies to the other pair (no mirrors 100 cm×100 cm and 2 mirrors 50 cm×50 cm). The simulation supports the claim that the efficiency of a module with mirrors is equal to that of a four times as large module without mirrors. It also confirms that at equal sizes the module without mirrors performs

better, owing to the longer average pathlength to the cells when mirrors are present, as seen by comparing the two 50 cm×50 cm configurations.

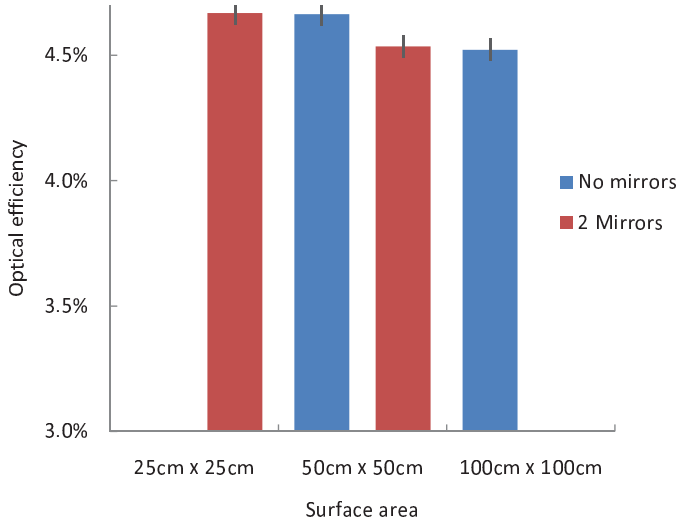

FIGURE 4.9: A raytrace comparison between LSCs with no mirrors and with mirrors on two adjacent edges. The optical efficiency is plotted for different top surface areas of the modules. The decrease of the optical efficiency with size due to increased self-absorption and background absorption is evident. Moreover, the optical efficiency of a module with mirrors is identical (within errors) to that of a four times as large module without mirrors.

4.3.4 Conclusion

The effect of mirrors on LSC edges, used to save solar cell area, was investigated. While mirrors virtually increase the area of the LSC and produce a greater effective geometric gain, they also lead to a lower optical efficiency since self-absorption and background absorption are increased. It was found by geometrical arguments and raytracing that a given area covered with several mirrored LSC modules produces the same power as a large individual module with cells on all edges. Moreover, the real geometric gain (based on real areas) is not increased by mirrors in this case. The additional cost of the mirrors gives the mirrored configuration an unfavourable cost-to-power ratio, even under the assumption of 100% reflecting mirrors. With real mirrors, this ratio would be even worse. The only situation in which mirrors on the edges would be preferable is when the available area restricts the size of the LSC to one that is smaller than the optimum. Since this is unrealistic in most practical applications, given the fact that efficient LSCs

are currently expected to be smaller than 1m^2 in area, it is concluded that the use of mirrors on the edges of an LSC module is disadvantageous in general.

4.4 Back Surface Reflectors

Back surface reflectors have been considered as a way to improve the LSC performance since the early years of LSC research (see for example Ref. 171). In this section the Raytrace Model was applied to quantify the improvement in light capture with the use of reflectors on the back surface. The two types of reflectors examined were the specular and the diffuse (see Section 2.5.1 for descriptions). In both cases an air gap was left between the LSC and the reflector in order to retain total internal reflection (TIR) (see Figure 4.10). It should be noted that with an air gap, any ray which exits the LSC and is reflected so as to re-enter the LSC will do so at an internal angle inside the LSC escape cone (in the limit of a ray parallel to the bottom surface of the light cone it will enter at the critical angle). Consequently the reflected light will leave the LSC out of the front unless it is absorbed or subject to Fresnel reflection. The dimensions of the modelled LSC were $1\,\text{m}\times1\,\text{m}\times3\,\text{mm}$, the refractive index was constant at 1.49, the background absorption coefficient was $2\,m^{-1}$ and the luminescent material was a hypothetical quantum dot (see Figure 4.11) with a QY of 90 %. A constant reflectance of 96% was input, which is considered the upper limit for realistic reflectors in the visible.

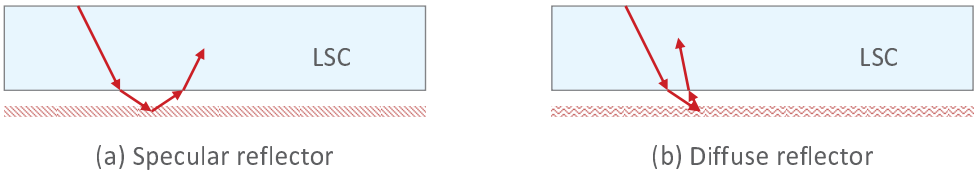

FIGURE 4.10: Schematic of LSCs with specular (a) and diffuse (b) back reflector. The air gap between the waveguide and the plate is required to preserve total internal reflection.

4.4.1 Simulation Results and Discussion

The Raytrace Model was used to compare photon distributions for a plain LSC without a back reflector, one with a specular reflector and one with a diffuse reflector under direct and diffuse light, separately. A monochromatic reflectance of 96 % was assumed

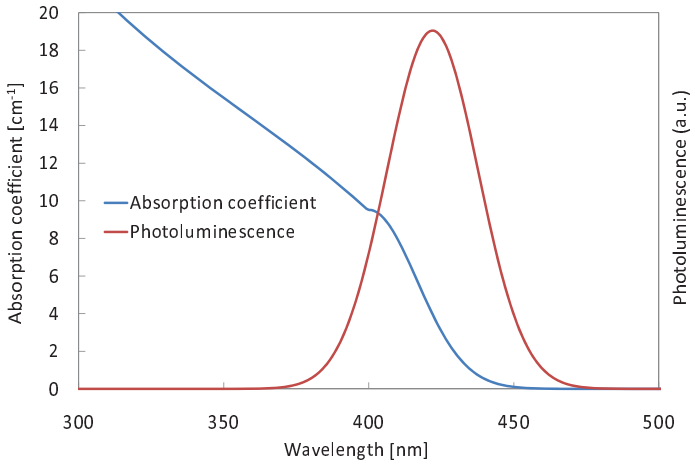

FIGURE 4.11: The absorption and emission spectra of a hypothetical QD labelled QD400 with a quantum yield of 90 %. The spectra are based on spectra of commercially available core-shell QDs, but shifted towards the blue.

for both types of reflectors. Under direct light (see Figure 4.12) it was found that both reflectors yield a ∼25 % relative improvement in optical efficiency compared to the case without reflectors. The diffuse reflector can, on average, produce longer pathlengths on the second pass for normally incident light. This results in a slight advantage in optical efficiency of ∼0.5% absolute. There is also a small contribution of incident light reflected back into the LSC by the diffuse reflector in a way that it directly exits the edge of the LSC without absorption, but at ∼ 0.1 % this contribution is too small to show up in Figure 4.12. The sub-unity reflectance leads to a small amount of light absorption in the reflector material, which is treated as transmission through the bottom by the model and shown as such in Figure 4.12. As expected, the reflectors produce a large amount of light reflected out of the top, compared to the plain LSC. The simulation also quantifies the enhanced absorption with the aid of the reflectors, which is between 23 % and 27 % relative to the plain LSC at the given absorbance. As a result of the higher absorption, the overall internal losses are also higher with reflectors, but there is still an overall gain in optical efficiency of ∼25 % with reflectors.

Under diffuse light (see Figure 4.13) the optical efficiency enhancement from the reflectors is around 20 % and thus smaller than the ∼25 % under direct light. This is in line with the smaller increase in the absorption of incident light via reflectors by 18 % in the diffuse case compared with the 23 % to 27 % in the direct case. The reason for this is that the pathlength of diffuse light entering the LSC is already relatively large and the relative increase in absorbance with the aid of reflectors therefore smaller. With both

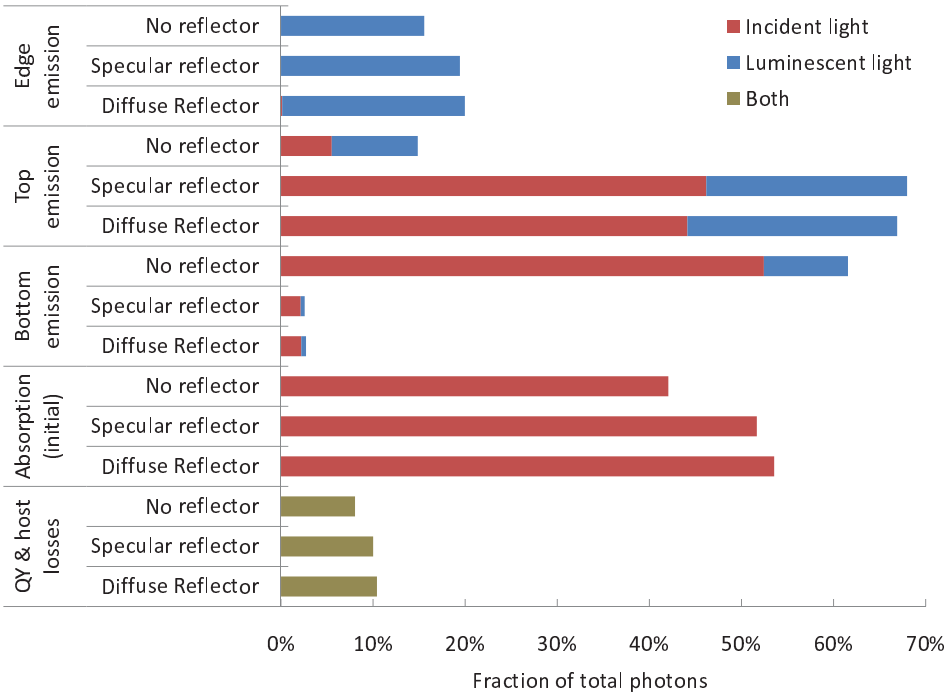

FIGURE 4.12: The effect of back reflectors under direct irradiation, simulated with the Raytrace Model. A constant reflectance of 96 % and an air gap between reflector and LSC were modelled. The reflection profile of the diffuse reflector was assumed to be lambertian. Excluding the absorption, which subsequently leads to a loss or an emission, the bars add up to 100 % for each modelled case.

reflectors there is an insignificant contribution of incident light reflected out of the edges without absorption (less than 0.2 % in optical efficiency). It is evident that under diffuse irradiation the effects of both types of reflectors are virtually identical.

These results also quantify the effect of light being directly reflected towards the edges and into the PV cells. In the case of the large concentrator modelled in this study, the contribution was found to be less than 0.2 %. This is in agreement with an investigation by Pravettoni *et al.* [172] that showed that this direct reflection of light into the cells originates almost exclusively from locations close to the cells. It was found that a small coverage by a diffuse back reflector in form of a thin frame drawing out the perimeter of the LSC produced virtually the same increase as a full back surface coverage. This confirms that the contribution of direct coupling into the cells scales approximately with the inverse of the geometric gain, as claimed in Section 2.5.1.

For each illumination spectrum and for each back surface reflector type there should be an optimal doping level that maximises the optical efficiency. If time had permitted, a

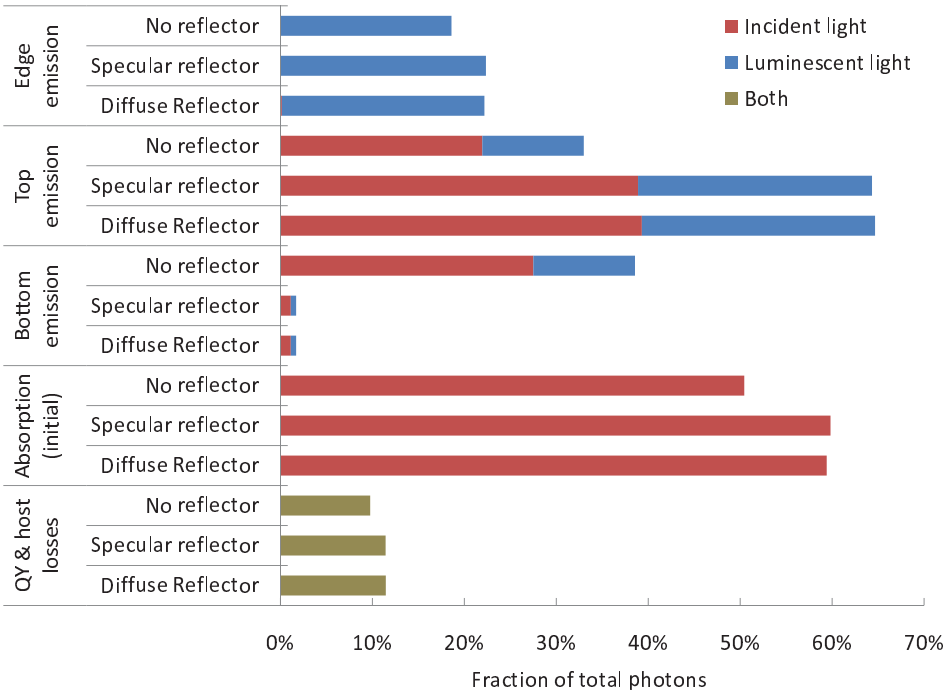

FIGURE 4.13: The effect of back reflectors under diffuse irradiation, simulated with the Raytrace Model. The diffuse light was assumed to be isotropic over a hemisphere.

comprehensive study would have included varying the doping level to find the optimum for each of the cases modelled (including no reflector) and conducting the comparison on the basis of these optimal doping levels. However, it is safe to assume that a back surface reflector will always produce a higher output since the doping level and thus the losses can be lower to absorb a given amount of light. Under direct light a lambertian mirror is preferable over a specular as it would increase the pathlength within the LSC the most whereas under diffuse light the type of mirror is expected to be rather irrelevant.

4.5 Tapered Geometry

This section addresses the question whether a new type of tapered geometry can improve the waveguiding efficiency of the LSC. Two types of tapering with the aim to improve the LSC performance have been considered in the past. Goetzberger *et al.* [173] proposed a taper along the LSC edge consisting of a higher refractive index material than the bulk of the LSC. This concept, depicted in Figure 4.14, received further attention from other groups [24, 25] due to its potential to boost the concentration ratio by reducing the required area of solar cell material.

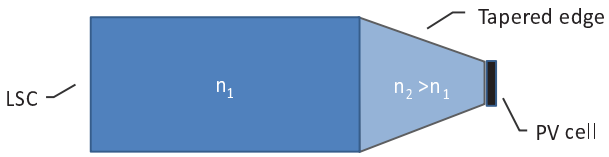

FIGURE 4.14: Schematic of an LSC with a tapered edge, enabling a reduction of the required solar cell material. The taper needs to have a higher refractive index than the rest of the LSC in order to boost the concentration.

Kennedy *et al.* [59] carried out raytrace simulations on a variant that had a PV cell only on one LSC edge and was tapered towards that PV cell edge (see Figure 4.15), with the motivation to reduce the PV cell area and improve the cost per unit power. However, it was found that in this case light originally trapped by TIR can escape while travelling towards the cell as the angled bottom surface gradually changes the internal angle upon reflection. The overall outcome was that tapering towards the edge with the PV cell always leads to a loss in optical concentration and hence in the cost per unit power.

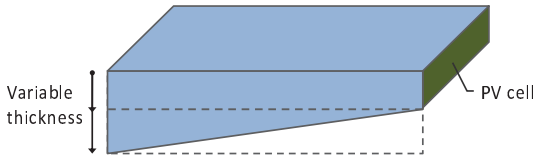

FIGURE 4.15: Schematic of a tapered LSC that gets thinner towards the PV cell edge, as discussed by Kennedy *et al.* [59].

A different type of tapered geometry is examined in this section, one that also has only one PV cell edge, but is tapered towards the edge opposing the PV cell, as shown schematically in Figure 4.16. In contrast to the previous two concepts, where the tapering had the purpose of reducing the cell area and thereby increasing the geometric gain and hence the optical concentration, in this concept, the tapering is intended to improve the light guiding properties. The idea behind this is similar to the principle of the wedge-shaped concentrator proposed by Maruyama *et al.* [174]: the angle of the bottom surface can impart a preferential direction upon reflection that facilitates the light transport towards the PV cell edge. This design could be modified to allow for PV cell coverage on all four LSC edges, for example by tapering the LSC radially towards the centre. However, the simplified case with only once PV cell edge should suffice for the purpose of determining the benefit of the tapered design.

Raytrace simulations were carried out on an LSC with $50 \times 50\,\mathrm{cm}^2$ top surface area where the thickness of the PV cell edge was held constant and the thickness of the opposing

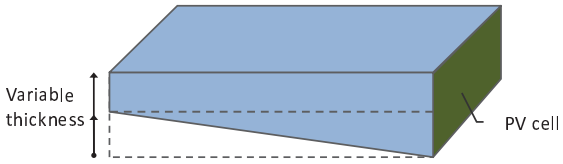

FIGURE 4.16: Schematic of a tapered LSC that gets thinner away from the PV cell edge. This is the design discussed in this section.

edge was varied, as illustrated in Figure 4.16. A refractive index of 1.49 and constant background absorption of $2\,m^{-1}$ were input, and the QD400 (see Figure 4.11) with a QY of 90 % was modelled as the luminescent species. The photon flux into the PV cell relative to the case without tapering was recorded. This relative photon flux is proportional to the optical concentration since the dimensions of the PV cell and the LSC top surface area were kept constant. Clearly, the average thickness of the LSC decreases as the tapering becomes more pronounced, so a decrease in the overall absorption of incident light is expected with increasing tapering.

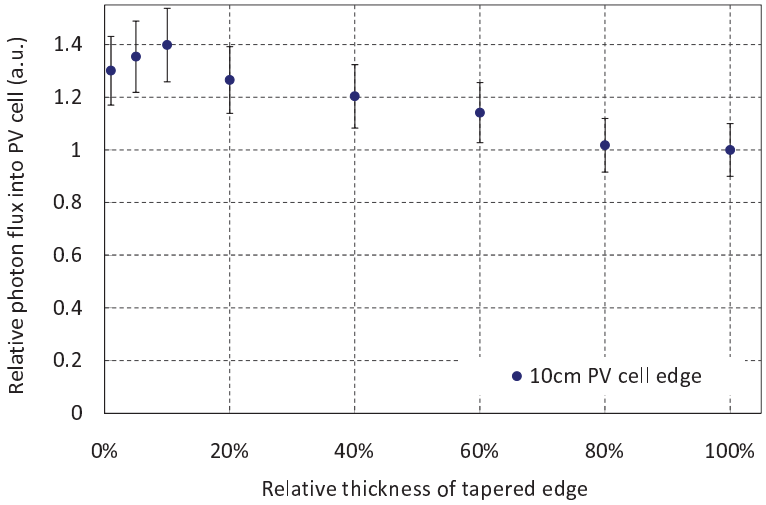

FIGURE 4.17: Modelling of a thick tapered LSC with a surface area of $50\times50\,\mathrm{cm}^2$ and a PV cell edge thickness of 10 cm. The thickness of the edge as in Figure 4.16 was varied. A relative thickness of 100 % refers to the case without tapering. The resulting photon flux into the PV cell is shown relative to the case without tapering. The relative photon flux is proportional to the optical concentration. The results show that the tapering can indeed improve the LSC performance, by up to $\sim$40 % in this example. When the tapered edge goes below 10 % of the thickness of the PV cell edge, there is a decrease in the photon flux, which is attributed to a weakened absorptance due to an insufficient LSC thickness.

Initial simulations based on an LSC with a 10 cm thick PV cell edge showed improvements in the photon flux into the PV cell of 30-40 % with tapering (see Figure 4.17). Figure 4.17 also shows a decrease in the relative photon flux when the thickness of the

tapered edge is less than $\sim 10\,\%$ of the thickness of the PV cell edge. This loss is attributed to a weakened overall absorption due to the smaller average LSC thickness.

Since an LSC thickness of 10 cm is considered impractical, the simulations were repeated using a more realistic thickness of 3 mm. As can be seen from the results in Figure 4.18, the improvements with tapering in this case are insignificant and within the uncertainty of the simulation (below $10\,\%$).

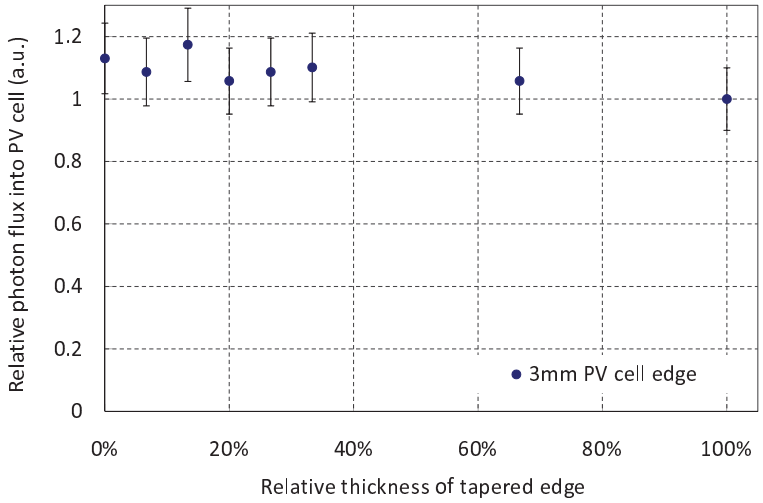

FIGURE 4.18: Modelling of a thin tapered LSC with a surface area of $50\times50\,\mathrm{cm}^2$ and a PV cell edge thickness of 3 mm. The thickness of the edge opposite to the PV cell was varied. The resulting photon flux into the PV cell is shown relative to the case without tapering. In this thin case, the advantage of the tapering is significantly smaller than in the thick case. The fluctuations in the trend are attributed to the modelling uncertainty.

In conclusion, the tapered geometry presented in this section can improve the light guiding within the LSC by supporting internal reflection towards the PV edge. However, to allow for a PV cell coverage on all LSC edges, a more complicated design would be required with a constant edge thickness and a tapered centre. Moreover, structural integrity arguments would limit the extent of the tapering in a real application. Given the complications and the marginal advantages, the tapered design was not pursued further.

4.6 Raytrace Study of Self-Absorption

Self-absorption (or re-absorption) is a major loss mechanism as it increases luminescence quantum yield losses and escape cone losses, thereby attenuating the waveguiding efficiency of the LSC. Several theoretical models have been proposed in the past that describe self-absorption losses. In this section the Raytrace Model is applied to further illuminate the nature of self-absorption. In particular, this section examines the re-absorption probability for each generation of re-emission in order to determine why the well-known and apparently sound analytical model by Batchelder *et al.* [20] is found to break down when the self-absorption is significant.

4.6.1 Review of Theoretical Models

In the first proposal of the LSC by Weber and Lambe [17] an analytical model of the LSC was presented that equated the optical efficiency to the product of the absorption efficiency, the luminescence quantum yield and the collection efficiency, defined as the ratio of collected flux (at the edges) to luminescent flux. This model made the approximation that re-absorbed photons were considered to be lost.

Batchelder *et al.* [20] extended the analytical model of Weber and Lambe by taking multiple re-absorptions into account via a geometric series. Based on the re-absorption probability, the trapping efficiency η_{trap} (see Equation 2.25) and the QY of the luminescent centre they derived an expression for the waveguiding efficiency:

$$\eta_{\text{waveguide}} = \frac{(1-r)\eta_{\text{trap}}\,QY}{1 - QY\,[\bar{r}(1-\eta_{\text{trap}}) + r\,\eta_{\text{trap}}]} \tag{4.10}$$

where r is the probability of re-absorption of light trapped in a waveguide mode and $\bar{r}$ is the probability of re-absorption of light emitted into an escape cone. Equation 4.10 shows that in the limit of no re-absorption, i.e. $r = 0$ and $\bar{r} = 0$, the waveguiding efficiency equals $\eta_{\text{trap}}\,QY$. Conversely, as r approaches 1 the waveguiding efficiency vanishes.

Kittidachachan *et al.* [175] derived the model of Batchelder *et al.* [20] from a two-photon flux model based on the detailed balance method. Moreover, through comparison

with raytrace simulations they verified the re-absorption probability for first generation emission predicted by the Weber and Lambe model.

Another model was proposed by Roncali and Garnier [60], who made the same approximation as Weber and Lambe by taking only the first generation of emitted photons into account, thereby neglecting re-emissions. This model accounted for imperfect internal reflection and host matrix absorption. A key parameter in this model is the mean optical pathlength, which is used to calculate the efficiency of internal reflections as well as the probability of self-absorption.

Earp *et al.* [132, 145, 176, 177] presented a theoretical model with the aim to predict the luminous efficiency of the LSC since their research was related to daylighting applications. Their model accounts for re-absorption and matrix losses. A key variable in the model is the LSC half-length, defined as the distance over which the light intensity drops by 50 %. This quantity is practical for comparison with experimental measurements.

Currie *et al.* [65] adopted a simplified version of the model by Batchelder *et al.* shown in Equation 4.10 by assuming that the contribution from re-absorbed escape cone light is negligible compared to the contribution from re-absorbed trapped light, i.e.:

$$\bar{r}(1-\eta_{\text{trap}}) \ll r\,\eta_{\text{trap}}\,. \tag{4.11}$$

This assumption is justified because the probability of re-absorption depends on the photon pathlength, and in a typical LSC the pathlength of escaping light is significantly shorter than that of trapped light. The resulting expression for the waveguiding efficiency is

$$\eta_{\text{waveguide}} = \frac{(1-r)\eta_{\text{trap}}\,QY}{1-r\,\eta_{\text{trap}}\,QY}\,. \tag{4.12}$$

The waveguiding efficiency for an LSC with a trapping efficiency of 74 % and a QY of 63 % (based on a real sample, Sample 831), calculated using the simplified Equation 4.12, is plotted in Figure 4.19.

Solving Equation 4.12 for the re-absorption probability r yields:

$$r = \frac{\eta_{\text{trap}}\,QY - \eta_{\text{waveguide}}}{\eta_{\text{trap}}\,QY(1-\eta_{\text{waveguide}})}\,. \tag{4.13}$$

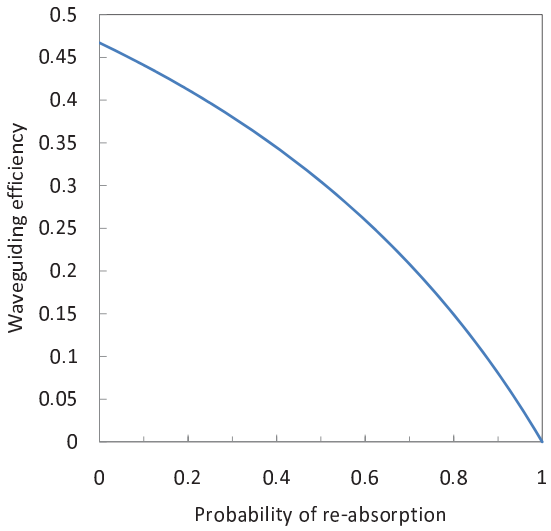

FIGURE 4.19: The analytical relation between the waveguiding efficiency and the re-absorption probability r, plotted for a QY of 63 % and a trapping efficiency of 74 %.

This expression for the re-absorption probability is examined with the aid of the Raytrace Model. Wilson *et al.* [94] also presented a raytrace study of re-absorption. They carried out an experimental determination of the re-absorption probability by comparing the edge spectrum with the spectrum in the absence of re-absorptions and using the red-shift to deduce the degree of re-absorptions. They studied the probability of photons from initial emission reaching the edge as a function of the optical density of luminescent centres and supported their data points with raytrace simulations. The study presented in this section differs from previous ones in that it focusses on the probability of re-absorption as a function of the number of previous re-absorptions (presented in Figure 4.21. This probability, however, is specific to a given luminescent material as it depends on the overlap between absorption and emissions spectra.

4.6.2 Raytrace Simulations and Discussion

The waveguiding efficiency and the probability of re-absorption were calculated using the Raytrace Model for a range of LSC sizes. The LSCs were based on Sample 831 (see Section 3.3) with a refractive index of 1.49, hence a trapping efficiency of 74 % and doped with JHN46 nanorods with a QY of 63 %. A monochromatic illumination at a wavelength of 404 nm was used in the simulation. By substituting the waveguiding efficiency from the model into Equation 4.13, the analytical re-absorption probability is

obtained. While a QY of 63 % can be considered low, simulations were also carried out for the upper limit of 100 % QY. Figure 4.20 shows a comparison of the analytically and computationally derived re-absorption probabilities for a quantum yield of 63 % (i) and of 100 % (ii). A large discrepancy is evident between the analytical value for r and the value obtained from the Raytrace Model, even in the limit of a QY of 100 %. Since the Raytrace Model has been proven to make reliable predictions, it is concluded that the analytical model is flawed.

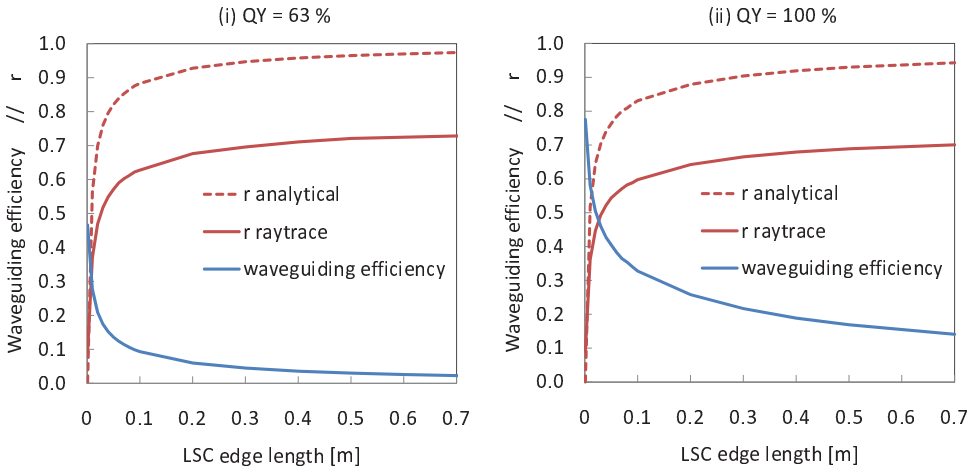

FIGURE 4.20: Comparison of the total re-absorption probability r as a function of LSC size, derived from the analytical expression (Equation 4.13) and computed with the Raytrace Model. The modelled LSC was based on Sample 831 (see Section 3.3), which has a QY of 63 %. Monochromatic illumination at 404 nm was simulated. In both cases (QY of 63 % and 100 %) the analytical model is found to deviate strongly from the Raytrace Model.

The flaw of the analytical model is found to lie in the assumption of a constant re-absorption probability r. The experiments presented in Section 7.2.5 also indicate that the re-absorption probability varies with the number of previous re-absorptions. Each re-emission produces a redshift in the emission spectrum, which changes the overlap of the emission with the absorption spectrum and hence the probability of re-absorption. The variation of r with the number of re-absorptions in the case of a 25 cm×25 cm LSC based on the properties of Sample 831 is plotted in Figure 4.21. It is evident that the assumption of a constant r is invalid in this case. The probability of re-absorption decreases with an increasing number of previous re-absorptions. The sharp drop of r after 7 re-absorptions is attributed to the shape of the absorption spectrum (see Figure 3.2). As the re-emitted photons get further red-shifted, they reach the declining tail

of the absorption spectrum in the long wavelengths, where the re-absorption probability diminishes. It is important to note that the constant r assumption would be valid for luminescent materials with a very small overlap between absorption and emission. This would explain the good agreement between experimental results and the analytical model reported by Currie *et al.* [65].

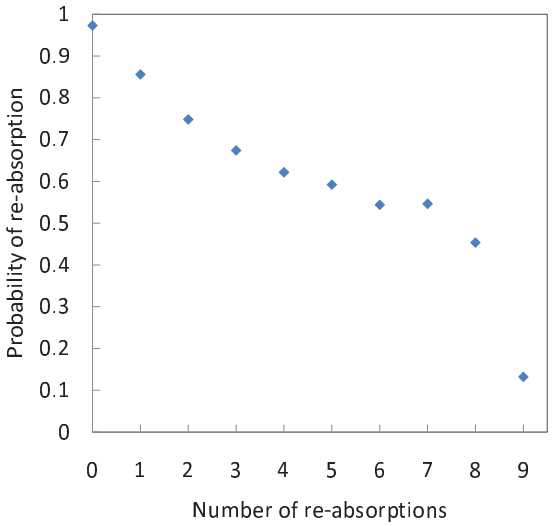

FIGURE 4.21: The variation of the re-absorption probability with the number of re-absorptions (which equals the number of luminescent centre interactions minus 1) was modelled for a 25 cm×25 cm LSC based on the properties of Sample 831. The plot shows how the probability of re-absorption of a luminescent photon decreases with the number of previous re-absorptions. The sharp drop after 7 re-absorptions is attributed to the shape of the absorption spectrum (see Figure 3.2). As the re-emitted photons get further red-shifted, they reach the declining tail of the absorption spectrum in the long wavelengths, where the re-absorption probability diminishes.

4.7 Transparent LSC

Building integrated PV has much potential, since buildings are ubiquitous in urban areas, since part of the cost of PV modules can be offset by substituting other building materials with the modules and since the electricity demand in buildings usually peaks during periods in which solar energy is available, i.e. during daytime. This section discusses the feasibility of a power generating window comprising an LSC that is transparent to visible light. The results presented here originate from raytrace simulations and are based on a feasibility study carried out by the author in collaboration D. J. Farrell, A. J. Chatten and K. W. J. Barnham from 2007 to 2008. Both the author and D. J. Farrell

carried out separate simulations in parallel using different raytrace models, in order to provide more confidence in the results.

Figure 4.22 shows the response of the human eye in relation to the AM1.5 global spectrum. The energy available in the UV and the IR regions of the solar spectrum is invisible to the human eye, so that an LSC that only absorbed the UV or IR would effectively be transparent. Such an LSC could provide for indoor daylighting whilst generating energy. To be fully transparent, the LSC should have no absorption between 400 nm and 750 nm. However, it is safe to assume that some absorption at the tails of the eye response would be acceptable to produce a sufficiently transparent LSC. In this study the focus is on UV absorbing LSCs only due to the poor availability of IR absorbing luminescent materials with high QYs. Of course, a transparent LSC cannot generate as much energy as an opaque one. However, a transparent LSC should not be in direct competition with standard LSCs. In fact, it should be in competition with standard windows, which do not generate any energy.

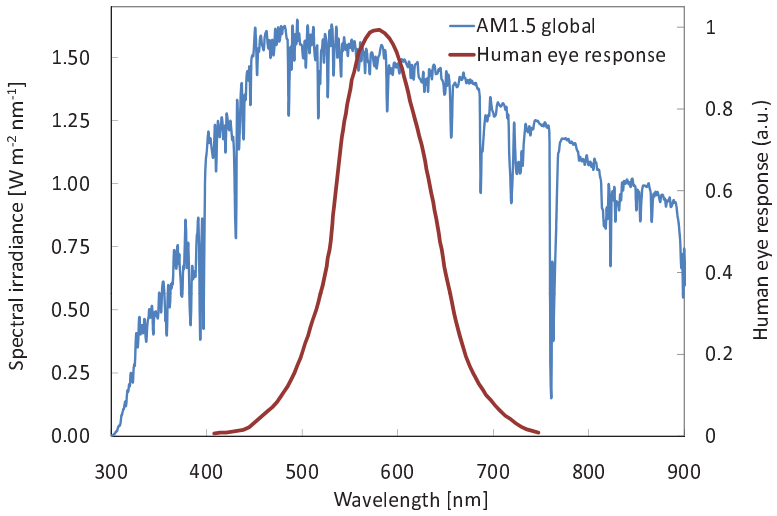

FIGURE 4.22: The human eye response [178] in relation to the AM1.5 global solar spectrum. The solar spectrum contains energy in the UV and the IR that is invisible to the human eye and could be harnessed by a transparent LSC acting as a power generating window. To be fully transparent, the LSC should have no absorption between 400 nm and 750 nm.

4.7.1 Materials

Two transparent LSCs were modelled, one doped with a dye and one with a quantum dot. The dye was Lumogen F Violet 570 from BASF, which has an absorption spectrum

predominantly in the UV. The spectra were experimentally measured, and a QY of 95 % was assumed in line with other, comparable dyes from BASF (and at the lower end of the QYs measured by Wilson *et al.* [152], who reported a range from 95 % to 100 % for this dye). The quantum dot modelled was the hypothetical QD400 (see Figure 4.11), which was based on a commercially available QD, but with a blue-shifted spectrum. A QY of 90 % was modelled. The spectra of the two luminescent materials are shown in Figure 4.23.

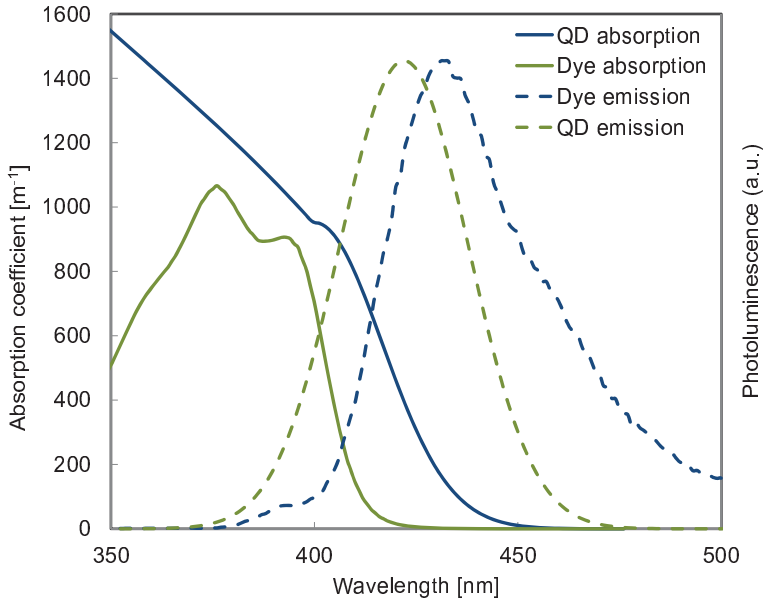

FIGURE 4.23: Luminescent centres suitable for a transparent LSC: a Lumogen F Violet 570 dye from BASF and a hypothetical quantum dot labelled QD400.

Transparency in the visible spectrum is an important property for a window. Figure 4.24 shows the transmittance of the modelled LSCs compared to the AM1.5 irradiation. Only 4-5 % of the photons in the entire solar spectrum would be absorbed by the modelled LSCs, but the high energies of the absorbed photons could still permit a reasonable power output.

The dimensions of the modelled LSCs were 50 cm×50 cm×3 mm. The absorption coefficients shown in Figure 4.23 apply to a homogeneously doped LSC. In practice, a thin-film structure with the same overall absorbance may be more suitable as a power generating window, especially since windows are generally made of glass and since glass manufacturers routinely work with coatings, so that the fabrication of thin-film LSCs

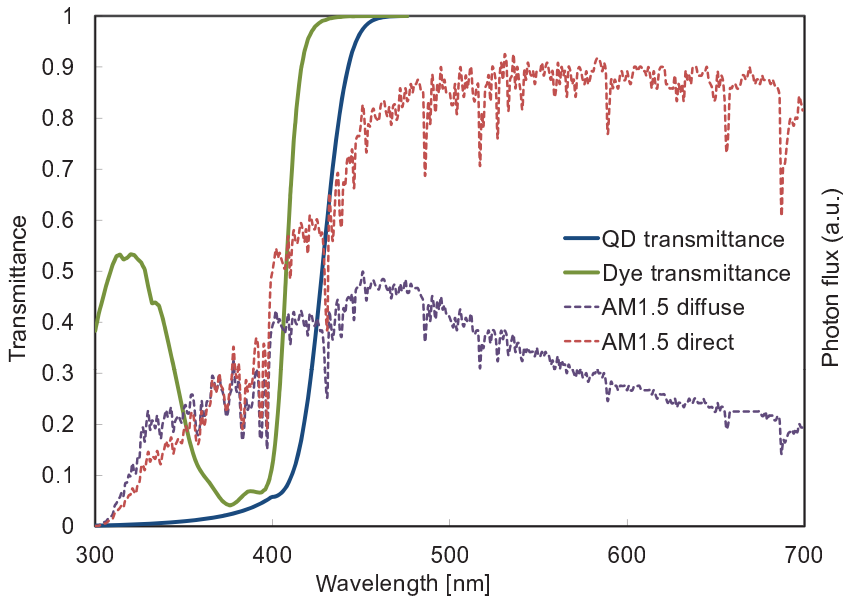

FIGURE 4.24: Transmittance of UV absorbing luminescent materials for a power generating window.

may fit their core competencies. When calculating the cost per watt of the power generating window one would have to subtract the cost of the conventional window to be replaced, which would certainly benefit the economics of the power generating window.

The host material would ideally be transparent to UV light, because otherwise it would be in competition with the luminescent material. The simulations were based on a thin-film structure using a commercial glass with a relatively low UV absorption and high transparency in the visible (absorption coefficients of $\sim 40\,\mathrm{m}^{-1}$ around 300 nm and below $\sim 2\,\mathrm{m}^{-1}$ above 400 nm) as the substrate.

Solar cell coverage on all four LSC edges was assumed, and an InGaP cell (see Figure 4.25) was chosen due to its relatively high bandgap compared to Si cells. The high bandgap is required for a good match with the short wavelength emission spectra from the luminescent materials. The higher bandgap also enables a higher open-circuit voltage, thereby utilising the higher energy of the UV photons better. A cell with an even higher bandgap then InGaP would have been preferable given the higher voltage and higher efficiency due to less thermalisation energy loss in the solar cell, but the choice was limited by the availability of QE and dark current data. The dark current characteristics of the modelled InGaP cell is shown in Figure 4.26.

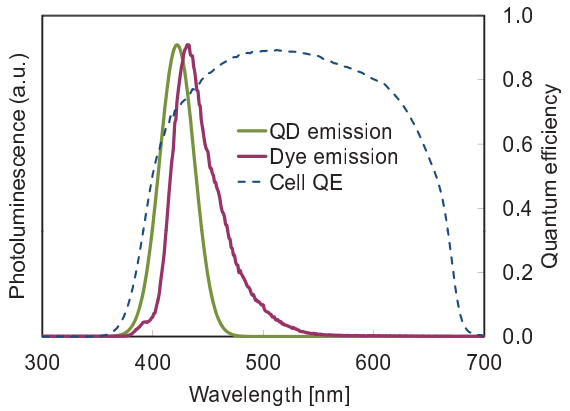

FIGURE 4.25: Spectral match of transparent LSC emission with InGaP cell. The external QE of the cell is high at the emission wavelengths of the dye and the QD, but ideally, the cell would have a higher bandgap.

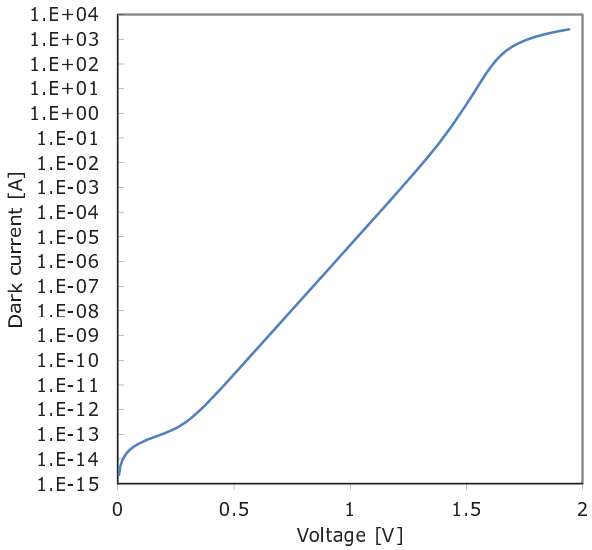

FIGURE 4.26: Dark current curve of the modelled InGaP cell.

4.7.2 Incident Sunlight

The simulation was carried out for two locations: London, where there is a relatively high proportion of diffuse sunlight, and Marseille, where the direct light dominates. Realistic insolation data was provided by M. Mazzer, who obtained daily and annual solar insolation data for a given location from the standard NREL insolation software BIRD by inputting appropriate parameters for aerosol absorption and humidity from a NASA database. Figure 4.27 shows the available solar energy per day over the course of the year. The *direct* component refers to the energy available with solar tracking. The power generating windows were assumed to be statically integrated in a vertical, south

facing building wall, and in such an orientation, the direct component reduces to the curve labelled *incident*.

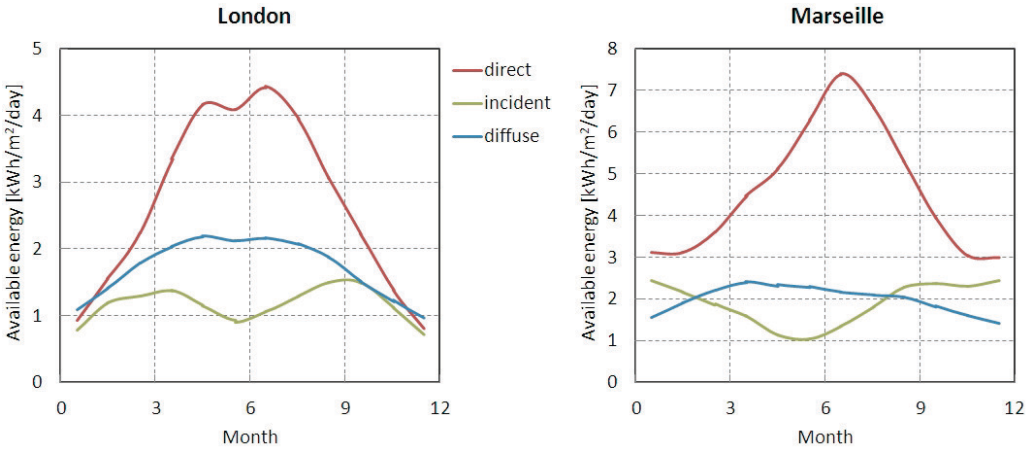

FIGURE 4.27: Solar energy available over the year in London and Marseille. The *incident* energy is the part of the *direct* solar energy that is available in the absence of tracking, in a vertical, south facing orientation. This data was provided by M. Mazzer from the IMEM CNR Laboratory, Parma.

The *diffuse* light was assumed to be isotropic in the upper half-hemisphere on the window. To model the angle of incidence of the direct light, an approximation was made since computing the actual angles over the course of the year would have been very complex. It was assumed that the *incident* beam is approximately related to the *direct* by the square of the cosine of the angle of incidence. Thus, the average angle of incidence over each month was deduced from the average ratios of *incident* to *direct* insolation. The annual insolation quantities for London and Marseille are given in Table 4.1. Running the simulation with one million rays for each case and each month produced stable results.

	Insolation [kWh/m^2/year]	
	direct	*diffuse*
London	979	623
Marseille	1614	700

TABLE 4.1: Annual insolation in London and in Marseille.

4.7.3 Results

Raytrace simulations of power generating windows were carried out for the locations London and Marseille. Two variants were modelled, one with a dye and one with a QD, as described above. The annual energy yield and power conversion efficiency were calculated by averaging the monthly outputs based on realistic insolation data. The results shown in Table 4.2 suggest that, despite relatively low absorptance, efficiencies slightly above 1 % are achievable with an LSC/cell system, which simultaneously acts as a window. The Lumogen Violet 570 dye was found to perform better than the hypothetical quantum dot QD400 owing to lower self-absorption losses. The system would have a higher efficiency in locations like London, where there is a large diffuse component. However, despite a lower efficiency, the energy delivered by the system over the year would be higher in a location like Marseille, where the total solar insolation is higher. Since the power generating window described in this section would absorb short-wavelength light, a high bandgap cell would be more suited to absorb the high energy photons emitted and would thus enable higher system efficiencies.

		Yield [kWh/m^2/year]	System efficiency [%]
London	Lumogen F Violet 570	23	1.4
	QD400	13	0.8
Marseille	Lumogen F Violet 570	28	1.2
	QD400	16	0.7

TABLE 4.2: Simulations of a power generating window placed in a vertical south facing orientation in the locations London and Marseille. The efficiencies are based on the yield in comparison to the sum of the *direct* and the *diffuse* insolation (see Table 4.1). Though the energy delivered in London would be lower than in Marseille, the system efficiency in London would be higher due to a proportionally larger diffuse component.

4.8 Chapter Conclusion

This chapter presented a variety of simulations carried out with the Raytrace Model. In the first section, the effectiveness of the LSC under indirect light was demonstrated, validating the claim of its usefulness in regions with high diffuse irradiation and in a static, non-tracking installation. It was shown that the angular response of the LSC is comparable to that of standard encapsulated silicon cells. Having established that the

coupling of incident radiation into the LSC is very efficient, it is the author's opinion that further reductions of the reflection off the top surface should have a low priority. Anti-reflective coatings are important for solar cells since their refractive indices are around 3.5 and hence their reflectances are considerably higher than that of the LSC. In the case of the LSC it is questionable whether the efficiency enhancement from an AR coat, which typically comprises several layers of varying refractive indices, justifies the additional cost.

The use of mirrors on some of the LSC edges as a method to enhance the geometric gain was examined. While mirrors increase the effective area of the solar cells and produce a greater geometric gain, they also lead to a lower optical efficiency. Using a graphical reasoning, an analytical approach and raytrace simulations, it was established that even perfect mirrors on the edges do not benefit the cost-to-power ratio in general. Realistic mirrors with sub-unity reflectance would perform even worse. Edge mirrors could only be of advantage in the case where the available deployment area restricts the size of the LSC. Given that the anticipated optimal sizes of LSCs are considerably smaller than realistic deployment areas, it is concluded that for the purposes of practical application, edge mirrors should be omitted, and PV cells should be placed on all edges of the LSC.

It was found that both specular and diffuse back surface reflectors perform about equally well in improving the optical efficiency of the LSC by increasing the pathlength of incident light. The choice of reflector should be made depending on cost and reflectance considerations. It should be noted that a back reflector would not allow for a semi-transparent LSC, so the advantage in optical efficiency may need to be weighed up against aesthetic requirements.

The concept of a specific tapered geometry was considered, and though raytrace simulations suggest that it could improve the light guiding properties of the LSC it was not pursued any further due to impracticalities in the design and rather insignificant advantages of less than 10 % in terms of optical efficiency assuming reasonable geometries. Based on considerations such as the ease of fabrication and attaching of solar cells to the edges, the square planar geometry is considered preferential. Consequently the majority of investigations in this thesis are limited to the square planar geometry.

It was shown with the Raytrace Model how the probability of re-absorption decreases with every re-emission due to the progressive red-shift. This explains why the theoretical

models that assume a constant re-absorption probability fail to accurately predict the performance of LSCs with significant self-absorption.

Finally, the concept of a power generating window based on a transparent LSC was presented, a novel application of the LSC. From raytrace simulations it was concluded that, with the right choice of luminescent material, LSC/cell systems are feasible that are mostly transparent to visible light and have a power conversion efficiency around one percent. Though this is small compared to other photovoltaic devices, this type of LSC should be compared to standard windows, which do not produce any power. In the author's opinion, BIPV is the most suitable field of application for LSCs, and a power generating window could be an attractive device.

Chapter 5

Thin-Film versus Homogeneous LSC Configurations

5.1 Chapter Introduction

The main research question of this chapter is whether the thin-film (TF) LSC (introduced in Section 2.7) has an advantage over the conventional, homogeneously doped LSC. This question is addressed using experimental and computational comparisons. In a broader sense, this chapter also investigates the general differences between TF and homogeneous LSCs.

The TF LSC was originally proposed as a configuration to reduce self-absorption by Rapp and Boling in 1978 [179] and supported by Viehmann and Frost in 1979 [180], with the reasoning that luminescent photons are only susceptible to re-absorption in the thin film; they have long pathlengths in the transparent substrate. Overall, this would arguably lead to reduced re-absorptions, in particular when the absorption of incident light by the TF LSC is equal to that of its homogeneous counterpart. However, this reasoning was subsequently contested by Rapp and Boling themselves [181] as well as by A. Zastrow [182], with the argument that the pathlength gained in the substrate is compensated by an increased re-absorption probability in the optically dense film, resulting in equal re-absorptions between thin-film and homogeneous LSCs. However, no experimental evidence for this argument was provided, only a graphical reasoning was given.

In the recent past, many research groups have studied the TF LSC to the homogeneous LSC (see for example Refs. 90, 183, 104, 184, 149). Yet no experimental plus modelling comparison of the performance of a thin-film LSC with that of a homogeneous LSC had been published prior to the author's conference paper in 2007 [185]. Reisfeld *et al.* published research on TF LSCs in 1988 [160], where they referred to Rapp and Boling [179] and their claim that the TF configuration had reduced losses. In 1994 the same group published Monte Carlo simulations of TF LSCs [163], but there was no comparison between TF and homogeneous LSCs.

The results presented in this chapter show that the thin-film LSC has virtually the same re-absorption losses as an equivalent homogeneous one and offers no notable advantage in terms of optical efficiency. A publication by Meyer *et al.* from 2009 [162] showing a raytrace comparison of the re-absorption probabilities of the two variants (thereby partly duplicating the work presented by the author in 2007 in Ref. 185) supports the author's conclusion. A review paper from 2010 by R. Reisfeld [124] stating that the thin-film design reduces self-absorption losses indicates that the work described in this chapter and reported in part in Ref. 185 is not yet widely accepted or known.

5.2 Experimental Comparison

For the experimental comparison, two sets of homogeneous and thin-film samples were fabricated by our collaborators at the Fraunhofer-IAP. The dye concentrations were intended to produce equal absorption between TF and homogeneous samples in each of the two sets. Figure 5.1 shows that the Fraunhofer-IAP achieved similar absorbances between homogeneous and TF samples in each set as requested. The homogeneous samples had a polymer matrix made from Plexit 55, a commercially available acryl-resin. The TF samples were fabricated by evaporation of dye layers from a chloroform solution on a PMMA substrate. It was seen that the resultant doped layer extended into the PMMA substrate, possibly indicating partial solvation of the surface PMMA during this process. Both types of samples had comparable refractive indices of ~ 1.49 (as stated by the collaborators from the Fraunhofer IAP). The dimensions of the samples were $5\,\mathrm{cm} \times 5\,\mathrm{cm} \times 3\,\mathrm{mm}$, yielding a geometric gain of ~ 4.2. Detailed descriptions of the samples are given in Section 3.3.

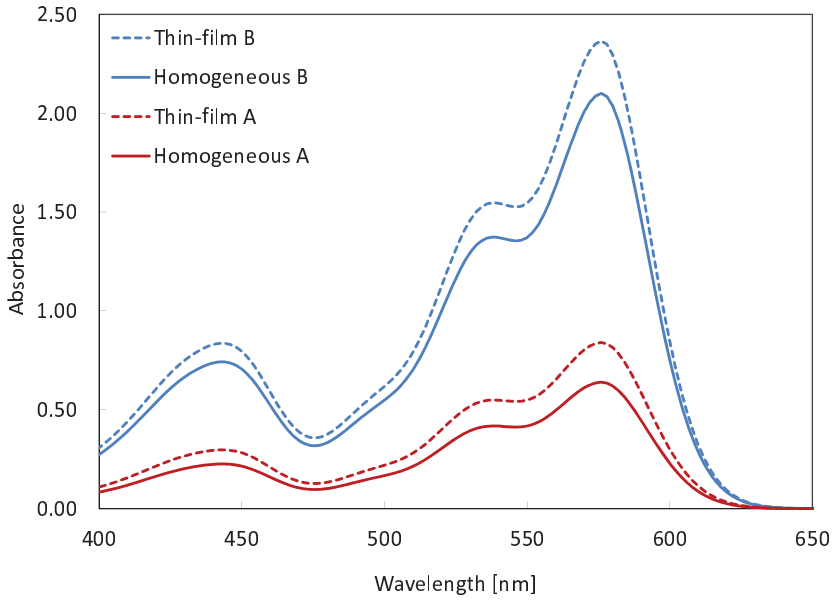

FIGURE 5.1: Measured absorbances of the two pairs of TF and homogenous samples discussed in the text.

Short-circuit current measurements as described in Section 3.4.2 were carried out on the samples using a tungsten-halogen light source with a blue filter. The optical efficiencies, as defined in Section 2.3.4, relative to the light source (as opposed to AM1.5) are shown in Table 5.1. Errors were estimated from the spread in short-circuit current measurements as described in Section 3.4.2. One can see that set B has a higher optical efficiency, i.e. a higher output than set A, which is due to the higher dye concentration and hence stronger absorption of incident light. More importantly, the optical efficiencies within each set (A and B) agree within errors. This indicates that there is no measurable difference in performance between a thin-film and a homogeneous LSC and provides the first experimental support for the claim in Refs. 181, 182 that the longer pathlength in the undoped region of the TF sample is compensated by a shorter pathlength in the active film.

5.3 Raytrace Comparison

This section consists of raytrace simulations that complement the experimental comparison of thin-film and homogeneous LSCs. Following a reproduction of the experimental

	Optical efficiency [%]
Homogeneous A	19 ± 2
Thin-film A	22 ± 2
Homogeneous B	39 ± 3
Thin-film B	38 ± 3

TABLE 5.1: Comparison of experimentally determined optical efficiencies of the two thin-film and homogeneous LSC sets. The optical efficiencies are presented relative to the tungsten-halogen light source with a blue filter as opposed to AM1.5 irradiation. Within each set (A and B) they are consistent, within errors.

measurement, different parameters were varied in order to test the sensitivity of the experimental results to these parameters.

5.3.1 Reproduction of Experiment

The Raytrace Model was applied to sample set A to reproduce the experimental measurement. The dye spectra were fitted for the model using Gaussian curves (see Figure 5.2), and a host absorption of $1\,\mathrm{m}^{-1}$, a typical absorption coefficient for polymer matrices like the ones in these samples (see Section 3.2.1), was used. The smooth tail of a Gaussian curve is important for accurate raytracing as fluctuations in the tail (within measurement errors) can easily skew the results when the absorbance or the self-absorption are high. The lamp spectrum given Figure 3.12 was used, and the incident light was assumed to be at normal incidence. To ensure that any differences due to configuration were not masked by the small absorbance differences between the two configurations shown in Figure 5.1, the simulation was carried out by matching the absorbance of the TF sample to that of the homogeneous one for both pair A and pair B. While the real TF sample had an overall thickness made up of the 3 mm substrate and a 74 µm active layer combined, the simulation was based on an overall thickness of 3 mm (with a 2.926 mm substrate), identical to the homogeneous sample. One million rays were simulated to produce relatively small statistical uncertainties. The model was found to be in good agreement with the experimental results (see Table 5.2). The results showed only a small, yet statistically significant difference between the two LSC configurations: a slightly higher optical efficiency was found in the homogeneous case. Though a small effect, making up for only a $\sim 0.5\,\%$ and smaller than the experimental error, it is larger than the uncertainty in the simulated efficiencies estimated from the spread of

ten runs amounting to one million photons. The origin of this difference is worth further investigation.

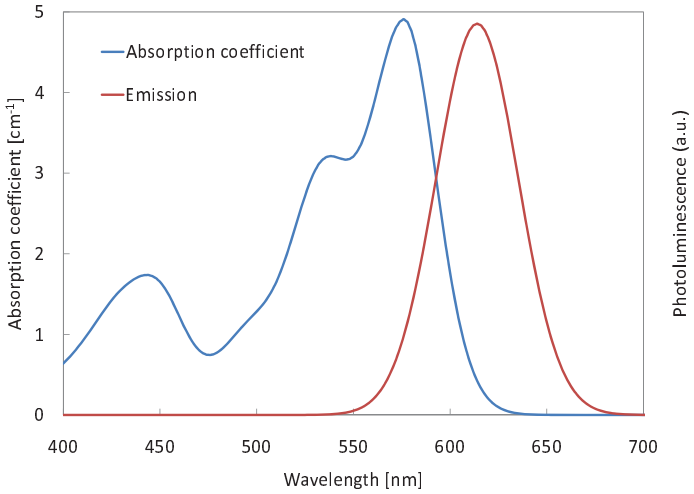

FIGURE 5.2: Absorption and emission spectra of the Lumogen F Red 300 dye with a QY of 98 %. The absorption coefficient is that of the Homogeneous A sample.

	Optical efficiency [%]
Homogeneous A	20.0 ± 0.1
Thin-film A	19.5 ± 0.1

TABLE 5.2: Reproduction of the comparison of optical efficiencies within sample set A using the Raytrace Model. The optical efficiencies are presented relative to the modelled tungsten-halogen light source with a blue filter as opposed to AM1.5 irradiation. The results are in good agreement with the experimental measurements (see Table 5.1). The uncertainties shown here are a result of multiple simulation runs.

Figure 5.3 sheds more light on the properties of the two configurations by showing the final photon distributions as a percentage of incident photons in each case. Some of the incident photons are reflected from the top due to Fresnel reflection. Most photons are transmitted through the bottom as they are not absorbed within the LSC. There are emitted fractions out of the top, the bottom and the edges, and there are photons lost due to the less than unity dye QY and host absorption. The photon distributions of the homogeneous and the TF configurations are very similar, but one can notice a difference in the emission out of the edges, which is greater than the statistical uncertainty. This difference leads to the optical efficiency advantage of ~ 0.5 % in the homogeneous case, which is accompanied by less emission out of the top and the bottom surfaces (smaller by ~ 0.2 % each) and by lower QY and host absorption losses (smaller by ~ 0.1 %).

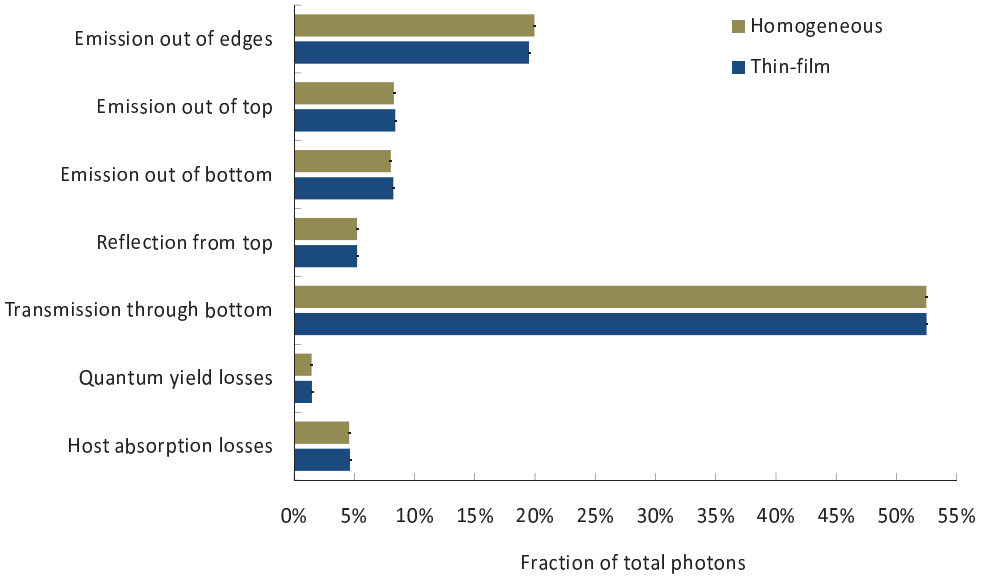

FIGURE 5.3: Raytrace comparison between Thin-film A and Homogeneous A, showing the losses and photon fractions exiting the different surfaces as a percentage of incident photons. The statistical uncertainty is $\sim 0.1\,\%$. Apart from some minor differences, the two types of concentrators are virtually indistinguishable.

As a result of the absorbances of the two configurations being assumed equal, the number of photons transmitted through the bottom are equal as observed. In the presence of a high host absorption coefficient, one would expect a slightly higher capture efficiency in the TF case (with the film oriented towards the light source) because the incident light is not attenuated by host absorption in the substrate before it can be absorbed by the luminescent centres. With a host absorption of $1\,\mathrm{m}^{-1}$ and a sample thickness of 3 mm this effect would contribute to a less than $0.3\,\%$ relative difference and therefore be negligible.

The average pathlength of photons was found to be (43.7 ± 0.1) mm in the homogeneous and (44.6 ± 0.1) mm in the TF case. This slight difference is a result of the way this pathlength is computed: only luminescent photons exiting the edges are taken into account; the pathlengths of photons exiting the front (top) or back (bottom) surface or absorbed without further emission by a luminescent centre or the host material are disregarded. In the TF case it is likely that the photons which exited out of the edges were the ones that travelled a significant distance in the substrate, thus having a larger average pathlength. The photons that underwent re-absorptions in the film had short pathlengths, but were not taken into account, which gave the edge photons a greater

weighting and resulted in the slightly longer average pathlength in the TF case compared to the homogeneous.

$5\times5\,\mathrm{cm}^2$, QY 98 %	η_{capture} [%]	$\eta_{\mathrm{waveguide}}$[%]	Relative re-absorption [%]
Homogeneous A	42.1 ± 0.1	47.4 ± 0.1	74.3 ± 0.2
Thin-film A	42.1 ± 0.1	46.3 ± 0.1	77.4 ± 0.2

TABLE 5.3: Further results of the raytrace comparison of Thin-film A and Homogeneous A. As assumed in the model, the capture efficiencies are identical. There are some minor differences between the two configurations. The relative re-absorption shows the number of re-absorptions in relation to the number of first generation luminescent photons. The pathlength in this case is defined as the distance a photon exiting out of one of the LSC edges has travelled since its emission from a luminescent centre.

The smaller escape cone and QY losses that were found in the homogeneous configuration are typical for re-absorption related losses and suggest that the TF LSC has greater re-absorptions than the homogeneous one. This relationship is verified by the data in Table 5.3, which compares the capture efficiencies, the waveguiding efficiencies and the relative re-absorptions of the two configurations. As assumed in the model, the capture efficiencies are identical to allow for a fair comparison. The difference in the waveguiding efficiency is shown to be linked to the relative re-absorptions in the respective configurations, which are (74.3 ± 0.2) % (in relation to the number of first generation luminescent photons) for the homogenous and (77.4 ± 0.2) % for the TF LSC.

The outcome of this section is that whilst the TF and the homogeneous LSCs examined in this study have very similar performances, the homogeneous one has a slightly better optical efficiency by ~ 0.5 % due to fewer re-absorptions. Since this outcome is only valid for the specific LSCs used in this comparison, further raytrace analyses based on different LSC properties are carried out in the following sections to provide a more general result.

5.3.2 Variation of Geometric Gain

For further comparison, LSCs based on the sample set A with a larger geometric gain of ~ 42 were simulated by extending the top surface area of the samples to $50\,\mathrm{cm}\times50\,\mathrm{cm}$ while maintaining an overall thickness of 3 mm. Apart from the surface area, all other parameters remained as in the previous section, including the light source. The key results are shown in Table 5.4. There is no change in the capture efficiency (beyond the uncertainty) compared to the $5\,\mathrm{cm}\times5\,\mathrm{cm}$ case, since it is independent of the top

surface area. As expected, there is a decrease in the waveguiding efficiency in the case of a larger geometric gain. More importantly, the results show identical waveguiding efficiencies as well as identical relative re-absorption percentages for both configurations. This suggests, that the small difference noticed in the previous section could be due to edge effects, which can be significant in small LSCs, but become insignificant as the geometric gain increases.

$50\times50\,\mathrm{cm}^2$	η_{capture} [%]	$\eta_{\mathrm{waveguide}}$ [%]	Relative re-absorption [%]
Homogeneous	42.2 ± 0.1	26.5 ± 0.1	105.4 ± 0.3
Thin-film	42.2 ± 0.1	26.5 ± 0.1	105.4 ± 0.3

TABLE 5.4: Results of a raytrace comparison of a thin-film and a homogeneous LSC based on the sample set A, but with a larger top surface area of $50\,\mathrm{cm}\times50\,\mathrm{cm}$ and hence a geometric gain of ~42. The results show no noticeable difference between the two configurations in terms of waveguiding efficiency and relative re-absorption percentage, indicating that at practical LSC dimensions the performance is independent of the configuration.

To support the hypothesis that the small difference in waveguiding efficiency between the thin-film and the homogeneous sample found in Section 5.3.1 is a result of edge effects, a further simulation was carried out of a sample with a top surface area of $5\,\mathrm{mm}\times5\,\mathrm{mm}$ and thus a geometric gain of ~0.42 (see Table 5.5). As expected, the capture efficiency is unaffected by the change in surface area, but the waveguiding efficiency increases as the geometric gain decreases. The interesting result from the comparison with Table 5.3 and Table 5.4 is that the discrepancy between the waveguiding efficiencies of the thin-film and the homogeneous configuration is more substantial when the LSC is small (59.2 % in the homogeneous case compared to 53.4 % in the thin-film case). This supports the hypothesis that edge effects are the cause of the higher waveguiding efficiency of the homogeneous LSC.

$5\times5\,\mathrm{mm}^2$	η_{capture} [%]	$\eta_{\mathrm{waveguide}}$[%]	Relative re-absorption [%]
Homogeneous	42.1 ± 0.1	59.2 ± 0.1	43.5 ± 0.3
Thin-film	42.1 ± 0.1	53.4 ± 0.1	61.6 ± 0.3

TABLE 5.5: Results of a raytrace comparison of a thin-film and a homogeneous LSC based on the sample set A, but with a smaller top surface area of $5\,\mathrm{mm}\times5\,\mathrm{mm}$ and hence a smaller geometric gain of ~0.42. A comparison between Table 5.3 and Table 5.4 shows that the discrepancy in the waveguiding efficiencies of the two configurations increases as the geometric gain decreases. As discussed in the text, this suggests that edge effects are the cause of the discrepancy.

5.3.3 Central spot illumination

This section further investigates the hypothesis that edge effects are the only source of performance differences between thin-film and homogeneous LSCs. The sample set A was modelled again, but this time under point illumination at the centre of the top surface. This allows for a comparison of the two configurations in absence of edge effects. The results presented in Table 5.6 show that the waveguiding efficiency is lower than in the uniformly illuminated case (see Table 5.3), which is due to the longer path-lengths required for collection. More importantly, the results show identical waveguiding efficiencies for both configurations, which confirms that the slight advantage of the homogeneous LSC observed in Section 5.3.1 is purely due to edge effects. These effects can be explained as follows: In the homogeneous case, photons incident close to the edge are absorbed over the entire thickness following an exponential distribution. If they are re-emitted towards the edge there is a high probability of collection at the edge with no need for internal reflection. In the thin-film case, all photons are absorbed in the dense active film, where re-emission directly towards the edge, i.e. in the plane of the film has a high probability of re-absorption before collection can occur. When the luminescence originates further away from the edge the main mode of transport is waveguiding via TIR, in which both thin-film and homogeneous LSCs are evenly matched.

$5\times5\,\mathrm{cm}^2$	η_{capture} [%]	$\eta_{\mathrm{waveguide}}$ [%]	Relative re-absorption [%]
Homogeneous	42.2 ± 0.1	45.9 ± 0.1	79.0 ± 0.3
Thin-film	42.2 ± 0.1	45.9 ± 0.1	79.0 ± 0.3

TABLE 5.6: Results of a raytrace comparison of a thin-film and a homogeneous LSC based on the sample set A, with simulated photons incident only on a spot at the centre of the top surface. The purpose of the central illumination is to eliminate edge effects from the performance comparison. It is evident that in this case both the thin-film and the homogeneous LSC perform identically.

It is concluded that except for edge effects, the thin-film and the homogeneous LSC configurations in sample set A have identical efficiencies. It is safe to neglect edge effects with regards to practical LSC sizes (of $25\times25\,\mathrm{cm}^2$ and above) as they diminish with increasing size.

5.3.4 Orientation of Film

The previous sections assumed an orientation of the TF sample in which the film was facing the light source. This section examines the significance of the film orientation by comparing the key performance indicators with the film on the upper and on the lower surface, separately. The simulations were based on the TF sample modelled in the previous section, which was a large geometric gain version of sample Thin-film A under lamp illumination. The results are shown in Table 5.7, where the default orientation with the film facing the light source is labelled thin-film, while the orientation with substrate facing the light source is labelled inverted thin-film. There is no difference beyond the modelling uncertainty between the two orientations. The inverse structure is expected to absorb slightly less of the incident light since it has to pass through the substrate before it can be absorbed by the luminescent centres, but with the modelled host absorption coefficient of $1\,\mathrm{m}^{-1}$ this effect appears to be negligible. It is concluded that the results for the default orientation of the TF LSC are also valid in the inverted case.

$50\times50\,\mathrm{cm}^2$	η_{capture} [%]	$\eta_{\mathrm{waveguide}}$ [%]	Relative re-absorption [%]
Thin-film	42.2 ± 0.1	26.5 ± 0.1	105.4 ± 0.3
Inverted thin-film	42.1 ± 0.1	26.6 ± 0.1	105.1 ± 0.3

TABLE 5.7: Raytrace simulations examining the significance of the orientation of the thin-film LSC. The simulations are based on a $50\,\mathrm{cm}\times50\,\mathrm{cm}\times3\,\mathrm{mm}$ TF LSC as modelled in Section 5.3.2. The orientation with the film facing the light source is labelled thin-film, and the opposite orientation is labelled inverted thin-film. The performances under the two different orientations are found to be identical within the uncertainty of the simulations.

5.3.5 Lower QY

The outcome of Section 5.3.2 was that the TF and homogeneous LSCs investigated had the same waveguiding efficiencies and the same amount of re-absorptions. Since re-absorptions lead to more significant losses when the quantum yield is low, further simulations were carried out under the assumption of a low QY of 50 % in order to support the general validity of the result. Both $5\times5\,\mathrm{cm}^2$ and $50\times50\,\mathrm{cm}^2$ LSCs were modelled, with all parameters apart from the QY being the same as in Section 5.3.1 and Section 5.3.2, respectively. As expected from the lower QY, the results presented

in Table 5.8 show a drop in all waveguiding efficiencies compared to the high QY case. In the $5\times5\,\mathrm{cm}^2$ case the homogeneous configuration has a slightly higher waveguiding efficiency and less re-absorptions, while in the $50\times50\,\mathrm{cm}^2$ the performances are equal. These outcomes qualitatively match the ones for the high QY cases from Section 5.3.1 and Section 5.3.2 and provide further confirmation of the conclusion regarding the comparison of the TF and the homogeneous LSC.

QY 50 %	η_{capture} [%]	$\eta_{\mathrm{waveguide}}$ [%]	Relative re-absorption [%]
Homogeneous ($5\times5\,\mathrm{cm}^2$)	42.1 ± 0.1	16.7 ± 0.1	61.3 ± 0.2
Thin-film ($5\times5\,\mathrm{cm}^2$)	42.2 ± 0.1	16.0 ± 0.1	63.0 ± 0.2
Homogeneous ($50\times50\,\mathrm{cm}^2$)	42.1 ± 0.1	7.6 ± 0.1	80.0 ± 0.2
Thin-film ($50\times50\,\mathrm{cm}^2$)	42.2 ± 0.1	7.6 ± 0.1	80.1 ± 0.2

TABLE 5.8: Raytrace comparison of thin-film and homogeneous LSCs with a relatively low quantum yield of 50 %. Apart from the QY and the size, the samples are based on the sample set A described in Section 5.3.1 and Section 5.3.2. As in the high QY case, the results show a small advantage in terms of the waveguiding efficiency of the homogeneous configuration in the $5\times5\,\mathrm{cm}^2$ case and equal performances in the $50\times50\,\mathrm{cm}^2$ case.

5.3.6 Higher Absorbance

Since any differences due to re-absorptions would be amplified when the absorbance is high, the simulations from Section 5.3.2 were repeated with five times as high an absorption coefficient for the luminescent centres. A comparison of Table 5.4 with Table 5.9 shows that the higher absorption coefficient leads to an increase in the capture efficiency from $\sim$42 % to $\sim$78 %. Again the TF and the homogeneous sample have identical performances. The re-absorption rate is significantly higher compared to the original case due to the high absorbance, which results in a decrease in the waveguiding efficiency from $\sim$27 % to $\sim$24 %.

$50\times50\,\mathrm{cm}^2$, absorbance×5	η_{capture} [%]	$\eta_{\mathrm{waveguide}}$ [%]	Relative re-absorption [%]
Homogeneous	77.5 ± 0.1	24.1 ± 0.1	297.3 ± 0.9
Thin-film	77.5 ± 0.1	24.1 ± 0.1	298.1 ± 0.9

TABLE 5.9: Raytrace comparison of thin-film and homogeneous LSCs with a relatively high absorbance. The simulations are based on the $50\times50\,\mathrm{cm}^2$ LSCs described in Section 5.3.2 with the absorption coefficient increased by a factor of five. As in the original case (with a lower absorbance), both configurations have identical performances.

5.3.7 Thickness of Film

Finally, the effect of the film thickness on the performance of the TF LSC was examined using simulations based on the $50\times50\,\mathrm{cm}^2$ LSC described in Section 5.3.2. While keeping the overall thickness of the sample constant at 3 mm, the ratio of the overall thickness to the active layer thickness (the film) was varied between 1, the limiting case of a homogeneous LSC, and 100,000. The absorption coefficient was adjusted according to the film thickness in order to maintain a constant capture efficiency. The results presented in Figure 5.4 show that the optical efficiency and thus the waveguiding efficiency is independent of the thickness of the active layer. This, along with the outcomes of the previous sections, confirms the general validity of the conclusion that thin-film and homogeneous LSCs have identical optical efficiencies and the same amount of reabsorptions, as long as the geometric gain is reasonably large so that edge effects can be ignored. For all practical purposes, there is no difference in the performance between the two configurations.

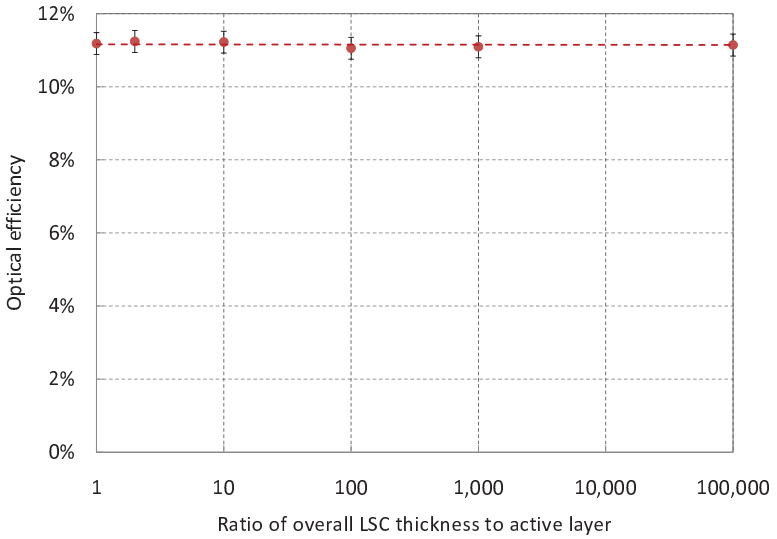

FIGURE 5.4: Raytrace simulations examining the effect of the thickness of the active layer. The ratio of the overall thickness to the active layer thickness was varied, and the absorption coefficient was adjusted accordingly to ensure a constant capture efficiency. The results, plotted on logarithmic scale show that, within the modelling uncertainty, the optical efficiency is independent of the film thickness.

5.4 Angular Emission Profiles of Thin-Film and Homogeneous LSCs

Previous sections showed that the only notable difference between the outputs of the homogeneous and thin film LSCs was in edge effects. These are dependent on the angular emission profile, which is examined in this section both experimentally and with the Raytrace Model. The emission profile should not strongly affect the performance of the concentrator, since solar cells index matched to the edges are likely to collect the bulk of the emission.

5.4.1 Experimental Method

This experiment was designed in collaboration with M. Pravettoni to measure the angular profile of the emission out of the LSC edge after refraction into air. The samples Homogeneous A and Thin-film A from Section 5.3.1 were compared in this experiment. In order to examine the emission from the LSC edge, a reference PV cell was set up to move in a semi-circle at a distance of 5 cm around a point on the edge surface in a plane perpendicular to the long axis (see Figure 5.5). The separation between the LSC edge and the PV cell had to be large enough to attenuate effects originating from the finite (as opposed to infinitesimal) thickness of the LSC, but small enough to produce a measurable signal. The LSC front surface was illuminated and J_{SC} measurements (see Section 3.4.2) were carried out as the cell was advanced to different angles. Because light emitted from other surfaces of the LSC also reached the PV cell, a correction technique was devised: the measurement was repeated with the edge surface under examination blackened out so that the unwanted background radiation could be isolated. By subtracting the background from the raw data, the signal from the edge surface alone was obtained (see Figure 5.6).

5.4.2 Emission Profile of the Homogeneous LSC

The angular emission profile of the homogeneous LSC is shown in Figure 5.7. It spans $\sim 180\,^{\circ}$ because light emitted just within the escape cone inside the LSC exits nearly parallel to the surface upon refraction. The measurement was also simulated with the same

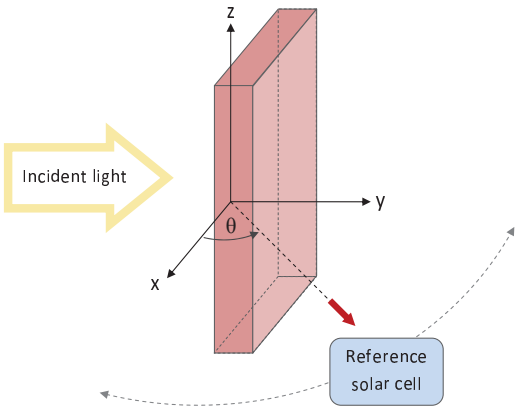

FIGURE 5.5: Experimental setup for the angular emission profile measurement. The reference solar cell is moved in a semi-circle to record the emission intensity as a function of angle.

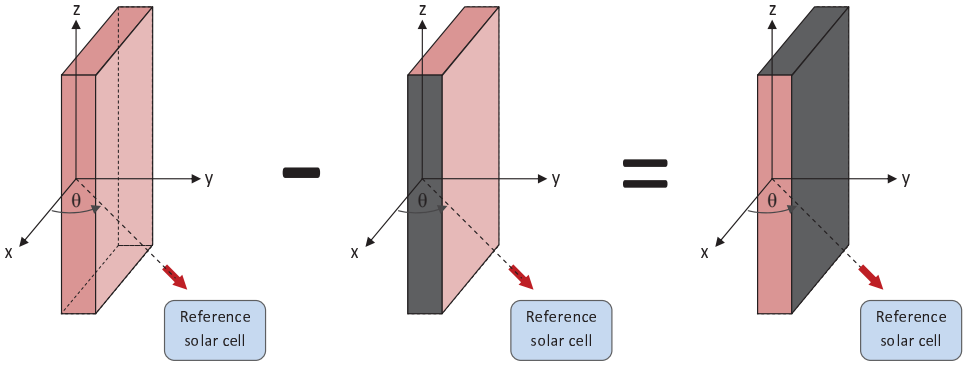

FIGURE 5.6: Correction technique for angular emission profile. To obtain the signal from the edge under examination alone, the background contribution from other LSC surfaces was isolated by blackening out the edge surface and subsequently subtracted from the raw signal.

Raytrace Model used in the previous sections (also shown in Figure 5.7), producing a good agreement with the experimental results. The measured profile of the homogeneous LSC is slightly asymmetric and exhibits a dip near the centre (0 °), which is reproduced by the model. At larger angles, the Raytrace Model agrees particularly well with the experiment. It deviates slightly around 0 ° degrees, exhibiting a stronger asymmetry and a shifted dip, which can be attributed to alignment errors in the experiment. As a measure of the asymmetry, the ratio of integrated areas of the right hand side to the left hand side of the profile is 1.12 from the experiment and 1.06 from the model.

The asymmetry and the central dip appear to contradict the symmetry of the homogeneous configuration at first sight. However, the nature of the light absorption creates

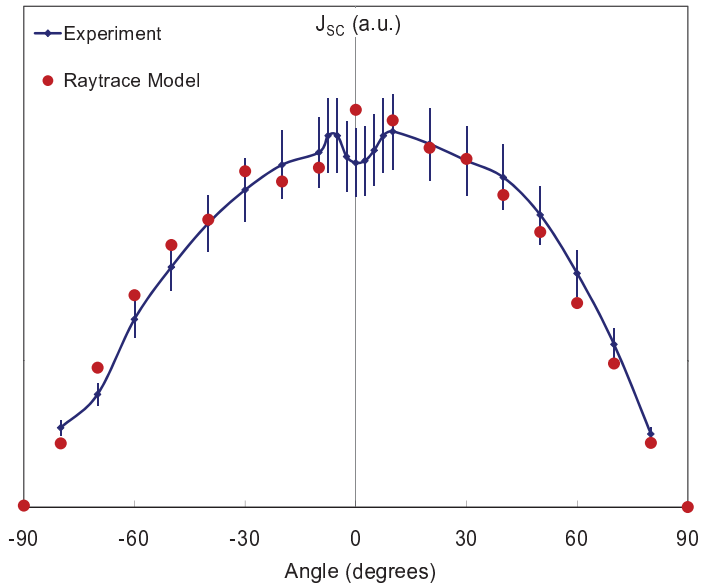

FIGURE 5.7: Normalised angular emission profile of the homogeneous LSC, where 0° is normal to the edge surface and 90° is parallel to the incident light (in the same direction). One can observe an asymmetry in the profile.

the asymmetry that leads to the observed emission profile. Most of the incident light is absorbed close to the LSC front surface, with exponential attenuation, as described by the Beer-Lambert law (Equation 2.17). As more light is absorbed close to the front surface, more light is also emitted from there, into directions away from it. This leads to the result that the emission profile is greater in the direction away from the light source, hence at positive angles (right hand side) in Figure 5.7.

A further investigation of the angular profile was carried out by our collaborator M. Pravettoni [186] using a simplified Monte Carlo model of the concentrator. The LSC was described by a flat cuboid with Fresnel reflection on all edges. Monochromatic light was modelled as non-interacting, ballistic particles with random starting directions, and secondary absorptions were disregarded. The emission profile from the experiment and the Raytrace Model could be reconstructed by accounting for the correct distribution of emission centres within the waveguide as required by the Beer-Lambert law, thereby supporting the interpretation of the emission profile.

An earlier measurement of the angular profile, shown in Figure 5.8, was carried out by A. Zastrow on a homogeneous, rod-shaped LSC [182, page 169]. The technique used in that case was different in that an index matched semi-cylinder was attached to one end of the LSC, so that emission from the LSC end could couple into the semi-cylinder

without reflection or refraction. Both the LSC and the semi-cylinder were made of Plexiglas. A photodiode was moved along the edge of the semi-cylinder to measure the output at different angles. This setup eliminated refraction and TIR at the point of exit. The rod-shaped LSC was illuminated from the side, over a small spot at the far end. This meant that the majority of the detected photons had to be travelling along TIR modes, so that the measured output angles did not extend all the way to 90°. Of course, photons that are re-absorbed and re-emitted close to the detection end could exit at larger angles, but most of the re-absorptions generally take place close to the origin of emission since consecutive re-emissions red-shift the light so that subsequent re-absorption becomes less likely. When comparing Zastrow's experiment with the one described in this section, one needs to bear in mind different LSC geometries (planar and rod-shaped) were examined in the two cases. Nevertheless, the central dip visible in the experimental data in Figure 5.8 agrees with the author's measurements, though it appears that Zastrow attributed that dip to a statistical fluctuation as he plotted a curve that ignored the dip.

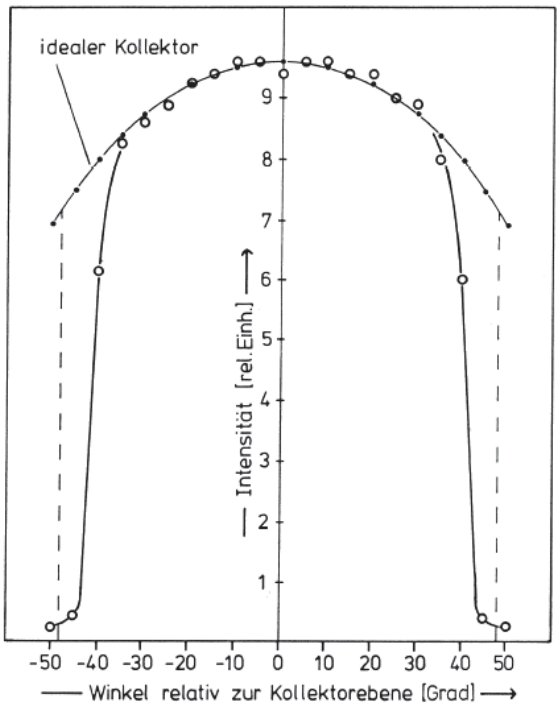

FIGURE 5.8: Angular emission profile of a homogeneous rod-shaped LSC measured by Ref. 182 using a method that eliminates the refraction of luminescence upon exit. One can identify the central dip in the experimental data points (circles).

Goldschmidt *et al.* [115] and Bending *et al.* [187] reproduced Zastrow's measurements

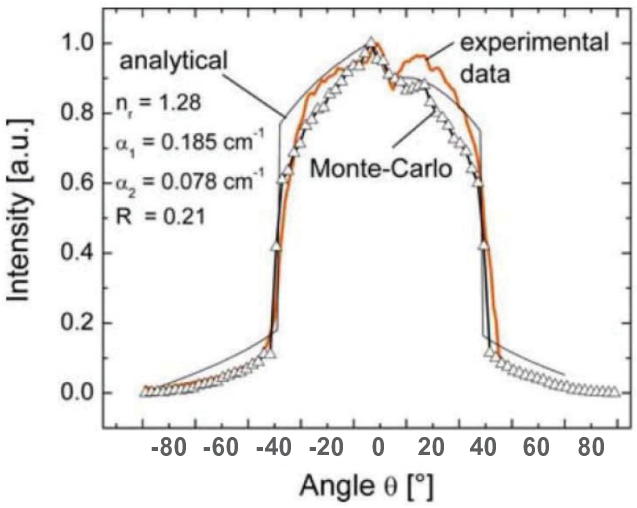

FIGURE 5.9: Angular emission profile of a homogeneous planar LSC measured and modelled by Ref. 115 using a method that eliminates the refraction of luminescence upon exit. The surface normal lies at 90°. The modelled results are in qualitative agreement with the experimental data, both showing the central dip in the profile, slightly shifted from the normal angle.

[182] on a homogeneous planar LSC (using an index matched semi-cylinder to eliminate refraction of the luminescence upon exit) with similar results, as shown in Figure 5.9. Their experimental results were complemented by raytrace simulations. The asymmetry of the profile and the slight shift of the central dip from the surface normal qualitatively agree with the profiles measured by the author.

5.4.3 Emission Profile of the Thin-Film LSC

Figure 5.10 shows the experimental and modelled profiles for the thin-film LSC. There is a strong dip around 0° and a pronounced asymmetry with a right hand side to left hand side integrated area ratio of 1.29 from the experiment and 1.17 from the model. The reason for the prominent minimum at the surface normal is that there are no luminescent centres in the bulk of the concentrator, i.e. the substrate. The majority of photons reaching the edge are guided by TIR and thus at an angle to the surface normal. The asymmetry in the profile can be attributed to the inherent asymmetry in the configuration and is well reproduced by the simulation.

As in the homogeneous case, there appears to be a slight shift in the dip between model and experiment due to alignment errors. The origin of the asymmetric profile is similar to the homogeneous case, but the effect is stronger since all emission centres are

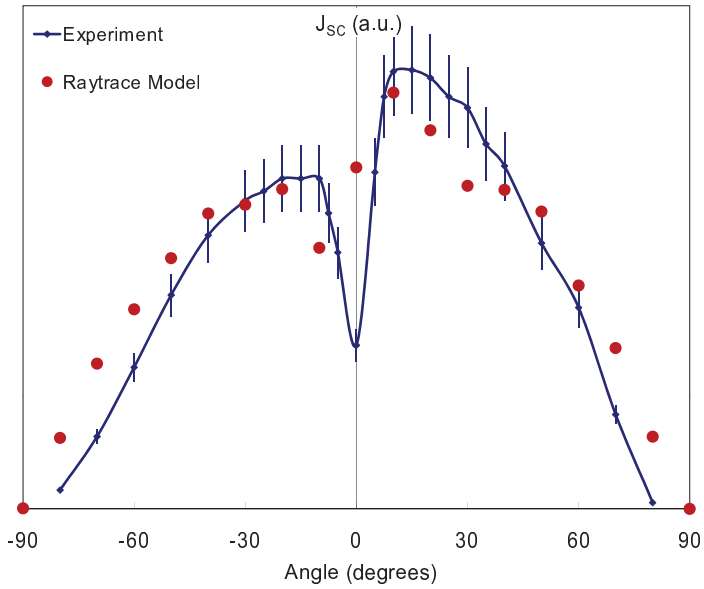

FIGURE 5.10: Normalised angular emission profile of the thin-film LSC, where 0° is normal to the edge surface and 90° is parallel to the incident light. The LSC was oriented with the film towards the light source. There is a pronounced asymmetry in the profile as well as a significant central dip.

concentrated on one surface. In particular, the higher peak at positive angles, away from the light source, is due to the fact that the film was placed towards the light source. As shown schematically in Figure 5.11, some of the luminescence from the film can directly exit the edge at positive angles, while it can only exit at negative angles after one or more reflections, which reduce the intensity, primarily due to emission out of escape cones. No angular emission profile of the TF LSC has been published by other researchers.

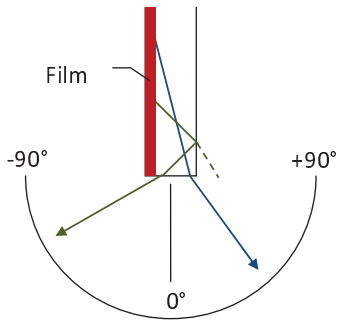

FIGURE 5.11: A schematic of the angular emission from the thin-film LSC. Emission at positive angles can exit directly, while emission at negative angles undergoes at least one reflection, which reduces the intensity.

5.5 Effect of Refractive Index Mismatch between Film and Substrate

It has been shown in this chapter, that a TF LSC with matching refractive indices of film and substrate produces the same photocurrent as an equivalent homogeneous LSC. This section examines whether a TF LSC with an index mismatch has any advantages over the homogeneous LSC. It is safe to assume that a film with higher refractive index than the substrate would be detrimental as it would lead to trapping within the film and amplify re-absorption losses. This study is therefore limited to cases where the refractive index of the film is between that of the substrate and air. Meyer *et al.* [162] also carried out similar simulations comparing the effect of varying refractive indices. The results presented in this section are in agreement with theirs.

Despite a higher refractive index of the substrate, there cannot be any light trapping by TIR within the substrate alone: all luminescence emitted within the film that enters the substrate, does so via refraction. Upon reflection from the bottom of the substrate, light will reach the substrate-film interface at the same angle to the surface normal at which it entered the substrate previously, and this angle must be smaller than the critical angle for TIR at the substrate-film interface, as illustrated in Figure 5.12. This means that the waveguiding efficiency cannot be improved by lowering the refractive index of the film. Nevertheless, a lower refractive index of the film would reduce the surface reflection for incident light from the top and therefore improve the light capture efficiency. At the same time, increased Fresnel reflection of luminescent light at the film-substrate interface due to the refractive index mismatch would trap more luminescence in the optically dense film and hence lead to waveguiding losses. To determine the net effect of these two competing processes, a typical LSC (based on the 50 cm×50 cm×3 mm LSC with a 74 µm film containing the Lumogen Red 300 dye as described in Section 5.3.2) was modelled with a refractive index of 1.5 for the glass substrate, while the index of the film was varied between 1.3 and 1.5.

The raytrace simulation in Figure 5.13 shows that the optical efficiency is maximised when the refractive indices of the film and substrate are perfectly matched. Even small deviations lead to substantial losses. The extent of the losses depends strongly on the self-absorption of the luminescent material. In the example presented here, a refractive

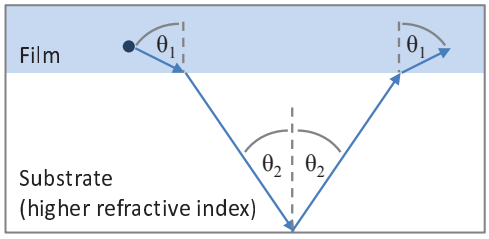

FIGURE 5.12: Schematic of refractive index mismatch between film and substrate. In this schematic, the substrate has a higher refractive index than the film, so that TIR could in principle occur at the substrate-film interface (within the substrate). However, since the luminescent centres are located in the film, all luminescence originates from there. Due to symmetry, no luminescent photons can reach the substrate-film interface (upon reflection from the bottom surface) at an angle larger than the critical angle. Therefore, a higher refractive index of the substrate cannot lead to better waveguiding of luminescence via TIR within the substrate.

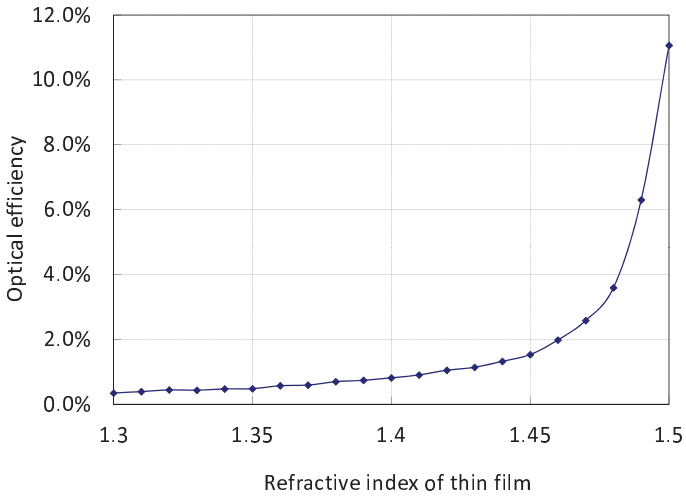

FIGURE 5.13: Raytrace simulations showing the optical efficiency of a thin-film LSC as a function of refractive index mismatch between the film and the substrate. The refractive index of the substrate was fixed at 1.5 while the index of the film was varied between 1.3 and 1.5. It is evident that the TF LSC performs best when the indices are matched.

index mismatch of 13 % (from 1.5 to 1.3) was found to lower the optical efficiency by 97 %. The results confirm that the waveguiding efficiency is the dominant factor in the optical efficiency and that matching the refractive indices of the thin film and the substrate is crucial. In conclusion, the optimal TF LSC has matching indices between film and substrate, as presumed in the previous sections of this chapter.

5.6 Chapter Conclusion

The thin-film configuration has been used by many LSC research groups to date. Yet throughout there appears to have been some disagreement regarding its capacity to reduce re-absorption losses. In a typical TF LSC the film and the substrate are index matched, so that the luminescence travels within the composite without refraction or reflection at the interface between the film and the substrate. While some have claimed that the enhanced light transport in the transparent substrate reduced re-absorption losses, others have argued that the optically dense film compensated for the gains, resulting in no net difference in re-absorption losses compared to a homogeneous LSC.

This chapter presented an experimental and modelling evaluation of two TF LSCs with different absorbances. Both were compared with homogeneous control samples with similar absorbance to their respective TF samples. The measured optical efficiencies for the two configurations agreed within errors, indicating that there is no difference in performance. A reproduction of the experiment with the Raytrace Model showed a good agreement with the measured results, but also a small, yet significant advantage in waveguiding efficiency in the homogeneous case due to fewer re-absorptions. However, this small advantage was attributed to edge effects since the performances of the two configurations were found to be identical at larger geometric gains. Several further simulations in which different parameters were varied confirmed the general validity of the conclusion that for all practical purposes thin-film and homogeneous LSCs have identical performances due to equal re-absorption losses. This means that the reduced re-absorptions in the substrate and the increased re-absorptions in the film are indeed in balance.

Angular emission profiles were also measured from both configurations, with an experimental approach which enabled the background to be subtracted. Both configurations showed an asymmetric profile with a dip near the centre. These features were more pronounced in the thin-film case. Comparison with the Raytrace Model led to the interpretation of these distinct features, attributing them to the nature of the absorption of light in the homogeneous LSC and to the asymmetry of the thin-film LSC. A good agreement between the experimental and the modelled emission profiles leads to the conclusion that the Raytrace Model could be used to infer details about the internal

processes of an LSC from its experimental emission profile, which could be useful for characterising directionally emitting luminescent layers.

A raytrace study of the effect of a refractive index mismatch between the film and the substrate of a TF LSC verified that the ideal TF configuration has matching indices, as presumed in the comparison of the performance of TF and homogeneous LSCs. In fact, it was found that the optical efficiency of the TF LSC is very sensitive to any index mismatch.

The demonstration that the optical efficiencies of the TF and homogeneous geometries are the same is important as it reduces the number of factors to be considered in deciding the appropriate geometry for a given application. The thin-film LSC offers advantages such as a wider choice of waveguide materials, simpler fabrication methods without polymerisation processes, the potential to facilitate fluorescence resonance energy transfer and suitability for building integrated PV. Therefore it is concluded that the thin-film configuration may be advantageous for many applications.

Chapter 6

The Light-Bar

6.1 Chapter Introduction

The light-bar is a linear, rod-like LSC for use as a secondary concentrator in a novel BIPV concept relevant to glass facades and smart, or energy generating windows [188]. This is a novel application for the LSC in that as a secondary it will only be concentrating direct sunlight.

Linear LSCs have been investigated before on several occasions. As mentioned in Section 2.3.6, McIntosh *et al.* [58] carried out theoretical studies on cylindrical LSCs, showing that a cylindrical LSC can outperform the square planar LSC in terms of optical efficiency by a factor of 1.0 to 1.9 when luminescence occurs close to the surface. These results are supported by a recent publication by Inman *et al.* [189], who carried out an experimental comparison demonstrating that hollow cylindrical LSCs have a higher absorption of incident radiation and less self-absorption than solid cylindrical or planar LSCs with comparable geometric gains. They used PMMA waveguides doped with near-infrared emitting lead sulfide quantum dots and measured homogeneity, optical properties, photo-stability and photocurrent of the samples. Batchelder *et al.* used a semi-infinite cylinder in order to develop a self-absorption formalism and a theoretical expression for the optical efficiency [20, 21]. Sulima *et al.* [190, 191] coupled scintillating fibres (with diameters of less than 1 mm and a length of 30.5 cm), essentially cylindrical LSCs, to miniature AlGaAs/GaAs PV cells via optical epoxy for the purpose of

recharging batteries in unattended ground sensors. The main motivation for this approach was that they needed to uniformly illuminate an array of PV cells connected in series in order to generate the desired voltages, and that the illumination via the fibres was less sensitive to orientation and partial shading than the direct illumination of the cells. Fara *et al.* [192] reported on the physical characterisation of a cylindrical LSC made of PMMA. Smith *et al.* [193–195] proposed and patented linear LSCs for indoor daylighting applications. Wang *et al.* [147] also investigated a daylighting application, consisting of many thin fibres of 3 different colours arranged in parallel.

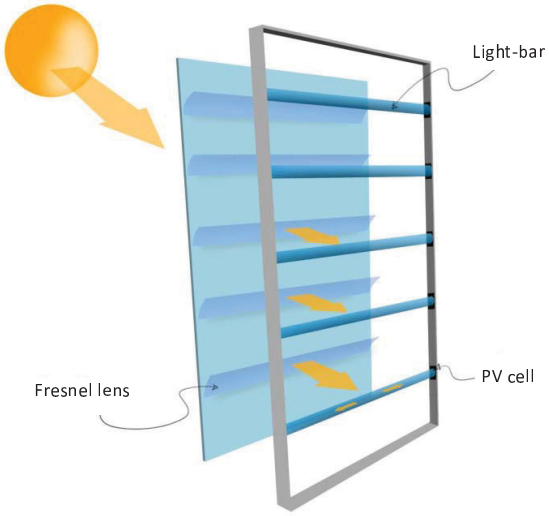

FIGURE 6.1: Illustration of a BIPV concept comprising light-bars in a Venetian blind-like system. The entire system is contained in the building facade. Fresnel lenses focus direct sunlight onto the light-bars, thereby eliminating the solar glare, while diffuse light can still contribute to indoor lighting and the view out of the window is preserved. PV cells at the ends of the light-bars generate electricity. This illustration was made by A. Alandry for a joint submission under the title Solar Blinds to the CleanTech Challenge 2010 hosted by the London Business School.

The use of planar LSCs as secondary concentrators has been proposed by Tsoi emphet al. [196, 197]. In this design, a microlens system is used to focus sunlight onto a patterned thin-film LSC, where the luminescent material is arranged in a microstructure on the LSC surface in order to reduce the coverage and thus re-absorptions. Using only an LSC with a microstructured thin-film surface, it was found that the edge emission output could be increased significantly (from 16 % to 26 %) by moving from a 100 % surface coverage to 20 % [196]. However, this efficiency increase came at a loss of absorption of incident light. The microlens system, made up of (poly)carbonate [197], is proposed to maximise the absorption of incident light.

The concept investigated in this chapter is different and unique in that it is the only one to use a linear LSC as a secondary concentrator. The light-bar has been patented by Mazzer *et al.* [198], and a spin-off company was founded by K. W. J. Barnham and M. Mazzer under the name SolarStructure Ltd. in order to commercialise this technology. The functioning principle is illustrated in Figure 6.1. An array of geometric concentrators in the form of linear Fresnel lenses focuses sunlight onto an array of light-bars which, in turn, guide the light to solar cells attached to the two ends of each bar. Of course, the Fresnel lenses only focus direct light, and they require solar tracking. Ideally, a so-called 1.5 axis tracking would be used, where, in addition to a rotation, the lens can move towards and away from the light-bar to better focus off axis rays, which have shorter focal lengths. The tracking could be incorporated in existing systems used to control Venetian blinds. In fact, the entire concept resembles a Venetian blind in that it eliminates unwanted solar glare whilst still preserving the view out of the window to some extent, but it generates electricity in addition. A window with a semi-transparent solar cell layer or patterned with solar cells would also generate electricity from sunlight, but it would absorb direct and diffuse light alike. Since Fresnel lenses only focus the direct light onto the light-bars, diffuse light would still be able to enter the building and contribute to indoor lighting. Though a Fresnel lens generally does not have the same optical quality as a normal lens, it is sufficient for this application and has the advantages that it is flat, light, uses less material and is cheaper. Realistic dimensions would be a system spanning a width of 50-100 cm, with each Fresnel lens being approximately 5-20 cm high. Primary concentration by a factor of 25 seems reasonable [199]. The light-bar can be a homogeneously doped structure or a composite structure comprising an active core and a transparent shell. The higher solar concentrations enabled by this two-stage system may permit high efficiency cells to be used on the light-bar ends without incurring a significant cost increase when collateral benefits such as reduced air-conditioning and interior lighting demand plus hot water from cell cooling are taken into account.

No study of light-bars as a secondary in a BIPV application as described here has been previously published by others. The research question of this chapter is what geometry of composite light bar is best suited as the secondary in a BIPV smart window. This study is based on modelling using the author's Raytrace Model and some measurements made by an ERASMUS student co-supervised by the author.

6.2 Composite Light-Bar

A design of particular interest is the composite light-bar consisting of a heavily doped luminescent core encased in an index matched transparent shell (see Figure 6.2). Though the literature review [58, 189] revealed, that a hollow cylinder should be superior to a doped core design under normal irradiation, this need not be the case when the incident light is focused. The proposed design is based on the assumption, that the primary concentrator would focus the light onto the doped core, while the transparent shell would allow for the luminescence to propagate with a reduced re-absorption probability. The shape of the core is relatively insignificant as long as its cross-section is small compared to the bar because no reflection or refraction takes place at the core-shell interface if there is good index matching. In this study a cylindrical shape was chosen for the core. In contrast to the homogeneous case, where light from the primary concentrator is incident over the entire width of the bar, the light incident on the composite needs to be focussed down to the width of the core. This imposes higher constraints on the tolerance of the lens and tracking system, which, in turn, could increase the system cost.

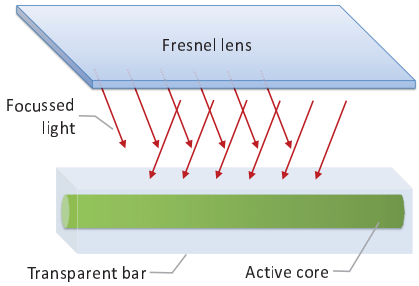

FIGURE 6.2: Schematic of a composite light-bar (linear LSC) as a secondary concentrator behind a Fresnel lens. Light is focussed onto the core of the light-bar where it is absorbed and emitted as luminescence. Solar cells would be placed on either end of the light-bar.

The motivation behind the composite structure is to reduce re-absorptions. Index matching allows the luminescence from the active core to travel unhindered in the entire composite, and by covering relatively large distances in the transparent shell the probability of re-absorption is reduced. This may seem contradictory to the conclusion drawn from Chapter 5, where the planar equivalent of the composite light-bar, the thin-film LSC was studied. It was shown that there is no net reduction of re-absorption losses in the thin-film LSC compared to the homogeneous variant, because trapped light has to pass through the optically dense active layer upon each reflection (unless it is collected at the

edge), thus defeating any gains from the path in the transparent medium. However, the composite light-bar behaves differently. Firstly, the primary concentrator is required to ensure that the incident light is directed entirely towards the active core, where there is a high probability of absorption. Secondly, the spatial distribution of the active material is reduced in two dimensions in the light-bar (and not just one), making it possible for luminescent light to traverse the length of the bar (via internal reflections) with fewer or even no intersections with the active region, thereby reducing re-absorptions.

The aim of this first study is to verify and quantify the reduction of losses in the composite light-bar compared to a homogeneous one of the same outer dimensions and hence the same geometric gain. The Raytrace Model was used to compare the homogeneous and composite light-bar configurations while varying key parameters. The outer dimensions were chosen to have a square cross-section. A 1 m long light-bar with a refractive index of 1.49 and a host absorption of $0.3\,\mathrm{m}^{-1}$ (attainable with high quality PMMA as mentioned in Section 3.2.1) was modelled. Index matching to cells on both ends was assumed, so that every ray reaching an end surface contributed to the optical efficiency. The thickness of the bar, the radius of the core and the absorption coefficient of the homogeneous bar were varied. The luminescent centre was based on the Fluorescent Yellow dye from Bayer (see Figure 6.3), which has a QY of 95 %. Though a luminescent centre with a large Stokes shift would enhance the performance, it should be noted that the advantage of the composite over the homogeneous bar is lost in the absence of re-absorptions.

Since the Fresnel lens would only focus direct light, the AM1.5 direct spectrum was input at normal angles over the diameter of the core in the composite case and over the width of the bar in the homogeneous case. In reality, the Fresnel lens would focus light onto the bar with a spread of incident angles. Two competing effects would be expected were the Fresnel lenses to be included in the modelling: firstly, the Fresnel reflection from the top surface would be greater due to contributions from larger angles, reducing the performance slightly; secondly, incident light, if focussed perfectly, would always travel through the centre of the bar, which means that the pathlength inside the core would be the maximal for all rays. This would lead to higher absorption and have a positive effect on the overall performance. The impact of the concentrated sunlight on the stability of the luminescent material was not explored.

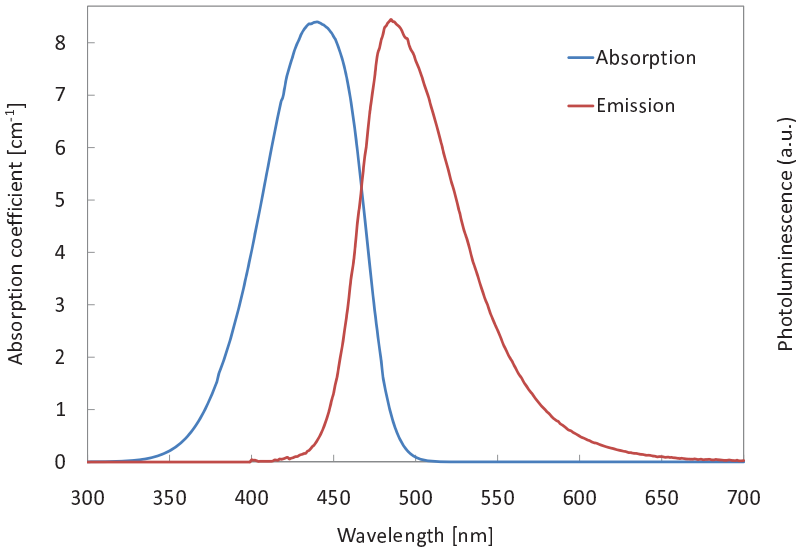

FIGURE 6.3: Absorption coefficient and photoluminescence spectra of the Fluorescent Yellow dye from Bayer with a quantum yield of 95 % used in the light-bar simulations.

Composite light-bars with two different core radii were modelled, 2 mm and 0.5 mm. The absorption coefficient shown in Figure 6.3 was used for the bar with the 2 mm core radius, while the absorption coefficient for the 0.5 mm core radius bar was chosen such that the absolute amount of dye in the active core was identical to the 2 mm case. For the homogeneous light-bar, three different absorption coefficients were considered: one identical to the composite core, one based on the same amount of dye as the composite and one producing the same absorptance at normal incidence. Realistically, a homogeneous bar would not be as highly doped as the relatively small core of the composite, so the first choice represents an upper bound for the absorption coefficient. The second choice is regarded as the lower bound. The third choice of absorption coefficient appears to be most appropriate one for comparison.

The results presented in Table 6.1 show that, when a comparable amount of incident light is absorbed (same A_λ), the composite light-bar has a higher optical efficiency than the homogeneous one. In all cases, the composite had a better waveguiding efficiency than the homogeneous light-bar. The optical efficiencies were found to be small in general, with less than $\sim 6\,\%$ of the incident light being coupled out of the two ends. This is partly due to the small absorbed fraction of the incident AM1.5 spectrum of $\sim 17\,\%$. The majority of the incident light is transmitted out of the bottom. Despite the large aspect ratio of the bar, the loss of luminescence out of the long sides was found

Thickness	Configuration	Details	$\eta_{\text{capture}}[\%]$	$\eta_{\text{waveguide}}[\%]$	$\eta_{\text{optical}}[\%]$
1 cm	Composite	$r_{\text{core}} = 0.5\,\text{mm}$	17.1	30.7	5.2
		$r_{\text{core}} = 2.0\,\text{mm}$	17.0	28.0	4.8
	Homogeneous	same A_λ	17.6	26.6	4.7
		same α	21.5	26.4	5.7
		same N_{dopants}	12.3	27.3	3.4
10 cm	Composite	$r_{\text{core}} = 2.0\,\text{mm}$	16.9	35.9	6.1
	Homogeneous	same A_λ	17.5	32.4	5.7

TABLE 6.1: Comparison of the light capture, waveguiding and optical efficiencies of homogeneous and composite light-bar configurations simulated with the Raytrace Model. The homogeneous bar was modelled with three different absorption coefficients, one that yields approximately the same absorptance of incident light (same A_λ) as in the composite case, one that is identical to that of the composite (same α) and one based on the same number of dopants distributed homogeneously (same N_{dopants}). The composite light-bar was found to perform better than the homogeneous one when the absorptance is comparable.

to be smaller than the emission out of the two ends in the best cases, which indicated efficient waveguiding. In fact, waveguiding efficiencies of up to 30 % were computed by the model. In the case of a 1 cm thick bar and a 2 mm core radius the advantage of the composite is insignificant, less than 2 % relative to the homogeneous bar. The composite has a relative advantage of 7 % when the bar is 10 cm thick and the core radius is 2 mm and an advantage of 12 % when the bar is 1 cm wide and the core radius is 0.5 mm. The latter appears to be a reasonable geometry for the light-bar, granted that the material is stiff enough to avoid bending through gravity.

It should be noted that the dye modelled in the previous comparison had a narrow absorption spectrum. In a practical device a collection of different dyes or other luminescent centres would be employed in order to absorb a broad spectrum. To take this into account, a further comparison was carried out using a hypothetical, opaque absorber (see Figure 6.4) with a constant absorption coefficient up to 700 nm with a Gaussian tail, an emission spectrum based on the generalised Planck's law [200] and a QY of 95 %. A high dopant concentration was chosen to produce near unity absorptance over a large spectral range. The high absorption coefficient displayed in Figure 6.4 was used for a composite bar with an active core of 0.5 mm radius. It should be noted that such a high absorption coefficient not only increases the absorption of incident light, but

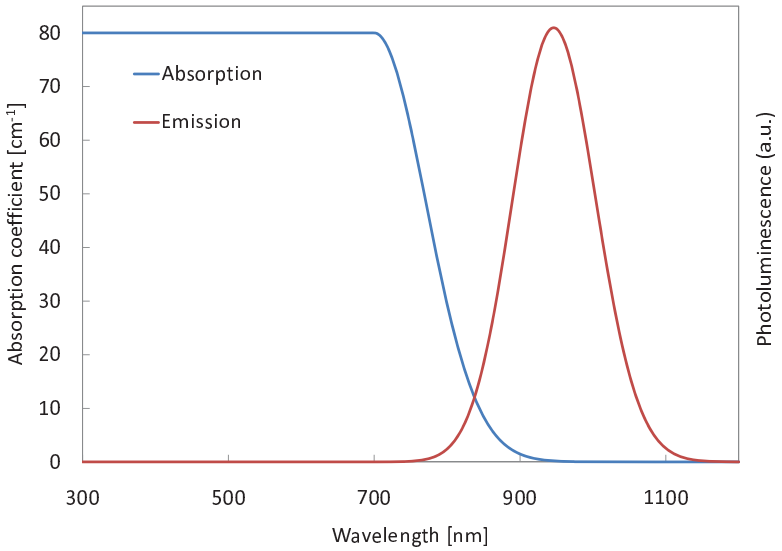

FIGURE 6.4: Spectra of a hypothetical, opaque luminescent centre with a QY of 95 %. A constant absorption coefficient with a Gaussian tail was modelled and the generalised Planck's law was applied to generate the emission spectrum.

also the self-absorption.

	$\eta_{\text{optical}}[\%]$	η_{capture} [%]	$\eta_{\text{waveguide}}$ [%]
Composite	23.5	72.5	32.4
Homogeneous	18.1	72.6	24.9

TABLE 6.2: Comparison between similar homogeneous and composite light-bars with broad absorption spectra. Both configurations had a bar thickness of 1 cm, and the composite had a core radius of 0.5 mm. Due to the choice of absorption coefficients, the capture efficiencies are comparable. The results show that the composite has a superior waveguiding efficiency, which leads to a higher optical efficiency.

The results in Table 6.2 show a better overall optical efficiency of the system in both cases, which is mainly due to the fact that the absorbed fraction of incident light, i.e. the capture efficiency, was increased to 72-73 %, an increase by a factor of more than four compared to the previous simulation. In the composite case, 32 % of the absorbed light is emitted out of the ends. As a result of a relatively large spectral overlap between the absorption and the emission of the modelled luminescent species, the number of re-absorptions in the homogeneous bar was found to be more than twice that of the composite. Consequently the composite offered a nearly 30 % higher waveguiding efficiency.

In conclusion, the advantage of the composite light-bar over a homogeneously doped one with respect to reduced re-absorption losses has been quantified using the Raytrace Model. The first set of simulations was based on realistic conditions and a bar length of 1 m. Out of the cases modelled, the most suitable one in terms of efficiency and practicality appeared to be a 1 cm thick bar with a 0.5 mm core radius. The most appropriate comparison is between a composite and a homogeneous bar of equal absorptance. In this case, the composite structure showed a relative advantage of 12 % in optical efficiency. Though adding mirrors may increase the overall efficiency of the light-bar, they are unlikely to increase the advantage of the composite over the homogeneous bar.

A second set of simulations was carried out, in which a higher absorbance and an idealised luminescent material was modelled. Due to a larger overlap between the emission spectrum and the absorptance this set yielded a 30 % advantage of the composite over the homogeneous light-bar. However, the composite structure may involve higher fabrication costs than the homogeneous as well as a more accurate tracking system to focus light onto the thin core. The results suggest that only at high dopant concentrations the anticipated higher cost associated with the composite is justified by a significant efficiency improvement. One should bear in mind that high dye concentrations are indeed needed for the lens/light-bar system to fulfil its objective of acting as a blind, i.e. blocking out direct sunlight.

6.3 Effect of Transparent Shell on Light Transport

The simulations carried out in Section 6.2 showed that a composite light-bar, consisting of a transparent shell around an active core, is more efficient than a homogeneous one. In this section the effect of the thickness of the transparent shell on the light-bar output is investigated in more detail using raytrace simulations. These simulations were preceded by experimental measurements on a homogeneous cylindrical light-bar, which was subsequently modelled as the core of the composite cuboidal light-bar.

Measurements on the homogeneous cylindrical light-bar shown in Figure 6.5 were carried out by C. Pardo-Sanchez, an ERASMUS student under the author's co-supervision. It consisted of PMMA doped homogeneously with the Fluorescent Yellow coumarin dye from Bayer (see Figure 6.3), had a length of 40 cm and a radius of 2 mm. As shown in

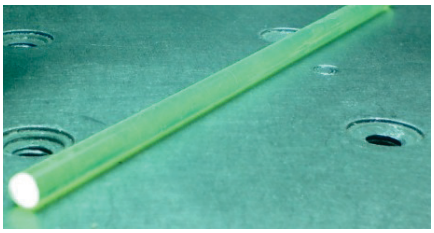

FIGURE 6.5: A picture of a homogeneous, cylindrical light-bar made of PMMA doped with a Fluorescent Yellow dye from Bayer. Such a cylinder could be the active core of a composite cuboidal light-bar.

Figure 6.3, the dye emits in the green with a luminescence quantum yield of 95 %. The absorption coefficient at the peak was $\sim 8\,\mathrm{cm}^{-1}$, as measured by inserting a small piece of the rod into the UV/Vis spectrometer. A PMMA background absorption of $2\,\mathrm{m}^{-1}$ was estimated. Since the dye has a relatively small Stokes shift and a narrow absorption band, this concentrator is not optimised for a high yield under a broad spectrum.

In order to investigate the waveguiding properties of the bar, a distance dependent optical response measurement was carried out. Figure 6.6 shows the setup, in which a blue (404 nm) laser was used to illuminate spots along the length of the cylinder while the photocurrent out of one end was measured with the silicon photodetector described in Section 3.4.2.

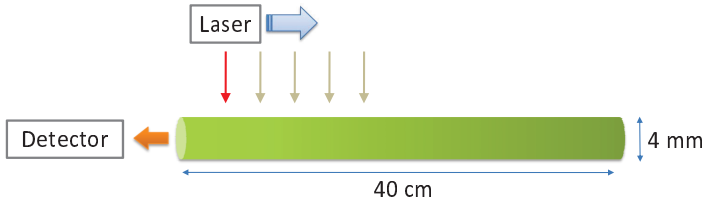

FIGURE 6.6: The experimental setup for a distance dependent response measurement of a cylindrical light-bar. The light-bar is illuminated with a laser spot (404 nm), which is moved along the length of the bar, while the emission out of one end is recorded with a photodetector.

The experimental results shown in Figure 6.7 are consistent with the raytrace simulations. Minor discrepancies at small distances are attributed to a greater effect of errors in the experimental measurement when the illumination spot is close to the photodetector. Figure 6.7 shows a steep decline of the LSC output with the distance of the illumination spot. This is due to multiple re-absorption losses resulting from the small Stokes shift and means that the cylinder has a poor optical efficiency as only light incident close to the end contributes significantly to the photocurrent.

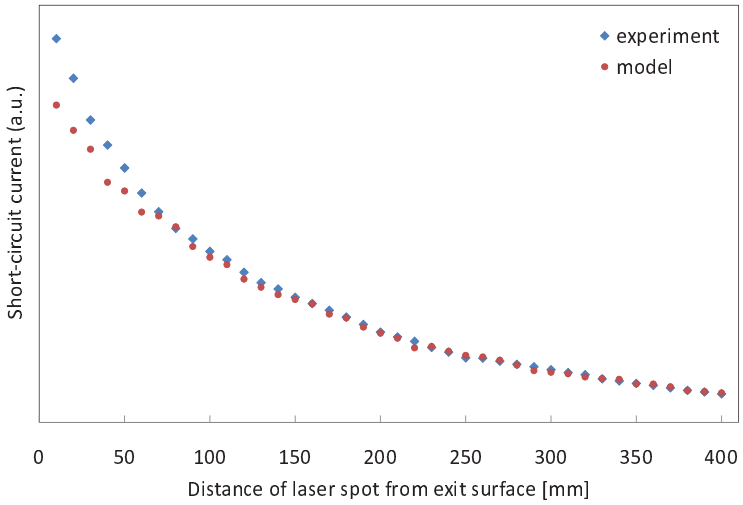

FIGURE 6.7: Experimental and modelling results showing the distance dependent response of the cylindrical light-bar. There is a good overall agreement between the experiment and the Raytrace Model. As expected, the short-circuit current decreases with distance due to a small Stokes shift. The response is shown in arbitrary units because the experimental and modelling results were normalised. The photodetector used in the experiment only collected part of the emission from the end while the raytrace model took the entire emission into account.

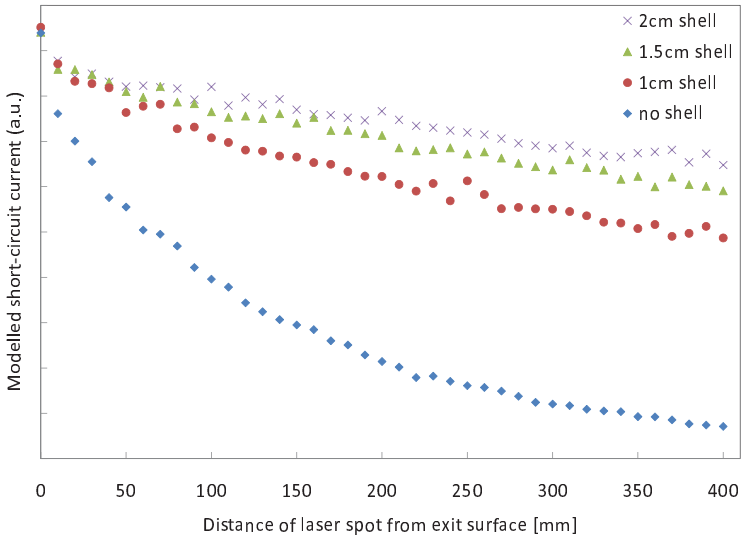

FIGURE 6.8: Distance dependent response for a composite cuboidal light-bar with different shell thicknesses, based on raytrace simulations. The modelled core radius was 2 mm and cross-sections of the composites were $1\times1\,\mathrm{cm}^2$, $1.5\times1.5\,\mathrm{cm}^2$ and $2\times2\,\mathrm{cm}^2$. It can be seen that a larger shell size makes the output of the light-bar less sensitive to the illumination position.

The Raytrace Model was subsequently applied to simulate transparent shells of square cross-section and varying thickness around an active cylindrical core. The effect on the light transport was evaluated by again plotting distance dependent optical response shown in Figure 6.8. The parameters of the modelled core were identical to the experimental values, and a constant background absorption coefficient of $0.3\,\mathrm{m}^{-1}$ was used for the transparent shell. Laser illumination at 404 nm was simulated. As expected from the initial investigation of the composite light-bar (see Section 6.2) and the fact that the additional shell increases the cross-section of the light-bar, the presence of the transparent shell was found to improve the light transport within the LSC so that even luminescence originating from the far end of the bar is guided to the detection end relatively efficiently. Re-absorptions are reduced as the light travels in the undoped part of the composite. The results show the increase in output with shell thickness: the longer the optical path in the shell (i.e. the thicker the shell and the smaller its background absorption coefficient), the flatter the curve in Figure 6.8.

		Bar thickness			
	Core alone	5 mm	10 mm	15 mm	20 mm
G	63.7	32.0	8.0	3.6	2.0
η_{capture}	76 %	72 %	72 %	71 %	70 %
$\eta_{\mathrm{waveguide}}$	21 %	25 %	32 %	35 %	37 %
η_{optical}	16 %	18 %	23 %	25 %	26 %
C	10.3	5.7	1.8	0.9	0.5

TABLE 6.3: The geometric gain, optical efficiency and concentration of cuboidal composite light-bars of varying thickness with a core radius of 2 mm and a length of 40 cm. Under the assumption of focussed illumination by a linear Fresnel lens, the illumination area was taken as the product of length and core diameter. The cell area was taken as twice the cross-section under the assumption of cells on either end of the bar. The modelled light source was a laser with a wavelength of 404 nm. The optical efficiency increases with increasing bar thickness, but the concentration factor is found to decrease because the reduction in the geometric gain dominates.

However, it is clear that a larger cross-section requires a larger PV cell area, which in turn leads to a loss in geometric gain. The effect of the shell on the geometric gain G, the waveguiding efficiency, optical efficiency and the optical concentration C was calculated for a constant core diameter, but a range of overall bar thicknesses. The results are shown in Table 6.3. As expected, the optical efficiency increases with increasing shell thickness, while the gain decreases. The resulting optical concentrations were found to decrease as well with increasing thickness since the rate of decrease of G is evidently faster

than the rate of increase of η_{optical}. The results indicate good waveguiding efficiencies in the presence of the transparent shell. The ideal dimensions would strike a balance between achieving a high optical concentration and maintaining a system efficiency that generates a reasonable amount of power. It should be noted that the optical efficiency was calculated relative to the monochromatic incident spectrum originating from the 404 nm laser (as opposed to the broad solar spectrum), such that $\sim$72 % of the incident light could be absorbed by the light-bar. Under AM1.5 direct irradiation a significantly smaller fraction (approximately 11 %) would be absorbed.

6.4 Light-Bar Outer Shell Geometries

Aside from the cuboidal light-bar described in the previous sections, one can conceive other geometries. In this section, three geometries are compared via modelling: the cuboid, the cylinder and the equilateral triangular prism. As with the conventional, planar LSC, the geometry affects both the capture and the waveguiding of light. In terms of light capture, the cylindrical geometry is ideal as the focussed light from the primary concentrator will in many cases, when the sunlight is in the plane perpendicular to the cylinder axis, be incident normal to the surface and therefore undergo minimal Fresnel reflection and no defocussing from refraction. However, since variations in the capture efficiency are generally less significant than those in the waveguiding efficiency, the waveguiding efficiency alone is considered in this section.

The primary focus of this section is on the escape cones and escaping fractions. Therefore the comparison of different geometries is carried out in the absence of re-absorption. Although this is an unrealistic condition, it allows for the isolated analysis of the escape cones. The escape cones for emission from an infinitesimally thin central core is easily calculated analytically. In the case of a core of finite thickness the calculations are less straightforward. Moreover, the escaping fraction on the first encounter of luminescence with the surface can be different to the escape on subsequent encounters. The Raytrace Model was used to determine the escaping fractions for different numbers of interface encounters (or iterations) in the absence of re-absorption. Instead of initial absorption by luminescent centres and subsequent emission, only the emission of photons randomly distributed across the active region was modelled. While the solid angle of escape Ω_{escape} always decreases with increasing refractive index n of the LSC, it should be noted that

the rate of change depends on the geometry. For example, in the case of the cuboidal light-bar it is

$$\Omega_{\text{escape,cuboid}} = 8\pi \left(1 - \sqrt{1 - \frac{1}{n^2}}\right) \tag{6.1}$$

where the critical angle for TIR is assumed to be smaller than $45\,^{\circ}$. In contrast, the solid angle of escape for the cylinder (with the emission originating from an infinitesimally narrow central core) is inversely proportional to n:

$$\Omega_{\text{escape,cylinder}} = \frac{4\pi}{n}\,. \tag{6.2}$$

However, since in practice there is limited freedom in the refractive index of LSC waveguides, this study was carried out using a constant refractive index of 1.49. Large geometric gains (1 m length and $\sim 1\,\text{cm}^2$ cross-section) were chosen for the simulations to render edge effects negligible. The radius of the active cylinder within the light-bar was varied from near zero to the largest radius that could be accommodated by the geometry (see Figure 6.9).

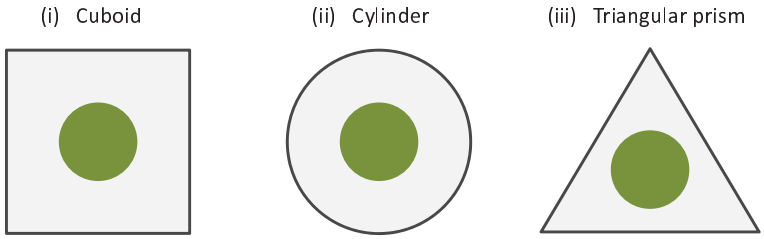

FIGURE 6.9: Schematic of the cross-sections of three light-bar geometries: (i) the cuboid, (ii) the cylinder and (iii) the triangular prism. The radius of the active core was varied in the raytrace simulations.

The simulation results are shown separately for each geometry in Figure 6.10. In the case of the cuboid, it is evident that on the first interface encounter the escaping fraction depends on the core radius and hence on the position of emission: emission close to the surface is less likely to escape than emission from the centre. With two or more iterations, i.e. at least one reflection, the escaping fraction becomes independent of the position of emission from within the cuboid. The cuboid has escape cones out of four sides. Due to the right angles between adjacent surfaces, any ray within any of the four escape cones will get a chance to escape after one reflection at the most. Fresnel reflection can also trap luminescence, but as this effect gradually diminishes with an

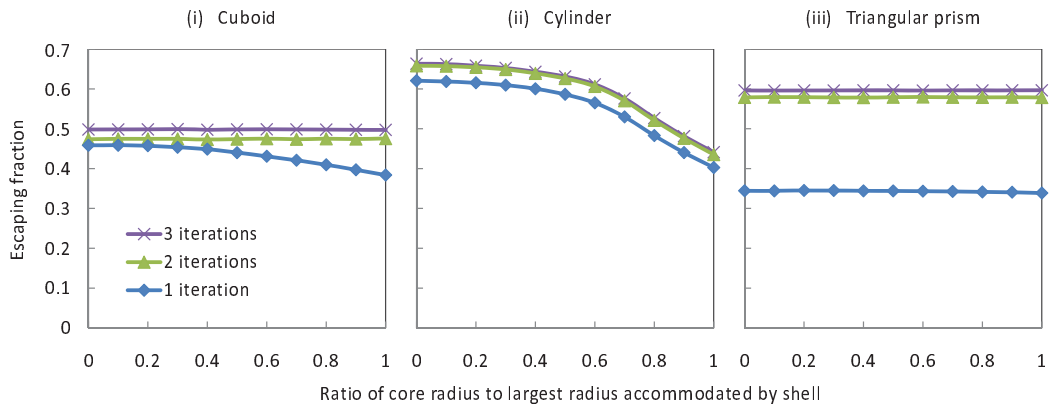

FIGURE 6.10: Escaping fractions after one, two and three interface encounters (iterations) as a function of core radius, modelled for the three light-bar geometries. Both TIR and Fresnel reflection are taken into account. With an increasing number of iterations the trapping due to Fresnel reflection diminishes.

increasing number of iterations, the escaping fraction approaches the analytical value in the absence of Fresnel reflection (see Equation 6.1), which is approximately 0.509.

Due to the radial symmetry of the cylinder, the shape of the curve remains constant with increasing number of iterations. The only effect of increasing iterations is that the case of no Fresnel reflection is approached. The strong dependence on the core radius and hence on the position of emission is apparent in the cylindrical geometry. With 3 iterations the escaping fraction for emission from an infinitesimally narrow core (ratio of radii of zero) approaches the analytical value (see Equation 6.2) of approximately 0.667 to an accuracy of 0.5 %.

The escaping fraction for the triangular prism is virtually independent of the position of emission for all iterations. With more than one iteration the escaping fraction almost doubles. This makes the triangular prism less competitive than the cuboid, assuming that more than 1 reflection is required before collection of luminescence.

A direct comparison of the escaping fraction after three iterations is shown in Figure 6.11. For the cuboid and the triangular prism, the escaping fraction is independent of the core radius. The cuboid has the smallest escaping fraction at most core radii. The triangular prism is found to be the least favourable geometry and is therefore disregarded in subsequent investigations. In agreement with Ref. 58 the cylindrical bar is found to have less light escape than the cuboidal one when the core radius is large and emission occurs close to the surface. However, it must be noted that this comparison

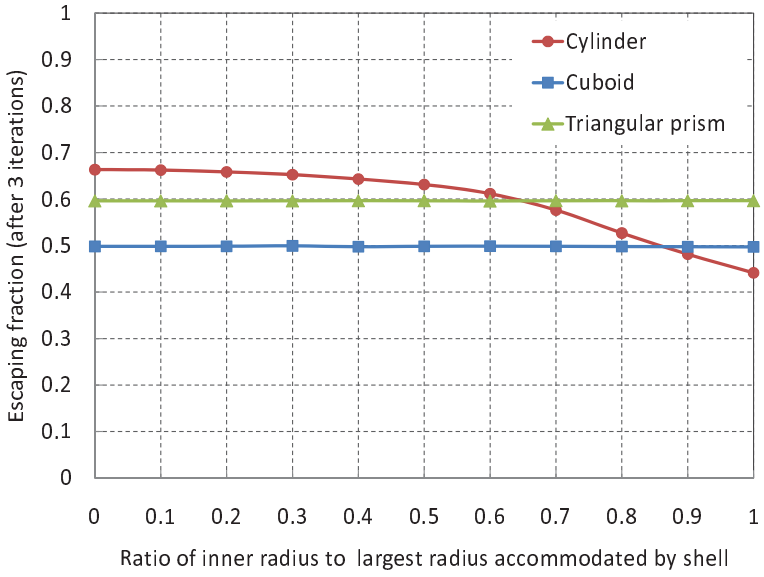

FIGURE 6.11: Comparison of the escaping fraction as a function of core radius after 3 iterations. In the case of the cuboid and the triangular prism the escaping fraction is independent of the core radius. When the core radius is large the cylindrical geometry yields the smallest escaping fraction.

only examined the escape of light and did not take re-absorptions into account. The results in Figure 6.11 show that in the absence of re-absorptions a homogeneous cylinder or one with a large active core (core-to-shell ratio above 0.9) traps more light than any cuboidal light-bar, composite or homogeneous. However, the outcome of Section 6.2 was that for a square cross-section in the presence of re-absorptions, the composite design is advantageous since part of the luminescence can be waveguided without intersecting the active region. Therefore, a composite cylindrical light-bar appears to be of interest.

6.5 Composite Cylindrical Light-Bar

As a result of the findings of the previous section, a further study was carried out on the composite cylindrical light-bar. Since emission close to the surface was found to lead to less escape, an inverted composite design was considered, comprising an active shell and a transparent core. First, raytrace simulations comparing the original and the inverted composite cylindrical structure as a function of core radius were carried out in a similar fashion as in Section 6.4, in the absence of re-absorption and only modelling the emission originating from the active region (randomly distributed). Two separate

cases were taken into account: the case without Fresnel reflection at the interface to air and the case with Fresnel reflection only upon the first encounter (or iteration). With multiple encounters the limiting case of no Fresnel reflection would be approached. The results are shown in Figure 6.12. It is not surprising that the largest loss occurs in the case of an infinitesimally thin active core, because in such a case, all of the emitted light intersects the (2-dimensional) circular cross-section at a normal angle, such that TIR can only be achieved through a sufficiently shallow angle of incidence along the long axis of the bar. It can be seen that the escaping fraction reduces as the ratio of inner radius to outer radius is increased. The main outcome of this investigation is that the inverted structure with the doped shell has the smaller escaping fraction than the active core structure. Moreover, the escape is minimised as the shell thickness is minimised. As required, the escaping fraction of the doped shell and the doped core approach the same value in the limiting case of a homogeneously doped cylinder.

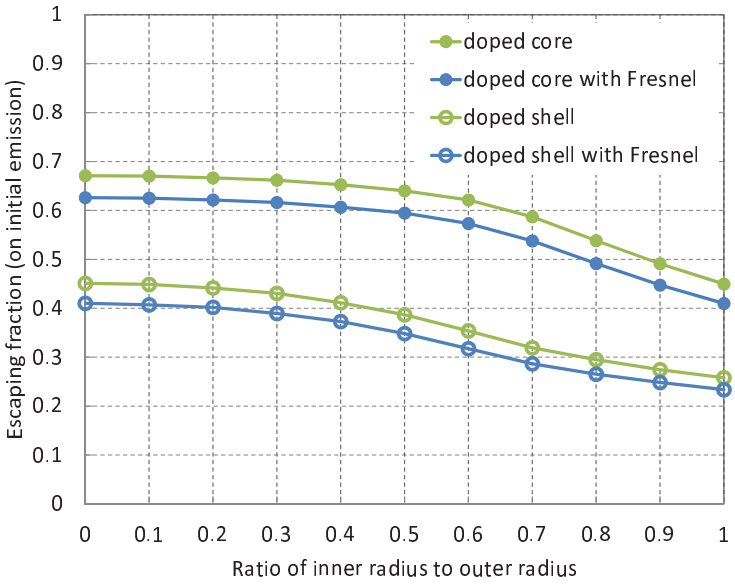

FIGURE 6.12: The escaping fraction of a composite cylindrical light-bar with an active core compared to one with an active shell. The simulations were carried out with and without Fresnel reflection at the interface to air (only upon first encounter). As expected, in the limiting case of a homogeneously doped cylinder (i.e. when the ratio of radii is 0 in the doped shell case and 1 in the doped core case) the escaping fractions of the doped shell and the doped core are identical.

Since this comparison of escaping fractions took neither the absorption of incident light nor the re-absorption of luminescence into account, a complete raytrace simulation including absorption and re-absorption effects was carried out subsequently, to fully evaluate the benefit of the cylindrical design. The simulation was based on a light-bar

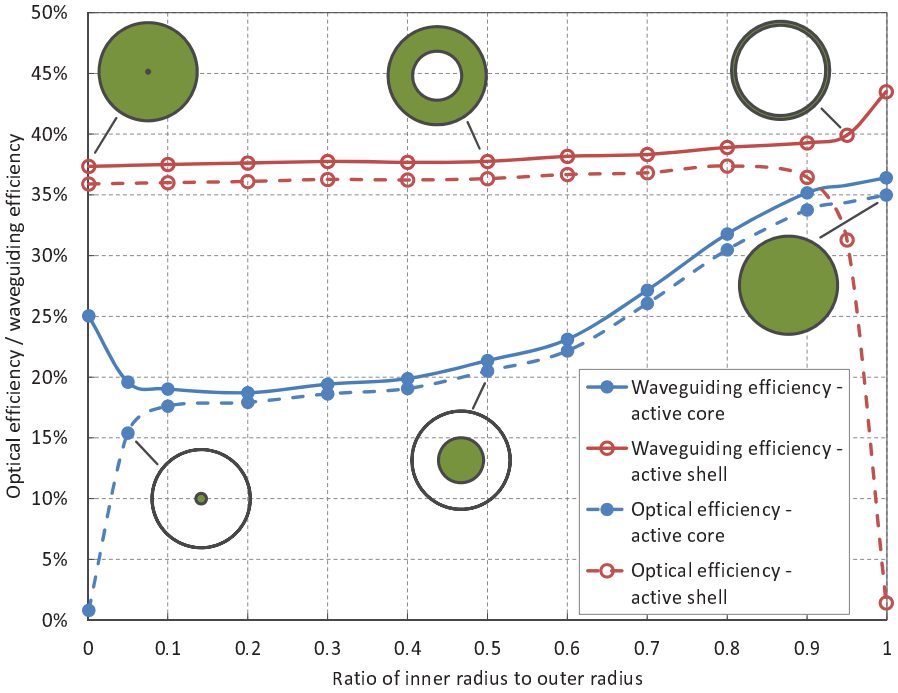

FIGURE 6.13: The optical efficiency and waveguiding efficiency of a composite cylindrical light-bar with an active core compared to one with an active shell, at constant absorption coefficient in both cases. The active shell structure converges towards the case of a homogeneously doped cylinder as the ratio of inner radius to outer radius goes to zero, and the active core structure converges to the same case as the ratio goes to 1.

doped with the Fluorescent Yellow dye introduced in Section 6.2 with a QY of 95 % (see Figure 6.3 for spectral characteristics) and a monochromatic light source at 440 nm at normal incidence along the axis of the bar. A length of 1 m, an outer radius of 1 cm and a background absorption coefficient of $0.3\,\mathrm{m}^{-1}$ were modelled. The radius of the core (the inner radius) was varied from close to zero to close to 1 cm, using 100,000 rays for each simulation. Two simulations were carried out: in the first, a constant absorption coefficient was used, twice as high as the one in Figure 6.3 in order to yield stronger absorption even in the case of thin active regions; in the second, the absorption coefficient was scaled with the thickness of the active region, such that the same amount of incident light ($\sim 79\,\%$) was absorbed in all cases. The resulting optical efficiencies and waveguiding efficiencies are shown in Figure 6.13 (constant absorption coefficient) and Figure 6.14 (scaled absorption coefficient).

In Figure 6.13 the optical efficiency nearly matches the waveguiding efficiency in most cases due to a high capture efficiency of $\sim 96\,\%$. In fact, due to the high absorption coefficient, virtually all of the light that enters the light bar (i.e. light that is not

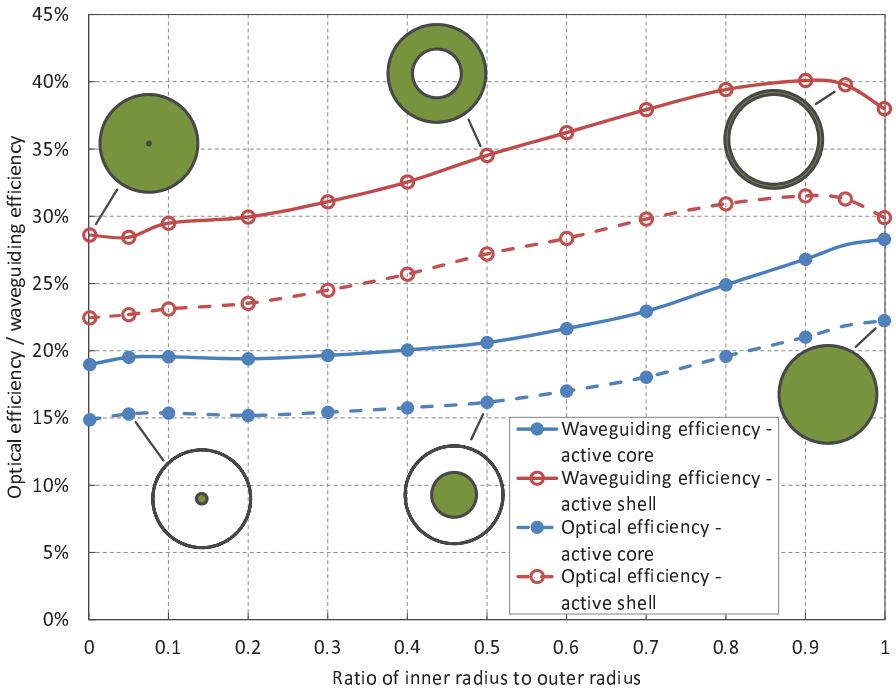

FIGURE 6.14: The optical efficiency and waveguiding efficiency of a composite cylindrical light-bar with an active core compared to one with an active shell, in both cases with an adapted absorption coefficient. The absorption coefficient is adapted such that the same amount of incident light ($\sim 79\,\%$) is absorbed in all cases. The absorption coefficient resembles the one from Figure 6.13 when the overall path through the active region is 1 mm, i.e. at a ratio of 0.05 in the active core case and a ratio of 0.95 in the active shell case. Consequently, at these points the optical and waveguiding efficiencies are identical to those shown in Figure 6.13.

reflected at the outer surface) is absorbed after passing through only ~ 4 mm of active material. When the thickness of active material is below this value, the optical efficiency drops off, as expected. The curves of the optical and waveguiding efficiencies for the active core structure slightly resemble the inverse of the corresponding escape curve shown in Figure 6.12. The active shell structure shows a slight increase in efficiencies with reducing shell thickness, but in general appears relatively insensitive to the shell thickness. This is due to the fact that almost all of the incident light is absorbed over the first few millimetres. Any further active material only leads to unwanted re-absorption. The noticeable increase in waveguiding efficiency for both structures when the optical efficiency goes towards zero may be explained by reduced re-absorption losses. Most importantly, the figure shows that the active shell structure has consistently higher efficiencies. The efficiencies of the two structures match each other only in the limiting case of a homogeneously doped cylinder (i.e. when the ratio of radii is one for the active core structure and zero for the active shell structure).

Arguably, Figure 6.14 shows a fairer comparison. In this case there is a larger discrepancy between the optical efficiency and the waveguiding efficiency due to a lower capture efficiency of $\sim 79\,\%$. Contrary to the previous simulation, the capture efficiency remains constant throughout due to a scaled absorption coefficient. The two main outcomes from these simulations are that a large ratio of inner to outer radius is favourable and that substantially higher waveguiding and optical efficiencies can be achieved with an active shell structure (more than $10\,\%$ higher waveguiding efficiency in this example). Both structures show a dip in efficiencies as the thickness of active material goes towards zero, which may be explained by increased re-absorption losses due to very high optical densities.

In summary, this section has shown that a cylindrical design with an active shell and a transparent core has higher optical and waveguiding efficiencies than one with a central active core and a transparent shell. Moreover, a relatively thin, heavily doped shell is preferential over a thicker one. While the work presented in this chapter is not fully comparable with the linear LSC work reported in the literature due to the assumption of using the light-bar as a secondary concentrator, the results presented here are in line with the ones reported by McIntosh *et al.* [58] and by Inman *et al.* [189], in that an active shell with a transparent core is found to be the more efficient design.

6.6 Square versus Circular Cross-Section

The ideal cylindrical design was found to be a composite light-bar with a thin active shell and a transparent core. In this section, such a cylindrical light-bar is compared against the ideal cuboidal light-bar, which comprises an active core inside a transparent shell as shown in Figure 6.15.

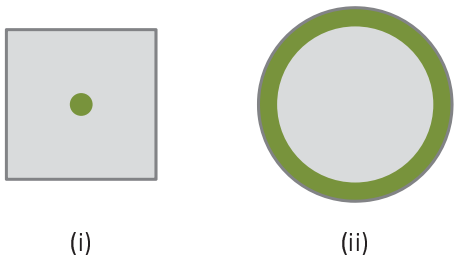

FIGURE 6.15: Comparison of a light-bar with a square cross-section and an active core (i) against one with a circular cross-section and an active shell (ii).

For this comparison, the cylindrical shell structure from Figure 6.14 with the highest waveguiding efficiency was chosen: one with an inner radius of 9 mm (i.e. a ratio of 0.9), an absorption coefficient of $\sim 8\,\mathrm{cm}^{-1}$ and a corresponding capture efficiency of $\sim 79\,\%$ under monochromatic illumination at 440 nm. The waveguiding efficiency of this structure was $\sim 40\,\%$. A cuboidal light-bar, one with a square cross-section and cylindrical active core, was modelled using the same method and input parameters as in Section 6.5. Different core diameters were modelled while adjusting the absorption coefficient to maintain a constant capture efficiency of $\sim 79\,\%$ for a fair comparison. Two alternatives were considered for the area of the square cross-section. One could argue, that a fair comparison requires identical cross-sectional areas between the cuboidal light-bar and the cylindrical shell. However, since standard solar cells are square, one could also argue, that the thickness of the cuboidal light-bar should match the diameter of the cylindrical one. The latter would make the cross-sectional area of the cuboidal bar slightly larger, giving it a slight advantage. Both alternatives were modelled.

Cross-section	Area [cm^2]	Core radius [mm]	$\eta_{\mathrm{waveguide}}$ [%]
Circular	3.14	9.0	40
Square	3.14	1.0	32
	3.14	0.5	33
	3.14	0.1	35
	4.00	0.1	35

TABLE 6.4: Waveguiding efficiencies of 1 m long light-bars with square and with circular cross-sections. The bar with the circular cross-section consists of an active shell with a transparent core. In the square case, the shell is transparent and the core is doped. Two different square cross-sections are considered: one with the same cross-sectional area as circular structure and one with a thickness identical to the diameter of the circular structure. The results show that the cylindrical light-bar with an active shell performs better than the cuboidal one.

The results in Table 6.4 show that in all simulated cases the cylindrical shell structure outperforms the cuboidal light-bar, even when unrealistically small active core radii of 0.1 mm are chosen for the cuboidal structure. The waveguiding efficiency of the cuboidal bar improves as the core radius is reduced, but a core radius much below 1 mm seems impractical since it would pose large constraints on the accuracy of the Fresnel lens. In fact, under the assumption of a primary concentration factor of 25 from a 5 cm high Fresnel lens, only the case with the 1 mm core would be realistic. As a result of the

comparison, the cylindrical structure with an active shell is found to be the favourable light-bar design.

6.7 Expected Power Output from a Light-Bar System

The conclusion of the analytic and raytrace studies of different light-bar geometries earlier in this chapter is that the composite light-bar with a circular cross section and doped shell offers the best optical efficiency in the presence of significant overlap between absorption and emission. In this section, the overall efficiency of a system with such a light-bar as secondary concentrator is estimated.

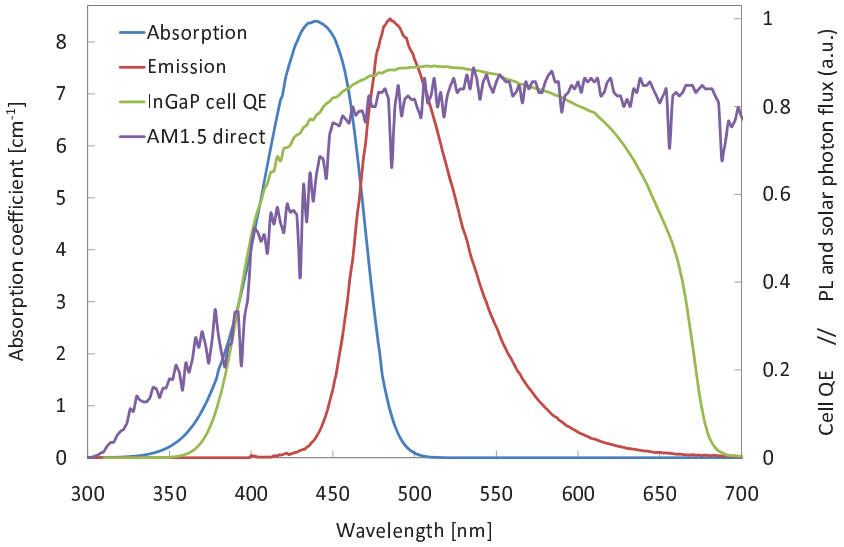

FIGURE 6.16: Absorption and emission spectra of a light-bar doped with Fluorescent Yellow dyes (with a QY of 95 %) in relation to the quantum efficiency of an InGaP cell and the AM1.5 direct solar spectrum.

For this estimation, a cylindrical light-bar of 1 m length, 2 cm diameter and a 1 mm thick active shell doped with the Fluorescent Yellow dye was modelled, as in the previous section. A primary concentration from a Fresnel lens by a factor of 20 was assumed, which is considered realistic [199]. Such a concentration would be achieved by a 40 cm high lens (with a width of 1 m, like the light-bar) focussing the sunlight onto the 2 cm thick light-bar. To account for losses from the Fresnel lens, a primary concentrator efficiency of 90 % was assumed [199]. The AM1.5 direct spectrum was used as the incident spectrum since the Fresnel lens focusses only direct light. Under the premise that the overall optical concentration factor of the system of over 15 might justify the use

of relatively expensive solar cells, InGaP cells (the same as in Section 4.7) were modelled on either end of the light-bar. The cell quantum efficiency is shown in comparison with the dye spectra and the AM1.5 direct spectrum in Figure 6.16. Using the superposition approximation (see Section 2.2.2), the power generated by the InGaP cells was calculated based on the short-circuit current and the dark current, as shown in Figure 6.17.

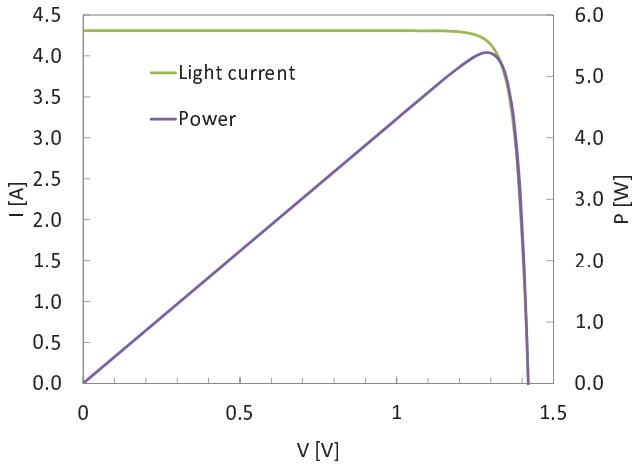

FIGURE 6.17: Calculation of the power generated by a modelled cylindrical light-bar system comprising a Fresnel lens focussing AM1.5 direct sunlight onto a light-bar of 1 m length, 2 cm diameter and a 1 mm thick active shell doped with Fluorescent Yellow dyes. The emission from the light-bar is coupled to InGaP cells on both ends. The superposition approximation was applied to obtain the light current from the short-circuit current and the dark current of the cell. The value at the maximum power point is 5.4 W.

The simulations yield a power of 5.4 W. Since the nominal power incident on the 1.0 m×0.4 m Fresnel lens is 400 W, the power conversion efficiency of this system is $\sim 1.3\,\%$. Given that the dye used in this study only absorbs $\sim 13\,\%$ of the AM1.5 direct spectrum, a more suitable light-bar would contain several different dyes or other luminescent materials such as quantum dots in order to absorb a broader spectrum. In order to estimate the yield from such materials, a simulation was carried out based a system with GaAs cells attached to the ends and an optimised absorption spectrum, as shown in Figure 6.18. The modelled PV cell was an epitaxial lift-off GaAs cell from Microlink. The QE and dark current data for the cell were provided by M. González from the Naval Research Laboratory.

With the optimised parameters, the model predicted a power of 23.4 W from a 1 m long cylindrical light-bar with a 2 mm radius in conjunction with a 1.0 m×0.4 m Fresnel lens.

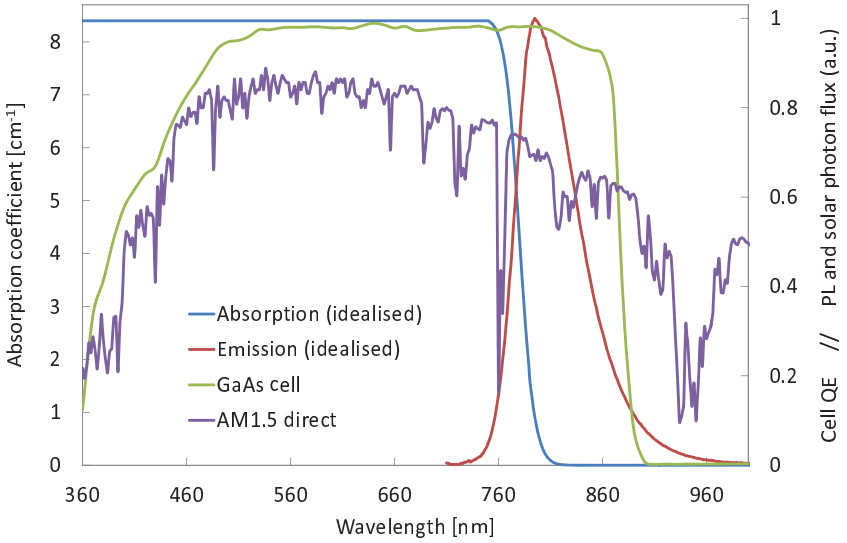

FIGURE 6.18: Optimised absorption and emission spectra of a light-bar matched to GaAs PV cells. The Fluorescent Yellow spectra were shifted to towards the red by 310 nm to obtain a better match with GaAs. A constant, high absorption level was modelled at the shorter wavelengths to improve the light capture. The QY of 95 % was maintained. The GaAs cell QE, provided by M. González from the Naval Research Laboratory, and the AM1.5 direct solar spectrum are also shown.

This translated into a system efficiency of ∼5.9 % and an optical concentration from the light-bar alone of almost 20.

The optical efficiency of the cylindrical light-bar may be further increased by surrounding part of the bar with a mirror (possibly with an air-gap) to trap even more luminescence, but this design was not investigated in this thesis. Finally, one could boost the power generation of the lens/light-bar system by combining it with the transparent window described in Section 4.7, which is transparent to most of the visible light. Since the lens/light-bar system only harnesses the direct sunlight, this combined BIPV device [201] would still facilitate indoor lighting.

6.8 Chapter Conclusion

A linear LSC that makes up the secondary concentrator in a two-stage concentrator proposed for building integrated photovoltaics relating to windows and glass facades has been studied experimentally and theoretically in this chapter. In this application, which has some similarity to a Venetian blind, linear Fresnel lenses with solar tracking are used to focus direct sunlight onto an array of light-bars, which in turn transfer the

radiant energy to solar cells. The system generates electricity whilst removing solar glare, allowing diffuse indoor daylighting and preserving the view out of the window.

This chapter investigated the design choices concerning the light-bar. The focus of the first section was the composite light-bar consisting of an active cylindrical core in a transparent, cuboidal outer bar. This study is of particular interest due to the similarity of the composite light-bar to the planar thin-film LSC discussed in Chapter 5. In contrast to the thin-film LSC, where the combination of a thin luminescent layer and a thick transparent waveguide fails to reduce re-absorption losses, it was shown through simulations that, in the case of the light-bar, the composite design does indeed reduce re-absorptions. This is achieved by the interplay of two factors, the focussing of incident light onto the core, so that it can be absorbed effectively, and the restriction of the active region in two dimensions, enabling luminescent light paths that have reduced or no intersections with the active region before reaching the solar cells.

Furthermore, the effect of the thickness of the transparent shell was examined in more detail, basing the set of raytrace simulations on experimental measurements on a thin, homogeneous, cylindrical light-bar. It was shown how the transparent shell significantly increases the waveguiding efficiency and hence the optical efficiency of the light-bar. However, a thicker shell also reduces the geometric gain, which in turn affects the optical concentration.

Next, three composite light-bar geometries, the cuboid, the cylinder and the triangular prism, were compared with respect to the fraction of escaping luminescence. While the cuboid was found to have smaller escaping fractions for most core diameters, the simulations indicated that the cylinder could be advantageous when the active core is relatively large, i.e. when emission occurs close to the surface, as expected according to Ref. 58. This result motivated the analysis of an inverted cylindrical light-bar with an active shell and a transparent core. The outcome was that such a structure has higher optical and waveguiding efficiencies than a homogeneously doped cylinder.

The cylindrical structure with the active shell was then compared against the composite cuboidal light-bar and found to be superior. Consequently, the cylindrical structure was used for a final estimation of the power generated by a lens/light-bar system: based on fairly moderate assumptions, a 1 m long light-bar with a 2 cm diameter could generate a power of ~ 5 W if used as a secondary concentrator under a primary concentration

factor of 20. With a luminescent material optimised to absorb a broad spectrum, the generated power could be increased to over 23 W at an overall system efficiency of $\sim$5.9 %. Further steps could be taken to improve the light-bar design by incorporating mirrors. In particular, one could improve the waveguiding efficiency (without affecting the light capture) by having the doped region only cover the part of the cylinder where the light is incident and by covering the remainder with a mirror. The smaller doped area would reduce re-absorption while the mirror would reduce the escape cone losses.

In conclusion, within the limits of this study, the cylindrical structure with an active shell was found to be the most suitable choice of light-bar for use as a secondary concentrator. The ideal ratio of active region to transparent region, which determines the power conversion efficiency as well as the concentration factor, would depend on the specific preferences for the application in terms of efficiency and cost.

Chapter 7

Novel Luminescent Materials

7.1 Chapter Introduction

To date, the optical concentration of LSCs has not been large enough to make the LSC truly competitive. Since escape cone losses are the predominant loss factor in the waveguiding efficiency of LSCs, three solutions to this problem exist in principle: the containment of luminescence using selective reflectors, the directional emission within the plane of the LSC and the reduction of re-emission using luminescent centres with low self-absorption. This chapter discusses the use of nanorods and phycobilisomes as novel luminescent materials in LSCs with the primary aim to reduce self-absorption.

7.2 Nanorods

As introduced in Section 2.4.2, nanorods are elongated, inorganic nanocrystals comprising a spherical (0-D) core (e.g. CdSe) and a rod-like (1-D) shell (e.g. CdS). While quantum dot LSCs have been fabricated and researched by several groups (see for example Refs. 25, 202, 203, 183, 204, 83, 72), so far only little has been published on nanorod doped LSCs. In 2004, Jones *et al.* [205] demonstrated the use of nanorods in a luminescent down-converter for solar cells. More recently, Ref. 206 published the fabrication of the nanorod LSCs presented in this section. In 2011 Ref. 207 simulated nanorod LSCs with a raytrace model and investigated the advantage of directional emission from aligned

nanorod layers. This section presents the experimental and computational characterisation of several nanorod LSCs, thereby demonstrating their feasibility and also examining the effectiveness. In particular, this section focusses on self-absorption related effects. Directional emission (see Section 2.4.5) was not considered in this work as this would require alignment of the nanorods in the LSC. Such alignment has been achieved on a micrometre scale [108], but the nanorods in the samples examined in this section were assumed to be randomly oriented. Even in the case of the thin-film LSCs, it was assumed that neither the separation between individual nanorods nor the fabrication process of the LSCs fostered interactions that would lead to self-alignment. Consequently, isotropic emission from the luminescent centres was assumed in the model.

Nanorods can offer a large Stokes shift and hence reduced self-absorption compared to quantum dots. Efros and Rodina [78] carried out a theoretical investigation of spherical and non-spherical nanocrystal shapes and came to the conclusion that Stokes shift was shape-dependent. Core-shell quantum dots exhibit a Stokes shift that is almost independent of the shell thickness. In the case of nanorods, the Stokes shift was found to increase with an increasing aspect ratio [79, 208]. Moreover, core-shell nanorods display a very high absorption coefficient at shorter wavelengths due to absorption in the shell [79]. The nanorods studied in this chapter had spherical CdSe cores and rod-like CdS shells, making them type I nanocrystals, in which the core has a smaller bandgap than the shell (see Section 2.4.2). In a CdSe/CdS nanocrystal, an electron in the valence band is delocalised over the entire structure due to its small effective mass and the small conduction band offset (0.2-0.3 eV [75]) between the CdSe core and the CdS shell, while a hole in the valence band is more likely to be confined to the core due to a larger effective mass and a larger band offset (approximately 0.5 eV [75]). Efros and Rodina [78] explain how the asymmetrical shape of nanorods leads to a splitting of the heavy and light hole ground states and manifests itself in a larger Stokes shift compared to quantum dots.

As detailed in Section 3.2.1 and Section 3.3, the samples characterised in this section contained AR DRT26 nanorods provided by NNL-National Nanotechnology Laboratory (see Figure 7.1) and JHN46 nanorods provided by the University of Berkeley.

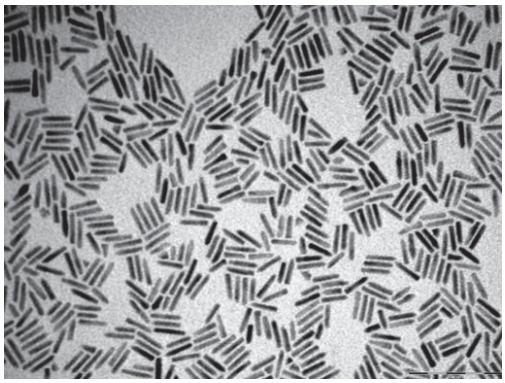

FIGURE 7.1: A transmission electron microscope image of CdSe/CdS core-shell nanorods with lengths of ∼32 nm and aspect ratios of 6-8 provided by the NNL-National Nanotechnology Laboratory [108].

7.2.1 Absorption and PLE Spectra of Nanorods

In the case of several nanocrystals examined for this thesis, comparisons of the spectral absorptance (defined as the fraction of light absorbed at a given wavelength, see Equation 2.15 and Equation 2.16) with the photoluminescence excitation (PLE) spectrum measured in the FluoroMax-3 spectrofluorometer (see Section 3.4.1) have shown a mismatch: the PLE drops off towards short wavelengths below 400 nm, while the absorptance continues to increase (see Figure 7.2).

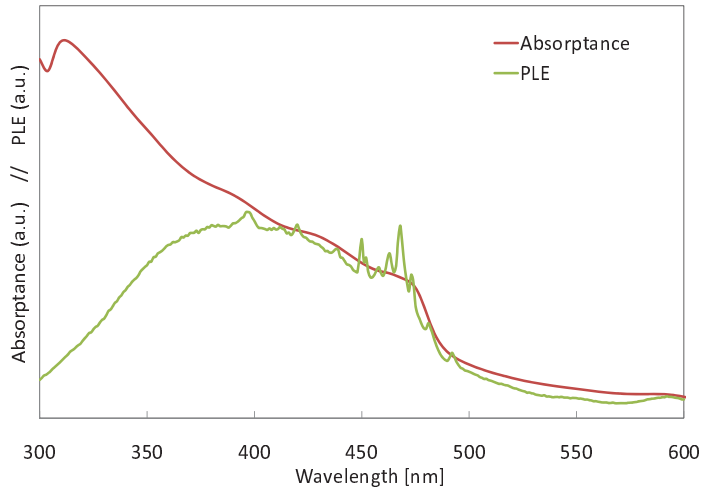

FIGURE 7.2: Comparison between the absorptance and the photoluminescence excitation (PLE) spectrum of a nanocrystal (in arbitrary units, scaled for comparison). These measurements were carried out on the nanorod sample labelled ECN823 (see Section 3.3 for details). Ignoring the noise, there is a good match at wavelengths above ∼400 nm, but at short wavelengths the PLE drops off in comparison to the absorptance.

This effect is unlikely to be explained by scattering processes affecting the absorptance measurements at short wavelengths. Such scattering effects have not been observed with dyes at these wavelengths. A more likely explanation could be a wavelength dependent luminescence quantum yield. A constant QY would produce a PLE spectrum that has the same shape as the spectral absorptance. Dyes, for instance, are generally believed to have a QY that is independent of the wavelength. This has been confirmed for the Lumogen F Rot 305 dye by Wilson *et al.* [94]. The nanocrystals, on the other hand, are assumed to have a QY that degrades at short wavelengths, due to the same reason that leads to the drop in the quantum efficiency of bulk semiconductor solar cells at short wavelengths: high energy photons above the bandgap of the shell are absorbed close to the surface and are therefore more likely to result in a non-radiative energy loss via surface recombination. Nevertheless, the absorption band of nanocrystals is still broader than that of most individual dyes.

7.2.2 Characterisation of Homogeneous and Thin-Film Nanorod LSCs

A homogeneous LSC (ECN785) and two thin-film LSCs (ECN1162 and ECN1165a) doped with AR DRT26 nanorods were characterised (see Section 3.3 for details of the samples and Figure 7.3 for a picture). The spectral absorptance of the three samples is shown in Figure 7.4. The short-circuit current measurements method was applied, based on the tungsten-halogen lamp setup (see Section 3.4.2). The emission from a single LSC edge was measured for each sample. In the case of ECN785 with a top surface area of 4.0 cm×1.3 cm the shorter edge was chosen.

The experimental short-circuit current density and the optical concentration are shown in Table 7.1. The optical concentration was deduced from the short-circuit current using a slightly more accurate relationship than the one given in Equation 3.6. Instead of neglecting the effect of angular variations of the edge output on the photocurrent, the distribution of polar angles θ of exiting rays was simulated with the Raytrace Model, and the angular response of the reference cell (see Figure 3.11) was taken into account:

$$\dot{N} = I_{SC} / \left(e \int_{\lambda} \int_{\theta} QE(\lambda, \theta)\, PL(\lambda, \theta)\, d\lambda\, d\theta \right) \tag{7.1}$$

As one would expect, Table 7.1 shows a correlation between the spectral absorptance A_λ and the optical concentration. Moreover, it is clear that these optical concentrations

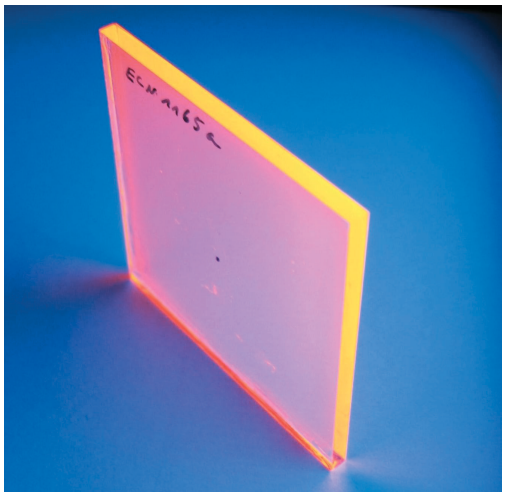

FIGURE 7.3: Photograph of a thin-film nanorod LSC (ECN1165a). Though the sample only contains a thin active layer on a glass substrate, it resembles a homogeneously doped LSC at this viewing angle. The picture was taken by J. Quilitz under UV illumination.

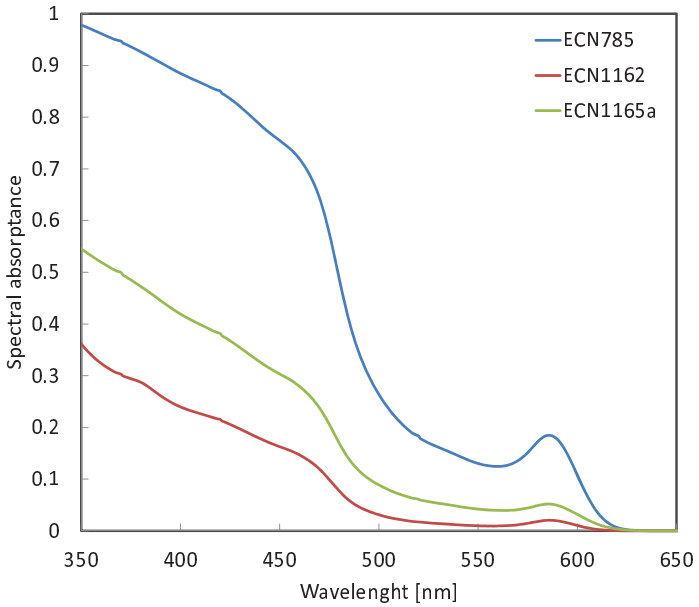

FIGURE 7.4: Measured spectral absorptance of homogeneous (ECN785) and thin-film (ECN1162 and ECN1165a) nanorod LSCs. The dopant concentration of ECN1165a was approximately twice as high as that of ECN1162. The absorptance spectra display the primary exciton peak from the CdSe core at longer wavelengths ($\sim$580 nm) and the absorption edge of the CdS shell at shorter wavelengths ($\sim$470 nm).

are very small (below unity). While these values are based on the lamp spectrum, the optical concentration under AM1.5 irradiation would also be too low to be viable. Higher dopant concentrations and larger geometric gains would be required to improve the performance of these LSCs.

	A_λ at 350 nm	J_{SC} [mA m^{-2}]	Optical concentration
ECN785	0.98	27 ± 1	0.13 ± 0.01
ECN1162	0.36	9 ± 2	0.04 ± 0.01
ECN1165a	0.55	14 ± 1	0.07 ± 0.01

TABLE 7.1: Optical concentration deduced from short-circuit current measurements on nanorod LSCs. The average incident J_{SC} was (0.26 ± 0.02) A m^{-2}, measured by the reference cell placed directly in the incident beam.

The Raytrace Model was applied to the three samples, and the fundamental PL and the QY were simultaneously fitted (see Figure 3.20 as an example). The model proved consistent in that the same fundamental PL spectrum was extracted for both thin-film samples.

The homogeneous sample had a slightly different fundamental PL, but this was not unexpected due to the different host material of the homogeneous sample, which is generally known to affect the spectral properties of the luminescent centres. In the homogeneous case, the extracted QY of 67 ± 4 matched the literature value reported in Ref. 108. However, the QYs of ECN1162 and 1165a were found to be $\sim$30 % and $\sim$40 %, respectively. This deterioration of the QY was attributed to either agglomeration of nanorods in the film or macroscopic defects in the film some of which were observable by eye.

7.2.3 Dependence on Nanorod Concentration

In order to investigate the LSC performance as a function of concentration of nanorods, five LSCs with varying dopant concentrations were fabricated, labelled C1-C5 in order of ascending concentration (see Section 3.3 for details). The samples consisted of PLMA waveguides with dimensions of $50 \times 50 \times 1$ mm^3, homogeneously doped with JHN46 nanorods from the University of Berkeley. The luminescence quantum yields were obtained using a Hamamatsu Absolute PL Quantum Yield Measurement System as described in Section 3.4.1. The dopant mass fractions and quantum yields are shown

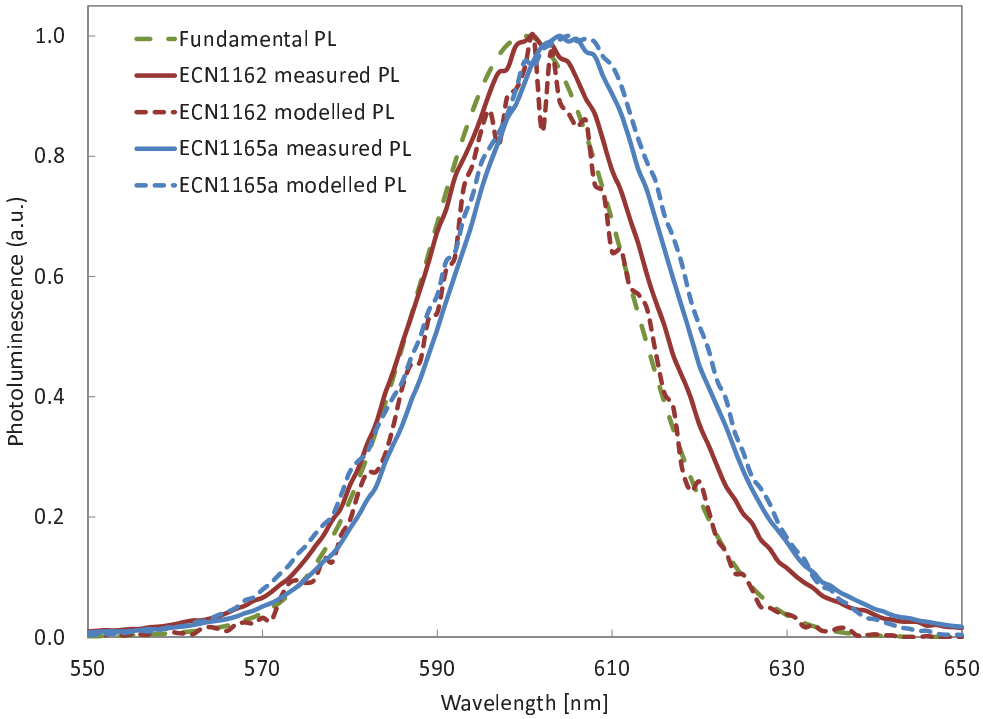

FIGURE 7.5: Experimentally measured and modelled photoluminescence spectra of thin-film nanorod LSCs ECN1162 and ECN1165a. The fundamental PL, peaking at 600 nm, was inferred by varying this parameter in the Raytrace Model until the measured and modelled PL spectra from the LSC edge were in agreement. The measured and modelled peaks coincided at ~ 601 nm for ECN1162 and were at ~ 604 nm and ~ 605 nm, respectively, for ECN1165a.

in Table 7.2. The mass concentration is a measure of concentration defined as the ratio of dopant mass to host matrix mass and is easily translated to the number density. A decrease of the QY was observed with increasing dopant concentration, probably as a result of a systematic error due to increasing self-absorption distorting the measurements. Wilson and Richards [152] have proposed a method of correcting for self-absorption in QY measurement of samples with higher absorbances. However, the QY measurement of the samples in this section were carried out by our collaborator at the Fraunhofer IAP using a Hamamatsu system (see Section 3.4.1), where no such correction was carried out. All other measurements presented in this section were carried out by the author.

The dopant concentration is proportional to the absorbance $\tilde{A}$, as observed in the experimental data in Figure 7.6.

The absorbances of the five samples of varying concentration were measured by the author using the UV/Vis spectrophotometer described in Section 3.4.1. Since no undoped control sample was available for the absorbance measurement, the host absorbance had

Sample	Mass concentration [%]	QY [%]
C1	0.03	53
C2	0.05	49
C3	0.06	49
C4	0.10	40
C5	0.16	43

TABLE 7.2: Samples with varying dopant concentrations. The mass fractions and the luminescent quantum yields are shown for each sample.

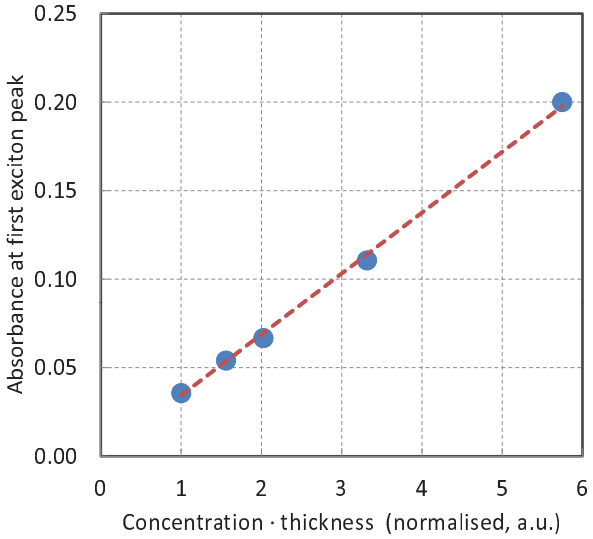

FIGURE 7.6: Proportionality between the measured absorbance and nanorod concentration (corrected for slightly varying sample thickness). The solid blue circles represent the data for the samples C1 to C5 (from left to right) and the red dotted line is the linear fit through the points. The experimental data follows the expected linear relationship.

to be subtracted subsequent to the measurements. A relatively constant host absorbance was assumed, so that the absorbance at long wavelengths beyond the nanorod absorption range could be taken as an approximation. The absorbance curves are shown in the left plot of Figure 7.7. The right plot displays the normalised absorbance obtained by dividing by the respective dopant concentrations and sample thicknesses. This plot indicates that the elimination of the host absorbance (absorption coefficient of $\sim 2\,\mathrm{m}^{-1}$) from the measurements was sufficiently accurate, because otherwise the rescaling of the different curves based on the respective dopant concentrations would not have yielded such a good agreement between the five curves.

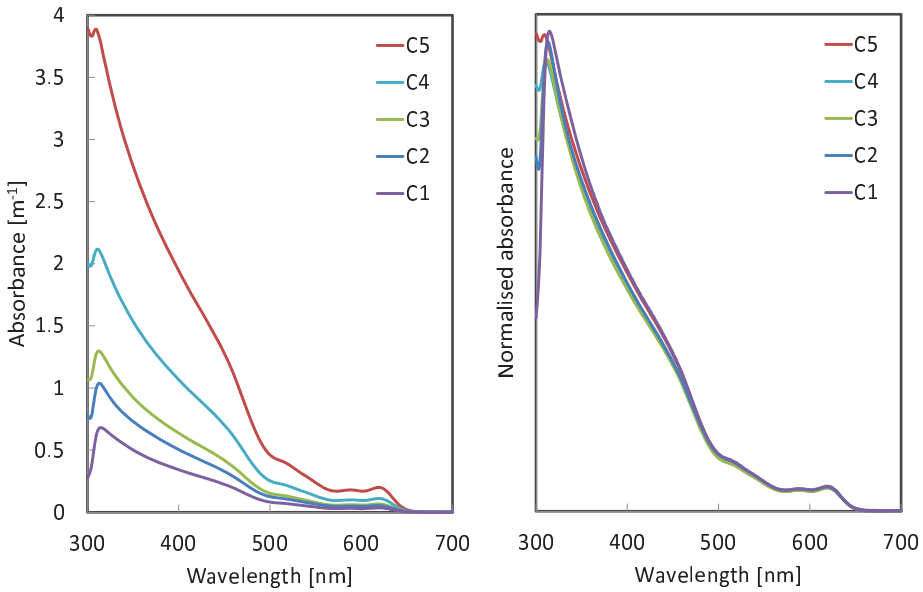

FIGURE 7.7: Comparison of absorbances of samples of different dopant concentrations. The left plot shows the actual absorbances. The right plot compares normalised absorbances, obtained by dividing by the respective dopant concentrations and sample thicknesses. The different curves are consistent, especially above 470 nm.

The absorbance $\tilde{A}$ is linked to the internal spectral absorptance $A_{\lambda,\text{internal}}$ (see Equation 2.19):

$$A_{\lambda,\text{internal}} = 1 - e^{-\tilde{A}}\,. \tag{7.2}$$

The internal spectral absorptance is a key factor in the light capture efficiency of the LSC (see Equation 2.20). Clearly, the absorptance increases with the absorbance. However, the rate of the increase approaches zero as the absorbance becomes larger:

$$\frac{dA_\lambda}{d\tilde{A}} = e^{-\tilde{A}}\,. \tag{7.3}$$

This means that as the dopant concentration is increased, the incremental gain in the light capture efficiency becomes smaller, so that variations in the waveguiding efficiency can become predominant.

The experimental emission spectra, measured as described in Section 3.4.1, are shown in Figure 7.8. The PL spectra were recorded in two ways, with the sample normal to the excitation beam of the spectrofluorometer and at a 45 ° angle. In the first orientation, one can see the expected red-shift of the PL peak with increasing dopant concentration as a result of a greater degree of self-absorption (with subsequent re-emission). The light

reaching the detector has a relatively long pathlength through the LSC since it has to travel from approximately the centre to the edge of the LSC. In the second case (at 45 °), the majority of the light reaching the detector only needed to pass through the thickness of the LSC (as an approximation). Therefore the PL spectrum at this orientation is expected to be close to the fundamental one, as mentioned in Section 3.4.1. This is confirmed by the fact that the peak position for all concentrations is found to be at the same wavelength (630 nm), as shown in Table 7.3.

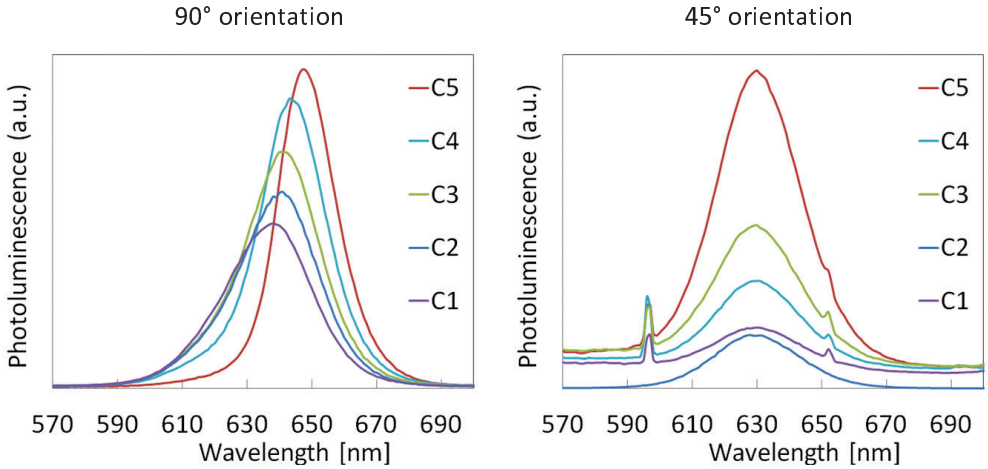

FIGURE 7.8: Photoluminescence spectra of samples with varying dopant concentrations measured in two different ways, with the sample oriented at a 90 ° angle to the excitation beam and at a 45 ° angle (facing away from the detector). In the first case (at 90 °), the increasing dopant concentration leads to an increasing red-shift of the PL peak. In the second case (at 45 °), the PL peak is measured at the same wavelength for all samples, indicating that this peak (630 nm) corresponds to the fundamental PL. The excitation wavelength in these measurements was 397 nm. The origin of the side peaks in the 45 ° orientation graph is unclear, but they are considered artefacts of the measurement setup since they are not observed in the 90 ° orientation.

Sample	Concentration [%]	PL peak at 90 ° [nm]	PL peak at 45 ° [nm]
C1	0.03	638 ± 1	630 ± 1
C2	0.05	641 ± 1	630 ± 1
C3	0.06	640 ± 1	630 ± 1
C4	0.10	643 ± 1	630 ± 1
C5	0.16	647 ± 1	630 ± 1

TABLE 7.3: Photoluminescence peaks of samples with varying dopant concentrations measured in two different ways, as described in Table 7.8. The fundamental PL is found to be at 630 nm.

The fact that the sample C2 deviates a little from the trend could be due to the slightly different host material composition, which included only 20 % of the cross-linking agent

EGDM whereas the other samples contained 25 % EGDM (see Section 3.2 and Section 3.3 for details).

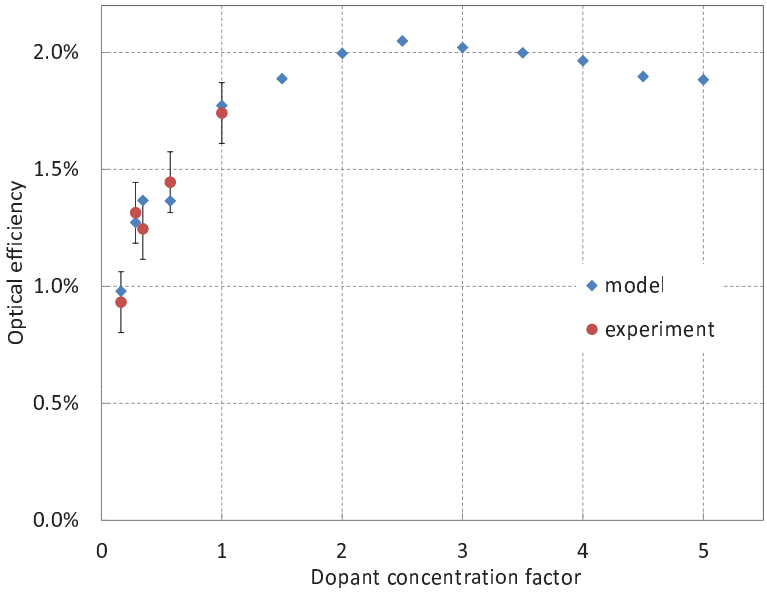

FIGURE 7.9: The optical efficiency of LSCs as a function of dopant concentration factor. The dopant concentrations are shown relative to the sample C1 (see Table 7.2). The optical efficiency peaks after an initial increase and eventually drops off with growing dopant concentration.

The samples were characterised under the solar simulator described in Section 3.4.2. The experimentally deduced optical efficiencies of the samples are shown in Figure 7.9. The Raytrace Model was applied to reconstruct the experimental measurements and to extend the range of dopant concentrations. The results are also shown in Figure 7.9. The model agrees with the experimental results, which cover a relatively small range of concentrations. Over this range an increase in optical efficiency was observed with increasing dopant concentration. The Raytrace Model was used to calculate the optical efficiency over an extended range of dopant concentrations. The optical efficiency was found to peak at $\sim 2\,\%$ and decrease at high dopant concentration (see Figure 7.9).

Recalling that the optical efficiency is the product of capture efficiency and waveguiding efficiency, the initial increase in η_{optical} suggests an improved light capture as a result of the increasing absorbance. To quantify this, the capture efficiency was approximated by the internal fraction of light absorbed, which was calculated using experimentally measured absorbances. This approximation neglects reflection losses from the top surface, but since normally incident light was modelled, the discrepancy is small. As expected,

the capture efficiency continuously increases with the dopant concentration (see Figure 7.10). The waveguiding efficiency is extracted by dividing the optical efficiency by the capture efficiency:

$$\eta_{\text{waveguide}} = \frac{\eta_{\text{optical}}}{\eta_{\text{capture}}} . \tag{7.4}$$

The resulting, modelled variation in the waveguiding efficiency with dopant concentration is also illustrated in Figure 7.10. It is evident that internal losses impair $\eta_{\text{waveguide}}$ as the concentration increases. Since the fraction of QY and escape cone losses associated with the initial absorption of incident light is constant, it is concluded that the relative increase in internal losses is due to increased self-absorption.

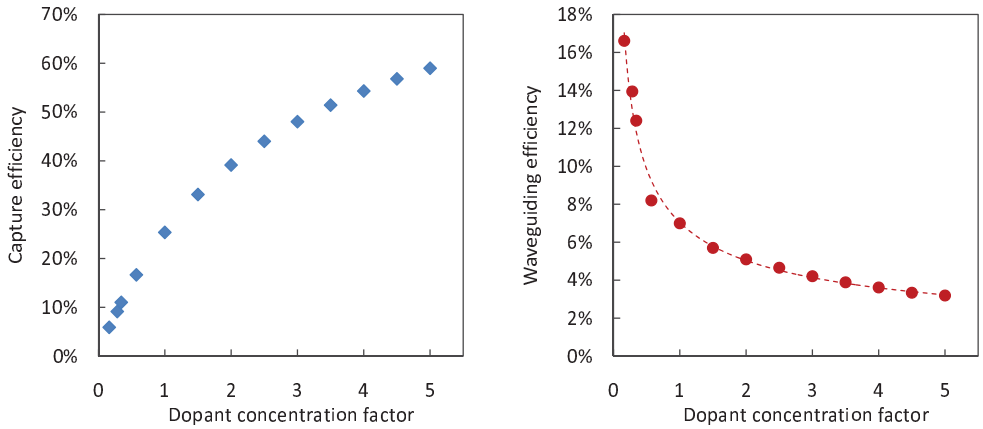

FIGURE 7.10: The light capture efficiency and the waveguiding efficiency as a function of dopant concentration factor. The capture efficiency increases with dopant concentration, while the waveguiding efficiency decreases following a power law (broken line).

7.2.4 Dependence on LSC Size

In order to investigate the relation between the size (or geometric gain) and the output of the LSC, five square samples of varying dimensions ranging from $10\times10\,\text{mm}^2$ to $30\times30\,\text{mm}^2$ (see Figure 7.11) were cut from a single 1 mm thick PLMA plate containing AR DRT26 nanorods from the NNL-National Nanotechnology Laboratory in Italy [108]. This ensured that the only difference between the samples was the top surface area. The samples were characterised using the short-circuit current method described in Section 3.4.2, and their optical concentrations were deduced for comparison. The Raytrace Model was used to support the experimental results and to extrapolate to device sizes up to $1\times1\,m^2$.

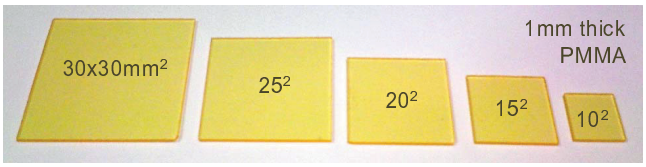

FIGURE 7.11: Five square LSCs of different dimensions were cut from a single 1 mm thick plate for the investigation of the size dependence.

In the case of a square LSC with edge length l and thickness d, the geometric gain G is proportional to l, as stated in Equation 2.28:

$$G = \frac{l}{4d}\,. \tag{7.5}$$

Recalling the relationship between G and the optical concentration C from Equation 2.27, one can see that a linear increase of C with increasing l is expected if the optical efficiency is constant:

$$C = G\,\eta_{\text{optical}} = \frac{l}{4d}\,\eta_{\text{optical}}\,. \tag{7.6}$$

Figure 7.12 shows the plot of C against l from the measurements. The experimental errors were calculated as described in Section 3.4.2. Due to low absorbances and small sample sizes, the signal strength was low and hence the standard deviation of the short-circuit current measurements carried out along one edge of each sample using the method described in Section 3.4.2 was relatively high (10-20 %). Nevertheless, the general trend matches the results of the raytrace simulations. There is a linear increase of the optical concentration with l up to a length of 50 mm in the model. This is also seen in the experiment up to 30 mm. From this it is inferred that the optical efficiency is approximately constant at small concentrator sizes. At larger dimensions the simulation predicts that the curve levels off, such that the 10-fold increase in geometric gain (and 100-fold increase in area) from $100\times100\,\text{mm}^2$ to $1000\times1000\,\text{mm}^2$ leads to an increase of only 4 % in optical concentration. This means that the optical efficiency drops by a factor of nearly 10 over that range. The substantial decline of η_{optical} cannot be due to the light capture efficiency as this is independent of the geometric gain and the size. The loss is therefore attributed to internal processes: at larger dimensions, the longer photon paths lead to an increased absorption by the host and, more importantly, increased self-absorption by the luminescent centres. As discussed in Chapter 2, self-absorption amplifies escape cone and luminescence quantum yield (QY) losses. The results indicate

that the gain in concentration with increasing LSC size becomes small after a size of approximately 10 cm×10 cm.

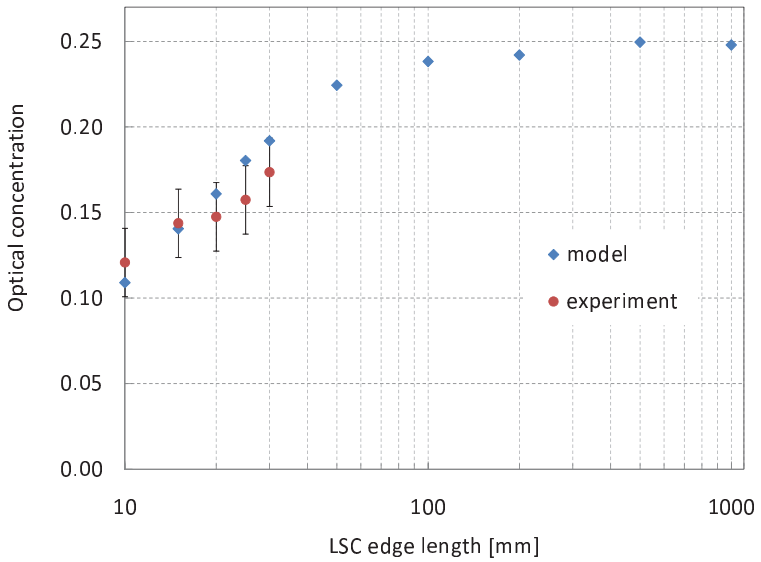

FIGURE 7.12: The size dependence of the LSC output. The optical concentration is plotted against the edge length of square LSCs on a logarithmic scale. The modelling results show an approximately linear relationship up to an edge length of 50 mm.

The optical concentrations of the samples were all below unity. Besides poor luminescence quantum yields ($< 50\,\%$) and a weak absorptance, this was also owing to re-absorption losses.

7.2.5 Dependence on Illumination Position

To investigate further the effects of self-absorption the effect of illumination position on the spectral shape and intensity of the LSC output was investigated. A blue laser (404 nm) was used to illuminate the LSC at varying positions with a spot size of $\sim 2\,\mathrm{mm}^2$. Figure 7.14 (i) depicts the setup for the short-circuit current measurement with a GaAs PV cell covering one entire edge of the LSC and attached using index matching fluid. The QE of the cell is shown in Figure 7.13. Photoluminescence measurements were carried out by replacing the PV cell with an optical fibre that coupled the LSC output to a spectrometer, as shown in Figure 7.14 (ii). These experiments were carried out in the dark.

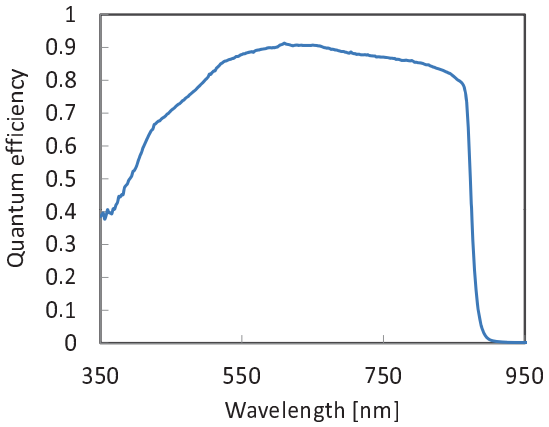

FIGURE 7.13: Quantum efficiency of the GaAs solar cell used for the position dependence measurements. This cell, labelled ECN2345-2/13, was fabricated by the Fraunhofer ISE and provided to our group by the Energy Research Centre of the Netherlands.

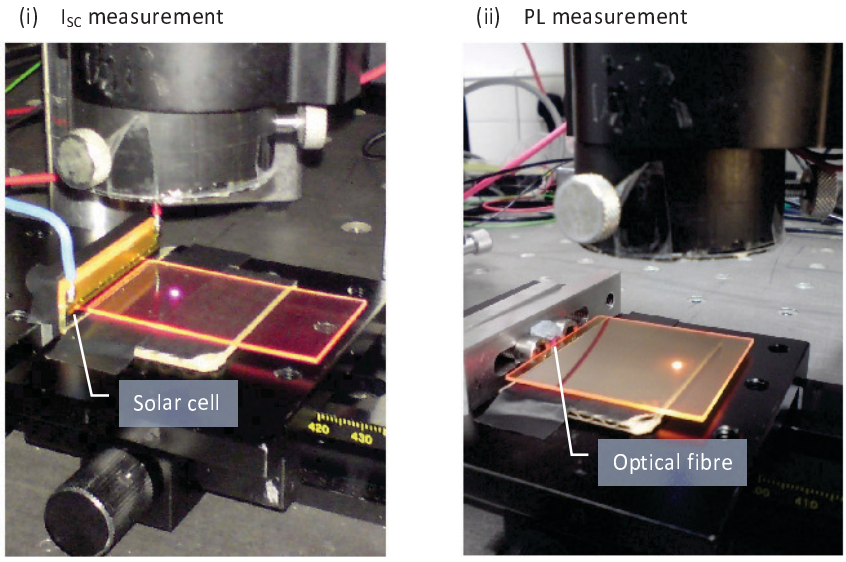

FIGURE 7.14: Photograph of the setup for the illumination position dependence measurement. While the LSC was illuminated with a blue laser at varying positions, short-circuit current measurements (i) were carried out with a solar cell covering one edge of the LSC, and photoluminescence measurements (ii) were carried out using an optical fibre coupling the LSC output to a spectrometer.

Two samples, denoted A and B, made of polymer plates with dimensions of 5 cm×5 cm×1 mm were used in this experiment (see Section 3.3 for details). The luminescent species were CdSe/CdS core-shell nanorods provided by the University of California, Berkeley (JHN46, sample A) and by the NNL-National Nanotechnology Laboratory in Italy (AR DRT26, sample B). These two kinds of nanorods had similar spectral properties, as shown in Figure 7.15. A comparison of the absorption coefficients and luminescence quantum yields of the samples is given in Table 7.4.

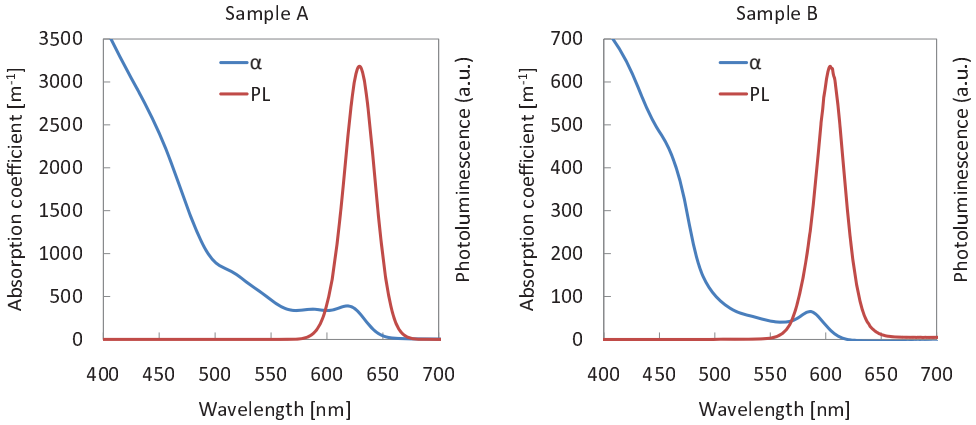

FIGURE 7.15: The spectral properties of the nanorods used in the illumination position dependence measurement.

	α at PL peak	QY
Sample A	$307\,\mathrm{m}^{-1}$	63 %
Sample B	$33\,\mathrm{m}^{-1}$	68 %

TABLE 7.4: The absorption coefficient α, measured at the photoluminescence peak, and the luminescence quantum yield of the two samples used in the illumination position dependent measurement. The absorption coefficient of sample A was 9.3 times as high as that of sample B.

The experimental measurements were carried out in collaboration with N. Chan and Y. Xiao, two MSci students supervised by the author. Figure 7.16 shows the variation in the output of sample A as a function of the distance of the illumination spot from the edge with the PV cell. There is a steep initial drop in the photocurrent with increasing distance, which eventually levels off. The drop is explained by re-absorption losses. The agreement between the modelled and the experimental results at greater distances is very good. There are minor discrepancies at illumination positions close to the LSC edge because, in the experimental measurement, some of the luminescence emitted out

of the top surface escape cone could reach a part of the solar cell that was protruding the LSC edge. For comparison, the transmittance of light at the wavelength of the photoluminescence peak across the distance from the illumination position to the PV cell was calculated. The exponential attenuation of the transmission with distance is significantly steeper than the decrease in the photocurrent. This indicates that the emission is redshifted as a result of multiple re-emissions, making subsequent re-absorption less likely.

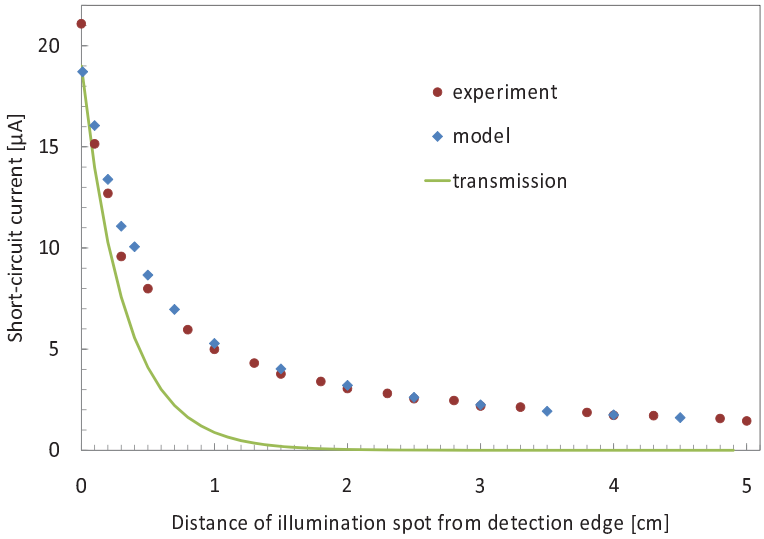

FIGURE 7.16: The variation in short-circuit current of sample A as a function of the distance of the illumination position from the edge with the PV cell. The calculated transmission of light at the photoluminescence peak wavelength is shown for comparison.

Sample B had a lower absorbance and a higher QY than sample A, which reduces both the probability of re-absorption and the QY loss associated with re-absorption. Consequently the reduction of the photocurrent with increasing distance of the illumination position is less steep for sample B (see Figure 7.17). The calculated transmission diverges from the distance dependent photocurrent only at larger distances, because the low absorbance of sample B at the PL peak leads to a small probability of re-absorption even without the additional redshift from re-emissions.

The higher absorption coefficients of sample A compared to sample B lead to a higher I_{SC} for sample A at small distances because of more incident light being absorbed, but a smaller I_{SC} at large distances, where self-absorption losses become dominant. For

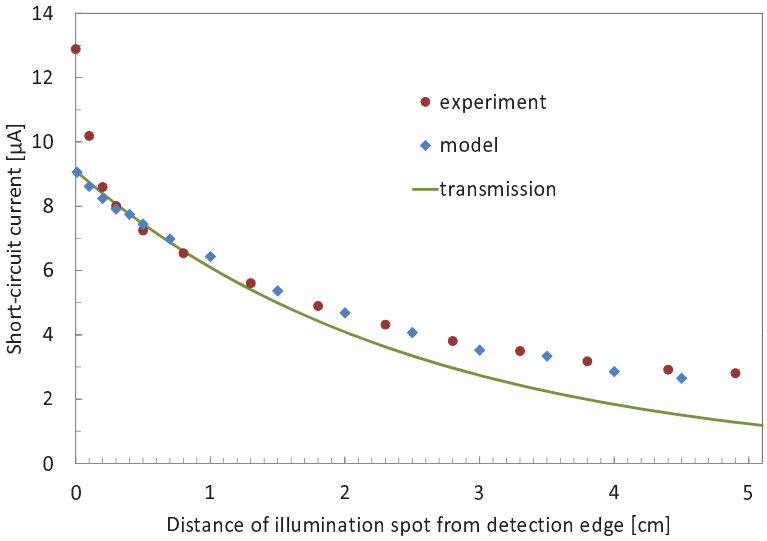

FIGURE 7.17: The variation in short-circuit current of sample B as a function of the distance of the illumination position from the edge with the PV cell. The calculated transmission of light at the photoluminescence peak wavelength is shown for comparison.

example, at an illumination distance of 5 cm the I_{SC} of sample A is approximately half that of sample B.

The decrease in the photocurrent with illumination distance was attributed to re-absorption losses. To verify this the number of re-absorptions as a function of illumination distance was computed using the model. Figure 7.18 (sample A) and Figure 7.19 (sample B) show the average number of re-absorptions that take place before a luminescent photon reaches the solar cell. As expected, this number is inversely related to the photocurrent and increases with illumination distance. The levelling of the curve with increasing distance indicates the effect of the progressive redshift. In line with the slower decrease in photocurrent with increasing illumination distance, sample B has significantly fewer re-absorptions than sample A. For example, at an illumination distance of 5 cm the probability of re-absorption in sample B is less than half of that in sample A.

The redshift of the PL peak as a function of illumination distance was measured for sample A and is shown in Figure 7.20. The results confirm that the redshift increases with illumination distance. The curve has a strong correlation with the re-absorption curve shown in Figure 7.18. Since an increasing redshift reduces the overlap between the emission and absorption spectra, the probability of further re-absorption decreases with the number of re-absorptions.

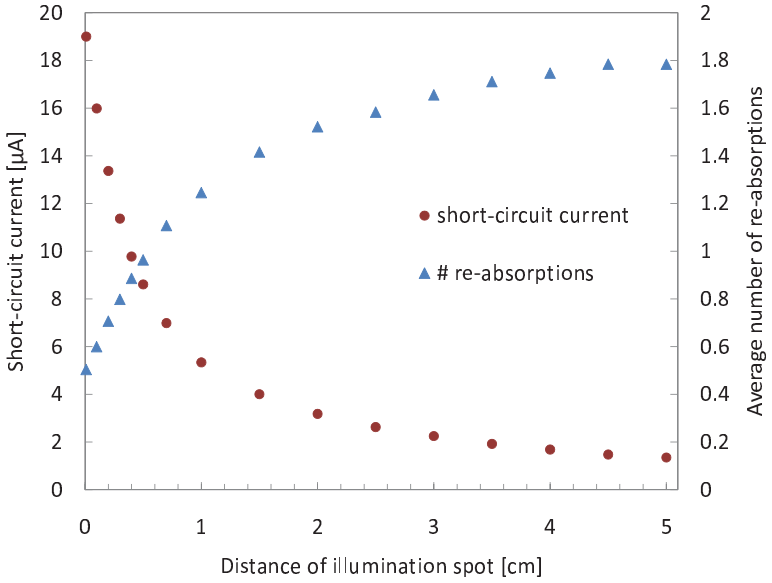

FIGURE 7.18: The average number of re-absorptions from the model as a function of illumination distance in comparison with the short-circuit current measured at the edge, in the case of sample A.

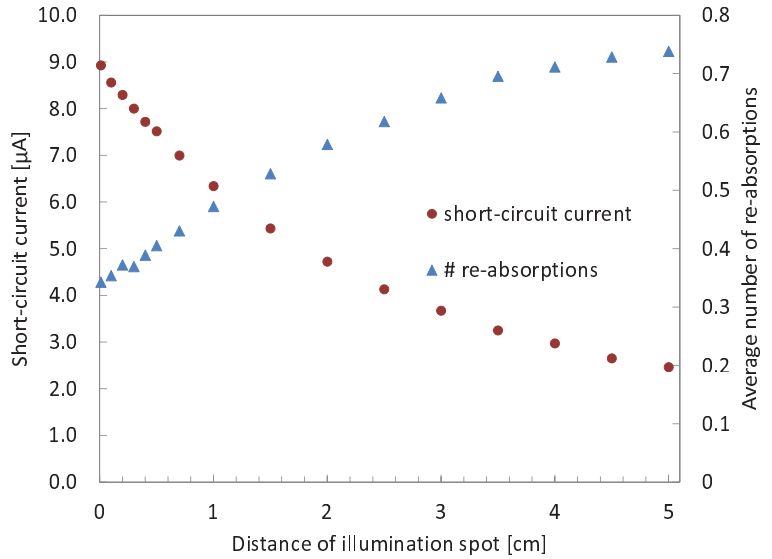

FIGURE 7.19: The average number of re-absorptions from the model as a function of illumination distance in comparison with the short-circuit current measured at the edge, in the case of sample B.

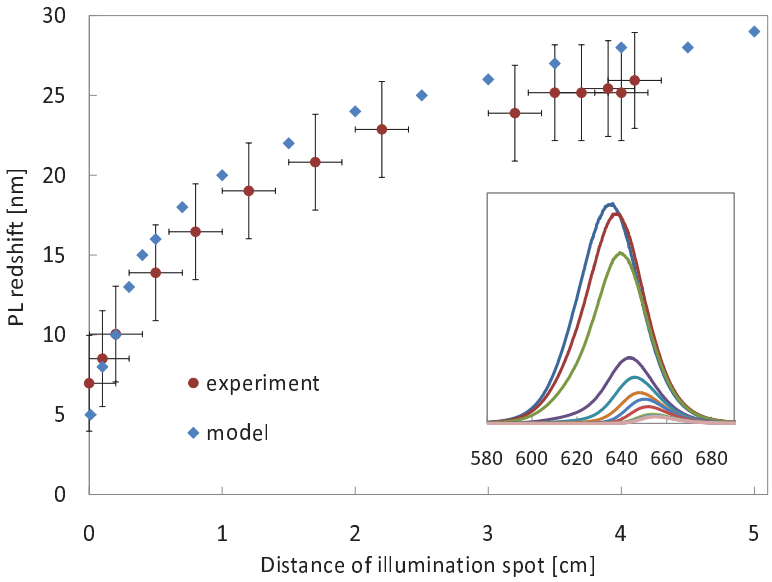

FIGURE 7.20: The redshift of the photoluminescence peak as a function of illumination distance, measured for sample A. The inset shows the PL measurements from which the redshifts were derived. There is a reasonable agreement between the experiment and the model.

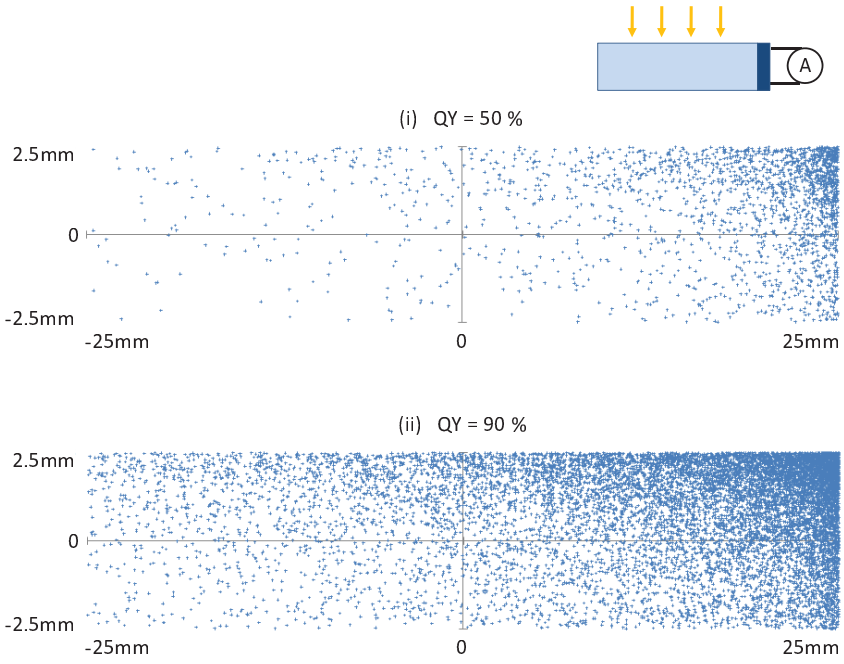

FIGURE 7.21: Simulated positional contribution to the LSC output. This graph shows a side view of the LSC, indicating the origin of luminescent photons that are detected at the edge on the right. Light is incident from the top, as illustrated in the inset. The simulation was carried out using a QY of 50 % (i) and of 90 % (ii).

A logical conclusion from the photocurrent dependence on illumination position is that a large part of the LSC output is generated by incident photons absorbed close to the LSC edges. Raytrace simulations were carried out on a 50 cm×50 cm LSC under uniform illumination to visualise the origins of luminescent photons reaching the edge. Two hypothetical QYs were modelled and the results are presented in Figure 7.21: 50 % (i) and 90 % (ii). There is a vertical variation of photon origins due to the exponential attenuation of incident light, as described by the Beer-Lambert law (see Equation 2.17). The horizontal variation is due to re-absorption losses in the form of QY and escape cone losses. In case (i) the majority of the contribution to the edge output is limited to a region close to the detection edge. Due to the higher QY modelled in case (ii) there is a significantly higher contribution from points far away from the detection edge.

7.2.6 Comparison of Nanorod LSCs with Quantum Dot LSCs

The experimental measurements of nanorod LSCs presented in this chapter showed that self-absorption is still a predominant loss factor in nanorods, despite expectations of larger Stokes shifts. In this section, the Raytrace Model was applied to compare nanorod LSCs with quantum dots LSCs.

The first comparison, labelled comparison A, was between the AR DRT26 CdSe/CdS nanorod (see Section 3.2.1) and a commercially available Nanoco CdSe Core 590 quantum dot, which was chosen because it consisted of the same material as the nanorod core and had a very similar emission spectrum, as can be seen in Figure 7.22 or Figure 7.23. The AR DRT26 nanorod spectra were experimentally measured, while Nanoco quantum dot spectra were obtained from the data sheet.

The modelled LSCs were homogeneously doped with dimensions of 50 cm×50 cm×5 mm, a refractive index of 1.49 and a background absorption of 0.3 m^{-1}. The incident spectrum was the AM1.5 direct, and the spectral range of the simulations extended from 400 nm to 700 nm. The upper boundary was chosen according to the absorption and emission range of the luminescent materials under examination, while the lower boundary was limited by availability of spectral data for the commercially available Nanoco quantum dot.

The QY of the AR DRT26 nanorod was ∼67 %. The QY of the Nanoco quantum dot core was expected to be very low (<10 %) because it lacked a shell that limits non-radiative recombination, but for the purpose of the comparison a QY identical to the nanorod was modelled. The simulations were also repeated using a QY of 33 % for both the nanorod and the quantum dot.

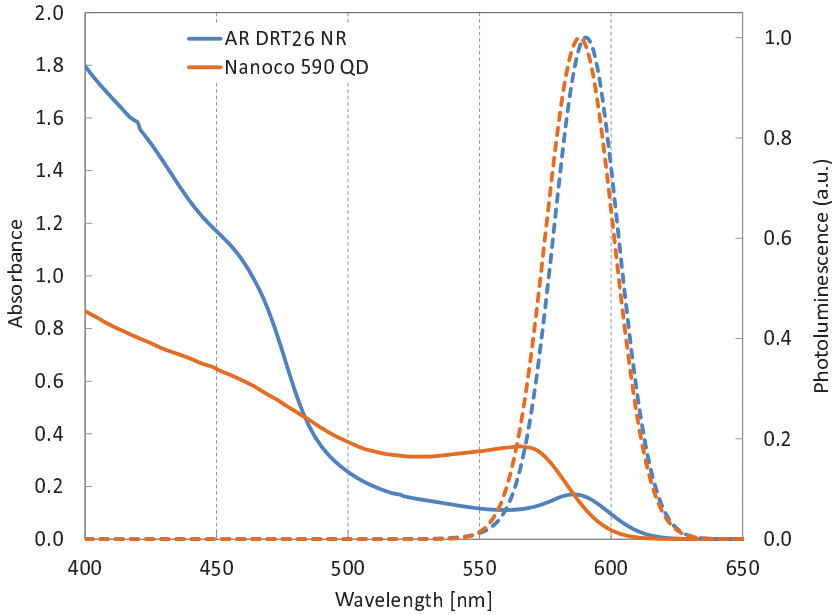

FIGURE 7.22: Comparison of the absorbance (solid line) and emission (dotted line) overlap of AR DRT26 CdSe/CdS core-shell nanorods and Nanoco Core 590 CdSe quantum dots. The absorbances were adjusted such that (20±1) % of the AM1.5 direct spectrum over the range from 400 nm to 700 nm would be absorbed by both types of luminescent centres. These spectra were partially fitted using Gaussian functions.

The simulations were carried out for two absorbance cases, a relatively low one, in which (20±1) % of the AM1.5 direct spectrum over the simulation range from 400 nm to 700 nm were absorbed by the luminescent centres, and a relatively high one, in which (40±1) % were absorbed. The absorbances for these two cases along with the emission spectra are shown in Figure 7.22 and Figure 7.23, respectively. Visual inspection suggests that the overlap between absorption and emission spectra grows faster for the nanorods than for the quantum dots as the absorbance is increased from the low to the high case.

The overlap between the photoluminescence spectrum and the spectral absorptance was also calculated for each luminescent material. In the low absorbance case, the fractional absorption of the PL spectrum was 12 % for the nanorods and 14 % for the quantum dots, as illustrated in Figure 7.24. Though this may seem to suggest less self-absorption in the nanorod LSC, one needs to bear in mind that this is just an approximation. The

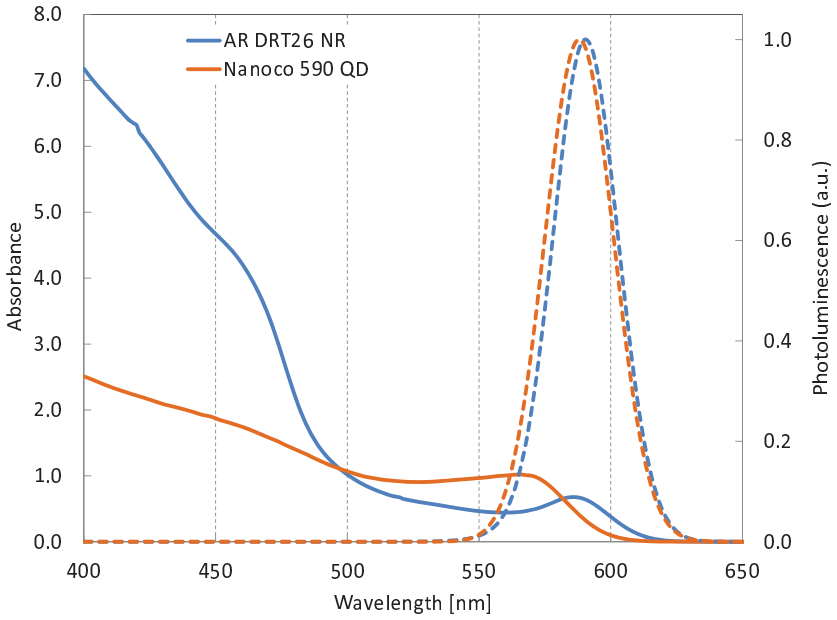

FIGURE 7.23: Comparison of the absorbance (solid line) and emission (dotted line) overlap of AR DRT26 CdSe/CdS core-shell nanorods and Nanoco Core 590 CdSe quantum dots. The absorbances were adjusted such that (40±1) % of the AM1.5 direct spectrum over the range from 400 nm to 700 nm would be absorbed by both types of luminescent centres. These spectra were partially fitted using Gaussian functions.

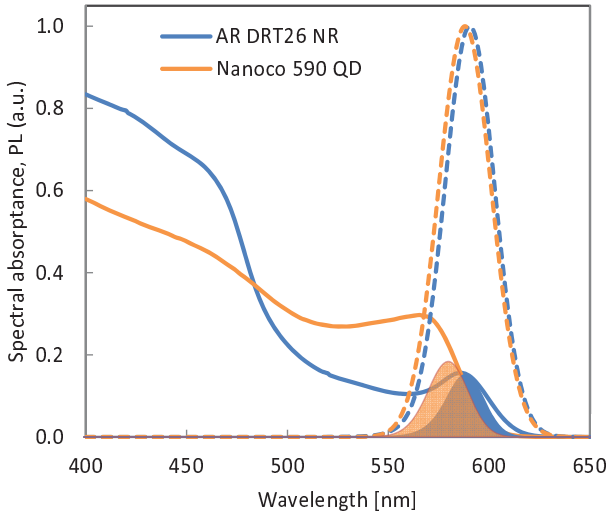

FIGURE 7.24: Comparison of the spectral absorptance (solid line) and photoluminescence (dotted line) of AR DRT26 nanorods and Nanoco Core 590 quantum dots in the low absorbance case. The spectral absorptance (fraction of light absorbed at a given wavelength) is shown here (instead of the absorbance) since it is proportional to the luminescence. The fractional absorption of the PL spectrum is shown in the shaded areas and amounts to 12 % for the nanorod and 14 % for the quantum dot.

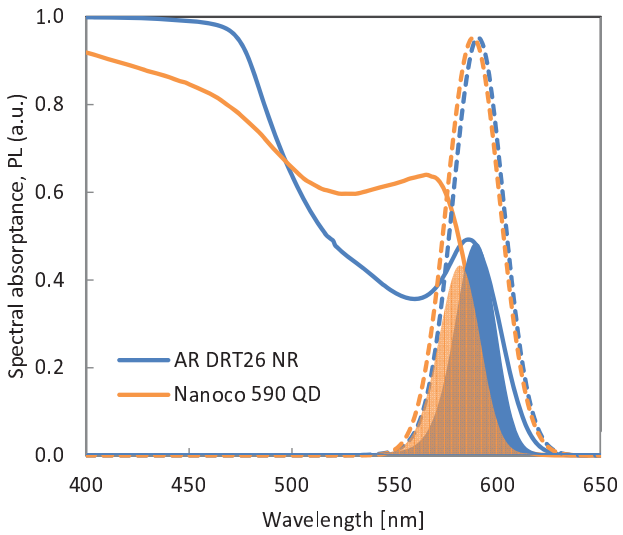

FIGURE 7.25: Comparison of the spectral absorptance (solid line) and photoluminescence (dotted line) of AR DRT26 nanorods and Nanoco Core 590 quantum dots in the high absorbance case. The fractional absorption of the PL spectrum is shown in the shaded areas and amounts to 38 % for the nanorod and 33 % for the quantum dot.

incident spectrum and the fact that on each emission the photon wavelength is red-shifted affect the self-absorption. In the high absorbance case, the fractional absorption of the PL spectrum was 38 % for the nanorods and only 33 % for the quantum dots (see Figure 7.25). To compare the self-absorption between the nanorods and quantum dots the waveguiding efficiencies were computed for the different absorbance cases using the Raytrace Model (see Table 7.5).

		$\eta_{\text{waveguide}}[\%]$	
		33 % QY	67 % QY
Low absorbance	AR DRT26 nanorod	2.5	8.9
	Nanoco Coree 590 QD	3.7	12.6
High absorbance	AR DRT26 nanorod	1.0	4.7
	Nanoco Core 590 QD	2.1	8.8

TABLE 7.5: Raytrace comparison of waveguiding efficiencies between nanorod and quantum dot LSCs. In the low absorbance case, (20±1) % of the AM1.5 direct spectrum over the range from 400 nm to 700 nm would be absorbed; in the high absorbance case (40±1) %. The QYs chosen for this comparison are arbitrary, except that 67 % is the approximate QY of the AR DRT26 nanorods.

The results in Table 7.5 showed that the AR DRT 26 nanorods had a significantly lower waveguiding efficiency and hence higher self-absorption than the Nanoco quantum dots

in all simulated cases. As expected from visual inspection of the spectra, it was found that the self-absorption increases faster for the nanorods as the absorbance is increased. It needs to be pointed out that these results are not generally valid as they are dependent on the LSC parameters, the incident spectrum, the absorbance strength and range and the luminescence quantum yield. For low absorbances one would have expected less self-absorption in the nanorod from the smaller spectral overlap, but the opposite was found. The results were considered inconclusive.

A second comparison, comparison B, was carried out based on nanorod and quantum dot samples published in Ref. 208. This comparison was assumed to be more suited than the previous one as the nanocrystals were more similar. Both the nanorod and the quantum dot were made from CdSe and had comparable dimensions. The ratio of long to short axis was 3.7/3.3 (nm) for the quantum dot and 6.6/3.6 (nm) for the nanorod. As can be seen in Figure 7.26 or Figure 7.27, the QD and the nanorod have very similar absorption spectra. The nanorod spectra display a clearly enhanced Stokes shift compared to the QD. This is also reflected in the fractional absorption of the PL spectrum, which was 26 % for the nanorod and 41 % for the QD in the low absorbance case and 56 % and 80 %, respectively, in the high absorbance case.

The larger Stokes shift of the nanorod is explained by its anisotropy and the associated splitting of states that are nearly degenerate in a spherical quantum dot [208, 209]. The excitation energy in the nanocrystal is governed by the lowest optically active level, while efficient relaxation to the band edge via acoustic phonons leads to a red-shifted emission. The splitting between absorbing and emitting states is larger in nanorods than in quantum dots of the same material.

The parameters for the simulations were identical to the ones for comparison A, except that the spectral range only extended from 500 nm to 700 nm due to limited data availability below 500 nm. Irrespective of actual QYs, the same cases as in the previous comparison, 33 % and 67 %, were modelled.

The raytrace results (see Table 7.6) showed a clear advantage of the nanorods in terms of waveguiding efficiency compared to the quantum dots due to a larger Stokes shift. This advantage was found to be more significant in the low QY case, as one would expect.

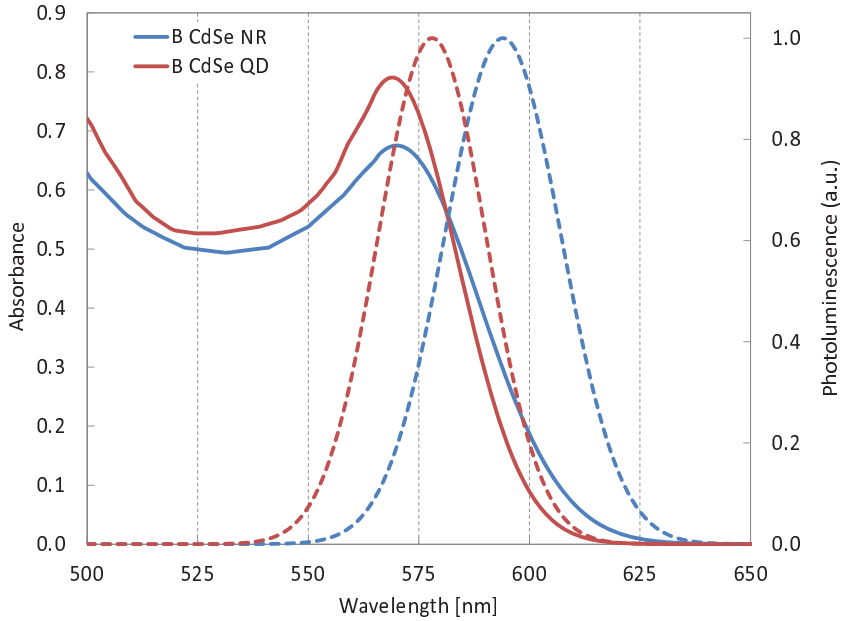

FIGURE 7.26: Comparison of the absorbance (solid line) and emission (dotted line) overlap of CdSe nanorods and CdSe quantum dots from Ref. 208. The absorbances were adjusted such that (20±1) % of the AM1.5 direct spectrum over the range from 500 nm to 700 nm would be absorbed by both types of luminescent centres. These spectra were partially fitted using Gaussian functions.

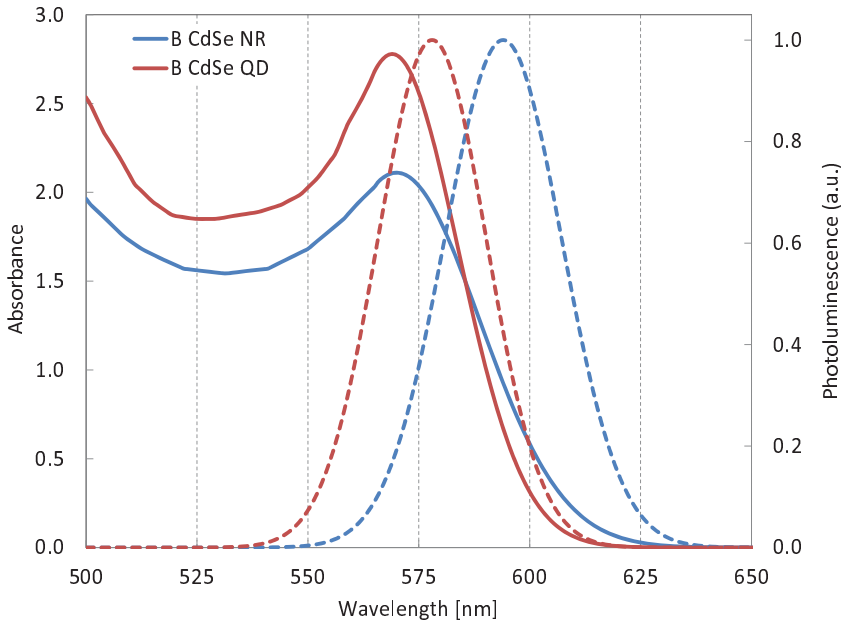

FIGURE 7.27: Comparison of the absorbance (solid line) and emission (dotted line) overlap of CdSe nanorods and CdSe quantum dots from Ref. 208. The absorbances were adjusted such that (40±1) % of the AM1.5 direct spectrum over the range from 500 nm to 700 nm would be absorbed by both types of luminescent centres. These spectra were partially fitted using Gaussian functions.

		$\eta_{\text{waveguide}}[\%]$	
		33 % QY	67 % QY
Low absorbance	B CdSe nanorod	2.0	7.9
	B CdSe QD	1.1	4.9
High absorbance	B CdSe nanorod	0.9	4.8
	B CdSe QD	0.5	2.9

TABLE 7.6: Raytrace comparison of waveguiding efficiencies between nanorod and quantum dot LSCs based on spectral data from Ref. 208. In the low absorbance case, (20±1) % of the AM1.5 direct spectrum over the range from 500 nm to 700 nm would be absorbed; in the high absorbance case (40±1) %. The QYs chosen for this comparison are arbitrary.

7.2.7 Conclusion

This section examined nanorods as a luminescent material with the potential to reduce re-absorption losses in the LSC. The experimental measurements and raytrace simulations on nanorod LSCs showed that self-absorption is still predominant in the nanorod LSC and limits the performance. In some of these experiments the influence of the Stokes shift compared to QY and dopant concentration was inconclusive. However, the final raytrace comparison clearly demonstrated that a nanorod with a larger Stokes shift than a QD approximately doubled the waveguiding efficiency at both low and high QY. Furthermore, nanorod ensembles can exhibit directional emission when aligned. Though not studied in this section, it is conceivable that this effect could lead to superior nanorod LSCs in the future.

Three experiments were carried out with the nanorod LSCs, which demonstrated behaviours that are qualitatively also applicable to the general LSC. The first was the effect of dopant concentration on the LSC performance. The dopant concentration in the LSC governs the absorption of incident light, but also affects the waveguiding properties. As anticipated, the results showed that above a certain concentration, the absorption gain becomes small and is outbalanced by self-absorption losses. It is concluded that there is an optimum dopant concentration for a given LSC that maximises the optical concentration. In the second experiment, the dependence on LSC size, i.e. geometric gain was investigated. The edge output was found to increase approximately proportionally at small gains, but level off at larger gains. This implied a decrease in the waveguiding efficiency, which was explained by increased self-absorption when pathlengths are long.

Though the optical concentration continues to increase with geometric gain, there is a point above which the additional concentration is marginal and comes at the price of a large increase in LSC area. Taking the LSC cost into account, it is concluded that there are optimal dimensions that maximise the cost-to-power ratio for a given LSC. The third experiment demonstrated under laser illumination how the LSC output decreased with the distance of the illumination position from the edge. This was explained by longer pathlengths to the edge leading to higher re-absorption probabilities. An eventual levelling of the output at larger distances indicated a reduction in self-absorption with increasing distance. This was explained by the incremental redshift with each re-emission, which reduces the overlap of the emission with the absorption spectrum and makes subsequent re-absorptions less likely.

7.3 Biological Luminescent Centres

Efficient FRET can be difficult to achieve in practice due to the constraints on the relative orientations and separations of donor and acceptor molecules (see Equation 2.44). A type of biological luminescent centre called the phycobilisome (PBS) was recently identified as a candidate for highly efficient FRET as the individual molecules involved in the energy transfer are already aggregated in an optimal configuration [98]. Phycobilisomes are photosynthetic antennae protein from algae, which can be grown and harvested inexpensively and in large quantities. Columbia Biosciences Corp. have established a patented process for extracting and stabilising the phycobilisomes. Furthermore, it has been demonstrated that the optical properties of the phycobilisomes can be well preserved in a solid state waveguide [98]. The phycobilisome absorption is naturally tuned to the spectrum of light transmitted underwater. However, by controlling the growth conditions the absorption spectrum as well as the stability of the phycobilisome under temperature and irradiation can be modified. In collaboration with M. González and R. Walters from the US Naval Research Laboratory (NRL) and Columbia Biosciences Corp. studies were carried out on PBS LSCs at NRL. With only one publication by Ref. 98 on this topic prior to the author's conference paper in 2010 [210], phycobilisomes are considered a novel luminescent material for LSCs. Using different variants besides those examined in Ref. 98, it was investigated whether phycobilisomes can effectively reduce self-absorption and enhance the output of the LSC.

7.3.1 Background on phycobilisomes

Phycobilisomes [211–214] are antenna proteins found in red algae and blue-green algae (cyanobacteria), where they act as light harvesting complexes. They are made up of many bilin chromophores, which can differ in chemical composition and thereby lead to different optical properties [214]. The phycobilisome complex [213] comprises an allophycocyanin (APC) core with several phycoerythrin (PE) or phycocyanin (PC) disks attached to it in rod-like structures (see Figure 7.28). In an intact complex the light absorbed in the rods is transferred via FRET to the APC core, leading to potentially large Stokes shifts. The FRET efficiency can be as high as 95 %, while the luminescence quantum yields of the constituent chromophores are typically 98 % for the PE, 51 % for the PC and 68 % for the APC [211, 212].

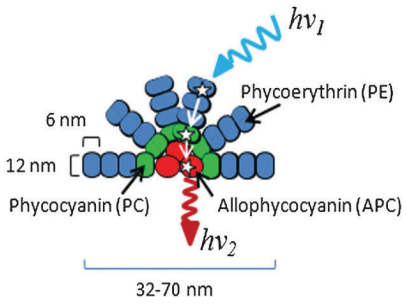

FIGURE 7.28: Schematic of a phycobilisome complex [98]. Most of the absorption takes places in the rods (in blue). Absorbed energy is transferred via multiple FRET processes to the core (in red) where photons are emitted with a large redshift.

Mulder *et al.* [98] compared intact phycobilisome complexes with partly decoupled ones and found that efficient FRET within intact complexes reduced self-absorption by approximately (48±5) % compared to their decoupled counterparts.

7.3.2 Experiment I

Initial measurements were carried out on a liquid LSC, which consisted of a glass cuvette containing a PBS solution. The advantage of this design was that the solution could be easily exchanged to measure different types and concentrations of PBS.

Two phycobilisome species were investigated, labelled P1 and RPE. P1 referred to an intact porphyridium cruentum PBS complex as shown in Figure 7.28, where the overall luminescence QY is limited by that of the APC. Such a complex had also been examined

before in Ref. 98. RPE referred to R-phycoerythrin, the protein located at the top of the light harvesting PBS antenna. Since RPE lacked the FRET cascade of the intact PBS complex it had a smaller Stokes shift than P1. The species were harvested from red algae, isolated, purified and stabilised by Columbia Biosciences Corp., who also provided luminescence QY estimates of 60 % for P1 and 84 % for RPE. The spectral properties of the P1 and RPE materials are shown in Figure 7.29. The P1 emission spectrum had its main peak between 650 nm and 700 nm, but it also exhibited a smaller one around the wavelength of the RPE emission peak. This indicated that the non-radiative energy transfer between the constituents of the complex was not perfectly efficient.

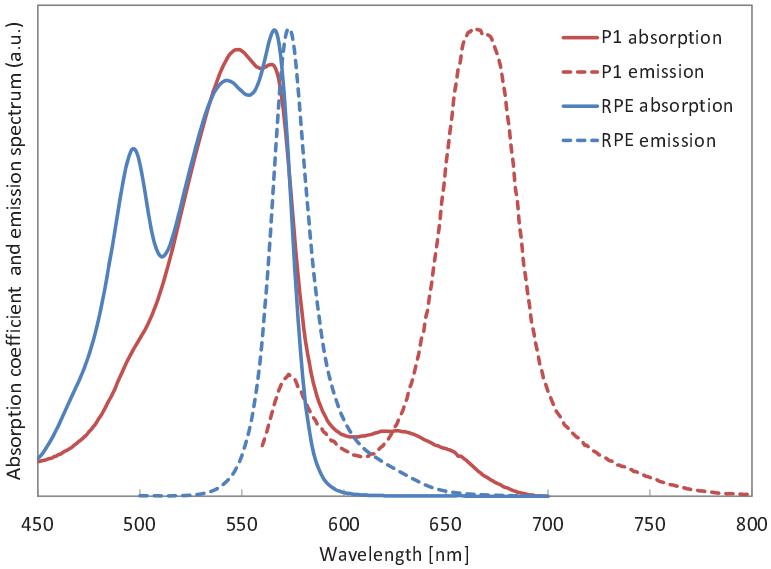

FIGURE 7.29: Absorption and fundamental emission spectra of the PBS species P1 and RPE used for the liquid LSC experiments.

Three different concentrations of RPE were tested, labelled "1 mg", "2 mg" and "6 mg" referring to the mass of the phycobilisomes in the original solution. Unfortunately, the volume of the solution had not been measured initially, so that the absolute phycobilisome concentration in the solution could not be determined. However, a relative comparison between the three concentrations was still possible. The solution was a 100 millimolar sodium phosphate buffer with an approximated refractive index of 1.1 to 1.2.

The experimental setup is illustrated in Figure 7.30. The liquid LSC in form of a filled glass cuvette was attached to a vertical screen facing a solar simulator. The cuvette was open on top, had 1 mm walls, a front surface area of 7.6 cm×2.7 cm and an overall

thickness of 0.5 cm. The cuvette was made of borosilicate with a refractive index of 1.51 to 1.54. This meant that there was a considerable index mismatch of more than 0.3 between the PBS solution and the cuvette. With the opening of the cuvette facing upwards it did not have to be closed off. Four different solutions were examined, one containing P1 and three containing the different concentrations of RPE. The solutions were filled into the cuvette with a syringe, and the cuvette was emptied and rinsed between the measurement runs.

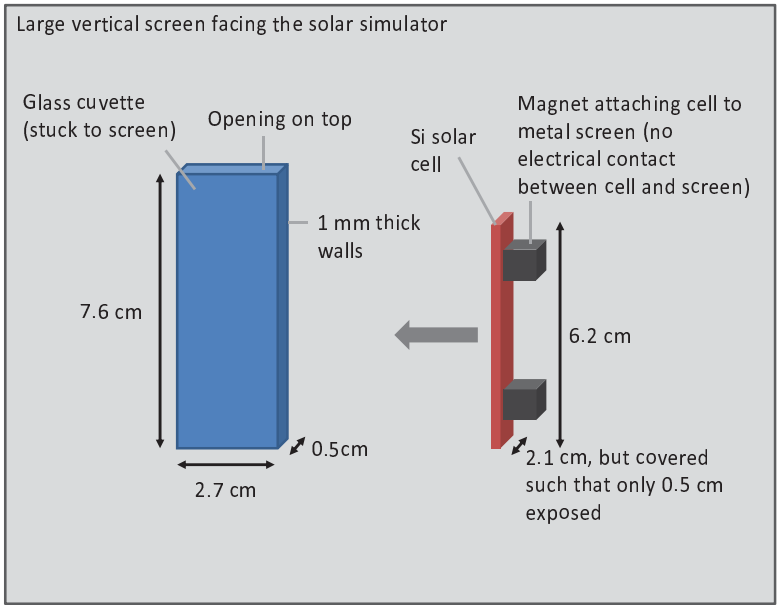

FIGURE 7.30: Schematic of the experimental setup for the liquid phycobilisome LSC. The photocurrent from the LSC was measured with a silicon solar cell, which was attached with an airgap to one LSC edge as indicated in the schematic.

The solar simulator, placed more than a meter away from the screen, was a Spectrolab X-25 model with a 2.5 kW xenon lamp. The solar simulator was equipped with an filter to output an AM1.5 global spectrum (one sun), as shown in Figure 7.31.

A silicon solar cell was used to characterise the LSC. The QE of the cell is shown in Figure 7.32. Since the screen was metallic, magnets could be used to attach a construction holding the solar cell to the screen (see Figure 7.30). This way the cell could be easily moved and placed against one edge of the LSC, with an airgap and hence not index matched. Since the cell had dimensions of 6.2 cm×2.1 cm, part of it protruded the 0.5 cm thick LSC edge and was covered with black tape to prevent ambient or stray light from entering it. The cell was also too short to cover the entire length of the LSC, which could be considered a further shortcoming of the experimental setup. However,

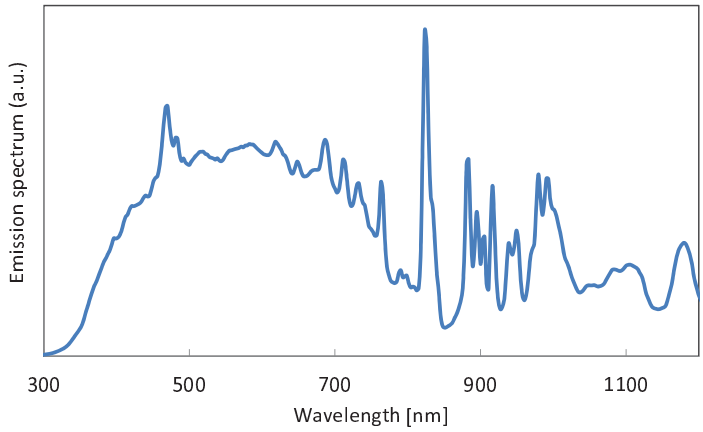

FIGURE 7.31: Spectrum of the solar simulator used at the US Naval Research Laboratory for the measurements on the phycobilisome LSCs. The simulator was a Spectrolab X-25 model with a 2.5 kW single source Xe lamp adjusted to AM1.5 global simulation and an 8-inch beam diameter.

the emission profile along the length of the LSC edge was assumed to be nearly homogeneous. Therefore, it seemed reasonable to approximate the photocurrent density over the cell surface by scaling up to obtain the photocurrent out of all LSC edges.

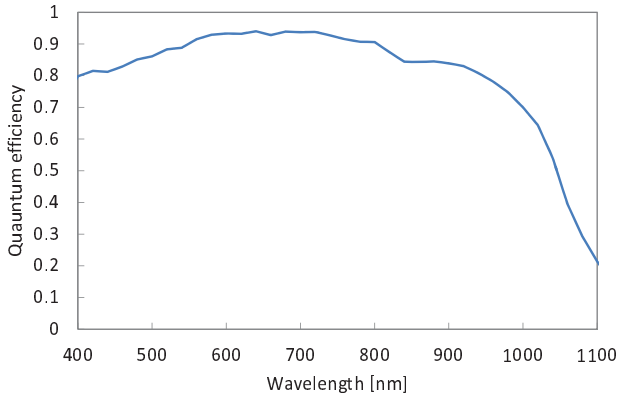

FIGURE 7.32: Quantum efficiency of the silicon solar cell used for the first characterisation at the Naval Research Laboratory.

The experimental method was a light current measurement, in which the photocurrent was measured as the bias of the solar cell was varied. Initially, the silicon cell was placed directly in the target area on the screen to measure the incident light from the solar simulator (see Figure 7.33). Figure 7.34 shows the results for the four different measurement runs along with a control run on an empty cuvette. The control run had a relatively high light current. Comparing the current density for the control run with the direct photocurrent in Figure 7.33 showed that at zero bias $\sim 21\,\%$ of the incident light was coupled into the solar cell in the absence of luminescent material. This meant

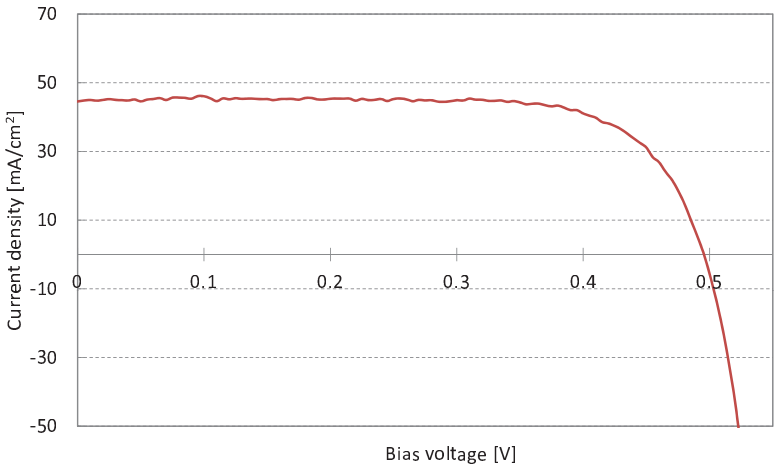

FIGURE 7.33: Incident light from the solar simulator quantified via light current measurements with a silicon solar cell (see Figure 7.32) placed directly in target area on screen. The data was averaged over three measurement runs with a standard error of less than $1\,\mathrm{mA\,cm^{-2}}$

that direct coupling of incident light into the cell, reflection in the experimental setup and scattering from the glass cuvette were significant.

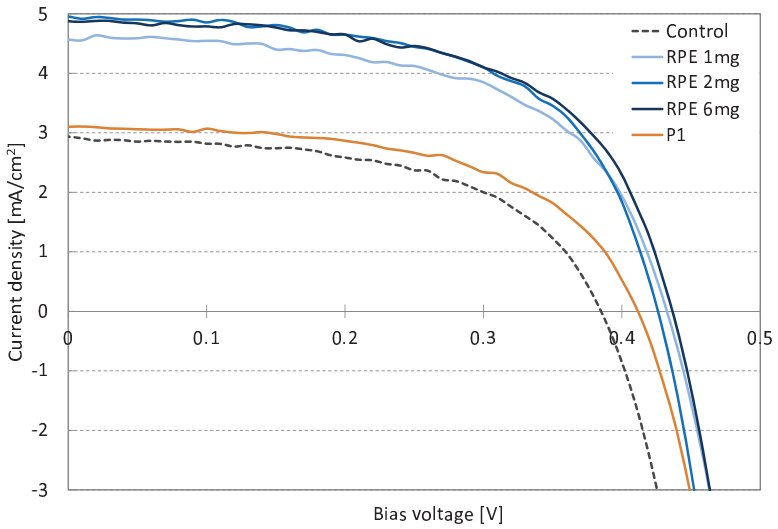

FIGURE 7.34: J-V curves of the liquid phycobilisome LSCs compared against a control sample, which consisted of an empty cuvette. It is evident, that in the absence of the luminescent material a significant amount of incident light was coupled into the solar cell directly from the light source or via scattering. The curves shown here were averaged over three measurement runs with a standard error of less than $0.2\,\mathrm{mA\,cm^{-2}}$ in all cases.

Despite a seemingly advantageous Stokes shift, the P1 material performed significantly worse than the RPE material and only slightly better than the control sample. This was attributed mainly to the poor QY of P1 compared to RPE. The power generated in

the solar cell and per LSC area for each of the LSC-cell systems is shown in Table 7.7. The power generated in the cell under direct illumination is also shown for comparison. Not accounted for in the power per LSC area was the systematic error in assuming comparable power densities between the short and the long LSC edges. The short edge is expected to have a slightly higher power density, but raytrace simulations indicated that the difference was small. As an approximation to the liquid LSC a homogeneous LSC with the dimensions of the cuvette was modelled under AM1.5 direct illumination. A refractive index of 1.5 and a background absorption coefficient of $2\,\mathrm{m}^{-1}$ were simulated. The P1-type PBS shown in Figure 7.36 was modelled with a peak absorption coefficient of $1000\,\mathrm{m}^{-1}$ and a QY of 68 %. No index matching between the LSC and the cells on the edges was assumed. At an optical efficiency of $\sim$8 % and a waveguiding efficiency of $\sim$41 % it was found that the photon flux out of the short edge was only a relative $\sim$4 % higher than out of the long edge.

Amongst the RPE samples, a higher power per LSC was achieved with higher concentration. The results show that for a given illumination area, all of the LSC-cell systems would generate significantly less power than an equal area Si cell. More importantly, a given Si cell area would generate approximately 12 times more power under direct illumination than attached to the best of these PBS LSCs. This is partly due to the small geometric gain of the liquid LSC of 2.0. It should also be noted, that more than half of the solar cell was blacked out in this experiment. This would lead to a comparably large dark current, which in turn leads to a smaller open circuit voltage and hence to a smaller power. Though the same, partially covered cell was used for the direct illumination measurement, the dark current would have had a larger impact on the LSC-cell systems, where the photocurrent was comparably low. A further limiting factor was the significant refractive index mismatch between the cuvette and the PBS solution.

The emission spectrum from the edge was also measured and is shown in Figure 7.35. The measurements were carried out with an Ocean Optics USB2000 spectrometer with a fibre optic cable to collect the emission. As expected, one can clearly see the progressive redshift with increasing concentration of the RPE species. This shows the still significant overlap between absorption and emission spectra in the RPE species; a material with a larger Stokes shift would be less sensitive to redshift with increasing concentration.

In summary, the initial experiments on phycobilisomes did not show any advantages

	Cell generated power [mW]	Power/LSC area [mW/cm^2]
Si cell direct	52.1 ± 0.3	16.4 ± 0.1
Control	1.93 ± 0.01	0.30 ± 0.01
P1	2.25 ± 0.08	0.36 ± 0.01
RPE 1 mg	3.65 ± 0.03	0.58 ± 0.01
RPE 2 mg	3.90 ± 0.09	0.62 ± 0.01
RPE 6 mg	4.0 ± 0.1	0.63 ± 0.02

TABLE 7.7: Comparison of cell generated power and power generated per LSC front surface area under an AM1.5 global spectrum from the solar simulator. Values are given for the silicon solar cell alone and the LSC-cell system. The errors stated here refer to measurement errors; possible systematic errors were not taken into account.

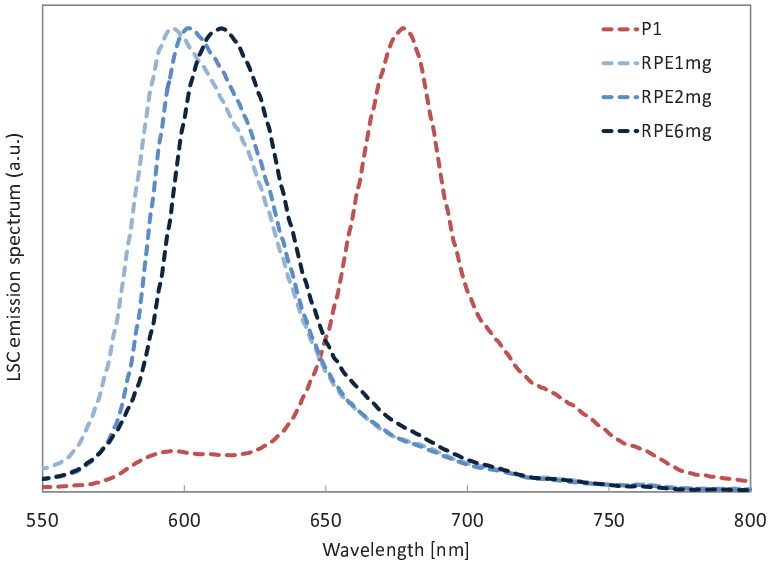

FIGURE 7.35: Edge emission spectra of the liquid phycobilisome LSC for the P1 species and the three dopant concentrations of the RPE species.

compared to other lumienscent materials. In fact, they showed that the LSC-cell system generated significantly less power than the cell alone under direct illumination. In part, the LSC-cell system performances were deteriorated by shortcomings in the setup. There was an index mismatch between the glass cuvette and the solution leading to reflections at the interfaces. The airgap between the cell and the LSC as well as the only partial coverage of the LSC edge by the cell meant that the coupling of the emission out of the LSC edge was not ideal. Moreover, the PBS QYs were not high enough to compensate for the various losses. A smaller power was also to be expected from the short absorption range of the phycobilisomes compared to the Si cell.

It would have been useful to model the experiments from this section with the Raytrace

Model to understand the loss mechanisms and future potential of the phycobilisomes better, but unfortunately this could not be carried out due to too many unknown parameters, such as the absolute absorbance, exact refractive indices, exact FRET efficiencies and luminescence quantum yields.

7.3.3 Experiment II

A second PBS experiment was carried out on the RPE material and a P1-type material. Columbia Biosciences had modified the P1 PBS to separate the absorption and emission peaks of the material even further. The spectra are shown in Figure 7.36. In comparison to Figure 7.29 one can indeed see an increased separation between the main absorption peak at $\sim 500\,\text{nm}$ and the main emission peak at $\sim 670\,\text{nm}$. However, the emission spectrum shows a secondary peak around 570 nm, presumably as a result of an incomplete FRET cascade, which can be caused by detachment of the outer parts of the PBS complex from the core. Moreover, there is also a secondary absorption peak and an absorption tail reaching up to $\sim 670\,\text{nm}$, into the range of the main emission peak. These factors would clearly hinder the reduction of self-absorption. The luminescence QY of the PBS was not determined, but is expected to be comparable to the values estimated for the first PBS experiment.

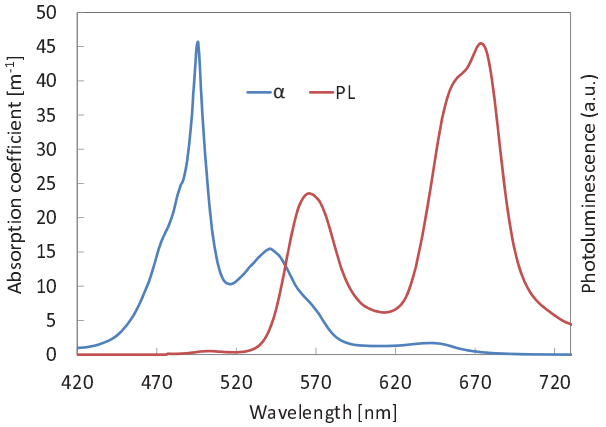

FIGURE 7.36: Absorption and emission spectra of a solid phycobilisome LSC based on a P1-type material.

After the liquid LSC had been found to be impractical, the second experiment was carried out on solid samples. The samples were homogeneously cast from an acrylamide/bis-acrylamide gel with 2-3 % added sucrose to smooth out the refractive index. The polymerisation was carried out using tetramethylethylenediamine (TEMED) as a catalyst

and by curing the samples for ∼30 min. The refractive index of the samples was ∼1.5. The dimensions of the RPE sample were 7.5 cm×2.5 cm×0.5 cm, while the P1-type sample had an identical front surface area, but was only 0.1 cm thick. A bespoke sample holder had been built to allow for better control of the experimental environment. As shown in Figure 7.37, the sample could be fully encased in the holder, with a solar cell attached (with an airgap) at the short edge. A cap ensured that no ambient light entered the part of the cell protruding the LSC edge.

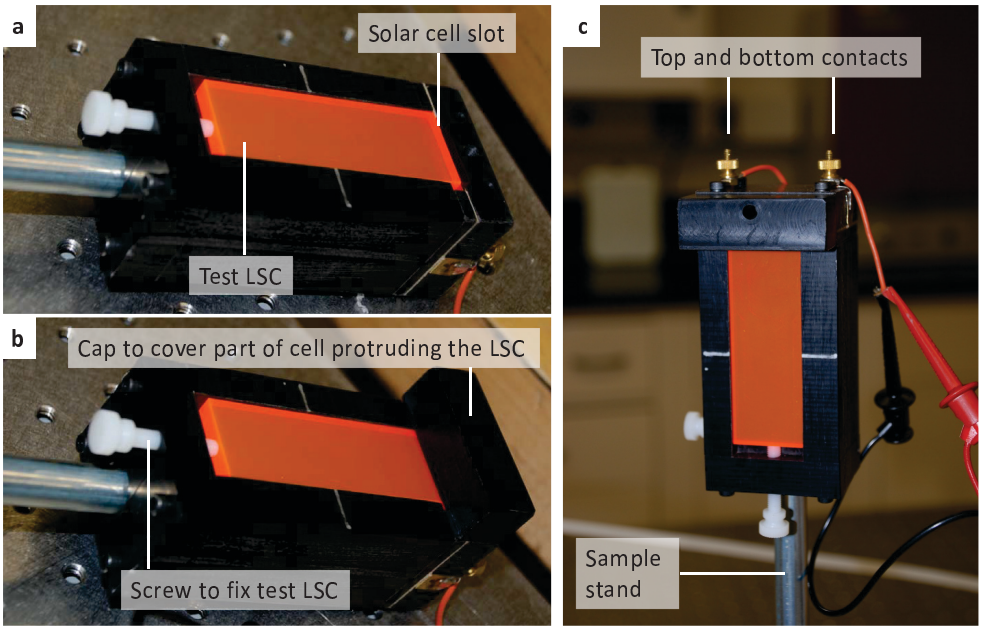

FIGURE 7.37: Pictures of solid RPE phycobilisome LSC sample (with 7.5 cm×2.5 cm front surface area) in the custom-made sample holder.

Since the solar cell used in the first experiment did not fit into the bespoke sample holder, a different, 2 cm×2 cm silicon cell was used for these measurements (see Figure 7.38 for the quantum efficiency). Due to the way the cell was attached to the LSC (see Figure 7.39), one corner area of 5 mm×6 mm was partially shaded. This was not accounted for in the analysis and is therefore considered a systematic error. The light source was the same solar simulator as in the first experiment with an AM1.5 global spectrum (see Figure 7.31).

The J-V curve for the Si cell directly illuminated by the solar simulator is shown in Figure 7.40. It should be noted, that the characteristics of this cell such as the QE and the fill factor differed from those of the cell used in the first PBS experiment.

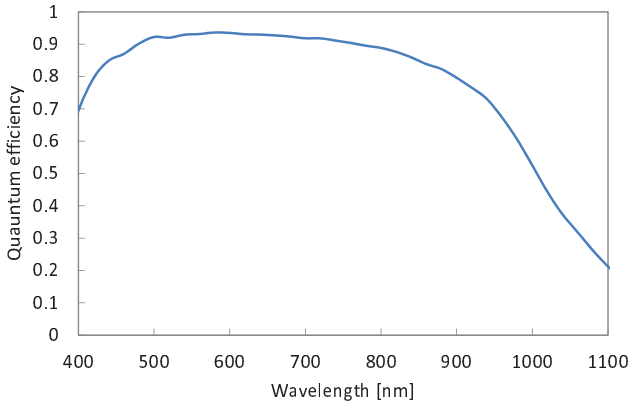

FIGURE 7.38: Quantum efficiency of the silicon solar cell used for the second experiment at the Naval Research Laboratory.

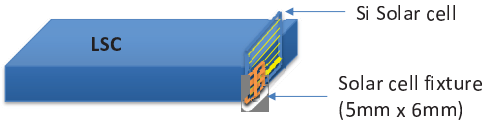

FIGURE 7.39: The fixture attaching the solar cell to the LSC partially shaded a 5 mm×6 mm area of the cell.

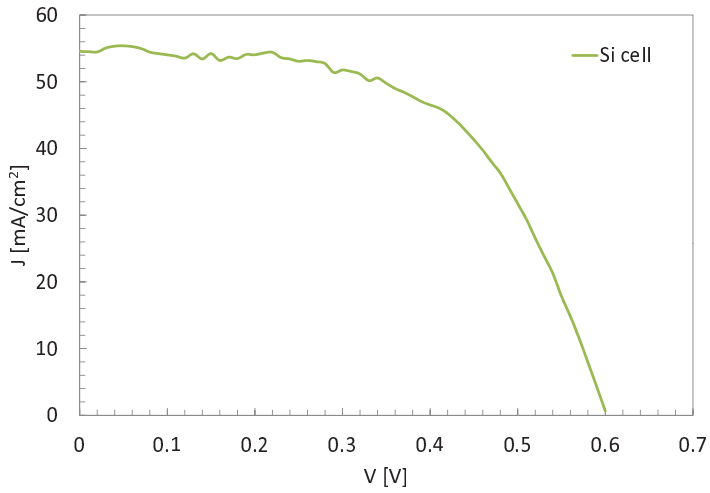

FIGURE 7.40: J-V curve from the Si cell used for the second PBS experiment (see Figure 7.38), placed directly in the target area of the solar simulator. Though within the LSC holder the cell was partly covered, the direct J-V measurements shown here were carried out with the entire 2 cm×2 cm area exposed.

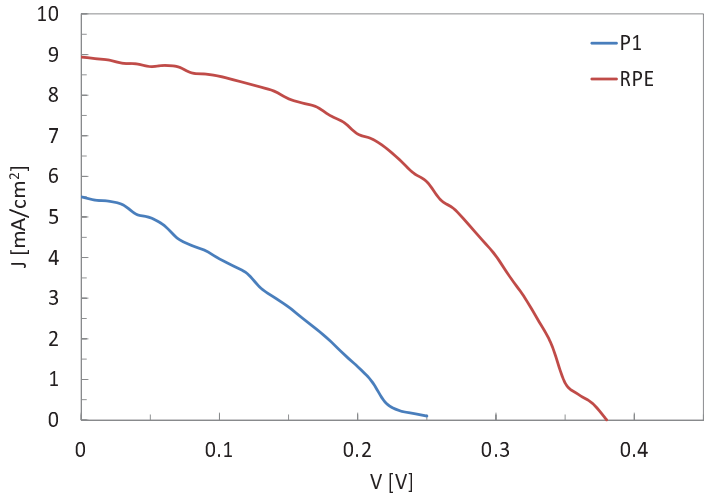

FIGURE 7.41: J-V curves of the solid phycobilisome LSCs in the sample holder under AM1.5 global illumination.

The J-V results for the two samples are shown in Figure 7.41. As in the first PBS experiment, the RPE sample was found to perform better than the P1-type sample. A systematic error that was introduced, but not quantified, was that different amounts of the silicon cell were exposed in the different measurements: in the direct illumination measurements (Figure 7.40) the entire 4 cm^2 cell area was exposed, whereas only 1 cm^2 and 0.2 cm^2 were exposed in the RPE and P1 cases, respectively. This would have put the LSC samples at a disadvantage due to large dark currents. Furthermore, it is possible that FRET in the P1 complex was affected by the solid matrix compared to the solution. Finally, it was found that the P1 sample degraded quickly (over the period of few hours) under the AM1.5 global irradiation.

The comparison of the power generated in the cell and the power per LSC area (see Table 7.8) showed that the LSC-cell systems studied here were still far from competitive. This was due to narrow absorption spectra, low QYs and possibly a still significant spectral overlap.

7.3.4 Raytrace Simulations

In order to determine the potential of phycobilisomes, the optical efficiency and the optical concentration were simulated, both under realistic and under idealised conditions. In both cases a range of LSC sizes were modelled, all at a thickness of 5 mm. For the host material a high quality polymer with a refractive index of 1.5 and a background

	Cell generated power [mW]	Power/LSC area [mW/cm^2]
Si cell direct	19 ± 1	356 ± 19
P1 (solid)	0.4 ± 0.1	0.79 ± 0.05
RPE (solid)	1.5 ± 0.1	0.05 ± 0.01

TABLE 7.8: Comparison of cell generated power and power generated per LSC front surface area under an AM1.5 global spectrum from the solar simulator for the solid LSCs. Values are given for the silicon solar cell alone and the LSC-cell system. The errors stated here refer to measurement errors; possible systematic errors were not taken into account.

absorption of 0.3 m^{-1} was assumed. The simulations were carried out for the case of optically coupled solar cells at the edges, so that internal reflection at the edges was omitted. The variant of the P1 phycobilisome introduced in the previous subsection was used as the basis for the simulations because of its large Stokes shift.

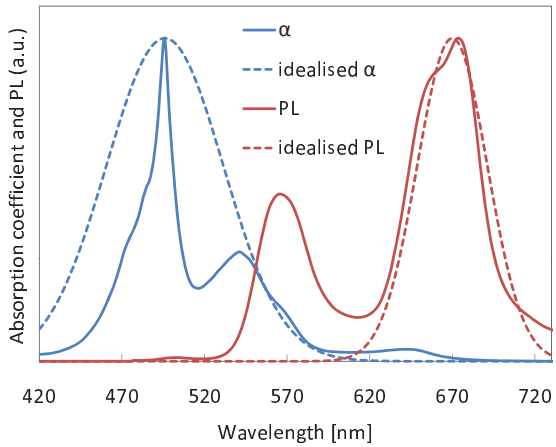

FIGURE 7.42: Original and idealised spectra of a P1-type phycobilisome.

The realistic simulations were based on the actual P1 spectra (see Figure 7.42). The results presented in Figure 7.43 show that the PBS has shortcomings that lead to low optical efficiencies and no effective optical concentration up to dimensions of approximately 50 cm×50 cm. The waveguiding efficiencies were found to drop from ∼ 41 % for a 5 cm×5 cm LSC to ∼ 23 % for a 50 cm×50 cm LSC and further to ∼ 17 % for a 100 cm×100 cm LSC (see Table 7.9).

As illustrated in Figure 7.42, the P1 spectra were idealised by broadening the absorption and by removing the secondary emission peak, thereby reducing self-absorption. The results for the idealised PBS simulations are shown in Figure 7.44. For such an idealised PBS, the optical efficiency would decrease only slightly with concentrator size. This

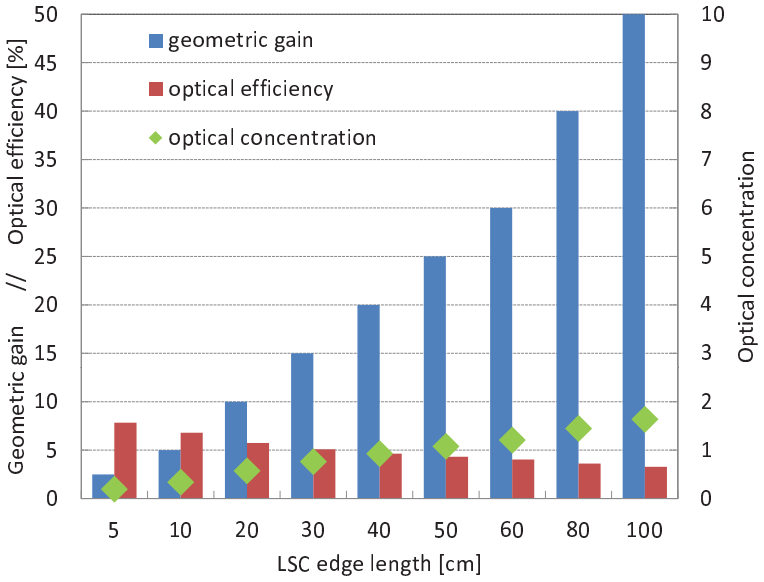

FIGURE 7.43: Performance projection for realistic phycobilisome LSCs with spectra as shown in Figure 7.42 (original spectra) under AM1.5 direct irradiation. Square LSCs with a thickness of 5 mm, a refractive index of 1.5 and a background absorption coefficient of $0.3\,\mathrm{m}^{-1}$ were modelled. The QY of the PBS was assumed to be 68 % (see Ref. 98), and the peak absorption coefficient was set to $1000\,\mathrm{m}^{-1}$. The optical efficiencies and concentration ratios are based on a wavelength range from 300 nm to 1160 nm, the approximate silicon band edge.

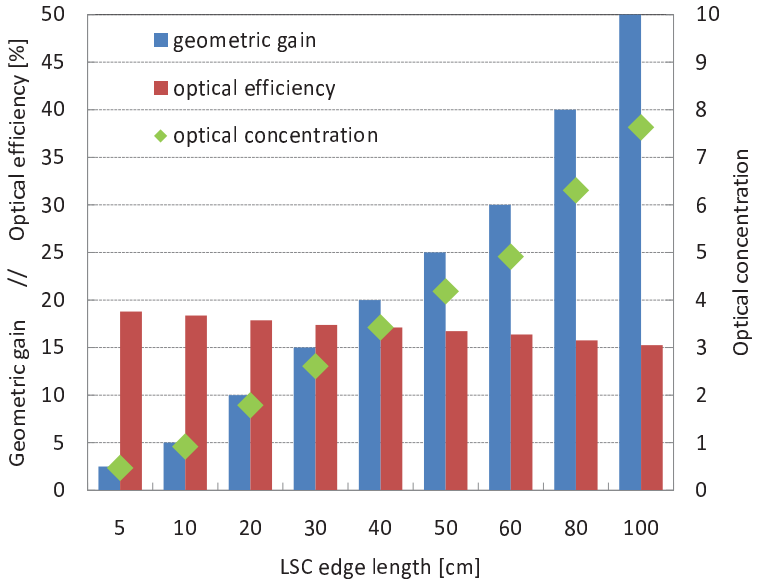

FIGURE 7.44: Performance projection for idealised phycobilisome LSCs with spectra as shown in Figure 7.42 (idealised spectra) under AM1.5 direct irradiation. Square LSCs with a thickness of 5 mm, a refractive index of 1.5 and a background absorption coefficient of $0.3\,\mathrm{m}^{-1}$ were modelled. The QY of the PBS was assumed to be 95 %, and the peak absorption coefficient was set to $5000\,\mathrm{m}^{-1}$. The optical efficiencies and concentration ratios are based on a wavelength range from 300 nm to 1160 nm, the approximate silicon band edge.

would make large LSC sizes feasible. Simulations of an idealised 1 m×1 m×5 mm PBS LSC with a QY of 95 % indicate that more than 15 % of the AM1.5 spectrum in the range from 300 nm to 1160 nm could be coupled to solar cells at the edges. For these dimensions the geometric gain would be 50, resulting in a photon concentration ratio of approximately 8. Since the narrow-band emission from the LSC would be well matched to the silicon absorption, the cells would produce around 13 times their output compared to direct illumination.

The waveguiding efficiency, a key quantity with respect to self-absorption losses, is shown in Table 7.9 for both the realistic and the optimised PBS LSC simulations. One can see that in the optimised case a high waveguiding efficiency of over 50 % is maintained even at large dimensions of 100 cm×100 cm, owing to low self-absorption.

	$\eta_{\text{waveguide}}[\%]$		
	5 cm	50 cm	100 cm
Realistic PBS	41	23	17
Optimised PBS	68	61	55

TABLE 7.9: Waveguiding efficiencies for selected LSC edge lengths from the realistic phycobilisome simulations shown in Figure 7.43 and the optimised simulations shown in Figure 7.44.

7.3.5 Conclusion

The topic of this section was phycobilisomes, a novel material for luminescent concentrators. The phycobilisome LSCs characterised in this section did not achieve the desired low self-absorption and high waveguiding efficiencies. Despite a clear separation of the main absorption and emission peaks due to FRET, secondary peaks and an extended absorption tail led to a significant spectral overlap and deteriorated the waveguiding efficiency. Moreover, the quantum yields of the samples were found to be too low to compete with dyes or quantum dots as luminescent materials. Further engineering of the phycobilisomes and of their integration in the LSC matrix would be required to make phycobilisomes a suitable luminescent material for LSCs.

Like organic dyes, phycobilisomes have the drawback of a narrow absorption spectrum. The absorption of a phycobilisome doped LSC could possibly be broadened by absorbing

the light with nanocrystals that are coupled via resonance energy transfer to phycobilisomes. The feasibility of this approach is supported by the fact that FRET between organic and inorganic luminescent centres has been successfully demonstrated (see for example Ref. 87).

Simulations based on optimised spectra suggest that, if phycobilisomes can be manipulated to produce a more pronounced Stokes shift, large LSCs with optical concentrations of approximately 8 could be obtained. One way to extend the Stokes shift would be to use an organism with a blue-shifted spectrum; the second would be to couple a dye to the phycobilisome and moving the emission wavelength from 665nm to about 700nm. Improving the quantum yield may be possible by metal enhanced fluorescence. The thin-film configuration would be required for metal enhanced fluorescence since the fluorophores have to be within the resonant range of the metal. This configuration does not fundamentally affect the photon concentration ratio compared to a homogeneously doped waveguide and would in fact improve the photo-stability of the fluorophores. The successful fabrication of thin-film PBS LSCs has recently been reported in Ref. 215.

The preliminary experiments have shown that photo-stability issues may also need to be overcome before phycobilisomes become viable. However, they could be an attractive alternative to conventional luminescent materials, especially if they can be grown and extracted inexpensively.

7.4 Chapter Conclusion

This chapter investigated nanorods and phycobilisomes as novel luminescent materials for LSCs with the aim to reduce re-absorption losses. Nanorods are similar to quantum dots as they have a broad absorption band. The investigations indicated that nanorods can in principle offer a larger Stokes shift than quantum dots, thereby reducing self-absorption. However, it was found that this effect was not significant enough to compensate for the relatively poor luminescence quantum yields. Therefore, the samples characterised in the chapter did not produce attractive optical efficiencies or concentration ratios. Nevertheless, nanorods are considered a promising luminescent material for LSCs, under the assumption that their QY can be improved in future. Moreover, nanorods may also enable directional emission due to their anisotropic geometry.

Phycobilisomes can exhibit highly efficient resonance energy transfer, which could, in principle, reduce the probability of re-absorption. Experimental results indicated that further research is still required to improve their spectral properties and fabricate viable LSCs based on phycobilisomes. The main challenge lies in minimising secondary absorption and emission peaks whilst maintaining a large Stokes shift.

The experiments presented in this chapter have shown that suitably low self-absorption in luminescent materials for the LSC is hard to achieve. Though self-absorption remains a major lever for improving the LSC performance, other routes to increasing the efficiency may be more viable, such as the integration of selective reflectors to contain the emission or possibly the optical engineering of the LSC as proposed by Ref. 142.

Chapter 8

Conclusion

This thesis has presented experimental and modelling analyses of a number of novel geometries and materials for the practical exploitation of LSCs. The results have been published in 15 conference proceedings and 2 refereed journal papers (see Appendix for full list), of which the author is first named on 8.

8.1 Chapter 4

Chapter 4 presented a variety of short experiments based on the Raytrace Model. The first one was a study of the angular response of the LSC, carried out using a combination of experimental measurements and raytrace simulations, which had not been previously published in this form before. The experiment showed that the LSC output is reasonably insensitive (less than 10 % of variation) to change in angle of incidence up to approximately 70 ° from the normal. This finding justifies the use of the LSC as a static, non-tracking concentrator, but also shows that the angular response of the typical LSC is not notably better than that of a standard silicon solar cell with an anti-reflective coating.

The second experiment investigated the use of mirrors on LSC edges as a means to reduce the solar cell area required. It was shown via analytical, graphical and raytrace analyses that edge mirrors do not yield any improvement in the cost of PV energy for a given area. Though many publications in the field include the use of edge mirrors, the result of this investigation has not been previously stated in the literature.

The third experiment was a raytrace study of specular and diffuse back reflectors and their effect under direct and diffuse illumination. It was found that both types of reflectors, attached to the LSC back surface with an air gap to maintain TIR, lead to similar improvements of the LSC output by increasing the pathlength of the light in the active medium and thus increasing the absorption probability of incident light. However, the effect was found to be larger under direct illumination than diffuse because the average pathlength is already relatively large in the latter case.

The fourth experiment considered a new tapered LSC design, with the aim of improving the waveguiding properties by directing trapped luminescence preferentially towards the solar cells on the edges. The purpose of this section was to determine the advantage of such a tapered design, that gets thicker towards the PV cell edge. The raytrace simulations indicated a photon flux enhancement could indeed be achieved when the tapering was very pronounced. A 30-40 % relative improvement was predicted in the case of a 50 cm×50 cm LSC with a 10 cm maximum thickness. However, for practical LSC dimensions the advantage was found to be of the order of the modelling uncertainty, $\sim 10\,\%$ (relative), and therefore insignificant. The advantage of the tapered design was not considered sufficient to pursue it further, especially in the light of the more complicated fabrication requirements and potential structural integrity issues.

The fifth experiment was a raytrace study of self-absorption, which, being a major loss mechanism, has been discussed extensively in the literature. The novelty of this study was the comparison of the established analytical model by Batchelder *et al.* with raytrace simulations, with the aim to understand why the analytical model was found to break down in the case of significant self-absorption. It was shown that the error was due to the assumption of a constant probability of re-absorption in the analytical model. The Raytrace Model illuminated how the probability of re-absorption varied with each generation of re-emission.

The sixth and final experiment of this chapter described a novel application of the LSC as a power generating window. Using UV-absorbing luminescent materials, the LSC can be made mostly transparent in the visible whilst still absorbing high energy photons to generate electricity. Such an LSC could be very attractive for building integrated applications. Based on the Lumogen Violet 570 dye, the annual energy yield of a 50 cm×50 cm transparent LSC/cell system was estimated to be $23\,\mathrm{kWh/m^2}$ and

28 kWh/m^2 in London and Marseille, respectively. The conversion efficiencies of little over 1 % can be considered a significant advancement compared to conventional windows, which produce no energy. Moreover, such a power generating window could be used in combination with the 2-axis tracking smart window described in Ref. 188, which is estimated to produce 90 kWh/m^2 annually in London. The transparent LSC would allow most of the direct light to pass into the tracking system while providing an energy boost to the overall system of approximately 25 %.

8.2 Chapter 5

The research question of Chapter 5 was whether thin-film (TF) LSCs have an advantage over conventional, homogeneously doped LSCs. The investigation of this question seemed appropriate since the thin-film structure has been studied by several research groups in the recent past, yet no comprehensive comparison of the performance had been published prior to a conference paper of the author's in 2007. In fact, the advantage of TF LSCs had been debated in the literature on several occasions, amongst others by the LSC pioneers Rapp and Boling, who had proposed the thin-film design in the first place. Originally, the expectation had been that the TF LSC had fewer re-absorptions and therefore a better optical efficiency. The analyses presented in Chapter 5 showed that TF LSCs and homogeneous LSCs perform equally well in terms of optical efficiency. This was concluded from both experimental and raytrace comparisons. The experimental comparison was carried out on two sets of 5 cm×5 cm concentrators with comparable absorbances between the thin-film sample and the homogeneously doped sample, where the photocurrent measured at the edge was found to be identical, within errors, for each set. A reproduction of this experiment with the raytrace model qualitatively supported the result, but also exposed a small, yet significant advantage in the waveguiding efficiency of the homogeneous variant. This was attributed to edge effects, which was confirmed by simulating larger samples where the contribution of these effects was found to vanish, as one would expect for edge effects. For a comprehensive comparison, the illumination position, film orientation, luminescence quantum yield, absorbance and film thickness were varied using the model. In all cases, an identical performance between the TF and the homogenous LSC was observed. The only notable difference in the output of the two LSC variants was found to be in the angular emission profile, which was

investigated using experimental measurements as well as raytrace simulations. The main result of this chapter was that the TF LSC does not lead to reduced self-absorption and better waveguiding efficiencies. However, the TF LSC is still considered advantageous compared to the homogeneous one because it can offer a wider choice of waveguide materials, enable potentially simpler and more scalable fabrication methods and possibly facilitate fluorescence resonance energy transfer. The fact that recent publications such as a review paper from 2010 by R. Reisfeld [124] claim reduced self-absorption losses with the thin-film design indicates that the main result of Chapter 5 is not yet widely known or accepted.

8.3 Chapter 6

Chapter 6 investigated a novel application of a linear LSC referred to as a light-bar. Designed to be part of a BIPV system, the light-bar acts as a secondary concentrator transferring the radiant energy collected over its length to solar cells attached to its ends. The BIPV system has a Venetian-blind like structure which blocks out solar glare and allows a substantial amount of diffuse light through for internal illumination. Linear Fresnel lenses act as the primary concentrators that focus the direct light onto the light-bars. The aim of this chapter was to determine the optimal design of the light-bar. It was demonstrated that, in contrast to the planar LSC, a composite linear LSC comprising an active core within a transparent shell had an enhanced waveguiding efficiency compared to a homogeneously doped one of the same dimensions. This effect is afforded by the primary concentration onto the active core. A comparison between triangular, square and circular cross-sections showed that the latter had the best waveguiding properties, provided that the emission occurred close to the surface. In fact, it was found that the optimal cylindrical structure comprised an active shell and a transparent core. Using realistic assumptions and actual dye spectra, it was estimated that a 1 m long cylindrical light-bar with a 2 cm diameter could generate a peak power of $\sim 5\,\mathrm{W}$ when used as a secondary concentrator in the proposed BIPV system, assuming a primary concentration factor of 20. Further simulations suggested that with optimised spectra, absorbing a larger part of the incident sunlight, a power of nearly $60\,\mathrm{W/m^2}$ could be generated under AM1.5 direct light at an overall system efficiency of $\sim 5.9\,\%$. This appears to be a competitive efficiency in comparison to the 7.1 % record efficiency from the opaque LSC

reported in Ref. 129, taking into account that this Venetian blind-like system would let much of diffuse light pass.

8.3.1 Chapter 7

Chapter 7 discussed novel luminescent materials. The research question of this chapter was whether these materials could considerably reduce self-absorption losses. The first topic were nanorods, a fairly new type of inorganic luminescent centres for LSCs. Like quantum dots, nanorods offer a broad absorption spectrum. The asymmetrical shape of nanorods was expected to give rise to a more pronounced Stokes shift compared to quantum dots. Experimental measurements and raytrace simulations were carried out on different sets of nanorod LSCs with the result that self-absorption was still found to be a prevailing performance limiting factor. It was found that nanorods are not generally preferable to quantum dots in terms of self-absorption since the structure and the composition of the particles plays an important role. However, a raytrace comparison of CdSe quantum dots and nanorods of comparable size and absorption spectra, with identical QYs, showed that the nanorod LSCs clearly exhibited less self-absorption. This resulted in almost twice the waveguiding efficiency being achieved with the nanorod LSCs compared to the quantum dot LSCs. It was concluded, that nanorods could in principle be exploited to fabricate LSCs with low self-absorption. In addition, nanorod ensembles can exhibit directional emission when aligned. Though not studied in this thesis, it is conceivable that directional emission could make nanorods more relevant for future LSCs.

The second topic of Chapter 7 were phycobilisomes (PBS), light harvesting proteins found in algae. The work presented on this topic was novel in that only one publication [98] prior to the author's conference paper in 2010 [210] had examined PBS as a luminescent material for LSCs. Phycobilisomes are particularly interesting because they exhibit efficient fluorescence resonance energy transfer (FRET), which leads to a larger spectral separation and can therefore be a way of reducing self-absorption. While FRET is generally constrained by donor and acceptor separation and orientation, the aggregation of the components in the PBS complex is conducive to FRET. In this chapter, new variants of PBS were examined in order to assess their feasibility as low self-absorbing material in LSCs. The PBS LSCs characterised in this chapter failed to achieve the desired

low self-absorption and high waveguiding efficiency. Despite a clear separation of the main absorption and emission peaks due to FRET, secondary peaks and an extended absorption tail led to a significant spectral overlap and deteriorated the waveguiding efficiency. Moreover, the quantum yields of the samples were found to be too low to compete with dyes or quantum dots as luminescent materials. However, raytrace simulations suggested that, if the problems with secondary peaks and low QYs can be resolved, large PBS LSCs with optical concentrations of approximately 8 could be obtained. In conclusion, both nanorods and phycobilisomes remain promising luminescent materials, but further particle engineering is required before their potential can be exploited in LSCs. In the light of this difficulty, other ways of reducing the LSC losses such as the containment of the emission using selective reflectors should be developed as well.

8.4 Outlook

The LSC is a feasible concept in that it could deliver a reduced cost per unit power for photovoltaic solar energy and that it could cater to specific markets such as the building integrated environment. Given the recent decline of crystalline silicon cell prices and the role of thin-film solar cell technologies in reducing the cost of PV, it is the author's opinion that the main application for the LSC lies in BIPV.

Currently the LSC still suffers shortcomings, mainly regarding the waveguiding properties. The feasibility of the LSC is subject to the suppression of the predominant loss mechanism: the escape cone loss, which is amplified by re-emissions. Three different solutions to this problem are being pursued by various research groups: the containment of luminescence using selective reflectors, directional emission within the plane of the LSC and the reduction of re-emission using luminescent centres with low self-absorption.

The concentration of sunlight to minimise the required area of solar cells reduces the specific cost of PV systems. Through reducing the cost and through enhancing the efficiency photovoltaic solar energy can be made cost-competitive with conventional energy sources. Cost-competitiveness is necessary to make solar energy a significant resource that could help to provide energy security and to mitigate anthropogenic climate change.

Appendix A

Author's Publications

A.1 Conference Proceedings

A. J. Chatten, D. J. Farrell, R. Bose, A. Dixon, C. Poelking, K. C. Gdel, M. Mazzer, and K. W. J. Barnham, "Luminescent and Geometric Concentrators for Building Integrated Photovoltaics," Proc. 37th IEEE Photovolatic Specialists Conference, Seattle: 2011.

M. González, R. Bose, M. Fisher, D. J. Farrell, A. J. Chatten, J. P. Morseman, M. W. Moss, C. McLain, A. Büchtemann, P. P. Jenkins and R. J. Walters, "Bio-derived luminescent solar concentrators using phycobiilisomes" Proc. 25th European Photovoltaic Solar Energy Conference, Valencia: 2010.

R. Bose, M. González, P. Jenkins, R. J. Walters, J. P. Morseman, M. Moss, C. Mclain, P. Linsert, A. Büchtemann, A. J. Chatten, and K. W. J. Barnham, "Resonance Energy Transfer in Luminescent Solar Concentrators," Proc. 35th IEEE Photovoltaic Specialists Conference, Honolulu: 2010.

R. Bose, D. J. Farrell, C. Pardo-Sanchez, M. Pravettoni, M. Mazzer, A. J. Chatten, and K. W. J. Barnham, "Luminescent Solar Concentrators: Cylindrical Design," Proc. 24th European Photovoltaic Solar Energy Conference, Hamburg: 2009.

M. Pravettoni, D. J. Farrell, A. J. Chatten, R. Bose, R. P. Kenny, and K. W. J. Barnham, "External quantum efficiency measurements of luminescent solar concentrators: a study of the impact of backside reflector size and shape," Proc. 24th European Photovoltaic Solar Energy Conference, Hamburg: 2009.

R. Bose, N. Chan, Y. Xiao, D. J. Farrell, A. J. Chatten, A. Büchtemann, J. Quilitz, A. Fiore, L. Manna, J. H. Nelson, A. P. Alivisatos, and K. W. J. Barnham, "The Role of Self-absorption in Luminescent Solar Concentrators," Proc. MRS Fall Meeting 2008, Boston: Materials Research Society, 2008, pp. 2-7.

R. Bose, D. J. Farrell, A. J. Chatten, A. Büchtemann, and K. W. J. Barnham, "The Luminescent Concentrator: Thin Films and Large Area Modelling," Proc. 4th Photovoltaics Science Application and Technology Conference, Bath: 2008, pp. 161-163.

R. Bose, D. J. Farrell, A. J. Chatten, M. Pravettoni, A. Buchtemann, J. Quilitz, A. Fiore, L. Manna, and K. W. J. Barnham, "Luminescent solar concentrators: Nanorods and raytrace modeling," Proc. 33rd IEEE Photovolatic Specialists Conference, San Diego: IEEE, 2008, pp. 24-28.

R. Bose, D. J. Farrell, A. J. Chatten, M. Pravettoni, A. Büchtemann, J. Quilitz, A. Fiore, L. Manna,J. H. Nelson, A. P. Alivisatos, and K. W. J. Barnham, "The Effect of Size and Dopant Concentration on the Performance of Nanorod Luminescent Solar Concentrators," Proc. 23rd European Photovoltaic Solar Energy Conference, Valencia: 2008.

M. Kennedy, A. J. Chatten, D. J. Farrell, R. Bose, A. Büchtemann, S. J. McCormack, J. Doran, K. W. J. Barnham, and B. Norton, "Luminescent Solar Concentrators: A Comparison of Thermodynamic Modelling and Ray-trace Modelling Predictions," Proc. 23rd European Photovoltaic Solar Energy Conference, Valencia: 2008.

M. Pravettoni, R. Bose, K. W. J. Barnham, A. J. Chatten, and R. P. Kenny, "Classical behaviour of output light emitted by the edge of a luminescent solar concentrator," Proc. 33rd IEEE Photovolatic Specialists Conference, San Diego: 2008, pp. 182-186.

M. Pravettoni, A. Virtuani, W. Zaaiman, R. Galleano, R. P. Kenny, E. D. Dunlop, R. Bose, and K. W. J. Barnham, "Indoor-Outdoor Characterisation of Luminescent Solar Concentrators at the European Solar Test Installation," Proc. 23rd European Photovoltaic Solar Energy Conference, Valencia: 2008.

R. Bose, D. J. Farrell, A. J. Chatten, and K. W. J. Barnham, "Luminescent Solar Concentrators," Proc. 3rd Photovoltaics Science Application and Technology Conference, Durham: 2007, pp. 63-66.

R. Bose, D. J. Farrell, A. J. Chatten, M. Pravettoni, A. Büchtemann, and K. W. J. Barnham, "Novel Configurations of Luminescent Solar Concentrators," Proc. 22nd European Photovoltaic Solar Energy Conference, Milan: 2007, pp. 210-214.

A. J. Chatten, D. J. Farrell, R. Bose, M. Debije, A. Büchtemann, and K. W. J. Barnham, "Thermodynamic Modelling of Luminescent Solar Concentrators with Reduced Top Surface Losses," Proc. 22nd European Photovoltaic Solar Energy Conference, Milan: 2007.

A.2 Refereed Journal Papers

J. Bomm, A. Büchtemann, A. J. Chatten, R. Bose, D. J. Farrell, N. Chan, Y. Xiao, L. H. Slooff, T. Meyer, A. Meyer, W. G. J. H. M. van Sark, R. Koole, "Fabrication and full characterization of state-of-the-art quantum dot luminescent solar concentrators," Solar Energy Materials and Solar Cells, vol. 95, no. 8, 2011, pp. 2087-2094.

W. G. J. H. M. van Sark, K. W. J. Barnham, L. H. Slooff, A. J. Chatten, A. Büchtemann, A. Meyer, S. J. McCormack, R. Koole, D. J. Farrell, R. Bose, E. E. Bende, A. Burgers, T. Budel, J. Quilitz, M. Kennedy, T. Meyer, C. D. M. Doneg, A. Meijerink, and D. Vanmaekelbergh, "Luminescent Solar Concentrators - A review of recent results," Optics Express, vol. 16, 2008, pp. 21773-92.

A.3 Book Chapter

A. J. Chatten, R. Bose, D. J. Farrell, Y. Xiao, N. Chan, A. Büchtemann, J. Quilitz, L. Manna, M. G. Debije, and K. W. J. Barnham, "Luminescent Solar Concentrators," Nanotechnology for Photovoltaics, L. Tsakalakos, Boca Raton, FL: CRC Press, 2010, pp. 323-349.

Bibliography

[1] OECD / IEA, "World Energy Outlook 2009," 2009.

[2] D. J. C. MacKay, *Sustainable Energy Without the Hot Air*. Cambridge: UIT Cambridge Ltd., 2009.

[3] IPCC, "IPCC Fourth Assessment Report: Climate Change 2007," 2007.

[4] OECD / IEA, "IEA Energy Statistics," 2009.

[5] IEA, "CO2 Emissions from Fuel Combustion," 2009.

[6] S. Hirschberg, G. Spiekerman, and R. Dones, "Severe accidents in the energy sector," 1998.

[7] United Nations, "Kyoto Protocol to the United Nations Framework Convention on Climate Change," 1998.

[8] IEA Photovoltaics Power Systems Programme, "Trends in Photovoltaic Applications: Survey report of selected IEA countries between 1992 and 2008," 2009.

[9] IEA, "Key World Energy Statistics," 2009.

[10] World Bank, "World Development Indicators 2008," 2008.

[11] M. A. Green, *Third Generation Photovoltaics*. Springer, 2006.

[12] D. M. Chapin, C. S. Fuller, and G. L. Pearson, "A New Silicon p-n Junction Photocell for Converting Solar Radiation into Electrical Power," *Journal of Applied Physics*, vol. 25, p. 676, 1954.

[13] M. A. Green, K. Emery, Y. Hishikawa, and W. Warta, "Solar cell efficiency tables (version 35)," *Progress in Photovoltaics: Research and Applications*, vol. 18, pp. 144–150, Mar. 2010.

[14] W. Guter, J. Schone, S. P. Philipps, M. Steiner, G. Siefer, A. Wekkeli, E. Welser, E. Oliva, A. W. Bett, and F. Dimroth, "Current-matched triple-junction solar cell reaching 41.1% conversion efficiency under concentrated sunlight," *Applied Physics Letters*, vol. 94, no. 22, p. 223504, 2009.

[15] R. R. King, A. Boca, W. Hong, X. Liu, D. Bhusari, D. Larrabee, K. M. Edmondson, D. C. Law, C. M. Fetzer, S. Mesropian, and N. H. Karam, "Band-gap-engineered architectures for high-efficiency multijunction solar cells," in *Proc. 24th European Photovoltaic Solar Energy Conference*, (Hamburg), 2009.

[16] L. Kazmerski, "Best research-cell efficiencies," 2010.

[17] W. H. Weber and J. Lambe, "Luminescent greenhouse collector for solar radiation," *Applied Optics*, vol. 15, p. 2299, Oct. 1976.

[18] A. Goetzberger and W. Greubel, "Solar energy conversion with fluorescent collectors," *Applied Physics*, vol. 14, no. 2, pp. 123–139, 1977.

[19] B. A. Swartz, T. Cole, and A. H. Zewail, "Photon trapping and energy transfer in multiple-dye plastic matrices: an efficient solar-energy concentrator.," *Optics Letters*, vol. 1, pp. 73–5, Aug. 1977.

[20] J. S. Batchelder, A. H. Zewail, and T. Cole, "Luminescent solar concentrators. 1: Theory of operation and techniques for performance evaluation," *Applied Optics*, vol. 18, pp. 3090–3110, 1979.

[21] J. S. Batchelder, A. H. Zewail, and T. Cole, "Luminescent solar concentrators 2: Experimental and theoretical analysis of their possible efficiencies," *Applied Optics*, vol. 20, p. 3733, Nov. 1981.

[22] R. W. Olson, R. F. Loring, and M. D. Fayer, "Luminescent solar concentrators and the reabsorption problem.," *Applied Optics*, vol. 20, pp. 2934–40, Sept. 1981.

[23] V. Wittwer, K. Heidler, A. Zastrow, and A. Goetzberger, "Theory of fluorescent planar concentrators and experimental results," *Journal of Luminescence*, vol. 24, pp. 873–876, 1981.

[24] A. M. Hermann, "Luminescent solar concentrators - a review," *Solar Energy*, vol. 29, no. 4, pp. 323–329, 1982.

[25] K. W. J. Barnham, J. L. Marques, J. Hassard, and P. OBrien, "Quantum-dot concentrator and thermodynamic model for the global redshift," *Applied Physics Letters*, vol. 76, no. 9, p. 1197, 2000.

[26] A. Extance, "The Concentrated Photovoltaics Industry Report 2010," 2010.

[27] J. Nelson, *The Physics of Solar Cells*. Imperial College Press, 2003.

[28] M. Planck, "Distributino of energy in the spectrum," *Annalen der Physik*, vol. 4, pp. 553–563, 1901.

[29] National Renewable Energy Laboratory, "Reference Solar Spectral Irradiance: ASTM G-173."

[30] P. T. Landsberg and P. Baruch, "The thermodynamics of the conversion of radiation energy for photovoltaics," *Journal of Physics A: Mathematical and General*, vol. 22, p. 1911, 1989.

[31] V. Badescu, "Maximum concentration ratio of direct solar radiation," *Applied Optics*, vol. 32, p. 2187, Apr. 1993.

[32] W. Shockley and H. J. Queisser, "Detailed balance limit of efficiency of pn junction solar cells 1961," *Journal of Applied Physics*, vol. 380, no. 1957, pp. 510–519, 1961.

[33] H. Pauwels and A. De Vos, "Determination of the maximum efficiency solar cell structure," *Solid-State Electronics*, vol. 24, no. 9, pp. 835–843, 1982.

[34] A. Luque, A. Martí, and A. J. Nozik, "Solar cells based on quantum dots: multiple exciton generation and intermediate bands," *Mrs Bulletin*, vol. 32, pp. 236–241, 2007.

[35] M. C. Hanna and A. J. Nozik, "Solar conversion efficiency of photovoltaic and photoelectrolysis cells with carrier multiplication absorbers," *Journal of Applied Physics*, vol. 100, no. 7, p. 074510, 2006.

[36] A. Shabaev, A. L. Efros, and A. J. Nozik, "Multiexciton generation by a single photon in nanocrystals.," *Nano Letters*, vol. 6, pp. 2856–63, Dec. 2006.

[37] R. J. Ellingson, M. C. Beard, J. C. Johnson, P. Yu, O. I. Micic, A. J. Nozik, A. Shabaev, and A. L. Efros, "Highly efficient multiple exciton generation in colloidal PbSe and PbS quantum dots," *Nano Letters*, vol. 5, no. 5, pp. 865–871, 2005.

[38] J. M. Olson, S. R. Kurtz, A. E. Kibbler, and P. Faine, "A 27.3% efficient Ga0.5In0.5P/GaAs tandem solar cell," *Applied Physics Letters*, vol. 56, no. 7, p. 623, 1990.

[39] R. R. King, "Multijunction cells: Record breakers," *Nature Photonics*, vol. 2, pp. 284–286, May 2008.

[40] B. Groß, G. Peharz, G. Siefer, M. Peters, J. C. Goldschmidt, M. Steiner, W. Guter, V. Klinger, B. George, and F. Dimroth, "Highly efficient light splitting photovoltaic receiver," in *Proc. 24th European Photovoltaic Solar Energy Conference*, (Hamburg), 2009.

[41] A. Luque and A. Martí, "Increasing the Efficiency of Ideal Solar Cells by Photon Induced Transitions at Intermediate Levels," *Physical Review Letters*, vol. 78, pp. 5014–5017, June 1997.

[42] A. De Vos and H. Pauwels, "On the thermodynamic limit of photovoltaic energy conversion," *Journal of Applied Physics*, vol. 25, pp. 119–125, 1981.

[43] J. E. Parrot, "Thermodynamics of solar cell efficiencies," *Solar Energy Materials & Solar Cells*, vol. 25, pp. 73–85, 1992.

[44] R. T. Ross and A. J. Nozik, "Efficiency of hot-carrier solar energy converters," *Journal of Applied Physics*, vol. 53, no. 5, p. 3813, 1982.

[45] P. Würfel, "Solar energy conversion with hot electrons from impact ionisation," *Solar Energy Materials & Solar Cells*, vol. 46, pp. 43–52, Apr. 1997.

[46] G. Araujo and A. Martí, "Absolute limiting efficiencies for photovoltaic energy conversion," *Solar Energy Materials & Solar Cells*, vol. 33, pp. 213–240, June 1994.

[47] J. D. Joannopoulos, S. G. Johnson, J. N. Winn, and R. D. Meade, *Photonic Crystals: Molding the Flow of Light (second edition)*. Princeton, NJ: Princeton Universtiy Press, 2008.

[48] M. van Gurp and Y. K. Levine, "Determination of transition moment directions in molecules of low symmetry using polarized fluorescence. I. Theory," *The Journal of Chemical Physics*, vol. 90, no. 8, p. 4095, 1989.

[49] M. van Gurp, T. van Heijnsbergen, G. van Ginkel, and Y. K. Levine, "Determination of transition moment directions in molecules of low symmetry using polarized fluorescence. II. Applications to pyranine, perylene, and DPH," *The Journal of Chemical Physics*, vol. 90, no. 8, p. 4103, 1989.

[50] M. G. Debije, P. P. C. Verbunt, B. C. Rowan, B. S. Richards, and T. L. Hoeks, "Measured surface loss from luminescent solar concentrator waveguides," *Applied Optics*, vol. 47, pp. 6763–8, Dec. 2008.

[51] R. W. MacQueen, Y. Y. Cheng, R. G. C. R. Clady, and T. W. Schmidt, "Towards an aligned luminophore solar concentrator," *Optics Express*, vol. 18, pp. A161–A166, May 2010.

[52] J. Klimke and A. Krell, "Polycrystalline ZrO 2 - Transparent Ceramics with High Refractive Index," 2005.

[53] G. Smestad, H. Ries, R. Winston, and E. Yablonovitch, "The thermodynamic limits of light concentrators," *Solar Energy Materials*, vol. 21, pp. 99–111, Dec. 1990.

[54] R. T. Ross, "Some Thermodynamics of Photochemical Systems," *The Journal of Chemical Physics*, vol. 46, no. 12, p. 4590, 1967.

[55] E. Yablonovitch, "Thermodynamics of the fluorescent planar concentrator," *Journal of the Optical Society of America*, vol. 70, no. 11, pp. 1362–1363, 1980.

[56] U. Rau, F. Einsele, and G. C. Glaeser, "Efficiency limits of photovoltaic fluorescent collectors," *Applied Physics Letters*, vol. 87, no. 17, p. 171101, 2005.

[57] T. Markvart, "Comment on Efficiency limits of photovoltaic fluorescent collectors [Appl. Phys. Lett. 87, 171101 (2005)]," *Applied Physics Letters*, vol. 88, no. 17, p. 176101, 2006.

[58] K. R. McIntosh, N. Yamada, and B. S. Richards, "Theoretical comparison of cylindrical and square-planar luminescent solar concentrators," *Applied Physics B*, vol. 88, no. 2, pp. 285–290, 2007.

[59] M. Kennedy, S. J. Mccormack, J. Doran, and B. Norton, "Modelling the effect of device geometry on concentration ratios of quantum dot solar concentrators," in *Proc. ISES World Solar Congress*, (Beijing), pp. 1484–1487, 2007.

[60] J. Roncali and F. Garnier, "Photon-transport properties of luminescent solar concentrators: analysis and optimization.," *Applied optics*, vol. 23, p. 2809, Aug. 1984.

[61] E. Loh Jr and D. J. Scalapino, "Luminescent solar concentrators: effects of shape on efficiency," *Applied Optics*, vol. 25, no. 12, pp. 1901–1907, 1986.

[62] A. Goetzberger, "Fluorescent solar energy collectors: operating conditions with diffuse light," *Applied Physics*, vol. 16, pp. 399–404, 1978.

[63] A. Goetzberger and V. Wittwer, "Fluorescent planar collector-concentrators: A review," *Solar Cells*, vol. 4, no. 1, pp. 3–23, 1981.

[64] V. Wittwer, W. Stahl, and A. Goetzberger, "Fluorescent planar concentrators," *Solar Energy Materials*, vol. 11, pp. 187–197, Nov. 1984.

[65] M. J. Currie, J. K. Mapel, T. D. Heidel, S. Goffri, and M. A. Baldo, "Supporting Online Material for High-efficiency organic solar concentrators for photovoltaics.," *Science*, vol. 321, pp. 226–8, July 2008.

[66] L. H. Slooff, T. Budel, A. R. Burgers, N. J. Bakker, R. Danz, T. Meyer, and A. Meyer, "The Luminescent Concentrator: Stability Issues," in *Proc. 22nd European Photovoltaic Solar Energy Conference*, (Milan), 2007.

[67] A. F. Mansour, "Optical efficiency and optical properties of luminescent solar concentrators," *Polymer Testing*, vol. 17, pp. 333–343, Aug. 1998.

[68] L. R. Wilson and B. S. Richards, "High-efficiency dyes for Luminescent Solar Concentrators - photostability and modelling," in *Proc. 23rd European Photovoltaic Solar Energy Conference*, (Valencia), 2008.

[69] A. P. Alivisatos, "Electrical Studies of Semiconductor-Nanocrystal Colloids," *MRS Bulletin*, vol. 23, no. 2, 1998.

[70] Evident Technologies, "Core Shell EviDots: High Yield , Narrow Emission, Photostable Fluorescent Labels," 2002.

[71] C. B. Murray, D. J. Norris, and M. G. Bawendi, "Synthesis and characterization of nearly monodisperse CdE (E = sulfur, selenium, tellurium) semiconductor nanocrystallites," *Journal of the American Chemical Society*, vol. 115, pp. 8706–8715, Sept. 1993.

[72] G. V. Shcherbatyuk, R. H. Inman, C. Wang, R. Winston, and S. Ghosh, "Viability of using near infrared PbS quantum dots as active materials in luminescent solar concentrators," *Applied Physics Letters*, vol. 96, no. 19, p. 191901, 2010.

[73] A. P. Alivisatos, "Perspectives on the Physical Chemistry of Semiconductor Nanocrystals," *Journal of Physical Chemistry*, vol. 100, pp. 13226–13239, Jan. 1996.

[74] S. Kim, B. Fisher, H.-J. Eisler, and M. Bawendi, "Type-II quantum dots: CdTe/CdSe(core/shell) and CdSe/ZnTe(core/shell) heterostructures.," *Journal of the American Chemical Society*, vol. 125, pp. 11466–7, Sept. 2003.

[75] X. Peng, M. C. Schlamp, A. V. Kadavanich, and A. P. Alivisatos, "Epitaxial Growth of Highly Luminescent CdSe/CdS Core/Shell Nanocrystals with Photostability and Electronic Accessibility," *Journal of the American Chemical Society*, vol. 119, pp. 7019–7029, July 1997.

[76] B. O. Dabbousi, J. Rodriguez-Viejo, and F. V. Mikulec, "(CdSe) ZnS Core Shell Quantum Dots: Synthesis and Characterization of a Size Series of Highly Luminescent Nanocrystallites," *J. Phys. Chem.*, vol. 101, pp. 9463–9475, Nov. 1997.

[77] J. Bleuse, "Optical properties of core/multishell CdSe/Zn(S,Se) nanocrystals," *Physica E*, vol. 21, no. 2-4, pp. 331–335, 2004.

[78] A. L. Efros and A. V. Rodina, "Band-edge absorption and luminescence of nonspherical nanometer-size crystals," *Physical Review B*, vol. 47, no. 15, pp. 10005–10007, 1993.

[79] D. V. Talapin, R. Koeppe, S. Götzinger, A. Kornowski, J. M. Lupton, A. L. Rogach, O. Benson, J. Feldmann, and H. Weller, "Highly Emissive Colloidal CdSe/CdS Heterostructures of Mixed Dimensionality," *Nano Letters*, vol. 3, no. 12, pp. 1677–1681, 2003.

[80] D. V. Talapin, J. H. Nelson, E. V. Shevchenko, S. Aloni, B. Sadtler, and A. P. Alivisatos, "Seeded growth of highly luminescent CdSe/CdS nanoheterostructures with rod and tetrapod morphologies.," *Nano Letters*, vol. 7, no. 10, pp. 2951–9, 2007.

[81] J. Quilitz, R. Koole, L. H. Slooff, A. J. Chatten, R. Bose, D. Farrell, N. Chan, Y. Xiao, T. Meyer, A. Meyer, W. G. J. H. M. van Sark, and A. Büchtemann, "Fabrication and full characterisation of state-of-the-art CdSe quantum dot luminescent solar concentrators," *submitted to Solar Energy Materials & Solar Cells*, 2010.

[82] X. Zhou, Y. Kobayashi, V. Romanyuk, N. Ochuchi, M. Takeda, S. Tsunekawa, and A. Kasuya, "Preparation of silica encapsulated CdSe quantum dots in aqueous solution with the improved optical properties," *Applied Surface Science*, vol. 242, no. 3-4, pp. 281–286, 2005.

[83] M. G. Hyldahl, S. T. Bailey, and B. P. Wittmershaus, "Photo-stability and performance of CdSe/ZnS quantum dots in luminescent solar concentrators," *Solar Energy*, vol. 83, no. 4, pp. 566–573, 2009.

[84] T. Förster, "Zwischenmolekulare Energiewanderung un Fluoreszenz," *Annalen der Physik*, vol. 437, no. 1-2, pp. 55–75, 1948.

[85] S. T. Bailey, G. E. Lokey, M. S. Hanes, J. D. M. Shearer, J. B. McLafferty, G. T. Beaumont, T. T. Baseler, J. M. Layhue, D. R. Broussard, and Y. Z. Zhang, "Optimized excitation energy transfer in a three-dye luminescent solar concentrator," *Solar Energy Materials & Solar Cells*, vol. 91, no. 1, pp. 67–75, 2007.

[86] M. Anni, L. Manna, R. Cingolani, D. Valerini, A. Creti, and M. Lomascolo, "Forster energy transfer from blue-emitting polymers to colloidal CdSeZnS core shell quantum dots," *Applied Physics Letters*, vol. 85, no. 18, p. 4169, 2004.

[87] A. R. Clapp, I. L. Medintz, J. M. Mauro, B. R. Fisher, M. G. Bawendi, and H. Mattoussi, "Fluorescence Resonance Energy Transfer Between Quantum Dot Donors and Dye-Labeled Protein Acceptors," *J. Am. Chem. Soc.*, pp. 301–310, 2004.

[88] G. Calzaferri, "Organic Inorganic Composites as Photonic Antenna," *Chimia*, vol. 55, no. 12, pp. 1009–1013, 2001.

[89] C. Minkowski and G. Calzaferri, "Förster-Type Energy Transfer along a Specified Axis," *Angewandte Chemie*, vol. 117, pp. 5459–5463, Aug. 2005.

[90] M. J. Currie, J. K. Mapel, T. D. Heidel, S. Goffri, and M. A. Baldo, "High-efficiency organic solar concentrators for photovoltaics," *Science*, vol. 321, pp. 226–228, 2008.

[91] O. Moudam, B. C. Rowan, M. Alamiry, P. Richardson, B. S. Richards, A. C. Jones, and N. Robertson, "Europium complexes with high total photoluminescence quantum yields in solution and in PMMA," *Chemical Communications*, pp. 6649–6651, 2009.

[92] B. C. Rowan, B. S. Richards, E. Bcrowanhwacuk, N. Robertson, A. C. Jones, P. Richardson, and O. Moudam, "Near-infrared emitting lanthanide complexes for luminescent solar concentrators," in *Proc. 23rd European Photovoltaic Solar Energy Conference*, (Valencia), 2008.

[93] B. C. Rowan, L. R. Wilson, and B. S. Richards, "Visible and near-infrared emitting lanthanide complexes for luminescent solar concentrators," in *Proc. 24th European Photovoltaic Solar Energy Conference*, (Hamburg), Jan. 2009.

[94] L. R. Wilson, B. C. Rowan, N. Robertson, O. Moudam, A. C. Jones, and B. S. Richards, "Characterization and reduction of reabsorption losses in luminescent solar concentrators," *Applied Optics*, vol. 49, p. 1651, Mar. 2010.

[95] R. Reisfeld, "Spectroscopy and nonradiative phenomena of rare earths in glasses: Future applications," *Inorganica Chimica Acta*, vol. 95, pp. 69–74, Aug. 1984.

[96] R. Reisfeld, "Industrial applications of rare earths in fiber optics, luminescent solar concentrators and lasers," *Inorganica Chimica Acta*, vol. 140, pp. 345–350, Dec. 1987.

[97] T. Saraidarov, V. Levchenko, A. Grabowska, P. Borowicz, and R. Reisfeld, "Non-self-absorbing materials for Luminescent Solar Concentrators (LSC)," *Chemical Physics Letters*, vol. 492, pp. 60–62, May 2010.

[98] C. L. Mulder, L. Theogarajan, M. J. Currie, J. K. Mapel, M. A. Baldo, M. Vaughn, P. Willard, B. D. Bruce, M. W. Moss, C. E. McLain, and J. P. Morseman, "Luminescent Solar Concentrators Employing Phycobilisomes," *Advanced Materials*, vol. 21, no. 31, pp. 3181–3185, 2009.

[99] B. S. Richards, "Ray-tracing simulations of luminescent solar concentrators containing multiple luminescent species," in *Proc. 21st European Photovoltaic Solar Energy Conference*, (Dresden), 2006.

[100] A. Burgers, L. H. Slooff, A. Buchtemann, and J. A. M. van Roosmalen, "Performance of Single Layer Luminescent Concentrators with Multiple Dyes," in *Proc. 4th World Conference on Photovoltaic Energy Conversion*, (Hawaii), pp. 198–201, IEEE, May 2006.

[101] B. S. Richards, A. Shalav, and R. P. Corkish, "A low escape-cone-loss luminescent solar concentrator," in *Proc. 19th European Photovoltaic Solar Energy Conference*, 2004.

[102] D. J. Farrell, *Characterising the Performance of Luminescent Solar Concentrators*. Ph.d. thesis, Imperial College London, 2008.

[103] M. G. Debije, D. J. Broer, and C. W. M. Bastiaansen, "Effect of dye alignment on the output of a luminescent solar concentrator," in *Proc. 22nd European Photovoltaic Solar Energy Conference*, pp. 87–89, 2007.

[104] P. P. C. Verbunt, C. W. M. Bastiaansen, D. J. Broer, and M. G. Debije, "The effect of dyes aligned by liquid crystals on luminescent solar concentrator performance," in *Proc. 24th European Photovoltaic Solar Energy Conference*, (Hamburg), 2009.

[105] C. L. Mulder, P. D. Reusswig, A. P. Beyler, H. Kim, C. Rotschild, and M. A. Baldo, "Dye Alignment in Luminescent Solar Concentrators: II. Horizontal Alignment for Energy Harvesting in Linear Polarizers," *Optics Express*, vol. 18, pp. 91–99, 2010.

[106] C. L. Mulder, P. D. Reusswig, A. M. Velázquez, H. Kim, C. Rotschild, and M. A. Baldo, "Dye alignment in luminescent solar concentrators: I. Vertical alignment for improved waveguide coupling," *Optics Express*, vol. 18, p. A79, Apr. 2010.

[107] P. P. C. Verbunt, A. Kaiser, K. Hermans, C. W. M. Bastiaansen, D. J. Broer, and M. G. Debije, "Controlling Light Emission in Luminescent Solar Concentrators Through Use of Dye Molecules Aligned in a Planar Manner by Liquid Crystals," *Advanced Functional Materials*, vol. 19, pp. 2714–2719, Sept. 2009.

[108] L. Carbone, C. Nobile, M. De Giorgi, F. Sala, G. Morello, P. Pompa, M. Hytch, E. Snoeck, A. Fiore, I. R. Franchini, M. Nadasan, A. F. Silvestre, L. Chiodo, S. Kudera, R. Cingolani, R. Krahne, and L. Manna, "Synthesis and micrometer-scale assembly of colloidal CdSe/CdS nanorods prepared by a seeded growth approach.," *Nano Letters*, vol. 7, pp. 2942–50, Oct. 2007.

[109] P. Hanrahan and W. Krueger, "Reflection from layered surfaces due to subsurface scattering," *Proceedings of the 20th annual conference on Computer graphics and interactive techniques - SIGGRAPH '93*, pp. 165–174, 1993.

[110] L. H. Slooff, E. E. Bende, and T. Budel, "The non-fluorescent flat plate concentrator," in *Proc. 24th European Photovoltaic Solar Energy Conference*, (Hamburg), 2009.

[111] L. Grabowski, "On the Theoretical Photometry of Diffuse Reflection," *The Astrophysical Journal*, vol. 39, p. 299, 1914.

[112] J. C. Goldschmidt, M. Peters, F. Dimroth, A. W. Bett, L. Steidl, R. Zentel, M. Hermle, S. W. Glunz, and G. Willeke, "Developing large and efficient fluorescent concentrator systems," in *Proc. 24th European Photovoltaic Solar Energy Conference*, (Hamburg), 2009.

[113] J. C. Goldschmidt, M. Peters, F. Dimroth, S. W. Glunz, and G. Willeke, "Efficiency enhancement of fluorescent concentrators with photonic structures and material combinations," in *Proc. 23rd European Photovoltaic Solar Energy Conference*, (Valencia), 2008.

[114] J. C. Goldschmidt, M. Peters, A. Bosch, H. Helmers, F. Dimroth, S. Glunz, and G. Willeke, "Increasing the efficiency of fluorescent concentrator systems," *Solar Energy Materials & Solar Cells*, vol. 93, pp. 176–182, Feb. 2009.

[115] J. C. Goldschmidt, M. Peters, L. Prönneke, L. Steidl, R. Zentel, B. Bläsi, A. Gombert, S. Glunz, G. Willeke, and U. Rau, "Theoretical and experimental analysis of photonic structures for fluorescent concentrators with increased efficiencies," *Physica Status Solidi (a)*, vol. 205, pp. 2811–2821, Dec. 2008.

[116] M. Peters, J. C. Goldschmidt, P. Loeper, B. Bläsi, and G. Willeke, "Lighttrapping with angular selective filters," in *Proc. 23rd European Photovoltaic Solar Energy Conference*, (Valencia), 2008.

[117] E. Yablonovitch, "Photonic band-gap structures," *Journal of the Optical Society of America B*, vol. 10, p. 283, Feb. 1993.

[118] M. G. Debije, R. H. L. van Der Blom, D. J. Broer, and C. W. M. Bastiaansen, "Using selectively-reflecting organic mirrors to improve light output from a luminescent solar concentrator," in *Proc. World Renewable Energy Congress IX*, (Florence), 2006.

[119] M. G. Debije, M. P. Van, P. P. C. Verbunt, D. J. Broer, and C. W. M. Bastiaansen, "The effect of an organic selectively-reflecting mirror on the performance of a luminescent solar concentrator," in *Proc. 24th European Photovoltaic Solar Energy Conference*, (Hamburg), 2009.

[120] M. G. Debije, M. P. Van, P. P. Verbunt, M. J. Kastelijn, R. H. L. van Der Blom, D. J. Broer, and C. W. M. Bastiaansen, "Effect on the output of a luminescent solar concentrator on application of organic wavelength-selective mirrors," *Appl. Opt.*, vol. 49, no. 4, pp. 745–751, 2010.

[121] A. J. Chatten, D. J. Farrell, R. Bose, M. G. Debije, A. Büchtemann, and K. W. J. Barnham, "Thermodynamic Modelling of Luminescent Solar Concentrators with Reduced Top Surface Losses," in *Proc. 22nd European Photovoltaic Solar Energy Conference*, (Milan), Jan. 2007.

[122] H. R. Wilson, "Fluorescent dyes interacting with small silver particles; a system extending the spectral range of fluorescent solar concentrators," *Solar Energy Materials*, vol. 16, pp. 223–234, Aug. 1987.

[123] H. R. Wilson, "Fluorescent quantum yields and long-term stability of silver island/polymer/dye systems, with applications to longer wavelength fluorescent solar concentrators," in *Proc. SPIE Conference*, (Hamburg), 1988.

[124] R. Reisfeld, "New developments in luminescence for solar energy utilization," *Optical Materials*, pp. 1–7, May 2010.

[125] S. A. Maier and H. A. Atwater, "Plasmonics: Localization and guiding of electromagnetic energy in metal/dielectric structures," *Journal of Applied Physics*, vol. 98, no. 1, p. 011101, 2005.

[126] Y. Zhang, K. Aslan, M. J. R. Previte, and C. D. Geddes, "Metal-enhanced fluorescence: Surface plasmons can radiate a fluorophores structured emission," *Applied Physics Letters*, vol. 90, no. 5, p. 053107, 2007.

[127] I. M. Pryce, D. D. Koleske, A. J. Fischer, and H. A. Atwater, "Plasmonic nanoparticle enhanced photocurrent in GaN/InGaN/GaN quantum well solar cells," *Applied Physics Letters*, vol. 96, no. 15, p. 153501, 2010.

[128] V. E. Ferry, L. A. Sweatlock, D. Pacifici, and H. A. Atwater, "Plasmonic nanostructure design for efficient light coupling into solar cells.," *Nano letters*, vol. 8, pp. 4391–7, Dec. 2008.

[129] L. H. Slooff, E. E. Bende, A. R. Burgers, T. Budel, M. Pravettoni, R. P. Kenny, E. D. Dunlop, and A. Büchtemann, "A luminescent solar concentrator with 7.1% power conversion efficiency," *Physica Status Solidi (RRL)*, vol. 2, no. 6, pp. 257–259, 2008.

[130] L. H. Slooff, E. E. Bende, A. R. Burgers, T. Budel, M. Pravettoni, R. P. Kenny, E. D. Dunlop, and A. Büchtemann, "Supporting information for "A luminescent solar concentrator with 7.1% power conversion efficiency"," *Physica Status Solidi (RRL)*, vol. 2, no. 6, 2008.

[131] J. M. Drake, M. L. Lesiecki, J. Sansregret, and W. R. L. Thomas, "Organic dyes in PMMA in a planar luminescent solar collector: a performance evaluation," *Applied Optics*, vol. 21, no. 16, pp. 2945–2952, 1982.

[132] P. D. Swift and G. B. Smith, "Color considerations in fluorescent solar concentrator stacks.," *Applied Optics*, vol. 42, pp. 5112–7, Sept. 2003.

[133] N. L. Boling, "Luminescent solar collector structure," *US Patent 4,190,465*, 1980.

[134] L. Prönneke, G. Gläser, Y. Uslu, and U. Rau, "Measurement and simulation of enhanced photovoltaics systems with fluorescent collectors," in *Proc. 24th European Photovoltaic Solar Energy Conference*, (Hamburg), 2009.

[135] T. Trupke, P. Würfel, and M. A. Green, "Up-and down-conversion as new means to improve solar cell efficiencies," in *Proc. 3rd World Conference On Photovoltaic Energy Conversion*, (Osaka), pp. 67–70, 2003.

[136] T. Trupke, A. Shalav, B. S. Richards, P. Wurfel, and M. A. Green, "Efficiency enhancement of solar cells by luminescent up-conversion of sunlight," *Solar Energy Materials & Solar Cells*, vol. 90, pp. 3327–3338, Nov. 2006.

[137] Y. Y. Cheng, T. Khoury, R. G. C. R. Clady, M. J. Y. Tayebjee, N. J. Ekins-Daukes, M. J. Crossley, and T. W. Schmidt, "On the efficiency limit of triplet-triplet annihilation for photochemical upconversion.," *Physical Chemistry Chemical Physics*, vol. 12, pp. 66–71, Jan. 2010.

[138] S. Baluschev, T. Miteva, V. Yakutkin, G. Nelles, A. Yasuda, and G. Wegner, "Up-Conversion Fluorescence: Noncoherent Excitation by Sunlight," *Physical Review Letters*, vol. 97, pp. 7–9, Oct. 2006.

[139] B. S. Richards, "Enhancing the performance of silicon solar cells via the application of passive luminescence conversion layers," *Solar Energy Materials & Solar Cells*, vol. 90, pp. 2329–2337, Sept. 2006.

[140] E. Klampaftis, D. Ross, K. R. McIntosh, and B. S. Richards, "Enhancing the performance of solar cells via luminescent down-shifting of the incident spectrum: A review," *Solar Energy Materials & Solar Cells*, vol. 93, pp. 1182–1194, Aug. 2009.

[141] M. G. Debije, "Solar Energy Collectors with Tunable Transmission," *Advanced Functional Materials*, vol. 20, pp. 1498–1502, Apr. 2010.

[142] N. C. Giebink, G. P. Wiederrecht, and M. R. Wasielewski, "Resonance-shifting to circumvent reabsorption loss in luminescent solar concentrators," *Nature Photonics*, Sept. 2011.

[143] Y.-F. Xiao, C.-L. Zou, Y.-W. Hu, Y. Li, L. Xiao, F.-W. Sun, and Q. Gong, "Broadband Enhancement of Light Harvesting in a Luminescent Solar Concentrator," *IEEE Journal of Quantum Electronics*, vol. 47, pp. 1171–1176, Sept. 2011.

[144] A. Zastrow and V. Wittwer, "Daylighting with mirror light pipes and with fluorescent planar concentrators," in *Proc. SPIE Conference*, vol. 692, pp. 227–234, 1987.

[145] A. A. Earp, G. B. Smith, J. Franklin, and P. D. Swift, "Optimisation of a three-colour luminescent solar concentrator daylighting system," *Solar Energy Materials*, vol. 84, pp. 411–426, 2004.

[146] C. Wang, H. Abdul-Rahman, and S. P. Rao, "Daylighting can be fluorescent: Development of a fiber solar concentrator and test for its indoor illumination," *Energy and Buildings*, vol. 42, pp. 717–727, May 2010.

[147] C. Wang, H. Abdul-Rahman, and S. P. Rao, "A new design of luminescent solar concentrator and its trial run," *International Journal of Energy Research*, 2010.

[148] R. Koeppe, A. Neulinger, P. Bartu, and S. Bauer, "Video-speed detection of the absolute position of a light point on a large-area photodetector based on luminescent waveguides.," *Optics express*, vol. 18, pp. 2209–18, Feb. 2010.

[149] D. Lefteros, "Characterisation of fluorescent collectors based on solid, liquid and Langmuir Blodget (LB) films," in *Proc. 21st European Photovoltaic Solar Energy Conference*, (Dresden), pp. 443–446, 2006.

[150] K. Heidler, "Design considerations for the fluorescent planar concentrator / III-V solar cell system," in *Proc. 7th EC Photovoltaic Solar Energy Conference*, (Sevilla), 1986.

[151] Schott AG, "Schott Optical Glass Data Sheets," 2011.

[152] L. R. Wilson and B. S. Richards, "Measurement method for photoluminescent quantum yields of fluorescent organic dyes in polymethyl methacrylate for luminescent solar concentrators.," *Applied optics*, vol. 48, pp. 212–20, Jan. 2009.

[153] A. J. Chatten, K. W. J. Barnham, B. F. Buxton, N. J. Ekins-Daukes, and M. A. Malik, *Quantum dot solar concentrators*, pp. 909–917. Springer, 2004.

[154] K. Heidler, A. Goetzberger, and V. Wittwer, "Fluorescent planar concentrator (FPC) Monte-Carlo Computer model limit efficiency and latest experimental results," in *Proc. 4th EC PV Solar Energy Conference*, (Stresa, Italy), 1982.

[155] M. Carrascosa, S. Unamuno, and F. Agullo-Lopez, "Monte Carlo simulation of the performance of PMMA luminescent solar collectors.," *Applied Optics*, vol. 22, p. 3236, Oct. 1983.

[156] J. Sansregret, J. M. Drake, W. R. L. Thomas, and M. L. Lesiecki, "Light transport in planar luminescent solar concentrators: the role of DCM self-absorption," *Applied Optics*, vol. 22, no. 4, pp. 573–577, 1983.

[157] V. Wittwer, K. Heidler, W. Stahl, A. Zastrow, and A. Goetzberger, "Fluorescent planar concentrators," in *Proc. Solar World Congress 1983*, (Perth), 1983.

[158] M. S. de Cardona, M. Carrascosa, F. Meseguer, F. Cusso, and F. Jaque, "Outdoor evaluation of luminescent solar concentrator prototypes," *Applied Optics*, vol. 24, pp. 2028–2032, 1985.

[159] M. Sidrach de Cardona, M. Carrascosa, F. Meseguer, F. Cusso, and F. Jaque, "Edge effect on luminescent solar concentrators," *Solar Cells*, vol. 15, no. 3, pp. 225–230, 1985.

[160] R. Reisfeld, M. Eyal, V. Chernyak, and R. Zusman, "Luminescent solar concentrators based on thin films of polymethylmethacrylate on a polymethylmethacrylate support 1," *Solar energy materials*, vol. 17, no. 6, pp. 439–455, 1988.

[161] A. Schüler, A. Kostro, C. Galande, M. Valle Del Olmo, E. de Chambrier, and B. Huriet, "Principles of Monte-Carlo Ray-Tracing Simulations of Quantum Dot Solar Concentrators," in *Proc. ISES Solar World Congress 2007*, pp. 1033–1037, 2007.

[162] T. J. J. Meyer, J. Hlavaty, L. Smith, E. R. Freniere, and T. Markvart, "Ray racing techniques applied to the modelling of fluorescent solar collectors," *Proc. SPIE Conference*, pp. 72110N–72110N–11, 2009.

[163] R. Reisfeld, D. Shamrakov, and C. Jorgensen, "Photostable solar concentrators based on fluorescent glass films," *Solar Energy Materials & Solar Cells*, vol. 33, pp. 417–427, Aug. 1994.

[164] A. J. Chatten, K. W. J. Barnham, U. Blieske, N. J. Ekins-Daukes, M. A. Malik, J. L. Marques, and M. L. Williams, "Characterising quantum dot concentrators," in *Proc. 28th IEEE Photovoltaic Specialists Conference*, (Anchorage), pp. 865–868, IEEE, 2000.

[165] A. J. Chatten, K. W. J. Barnham, B. F. Buxton, N. J. Ekins-daukes, and M. A. Malik, "A New Approach to Modelling Quantum Dot Concentrators," *Solar Energy Materials & Solar Cells*, vol. 75363, no. 75, pp. 363–371, 2003.

[166] A. J. Chatten, K. W. J. Barnham, B. F. Buxton, N. J. Ekins-Daukes, and M. A. Malik, "Quantum Dot Solar Concentrators and Modules," in *Proc. 19th European Photovoltaic Solar Energy Conference*, (Paris), pp. 109–112, 2004.

[167] A. J. Chatten, D. J. Farrell, C. M. Jermyn, P. Thomas, B. F. Buxton, A. Buchtemann, R. Danz, and K. W. J. Barnham, "Thermodynamic modelling of luminescent solar concentrators," in *Proc. 31st IEEE Photovoltaic Specialists Conference*, (Orlando), pp. 82–85, IEEE, 2005.

[168] A. J. Chatten, D. J. Farrell, B. F. Buxton, A. Buchtemann, and K. W. J. Barnham, "Thermodynamic modelling of luminescent solar concentrators," in *Proc. 21st European Photovoltaic Solar Energy Conference*, (Dresden), pp. 315–320, 2006.

[169] A. R. Burgers, L. H. Slooff, R. Kinderman, and J. A. M. van Roosmalen, "Modelling of luminescent concentrators by ray-tracing," in *Proc. 20th European Photovoltaic Solar Energy Conference*, (Barcelona), 2005.

[170] J. Balenzategui and F. Chenlo, "Measurement and analysis of angular response of bare and encapsulated silicon solar cells," *Solar Energy Materials & Solar Cells*, vol. 86, pp. 53–83, Feb. 2005.

[171] J. Roncali and F. Garnier, "No Title," *Solar Cells*, vol. 13, no. 2, pp. 133–143, 1984.

[172] M. Pravettoni, D. J. Farrell, A. J. Chatten, R. Bose, R. P. Kenny, and K. W. J. Barnham, "External quantum efficiency measurements of luminescent solar concentrators: a study of the impact of backside reflector size and shape," in *Proc. 24th European Photovoltaic Solar Energy Conference*, (Hamburg), 2009.

[173] A. Goetzberger and O. Schirmer, "Second stage concentration with tapers for fluorescent solar collectors," *Applied Physics*, vol. 42, pp. 712–58, May 1979.

[174] T. Maruyama, "Wedge-shaped light concentrator using total internal reflection," *Solar Energy Materials & Solar Cells*, vol. 57, pp. 75–83, Feb. 1999.

[175] P. Kittidachachan, L. Danos, T. J. J. Meyer, N. Alderman, and T. Markvart, "Photon Collection Efficiency of Fluorescent Solar Collectors," *CHIMIA International Journal for Chemistry*, vol. 61, pp. 780–786, Dec. 2007.

[176] A. Earp, G. B. Smith, P. D. Swift, and J. Franklin, "Maximising the light output of a Luminescent Solar Concentrator," *Solar Energy*, vol. 76, no. 6, pp. 655–667, 2004.

[177] P. D. Swift, G. B. Smith, and J. B. Franklin, "Light-to-light efficiencies in luminescent solar concentrators," in *Proc. SPIE Conference*, pp. 21–28, SPIE, 1999.

[178] B. Walker, *Optical Engineering Fundamentals, Second Edition*. Bellingham, WA: SPIE Press, 2008.

[179] C. F. Rapp and N. L. Boling, "Luminescent Solar Concentrators," in *Proc. 13th Photovoltaic Specialists Conference*, vol. 88, (Washington, DC), pp. 690–693, 1978.

[180] W. Viehmann and R. Frost, "Thin film waveshifter coatings for fluorescent radiation converters," *Nuclear Instruments and Methods*, vol. 167, pp. 405–415, Dec. 1979.

[181] C. F. Rapp and N. L. Boling, "Solar collector structures containing thin film polysiloxane, and solar cells," *US Patent 4,173,495*, 1979.

[182] A. Zastrow, *Physikalische Analyse der Energie-Verlustmechanismen im Fluoreszenzkollektor*. Ph.d. thesis, Albert-Ludwigs-Universität, Freiburg, Germany, 1981.

[183] A. Schüler, M. Python, M. Delolmo, and E. Dechambrier, "Quantum dot containing nanocomposite thin films for photoluminescent solar concentrators," *Solar Energy*, vol. 81, pp. 1159–1165, Sept. 2007.

[184] S. A. Evenson and A. H. Rawicz, "Thin-film luminescent concentrators for integrated devices: a cookbook," *Applied Optics*, vol. 34, p. 7302, Nov. 1995.

[185] R. Bose, D. J. Farrell, A. J. Chatten, M. Pravettoni, A. Büchtemann, and K. W. J. Barnham, "Novel Configurations of Luminescent Solar Concentrators," in *Proc. 22nd European Photovoltaic Solar Energy Conference*, (Milan), pp. 210–214, 2007.

[186] M. Pravettoni, R. Bose, K. W. J. Barnham, A. J. Chatten, and R. P. Kenny, "Classical behaviour of output light emitted by the edge of a luminescent solar concentrator," in *Proc. 33rd IEEE Photovolatic Specialists Conference*, (San Diego), pp. 182–186, May 2008.

[187] M. Bendig, J. Hanika, H. Dammertz, J. C. Goldschmidt, M. Peters, and M. Weber, "Simulation of Fluorescent Concentrators," in *IEEE Symposium on Interactive Ray Tracing*, pp. 93–98, 2008.

[188] K. W. J. Barnham, M. Mazzer, and B. Clive, "Resolving the energy crisis: nuclear or photovoltaics?," *Nature Materials*, vol. 5, pp. 161–164, Mar. 2006.

[189] R. H. Inman, G. V. Shcherbatyuk, D. Medvedko, a. Gopinathan, and S. Ghosh, "Cylindrical luminescent solar concentrators with near-infrared quantum dots.," *Optics express*, vol. 19, pp. 24308–13, Nov. 2011.

[190] O. Sulima, J. Cox, and P. Sims, "High-performance monolithic AlGaAs/GaAs photovoltaic arrays coupled to scintillating fibers for UGS application," in *Proc. SPIE Conference*, vol. 4743, p. 120, 2002.

[191] O. Sulima, J. Cox, P. Sims, M. Mauk, and N. Faleev, "AlGaAs photovoltaic arrays spectrally matched to photoluminescent fibers for UGS application," in *Proc. SPIE Conference*, vol. 5090, p. 360, 2003.

[192] V. Fara, A. Popa, I. Dorobantu, and R. Grigorescu, "Fluorescent solar concentrators. Experimental results," *Renewable Energy*, vol. 1, no. 3-4, pp. 469–471, 1991.

[193] G. B. Smith and J. B. Franklin, "Sunlight collecting and transmitting system," *US Patent 5,548.490*, 1996.

[194] G. B. Smith and J. B. Franklin, "Sunlight collecting and transmitting system," *US Patent 5,709,456*, Jan. 1998.

[195] G. B. Smith and J. B. Franklin, "Sunlight collecting and transmitting system," *US Patent 6,059,438*, Jan. 2000.

[196] S. Tsoi, C. W. M. Bastiaansen, and M. G. Debije, "Enhancing light output of fluorescent waveguides with a mircolens system," in *Proc. 24th European Photovoltaic Solar Energy Conference*, (Hamburg), 2009.

[197] S. Tsoi, D. J. Broer, C. W. M. Bastiaansen, and M. G. Debije, "Using Lenses to Improve the Output of a Patterned Luminescent Solar Concentrator," *Advanced Energy Materials*, vol. 3, no. 3, pp. 337–341, 2013.

[198] M. Mazzer, B. M. Clive, and K. W. J. Barnham, "Solar concentrators," *US Patent Application Publication 0277494*, 2009.

[199] N. Walker, "Advantages of the Microsharp Linear Fresnel Lens for Low Concentration Solar Optics," *Whitepaper - Microsharp Corporation Ltd*, 2010.

[200] P. Würfel, "The chemical potential of radiation," *Journal of Physics C*, vol. 15, no. January, pp. 3967–3985, 1982.

[201] A. J. Chatten, D. J. Farrell, R. Bose, A. Dixon, C. Poelking, K. C. Gödel, M. Mazzer, and K. W. J. Barnham, "Luminescent and Geometric Concentrators for Building Integrated Photovoltaics," in *Proc. 37th IEEE Photovolatic Specialists Conference*, (Seattle), 2011.

[202] Y. K. Olsson, G. Chen, R. Rapaport, D. T. Fuchs, V. C. Sundar, J. S. Steckel, M. G. Bawendi, A. Aharoni, and U. Banin, "Fabrication and optical properties of polymeric waveguides containing nanocrystalline quantum dots," *Applied Physics Letters*, vol. 85, no. 19, p. 4469, 2004.

[203] B. C. Rowan, S. Gallagher, J. Doran, and B. Norton, "Indoor characterisation of small-scale quantum dot solar concentrators of various geometries and quantum dot concentrations," in *Proc. 21st European Photovoltaic Solar Energy Conference*, (Dresden), pp. 2229–2232, 2006.

[204] M. Kennedy, S. J. McCormack, J. Doran, and B. Norton, "Improving the optical efficiency and concentration of a single-plate quantum dot solar concentrator using near infra-red emitting quantum dots," *Solar Energy*, vol. 83, pp. 978–981, July 2009.

[205] B. Jones, M. Scarpulla, J. Baker, K. Sivula, and K. Alberi, "Nanocrystalline Luminescent Solar Converters," 2004.

[206] J. Bomm, A. Büchtemann, A. Fiore, L. Manna, J. H. Nelson, D. Hill, and W. G. J. H. M. van Sark, "Fabrication and spectroscopic studies on highly luminescent CdSe/CdS nanorod polymer composites.," *Beilstein journal of nanotechnology*, vol. 1, pp. 94–100, Jan. 2010.

[207] D. Sahin, B. Ilan, and D. F. Kelley, "Monte-Carlo simulations of light propagation in luminescent solar concentrators based on semiconductor nanoparticles," *Journal of Applied Physics*, vol. 110, no. 3, p. 033108, 2011.

[208] X. Peng, L. Manna, W. Yang, J. Wickham, E. Scher, A. V. Kadavanich, and A. P. Alivisatos, "Shape control of CdSe nanocrystals," *Nature*, vol. 404, no. March, pp. 59–61, 2000.

[209] M. Nirmal, D. J. Norris, M. Kuno, and M. G. Bawendi, "Observation of the "Dark Exciton" in CdSe Quantum Dots," *Physical Review Letters*, vol. 75, no. 20, pp. 3728–3731, 1995.

[210] R. Bose, M. González, P. Jenkins, R. J. Walters, J. P. Morseman, M. Moss, C. Mclain, P. Linsert, A. Büchtemann, A. J. Chatten, and K. W. J. Barnham, "Resonance Energy Transfer in Luminescent Solar Concentrators," in *Proc. 35th IEEE Photovoltaic Specialists Conference*, (Honolulu), 2010.

[211] J. Grabowski and E. Gantt, "Excitation energy migration in phycobilisomes: comparison of experimental results and theoretical predictions," *Photochemistry and Photobiology*, vol. 28, no. 1, pp. 47–54, 1978.

[212] J. Grabowski and E. Gantt, "Photophysical properties of phycobiliproteins from phycobilisomes: fluorescence lifetimes, quantum yields and polarization spectra," *Photochemistry and Photobiology*, vol. 28, no. 1, pp. 39–45, 1978.

[213] E. Gantt, "Phycobilisomes," *Annual Review of Plant Physiology*, vol. 32, pp. 327–347, 1981.

[214] A. N. Glazer, "Phycobiliproteins - a family of valuable, widely used fluorophores," *Journal of Applied Phycology*, vol. 6, pp. 115–112, 1994.

[215] M. González, R. Bose, M. Fisher, D. Farrell, A. J. Chatten, J. P. Morseman, M. W. Moss, C. Mclain, A. Büchtemann, P. P. Jenkins, and R. Walters, "Bio-derived luminescent solar concentrators using phycobiilisomes," in *Proc. 25th European Photovoltaic Solar Energy Conference*, (Valencia), 2010.